UNIVERSITAT ROVIRA I VIRGILI

DEVELOPMENT AND APPLICATION OF PHOTONIC TECHNOLOGIES FOR INDUSTRY 4.0

Víctor Llamas Martínez

ADVERTIMENT. L'accés als continguts d'aquesta tesi doctoral i la seva utilització ha de respectar els drets de la persona autora. Pot ser utilitzada per a consulta o estudi personal, així com en activitats o materials d'investigació i docència en els termes establerts a l'art. 32 del Text Refós de la Llei de Propietat Intel·lectual (RDL 1/1996). Per altres utilitzacions es requereix l'autorització prèvia i expressa de la persona autora. En qualsevol cas, en la utilització dels seus continguts caldrà indicar de forma clara el nom i cognoms de la persona autora i el títol de la tesi doctoral. No s'autoritza la seva reproducció o altres formes d'explotació efectuades amb finalitats de lucre ni la seva comunicació pública des d'un lloc aliè al servei TDX. Tampoc s'autoritza la presentació del seu contingut en una finestra o marc aliè a TDX (framing). Aquesta reserva de drets afecta tant als continguts de la tesi com als seus resums i índexs.

ADVERTENCIA. El acceso a los contenidos de esta tesis doctoral y su utilización debe respetar los derechos de la persona autora. Puede ser utilizada para consulta o estudio personal, así como en actividades o materiales de investigación y docencia en los términos establecidos en el art. 32 del Texto Refundido de la Ley de Propiedad Intelectual (RDL 1/1996). Para otros usos se requiere la autorización previa y expresa de la persona autora. En cualquier caso, en la utilización de sus contenidos se deberá indicar de forma clara el nombre y apellidos de la persona autora y el título de la tesis doctoral. No se autoriza su reproducción u otras formas de explotación efectuadas con fines lucrativos ni su comunicación pública desde un sitio ajeno al servicio TDR. Tampoco se autoriza la presentación de su contenido en una ventana o marco ajeno a TDR (framing). Esta reserva de derechos afecta tanto al contenido de la tesis como a sus resúmenes e índices.

WARNING. Access to the contents of this doctoral thesis and its use must respect the rights of the author. It can be used for reference or private study, as well as research and learning activities or materials in the terms established by the 32nd article of the Spanish Consolidated Copyright Act (RDL 1/1996). Express and previous authorization of the author is required for any other uses. In any case, when using its content, full name of the author and title of the thesis must be clearly indicated. Reproduction or other forms of for profit use or public communication from outside TDX service is not allowed. Presentation of its content in a window or frame external to TDX (framing) is not authorized either. These rights affect both the content of the thesis and its abstracts and indexes.

UNIVERSITAT
ROVIRA i VIRGILI

Development and application of photonic technologies for industry 4.0

Víctor Llamas Martínez

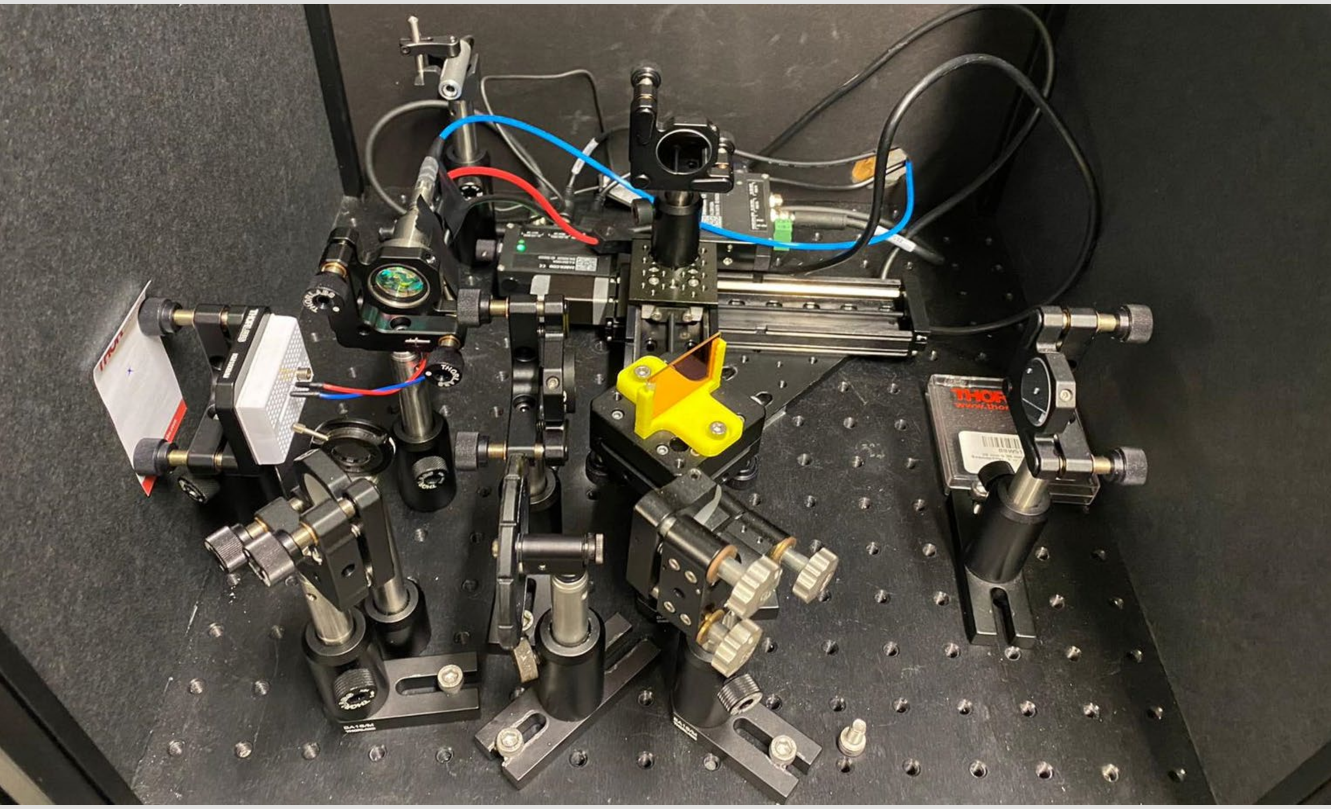

DOCTORAL THESIS

2021

Víctor Llamas Martínez

Development and application of photonic technologies for industry 4.0.

Doctoral thesis

Supervised by:

Prof. Dr. Francesc Díaz

Prof. Dr. Xavier Mateos

Dr. Josep Maria Serres

Doctoral Programme in Nanoscience, Materials and Chemical Engineering
Department of Physical and Inorganic Chemistry
Physics and Crystallography of Materials and nanomaterials (FiCMA-FiCNA)

UNIVERSITAT ROVIRA i VIRGILI

eurecat
Centre Tecnològic de Catalunya

TARRAGONA - 2021

Development and application of photonic technologies for industry 4.0.

Víctor Llamas Martínez

Física i Cristal·lografia de Materials i Nanomaterials (FiCMA - FiCNA)

Departament de Química Física i Inorgànica

Universitat Rovira i Virgili

Tarragona, Spain

UNIVERSITAT
ROVIRA I VIRGILI

DEPARTAMENT DE QUÍMICA FÍSICA
I INORGÀNICA

Campus Sescelades
Marcel·lí Domingo, s/n
43007 Tarragona
Tel. +34 977 55 81 37
Fax +34 977 55 95 63
www.quimica.urv.es

Prof. Dr. Francesc Díaz, Prof. Dr. Xavier Mateos i Dr. Josep Maria Serres del Departament de Química Física i Inorgànica de la Universitat Rovira i Virgili,

FEM CONSTAR,

que aquest treball, titulat **Development and application of photonics technologies for industry 4.0**, que presenta **Victor Llamas Martinez** per a l'obtenció del títol de Doctor, ha estat realitzat sota la nostra direcció al **Departament de Química Física i Inorgànica** d'aquesta universitat.

Tarragona 08/11/2021

Francisco Manuel Díaz González - DNI 33816818X (AUT)

Digitally signed by Francisco Manuel Díaz González - DNI 33816818X (AUT)
Date: 2021.11.04 22:37:25 +01'00'

Prof. Dr. Francesc Díaz

MATEOS FERRE, XAVIER (FIRMA)

Firmado digitalmente por MATEOS FERRE, XAVIER (FIRMA)
Nombre de reconocimiento (DN): c=ES, serialNumber=39722594F, sn=MATEOS, givenName=XAVIER, cn=MATEOS FERRE, XAVIER (FIRMA)
Fecha: 2021.11.04 10:59:32 +01'00'

Prof. Dr. Xavier Mateos

SERRES SERRES JOSEP MARIA - 47628394V

Firmado digitalmente por SERRES SERRES JOSEP MARIA - 47628394V
Fecha: 2021.11.04 10:34:59 +01'00'

Dr. Josep Maria Serres

ABSTRACT

Development and application of photonic technologies for industry 4.0.

- Victor Llamas Martínez –

In this thesis, photonic technologies such as lasers, sensors and detectors has been developed in order to provide solutions to Industry 4.0.

Special attention has been paid to waveguides inscribed in crystals thanks to the femtosecond-direct laser writing technique, with which microchip lasers in the range of $\lambda \sim 2\mu m$ have been developed, ideal for use in medicine. The lasered guides have different geometries, impossible to achieve by other methods, in order to optimize parameters such as the efficiency, the laser threshold or the maximum pump power.

On the other hand, photonic sensors have been created by using waveguides with different geometries and characteristics. These are capable of confining light inside and making it interact with different liquids, being able to detect changes in its refractive index and thereby determine the presence of impurities. Fabry-Perot evanescence and interferometry processes have been studied.

Finally, photonic sensors have been developed, adapted to the needs of each production chain. With them it has been possible to create control systems that offer an efficient, innovative and economically competitive service. The developed sensors technology was applied for innovative concepts for industry 4.0. This work emphasizes the needed of the industry for real and inline/online monitoring, machine learning systems for a better green manufacturing.

Keywords: Waveguide lasers, Industry 4.0, Femtosecond-direct laser writing, photonics-based sensing techniques

PREFACE

This PhD thesis was carried out within the research group Physics and Crystallography of Materials and Nanomaterials (FiCMA – FiCNA), of the Department of Physical and Inorganic Chemistry of the Universitat Rovira i Virgili (URV), Tarragona, Spain, between October 2018 and December 2021. It was supervised by Dr. Josep María Serres, Prof. Dr. Xavier Mateos and Prof. Dr. Francesc Díaz.

The study has been possible thanks to the financial support provided by Eurecat with the Vicente Lopez Grant, Spanish Government (project No. MAT2016-75716-C2-1-R (AEI/FEDER, UE), project FIS2017-87970-R), by the Generalitat de Catalunya (project No. 2017SGR755) and by the Junta de Castilla y León (project SA287P18). For international mobility was possible to the funding received by the European Union's Horizon 2020 research and innovation programme under grant agreement number MBI002493 Laserlab-Europe.

The research has been carried out in collaboration with several international research groups:

- Dr. Valentin Petrov and Dr. Uwe Griebner at the Max-Born Institute for Nonlinear Optics and Short Pulse Spectroscopy (Berlin, Germany)
- Dr. Pavel Loiko at the Centre de recherche sur les Ions, les Matériaux et la Photonique (CIMAP), Université de Caen (Caen, France)
- Dr. Javier Rodriguez Vazquez de Aldana at the Universtiy of Salamanca (Salamanca, Spain)

Víctor Llamas Martinez
Tarragona, 2021

ACKNOWLEDGMENTS

Quiero agradecer el tiempo y la paciencia conmigo de toda la gente que me ha ayudado en esta tesis doctoral, principalmente a mi tutor el Dr. Josep María Serres Serres quien con sus conocimientos y apoyo me guio a través de cada una de las etapas de este proyecto para alcanzar los resultados que buscaba. También quiero agradecer a la universidad Rovira i Virgili, así como a la fundación Eurecat por brindarme todos los recursos y herramientas que fueron necesarios para llevar a cabo el proceso de investigación. No hubiese podido conseguir estos resultados de no haber sido por su incondicional ayuda.

Por último, quiero agradecer a todos mis compañeros y a mi familia, por apoyarme aun cuando mis ánimos decaían. En especial, quiero hacer mención de mis padres y mi novia que siempre estuvieron ahí para darme palabras de apoyo y un abrazo reconfortante para renovar energías.

Muchas gracias a todos.

ACRONYMS

BS: Beam Splitter

CALGO: Calcium Gadolinium Aluminum Tetraoxide $CaGdAlO_4$

CR: Cross Relaxation

DOF: Depth Of Field

FFT: Fast Fourier Transform

FOV: Field Of View

Fs-DLW: Femtosecond-Direct Laser Writing

FT: Fourier Transform

FTIR: Fourier Transform Infra-Red

HG: Hermite Gauss

HTS: High-Temperature Solution

IR: InfraRed

KLuW: Potassium Lutecium double Tungstate $KLu(WO_4)_2$

LG: Laguerre Gauss

LR: Lateral Resolution

MV: Machine Vision

OSA: Optical Spectrum Analyzer

RI: Refractive Index

SNR: Signal-Noise Ratio

SR: Spectral Resolution

TEM: Transversal Electro-Magnetic

TOC, $\boldsymbol{T_{oc}}$: Transmission Output Coupler

TSSG-SC : Top-Seeded Solution Growth Slow-Cooling Method.

VA: View Angle

WG: Waveguide

ZR, $\boldsymbol{z_R}$: Rayleigh Zone

Table of contents

1

MOTIVATION OF THIS WORK

Talk about industry 4.0. is to talk about how industrial processes have changed the way of life of people in the last two centuries. In order to better understand what this revolution may entail; it is necessary to understand what the previous industrial revolutions entailed. To do this, we are going to start by explaining a brief history of the innovations that occurred since the 18th century.

The **First** industrial Revolution was the transition to new manufacturing processes in Europe and united states, in the period between 1760 and 1840 [1]. This transition started with the use of water and steam power, new chemical manufacturing and iron production processes which yields to the development of machine tools and the rise of the mechanized factory system. This revolution produces an improvement in the living conditions of the population, which began to exhibit unprecedented, sustained growth.

The **Second** Industrial Revolution, also known as the Technological Revolution, was a period between 1871 and 1914 characterized by a rapid industrial development, primarily in the United Kingdom, Germany and the United States, but also in France, the Netherlands, Italy and Japan [2]. This period was characterized by the build-out of railroads, large-scale iron and steel production, widespread use of machinery in manufacturing, use of the telegraph, petroleum, and the beginning of electrification. It also was the period during which modern organizational methods for operating large-scale businesses over vast areas came into use. This revolution was accompanied by a huge increase in the production efficiency of each worker, with technological and sanitary improvements. Those developments affect to crops, medicine, and the purchasing power of the population, giving rise to a demographic boom even greater than what happened in the first industrial revolution.

The **Third** Industrial Revolution, also known as the Digital Revolution, was a multipolar process, led by the United States, Japan and the European Union. Its beginnings date from the middle of the 20th century with the arrival of the new computing technologies that propitiates a new communication era [3]. Central to this revolution is the mass production and widespread use of digital logic, Metal Oxide Semiconductor Transistor (MOS transistors), integrated circuits (IC) chips, and their derived technologies, including computers, microprocessors, digital cellular phones, and the Internet [4]. These technological innovations have transformed traditional production and business techniques [5], allowing everyone to have access to new technologies and democratizing access to information, which, in turn, led to technological and commercial development in less developed countries.

In the last 20 years due to rising raw power of computers [6] and the emergence of new sensorics and algorithmic technologies, a new industrial revolution, **industry 4.0**, is rising. In this, machines and sensors communicate with each other to allow the optimization of industrial processes [7]. Industry 4.0 holds the promise of a new revolution that combines advanced production and operations techniques with smart technologies that will be integrated into organizations, people, and assets.

All of them are oriented in the optimization of the productivity, this involves creating new, more sustainable manufacturing techniques and the complete automation of processes, as well as a more exhaustive and automated data processing.

In this context photonics can be considered as one of the most important enabling technologies for Industry 4.0 [8][9]. Photonics provides communication links with the development and implementation of optical fibers and 5G, providing a higher data transfer between devices. In addition, photonics-based sensors have proven to be an ideal solution for a large number of applications, thanks to their reliability, speed, precision and miniaturization [10] capacity. Among those devices the most notable is the CMOS, detector of all digital cameras, which has allowed the development of artificial vision systems [11]. In addition, in recent years optical computing technology is being developed [12], which is expected to improve the processing speed of computers drastically, thus changing the current paradigm by replacing electrons with photons as a means of transmitting information.

In this thesis, in order to study and implement photonic technologies in Industry 4.0, a series of projects have been carried out, encompassed in the study of different light sources and detectors, as well as artificial vision systems, in order to create solutions for problems that exist in industrial processes. As will be seen in the following chapters, many systems have been developed; specific for each industry need, focused on providing solutions by applying the latest photonic technologies.

2

INTRODUCTION

This chapter gives us an overview about the history of the industrial revolutions, the technologies developed in each one as well as the improvements in the quality of life in the population and how we went from a mainly subsistence economy to the current model. It will also talk about the new industrial revolution that is starting, the industry 4.0. The most relevant technologies will be explained, as well as the future expectations of this. In particular, two topics that are especially relevant and that will be worked on in this thesis will be highlighted, the development of laser systems in the mid-IR λ≅2um, especially relevant in medicine and engineering, and the computational processes, essential in the development of new sensors for the industry in this field machine vision and digital signal processing are especially relevant.

2.1. Industrial revolutions.

Industrial revolutions have been a huge advance in the history of mankind. From the beginning of the first industrial revolution in the 18th century to the present day, the productive fabric of our society has totally changed and with it our quality of life and purchasing power. This section will explain the advances that occurred in each historical period and how they affected the population, as well as the characteristics of this new industrial revolution, Industry 4.0 and how it intends to change the world.

2.1.1. History of industrial revolutions

The Industrial Revolution or **First Industrial Revolution** is the process of economic transformation, which began in the Kingdom of Great Britain in 1760 [1] extending a few decades later to much of Western Europe and Anglo-Saxon America an ending in 1840. During this period, the largest set of economic, technological and social transformations in the history of mankind took place since the Neolithic [13].

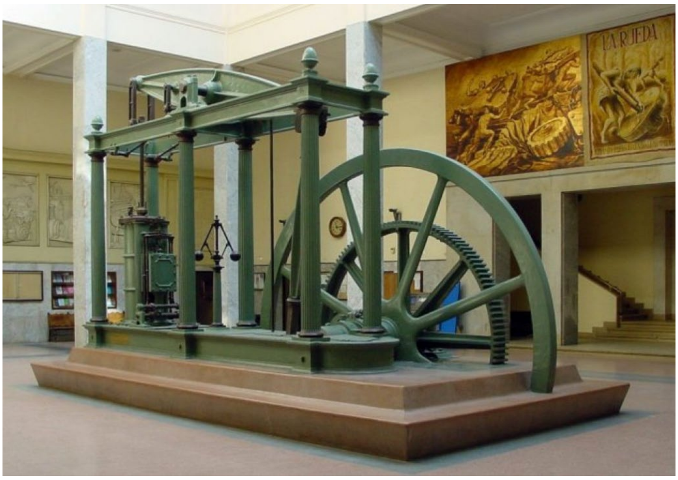

Figure 1. A Watt-type steam engine, built by David Napier & Son Limited (London) in 1859.

The introduction of James Watt's steam engine (patented in 1769) in the different industries marked the beginning of these changes, since its use meant a spectacular increase in production capacity [14]. This transition began in the textile industry, as well as in matters related to the extraction and use of coal. The expansion of trade was possible thanks to the development of communications, with the construction of railways, canals, and roads.

From this moment on, a transition began that would end centuries of a workforce based on manual work and the use of animal traction, these being replaced by machinery for industrial manufacturing and for the transport of goods and passengers.

This shift from a primarily agricultural economy to an industrial economy greatly influenced the population, which experienced rapid growth especially in urban areas. As a consequence of industrial development, new groups or social classes were born headed by the proletariat (industrial workers and poor peasants) and the bourgeoisie, owner of the means of production and possessor of most of the income and capital.

This industrial revolution marks a turning point in history, modifying and influencing all aspects of everyday life in one way or another. The production of both agriculture and the nascent industry multiplied while the production time decreased. From 1800 on, wealth and per capita income multiplied as it had never done in history, since until then per capita Gross domestic product (GDP) had practically remained stagnant for centuries [15].

The **Second** Industrial Revolution, also known as the Technological Revolution, was a phase of rapid standardization and industrialization. It is estimated that it began in 1871 and ended in 1914 with the First World War. These changes began in the United Kingdom and spread throughout Europe, North America and Japan [2].

Currently, technological and scientific advances begin to take on a more complex turn. With this, access to different natural resources, unavailable or not very useful until that moment, was achieved. Among them, the use of metals such as steel, zinc, aluminum, nickel, copper, magnesium and chromium stand out. In addition, chemical products are beginning to be taken into account thanks to the advancement of this industry. Products such as soda, artificial colors, explosive materials, cement or fertilizers are being used more and more frequently.

One of the most important effects of the Second Industrial Revolution can be found in transportation. During this new era the world of transport was modernized, in 1840 there were less than 4,000 kilometers of track; In 1870, 100,000 kilometers were exceeded in Europe and 70,000 in the United States. This improvement meant the possibility of putting in contact markets that until now did not maintain any type of relationship. Therefore, both the transport of people and goods were facilitated, facilitating and drastically cheapening trade between countries, peoples and cultures.

Figure 2. Steam locomotive.

In parallel, new forms of energy begin to appear. Technological advances made it possible to achieve an increase in available energy, which was also diversified. This phenomenon was possible, thanks to the improvement of those techniques that were already known, such as the steam engine, and the appearance of new, more efficient forms of energy, such as electricity or oil.

This period saw the greatest increase in economic growth in such a short period as ever in previous history. That was thanks to a tremendous growth in productivity, transportation networks, industrial production and agricultural output.

The work that people or animals normally did began to be carried out by machines such as the internal combustion tractor, in addition the use of fertilizers allowed a greater efficiency of the crops reducing the number of people who were needed in the field, in addition. Crop failures no longer resulted in starvation in areas connected to large markets through transport infrastructure. Massive improvements in public health and sanitation resulted from public health initiatives reducing the infection and death rates from many diseases.

Those changes resulted in the creation of a larger, increasingly professional, middle class, the decline of child labor and the dramatic growth of a consumer-based, material culture.

The **Third** Industrial Revolution, also known as the Digital Revolution,

It began in the middle of the 20th century, after the Second World War, in the countries that won it, progressively expanding throughout the world and ending at the beginning of the 21th century. It was characterized by the development of the Information and communications technologies (ICT) that propitiates a new communication era [3]. Where the rapid transmission of information became an economic asset capable of improving and simplifying people's lives. Talking about the third industrial revolution is talking about the history of the computers and how these have changed the way we work and communicate.

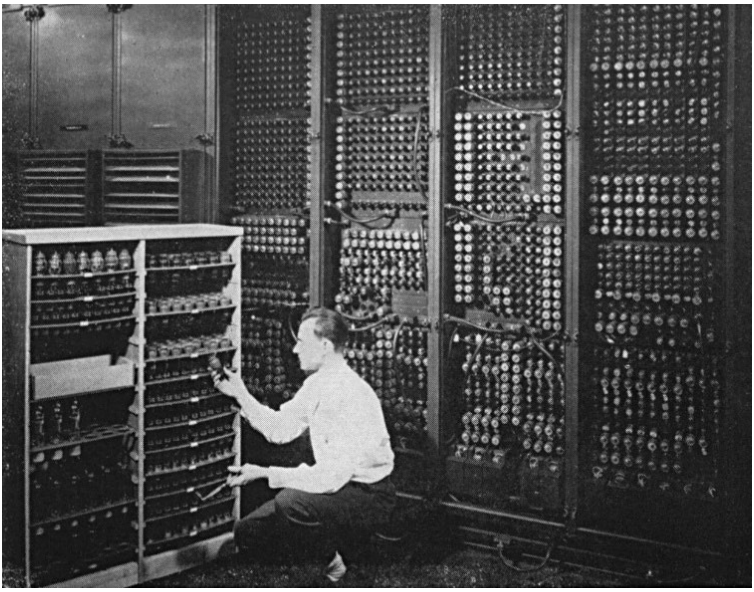

Figure 3. Stock image of a vacuum valve computer.

The starting point was in 1947 with the first germanium-based working transistor, much smaller and reliable than vacuum-valves transistors, giving the opportunity to companies and universities to replicate and automate previously manually performed mathematical calculations [16]. This technology created a new way of doing science, with the appearance of the first computational models [17].

In 1959 the first monolithic integrated circuit chip as well as the first metal-oxide-semiconductor field-effect transistor (MOS-MOSFET) was made, setting the basis of the first microprocessors and digital cameras.

In 1969 the first "web message" was sent setting up the beginning of internet [18]. With the introduction of the home computer in the 1970s, achieving semi-ubiquity during the 1980s as they made their way into schools, homes, business, and industry. By the late 1980s, many businesses were dependent on computers and digital technology. Those improvements propitiate automated teller machines, industrial robots, Computer-generated imagery (CGI) in film and television, electronic music, bulletin board systems, and video games. Millions of people purchased home computers, making household names of early personal computer manufacturers such as Apple, Commodore, and Tandy.

In 1991 digital cell phones were commercialized when 2G network started to be opened letting people communicate wherever they are in an easier way [19]. The first digital camera was marketed in 1989 eclipsing traditional film in popularity.

All these improvements in information and communication technologies simplified people's lives, allowing them access to previously limited knowledge, in addition to the moderate cost of many computers equipment together with the productive capacity they provide allowed many less developed countries They could break through in this market and become competitive, such is the case of China, India or Chile.

2.1.2. The industry 4.0

Since the beginning of the 21st century, due to the development of new information and telecommunication infrastructures and the appearance of new sensorial technologies, a new industrial revolution has begun, **Industry 4.0**, which comes to change the way in which goods and services are produced with the aim of improving the lives of people and the planet.

This revolution is marked by the appearance of new technologies, such as cyber-physical systems [20], 3Dprinting [21], the Internet of things [22] and cloud computing [23] being able to improve production processes.

Cyber-physical systems [24] allow an interconnection between robots and the workspace, allowing humans to work hand in hand with robots without risk. Assuming a substantial improvement over today, where robots perform their functions in delimited and isolated workspaces to avoid accidents.

The appearance of 3D printing [25] has allowed a faster and more accessible prototyping process. The appearance of new materials and manufacturing geometries, the ability to carry out prototypes in situ without the need for molds and with a variable internal structure at will; have allowed the manufacture of lighter parts, adapted to the needs of each client, and drastically reducing the costs of manufacturing small-scale parts.

Virtual and augmented reality [26] make it possible to provide real time information to operators on the working process being of great use in fields such as medicine; providing surgical information, robot path planning, and industry; helping in the assembly, maintenance, and repair of complex machinery. In addition, this technology is useful to customers by providing specific information on the products used, helping in the production and marketing process.

The internet of things [27] allows the collection of a large volume of data on assets, people and places connected to the network; Being able to treat this data with models of Machine learning, Deep learning and cloud computing to obtain predictive models capable of optimizing production processes and reducing defects in the production chain, achieving cleaner, more efficient and profitable industries.

All these new improvements affect productivity and the rigidity of the production chain, allowing a more efficient and cleaner industry; generating greater flexibility in production (small lots of large scale costs), shorter transfer time from prototype to mass production, greater productivity in terms of reduction set-up times, errors and machine downtime, higher product quality and competitiveness, greener industries (reduction of waste materials and failed pieces), and circular economy.

Apart from contributing to industrial processes, all these technologies will also contribute to improving our quality of life, the use of personalized medicine [28] allows a better adaptation of prostheses as well as making them cheaper. In addition the development of 4.0 crops it is remarkable, which through detection systems can nurture plants regardless of the soil where they are planted and using the least amount of water possible, allowing fruit and vegetable plantations in previously impossible places [29] making them cheaper and more accessible.

2.1.3. Future perspectives of industry 4.0.

In September 2015, world leaders adopted a set of global goals to eradicate poverty, protect the planet and ensure prosperity for all as part of a new sustainable development agenda with goals to be achieved in the next 15 years (Agenda 2030) **Figure 4**. They are specified in 17 goals and 169 sub-goals [30].

Figure 4. Sustainable development goals

To achieve them, a development plan has been drawn up where Industry 4.0 plays a fundamental role. This is of great interest to the countries subscribed to this agreement with the consequent economic boost to this project [31].

In addition to government investment, companies are also seeing a window of opportunity in Industry 4.0. It is estimated that in 2019 high technology systems with a total value of 71,700 million dollars were installed worldwide and that in 2024, this value will reach 156,600 million dollars [32], which represents an annual growth rate of 16% as can be seen in **Figure 5**.

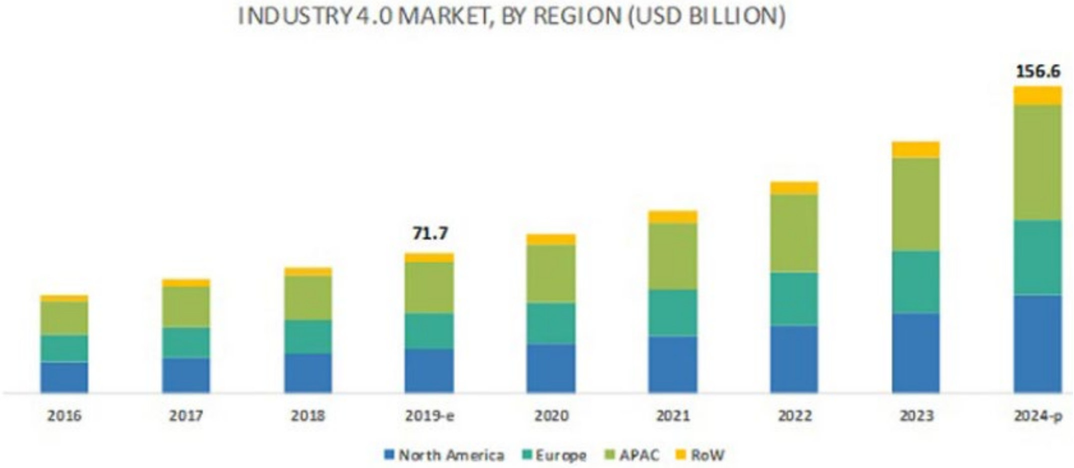

Figure 5. Expenditure on Industry 4.0 per year and per business group.

The development of industry 4.0 is not homogeneous and is strongly dependent on the sectors involved, however, studies show that this investment in technology is booming. Specifically, the degree of digitization is expected to increase by around 40% in 5 years [33]. This can be seen in Figure 6 where it can be seen the degree of industrialization of US companies depending on the sector in which they are involved.

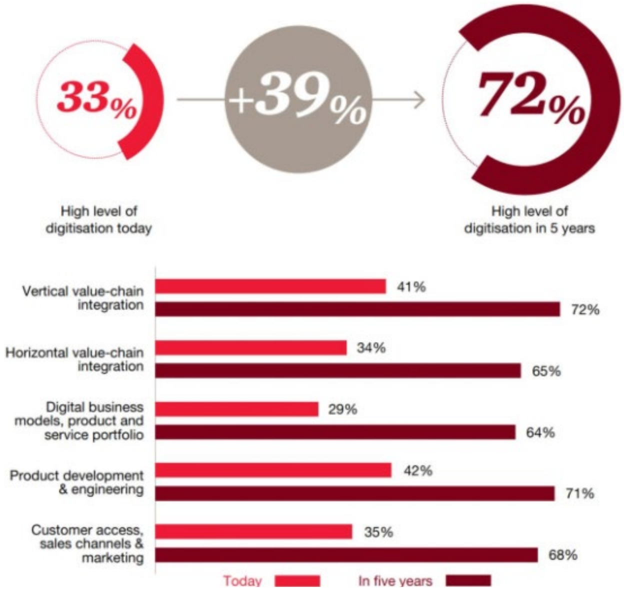

Figure 6. Percentage of companies surveyed reporting high degrees of digitalization and integration.

Furthermore, as previously explained, this revolution is associated with an increase in production efficiency, which is directly related to a reduction in production costs. In **Figure 7** you can see an estimate of cost reduction in different industrial areas thanks to the implementation of 4.0 technologies.

As can be seen, there is an enormous interest from both government administrations and private companies in the development of 4.0 technologies. Thanks to the fact that we are living the beginning of this new revolution, it is time to create new photonic technologies that can make their way into the market and help the industrial development that is coming.

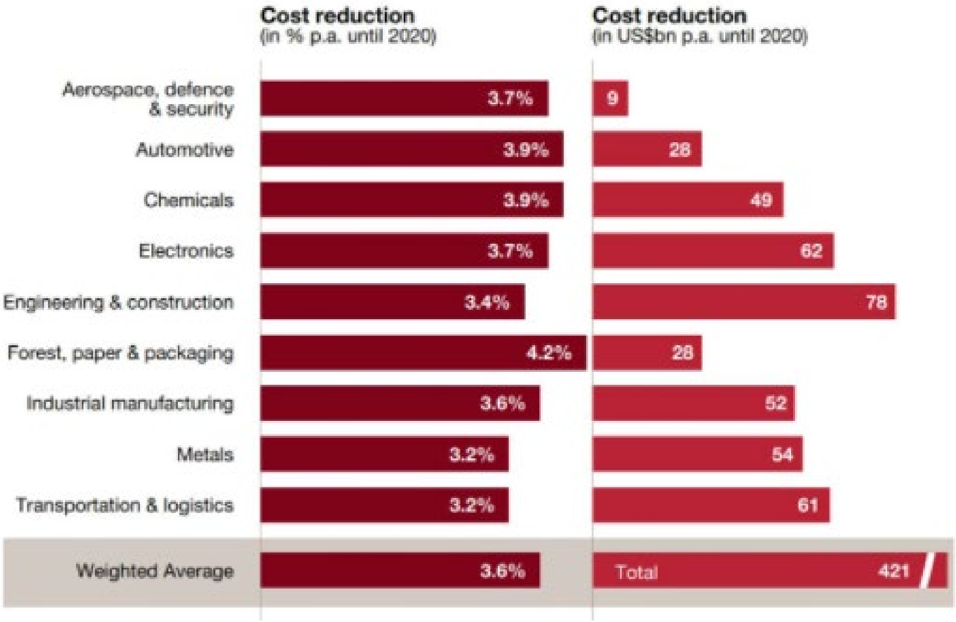

Figure 7. Cost reduction thanks to industry 4.0 per economic sectors.

2.2. Computational processes

In this doctoral thesis, several photonic systems focused on Industry 4.0 have been developed, these are not based solely on collecting information, but its treatment has also been essential. To achieve this, the use of computational methods such as those presented below has been essential.

Machine vision, also known as computer vision or technical vision, is a scientific discipline that includes methods for acquiring, processing, analyzing and understanding optical information of the real world in order to produce numerical or symbolic information so that they can be treated by a computer [34]. Just as humans use our eyes and brains to understand the world around us, computer vision tries to produce the same effect so that computers can perceive and understand an image or sequence of images and act as appropriate in each situation.

This understanding is achieved thanks to different fields such as geometry, statistics, or physics, being the last field one of the most relevant, especially photonics and solid-state physics. Photonics is the branch of physics that encompasses everything related to the propagation of light and its interaction with matter; fundamental aspect in the development of detectors and optical systems capable of capturing and focusing light, as well as in the study of devices that work in certain spectral range (UV, vis, IR…). On the other hand, solid state physics is a fundamental field for the development of these devices, since many are based on semi-conductors, such as CMOS cameras, power meters, and others [35]. Also, sophisticated image sensors even require quantum mechanics to provide a complete understanding of the image formation process [36].

This discipline comprises a large number of sensors [37], being not all of them purely optical, that is, within the field of artificial vision there is not only the treatment of images or videos; the treatment of data from multispectral cameras, electron microscopy or nuclear magnetic resonance can also be included in this discipline. In addition, the technologies used for data acquisition are also very diverse; among them are including object recognition, spectral analysis, event detection, image restoration and reconstruction of a scene (mapping).

The ultimate goal of computer vision is to achieve the development of automatic strategies for the recognition of complex patterns in data obtained from one of some of the sensors mentioned above. Currently, many are the fields that have benefited from this set of techniques [38]. One of the best known is that of robotics, since robots with a certain autonomy must accurately recognize the location of objects in their environment so as not to collide with them, for example. This is often achieved by means of sensors or cameras, the latter devices being ideal for the application of computer vision strategies.

However, robotics is not the only area that has benefited from this set of techniques. We can highlight the field of medical imaging [39], with systems capable of recognizing, for example, pathological patterns in a given imaging modality and diagnosing diseases in an automated way. They are also used in other areas, such as in security systems, object tracking (for example, tracking a footballer on video during a soccer game) or detecting anomalies in parts manufactured in a production line, the latter as a method of quality analysis.

Digital signal processing (DSP) is the mathematical manipulation of an information signal to modify or improve it in some way [40]. These signals have to be transformed from their original form (electromagnetic signals, vibrations, mechanical forces, etc.) to a set of discrete values, in time, frequency [41], or any other domain [42] capable of being understood by a computer. .

This information enters into the computer system thanks to a sensor and an analog digital converter [43] to later be processed computationally using numerical methods [44], this can be achieved through a system based on a processor or microprocessor that has a set of instructions, a hardware and software optimized for applications requiring very high speed numerical operations such as the Laplace transform or the fast Fourier transform FFT [45].

Among the most common numerical methods are noise filters, which work in different ways according to the needs of each experiment, there are noise filters that act directly on the function as well as others that need to carry out transformations on it, such as pass filters. band, which take advantage of the characteristics of the Fourier transform to eliminate certain frequencies.

2.3. Laser systems.

Since its discovery [46], lasers has become one of the most important industries and fields of study for our world. The laser technology market size is expected to grow at a compound annual grow rate of 8.6% from USD 11.7 billion in 2020 to USD 17.6 billion by 2025. Mainly thanks to its applications in fields like medicine and material processing [47].

There are many types of laser systems, which are fundamentally differentiated by their active medium. There are gas lasers [48], liquid lasers[49] , semiconductor lasers [50] and solid state lasers [51], the latter are of great interest in multiple areas of industry, medicine and science [52] thanks to their compactness and efficiency, as well as the possibility of generate high power pulses with them [53], being the only ones capable of generating mode locking [54].

Due to these characteristics, different types of specific methodologies for solid state lasers have been studied and developed [55]. Since its discovering [56], waveguide (WG) lasers present great advantages over conventional bulk lasers. Those are its higher gain, lower laser threshold, thermal lens compensation and good beam quality [57] attracting interest from various emerging applications [58].

Specifically, 2µm waveguide lasers are especially relevant due to its emission corresponds to the absorption bands of the most atmospheric molecules (H2O, CO2, N2O) [59]. Thanks to the water absorption bands it is possible to generate a controlled area of cauterization. Furthermore, these lasers are relatively safe for the human eye, making them an ideal device for medicine [60]. Normally this emission is obtained from solid state lasers doped with lanthanides, mainly with Tm^{3+} and Ho^{3+} ions or a combination (co-doping) of them.

2.4. Waveguide water sensors.

In recent years, both in industry and in public entities new needs for water quality control have arisen, either due to a broad commitment to the environment or greater regulation on discharges [61].

Currently there are ways to measure the composition of water accurately. The most common is to collect samples that are taken to a laboratory. This process takes time, usually 1 to 2 days, and is quite expensive. In addition, if there is a spill, it is not possible to detect it before the water reaches the consumer. Due to this, special attention is being paid to looking for new detectors that can control efficiently, accurately and in real time the composition of water sources [62]. This includes both drinking water for human consumption and that which circulates through rivers, lakes and oceans.

For this purpose, photonic sensors have the best possible characteristics, are compact, inexpensive, and can receive data in real time. Among them, it has been shown that those formed by a crystal with a waveguide inside are the most promising thanks to the good confinement of the light they provide and their great robustness [63].

Within the waveguide sensors there are several types that are well differentiated according to the physical principle that governs them, the three most notable are evanescence sensors, SPR sensors and interferometric sensors.

Evanescence sensors are based on the property of light to generate an evanescent wave [64] when undergoing total internal reflection on the discontinuity surface between two media, a surface such as that separating the core from the cladding in a waveguide. When this happens, a wave with an exponential decay appears in that area that travels a very short distance, on the order of a few microns. It can interact with a nearby medium, transmitting part of its energy to it. By measuring the spectrum of the light that has been absorbed it is possible to detect the composition of the liquid in contact with the sensor.

Surface plasmon resonance (SPR) sensors [65] work in a similar way to evanescent wave sensors, in this case the light guided in the waveguide also generates an evanescent wave, but a metal layer placed just on the surface of the crystal generates plasma waves in this. These waves have a unique resonance frequency that depends on the refractive index of the crystal, attenuating certain wavelengths. By detecting the absorption peak, the refractive index of the medium can be known.

Interferometric sensors [66][67][68] are based on the generation of interferences of a coherent beam (laser) when passing through certain structures, such as a grating, or etalon. These structures make the light interact with itself, generating interference figures characteristic of each type of sensor and closely related to the parameters of its environment, being able to detect changes in the composition of water in contact with those devices with great precision.

3

OBJECTIVES

The general objective of this study is to develop photonic technologies for monitoring several processes at real time with high precision, a key feature for industry 4.0. For this, it has been decided to research the most relevant points today in which photonics can be useful.

Those are englobed in three clearly defined points that are:

- The study of novel and compact laser systems for industrial and medical applications. Those must be eye safe in order to be suitable for multiple purposes.

- Research into new sensors to maintain the safety and health of the population, mainly in these years with the appearing of new diseases such as Covid 19.

- The development of photonic devices for the transition to Industry 4.0. Those sensors must be able to work in real time in order to provide a big amount of data and should be affordable enough to permit companies to put some of them.

All these points can be solved from photonics, thanks to its many advantages in the sensorics area. To respond to these needs, an action plan has been developed based on the following points:

- The study of new methods of microfabrication of waveguides within crystals by means of the femtosecond-direct laser writing method in order to achieve new forms of light guidance.

- The study of waveguide microchip laser systems in the range of $\lambda = 2$um, in order to develop efficient and compact laser systems, especially interesting from a biomedical and industrial point of view.

- Research on crystal-based sensors with waveguides inside them capable of detecting changes in the chemical composition in liquids, both by evanescence and by interferometry.

- The development of laser profilometry systems, capable of detecting small changes in the surface of a material, to be able to be used as quality control systems.

- The study of optical systems together with artificial vision algorithms in order to detect incidents in an assembly line.

- The study of new optical encoders as control systems to be suited in flammable and dangerous environments.

- The development of non-touch sensors that allow interacting with a device without touching it in order to fight the SARS coronavirus 2 pandemic.

4

MATERIALS AND METHODS

In this chapter the materials and methodology used for the development of this doctoral thesis will be discussed. All the steps that have been used from the study of the properties of a crystal, the development of the femtosecond-direct laser writing technique for the creation of guides in its interior and its use as an active medium in the generation of laser sources at λ = 2μm and the study of their properties.

Finally, a notion of the computer programs used for the development of photonic devices in Industry 4.0 will be given, essential for the development of this thesis.

4.1. Crystalline matrixes.

In this thesis, four types of crystalline matrices have been used. The crystal structure of potassium lutecium double tungstate $KLu(WO_4)_2$ (hereafter KLuW) [69], Magnesium tungsten oxide (MgWO4) [70] and Strontium Fluoride (SrF_2) [71] which are monoclinic systems with $a \neq b \neq c; \gamma = 90º, \beta < 90º$ and the calcium gadolinium aluminum tetraoxide CaGdAlO4 (or shortly CALGO) [72] which is an isotropic crystal. All doped with Tm^{3+} ions homogenially distributed substituting their rare earths. The local disorder originated from the second coordination sphere of Tm3+ [73] generates smooth and broad spectral bands both in absorption and emission.

Both have been manufactured with the Top-Seeded Solution Growth slow-cooling (TSSG-SC) method. This is a high-temperature solution (HTS) growth method used for fabricating single crystalline materials [74]. Is suited for fabricating materials that normally undergo a phase transition below their melting point.

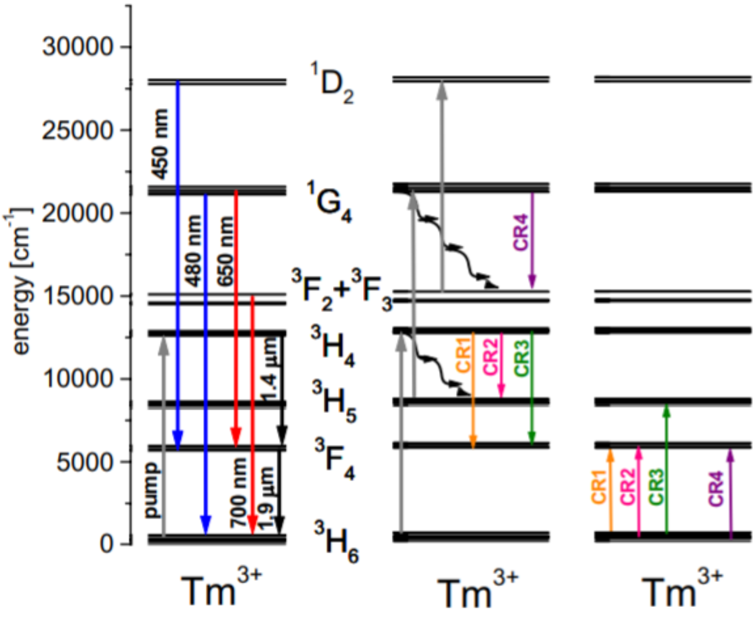

Figure 8. Energy diagram of Tm3+ in KLuW with arrows indicating radiative and non-radiative processes; CR: cross relaxation [75].

These crystals can generate laser light by pumping them with a beam at ~ 800nm generating an emission around 1.84um (**Figure 8**). This emission is thanks to the Tm^{3+} ions that are found as a dopant in our crystals. Due to the crystalline structure of the material, the energy levels of Tm^{3+} are unfolded depending on its orbital angular momentum by the Stark effect [76]. This results in the upper and lower states of certain allowed transitions being widened, generating a quasi-3-level laser system. Due to the degeneration of the ground state, the decay time is very low, requiring a lot of population inversion to start lasing. This differentiates it from the 4-level system by making the lasing threshold much higher [77].

The interaction of thulium ions with the crystal allows CR; a non-radiative electronic relaxation that allows scheme “two for one” in which a single photon of 800nm generates two photons of ~ 1840nm allowing a Stokes efficiency of $\eta_{st} \sim 0.86$. As the stokes efficiency is related to the heat generated in the crystals, an efficient CR process would lead to lower thermal stress favoring power scalability [78].

The up conversion also plays an important role in the active medium efficiency. In this case there are emissions at 770nm, 650nm and 450nm as can be seen in **Figure 8** reducing the heat generation in the crystal.

Due to the influence of the crystal lattice, the emission σ_a and absorption σ_e cross-sections of the Tm^{3+} vary. To determine which is the ideal area for pumping and emission of the material, spectroscopic measurements must be carried out [76][79]. Furthermore, for biaxial crystals it is important to note that each crystalline axis will have different characteristics [69],[80], [81] being necessary to measure each axis separately.

From the absorption and emission cross sections, the gain cross section σ_g can be calculated as:

$$\sigma_g(\lambda) = \beta * \sigma_e(\lambda) - (1 - \beta) * \sigma_a(\lambda) \qquad (1)$$

Where β is the is the population inversion level calculated as $\beta = \mathrm{N_u}/N_t$ being N_u and N_t the upper and total population levels. With this formula it is possible to calculate the laser gain as [82]:

$$G(\lambda) = \sigma_g(\lambda) N_t * 2L = -\ln\big(1 - L_{in}(\lambda)\big) - \ln(1 - T_{oc}(\lambda)) \qquad (2)$$

Where L is the cavity length, L_{in} is the intrinsic cavity loss (for WG lasers propagation losses) and T_{oc} is the transmission of the output coupling mirror. If the cavity losses L_{in} or the output coupler T_{oc} changes, the gain cross section also changes what means that the emission wavelength can also be different [83].

4.2. Femtosecond- Direct laser writing basics.

When an ultrashort pulsed laser (~ 100fs) of sufficient energy is focused on a material it produces a controllable modification of small dimensions in its interior. This is due to the low interaction time between light and material that makes it possible to produce this modification before thermal effects occur (**Figure 9**), Thanks to the multiphoton ionization [84] and avalanche ionization [85] processes; thus avoiding damage to the surrounding areas. These modifications produce a very well-defined change in the refractive index (RI) in the affected area with which structures can be generated within the material, such as diffraction gratings and waveguides.

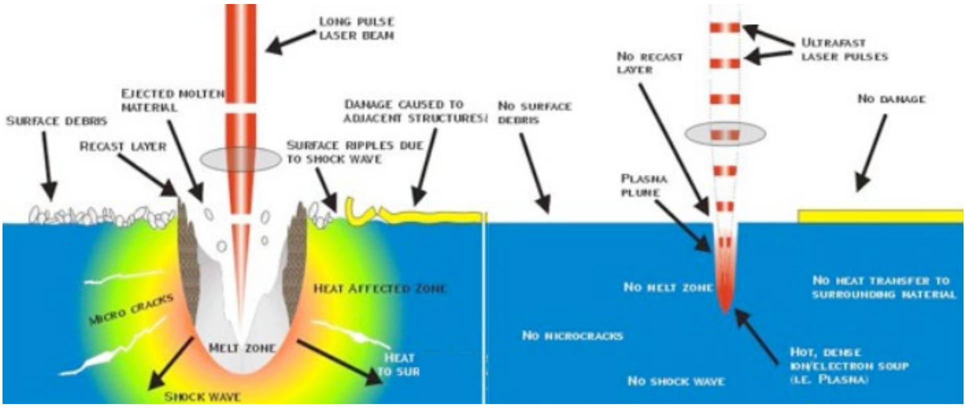

Figure 9. Differences between long time pulses (right) and ultrashort time pulses (left) in material damage.

Depending on the pulse energy there are two types of modifications (**Figure 10**).

Type I: "weak" damage

There is a densification in the focal zone, which leads to an increase in the refractive index. This type of modification occurs in most glasses and only in some crystals. To produce this damage, low energy per pulse is used, of the order of 0.1mJ, although it depends on the material. Only a few crystals, Nd3+:YCOB [86], ZnSe [87], under specific conditions have shown a refractive index increase at the laser damaged volume.

Type II: "severe" damage

Due to the interaction between the light and the material, the phenomenon of coulomb explosion occurs [88] that generates a decrease in the refractive index in the focal zone, in addition to a densification of the surrounding area. This process can occur both in crystals and in glasses and is irreversible in most cases.

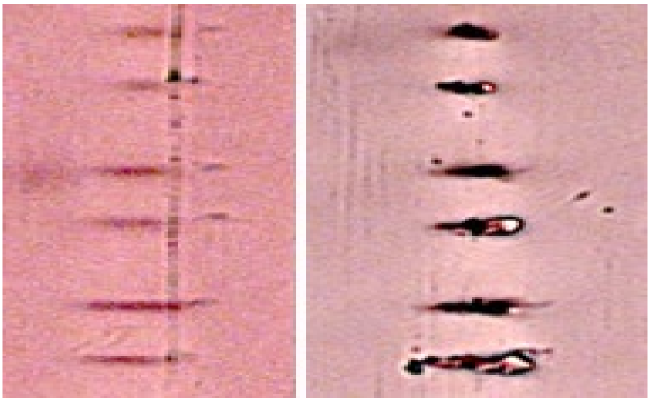

Figure 10. Image of weak or type I damage (left) and image of severe or type II damage (right).

Using this type of damage in a crystalline material, there are 3 types of waveguides[89], **Figure 11.**

Type I: This guide is built by making a line of type I damage in the material [90] (**Figure 11.A**), this increases the refractive index in the damaged area, confining the light inside and generating an area where the material becomes amorphous. Due to the use of low power, no amplification stage is necessary in the engraving laser, letting those waveguides be inscribed in a short time. Such WGs have been implemented in various glasses like germanate [91], chalcogenide [92] and bismuth-borate [93]. The transformation of this crystal into amorphous is problematic since the thermal dissipation is reduced [94].

Type II: Two parallel damage tracks are inscribed (**Figure 11.B**), producing an increase in the refractive index in the central zone. By varying the power of the laser beam and the separation between both tracks it is possible to create a smooth, higher refractive index core region capable of confining and guiding light [93]. In this case, a deformation also occurs in the crystalline structure of the material, giving rise to polarization favoring nature which might not be necessarily needed in naturally anisotropic laser gain media and phase matched frequency conversion [95].

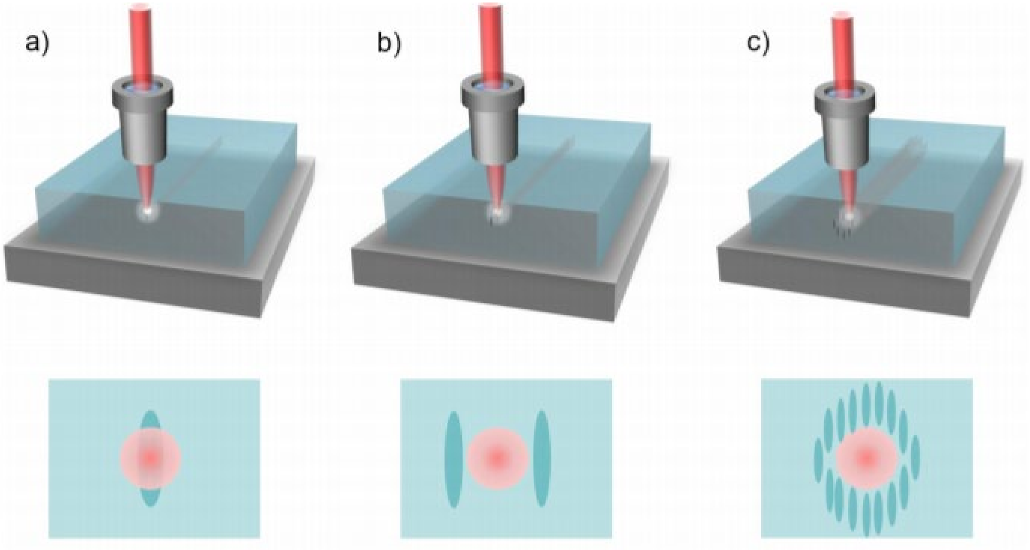

Figure 11. Schematic plots of the fabrication of the three categories by femtosecond laser irradiation and the spatial locations of the waveguide modes: a) waveguides based on Type I modification in single-line geometry, b) waveguides based on Type II modification in dual-line geometry, and c) waveguides based on Type II modification in depress cladding Type III geometry [96].

Type III: this type of waveguide is the most similar to conventional ones. In this case, an undamaged core is created surrounded by an array of tracks that confine the light inside working as a cladding. The size of the central area can be easily edited, in addition, the core crystalline structure remains intact, being the most suitable for laser applications [97].

4.3. Waveguide modes

Waveguide lasers are configured by a crystal which has an optical waveguide microfabricated with a femtosecond laser. This channel acts as an optical fiber and the light acquires very similar properties inside; it is confined from a certain angle of incidence and is transmitted as a sum of longitudinal modes [57]. To study its propagation in this type of channel, we start from Maxwell's equations in a medium without free charges or currents [98]:

$$\nabla \mathrm{x} \vec{H} = \varepsilon \frac{\partial \vec{E}}{\partial t} \qquad \nabla \mathrm{x} \vec{E} = -\mu \frac{\partial \vec{H}}{\partial t}$$

$$\nabla \cdot \vec{E} = 0 \qquad \nabla \cdot \vec{H} = 0 \tag{3}$$

Where $\vec{H}$ is the magnetic field, $\vec{E}$ is the electric field, ε is the electric permittivity and μ the magnetic permittivity. Operating with these equations, the wave equation of the electromagnetic field can be obtained:

$$\nabla \cdot \vec{E}(\vec{r},t) - \varepsilon\mu \frac{\partial^2 \vec{E}(\vec{r},t)}{\partial t^2} = 0 \tag{4}$$

Supposing a harmonic wave $\vec{E}(\vec{r},t) = \vec{E}(\vec{r})e^{-i\omega t}$ what oscillates at a certain angular frequency ω we achieve the equation:

$$\nabla^2 \vec{E}(\vec{r}) + \omega^2 \varepsilon\mu \vec{E}(\vec{r}) = 0 \tag{5}$$

From this simplified wave equation, using numerical simulation programs (COMSOL in our case) it is possible to determine the propagation of the modes within the waveguides as can be seen in **Figure 12** being able to calculate the optimal propagation parameters, as well as the maximum diameter from which the laser emission is no longer single mode.

In previous studies [99] it has been shown that for these waveguides the longitudinal TEM modes are very similar to those that can be found in a conventional optical fiber with a similar diameter.

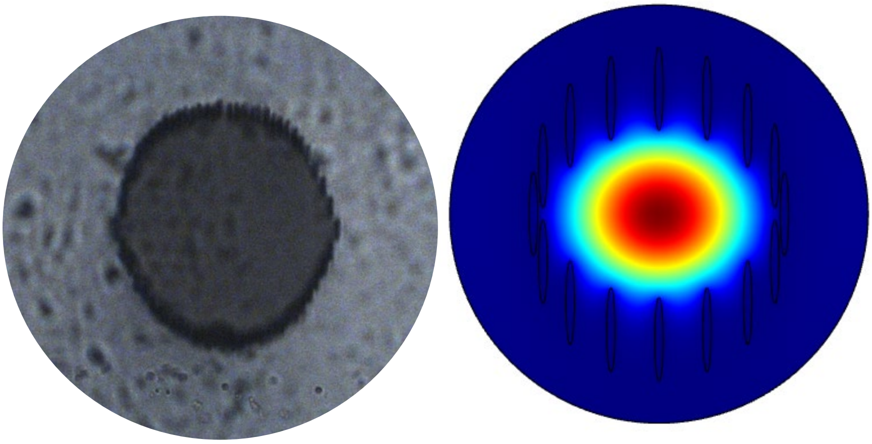

Figure 12. Confocal front view of a waveguide channel (Right) and beam propagation simulation with COMSOL of the TE_{00} mode inside the waveguide (Left)

Using this technology, it is possible to generate a microchip laser configuration [55] (in which the output coupler and the pump mirror are almost in contact with the crystal or the end faces are coated in order to work as pump mirror and output coupler) where both the pumping and the laser emission are confined only within the waveguide. This allows to confine the pumping inside the guide, drastically increasing the number of photons per unit area, significantly reducing the threshold and slope efficiency of the laser emission, as well as reducing thermal lens effects [100].

4.4. Laser modes

The difference between a laser and a non-laser source is clear. Unlike spontaneous emission, laser radiation tends to be coherent, polarized and collimated. However, not all laser beams have the same propagation.

In a laser, depending on the symmetry of the cavity, there are two types of transverse modes that are obtained numerically by solving the wave equation of a beam confined between two mirrors [101]. If the system has Cartesian symmetry, the Hermite-Gauss (HG) [102] polynomials will appear and if the symmetry is polar, the Laguerre-Gauss (LG) [103] modes will appear, **Figure 13**.

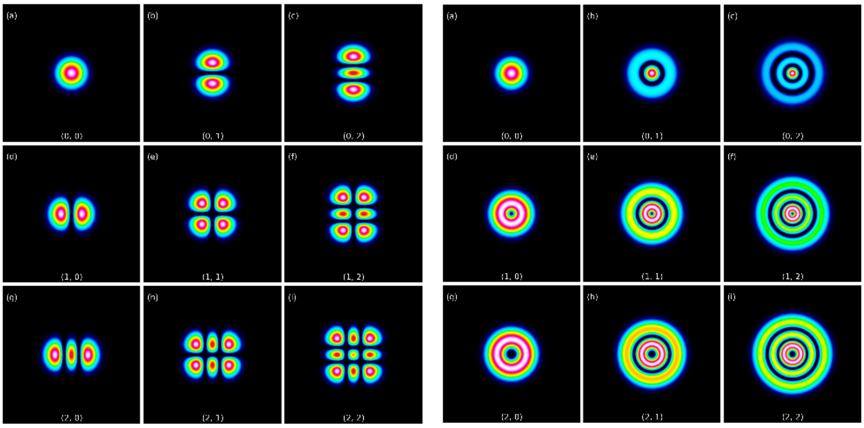

Figure 13. higher order modes of a laser. Hermite-Gaussian modes (Left). Laguerre-Gaussian modes (Right).

For both the laguerre-Gauss and Hermite -Gauss modes, the transversal electro-magnetic TEM_{00} fundamental mode is the same. This is called Gaussian mode and it has several characteristics that make it the most interesting in laser applications. One of the main reasons is because it has the smallest beam divergence as possible. Although many lasers are designed to output a fundamental mode (Gaussian beam), imperfections and/or cavity design [104] in the laser will often cause superimposed higher-order transverse modes.

4.5. Laser setup

The scheme of the laser setup is shown in **Figure 14**. The femtosecond direct laser writing (fs-DLW) waveguide laser was pumped by a Ti:Sapphire laser (MIRA 900, Coherent, ANNEX I) in continuous mode. This laser can operate between 700nm to 1000nm, being ideal for thulium transitions, which can be pumped around 800nm.

After the Ti:Sapphire laser there is an optical isolator (IO-5-NIR-LP, ANNEX I) which avoids back reflections inside the laser in order to nullify the risk of damaging it. This isolator is not showed in **Figure 14** because it is an optional device and only the core elements are showed to simplify the figure.

Right after it there is a half wave plate (WPV10L-780, Thorlabs) and a Glan-Laser calcite polarizer (GL10-B, Thorlabs) to control the incident power. The half wave plate changes the polarization direction of the laser and the polarizer split each polarization in a different optical path.

The horizontal direction is received by a power meter which is numerically correlated with the optical incident power in the sample, to avoid the addition of more components that could generate optical aberrations.

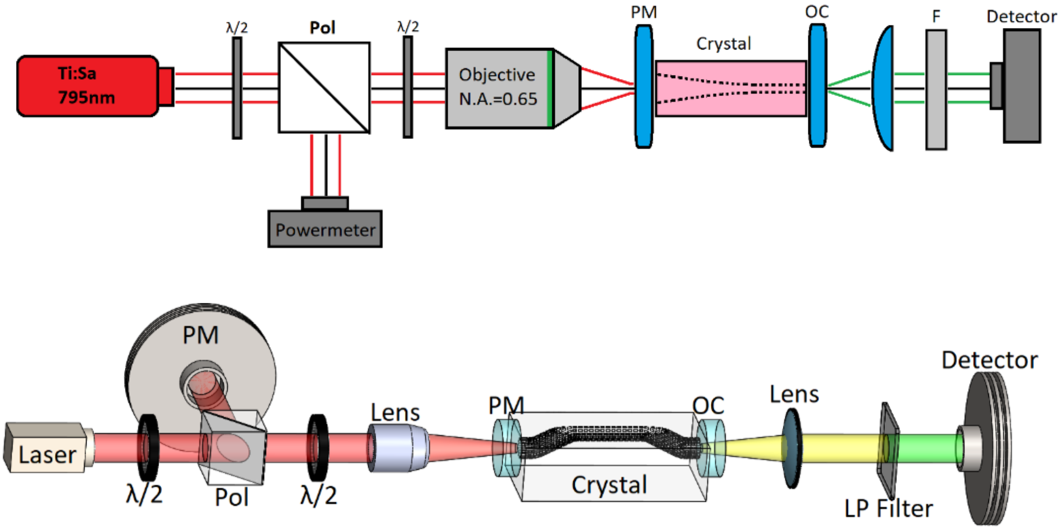

Figure 14. Scheme (Up) and 3D model (Down) of the laser setup.

The vertical polarization goes through another half wave plate (WPV10L-830, Thorlabs), that controls the polarization angle in order to adjust it with the maximum absorption axis of the crystal for this wavelength. It was coupled inside the waveguide with a 10× microscope objective (N.A. = 0.28, focal length f =20 mm) resulting in a spot diameter of 40 µm FWHM at the focus, located at the front end-face of the WG.

The sample containing the fs-DLW WGs was placed on a passively cooled Al-Fe support. The laser cavity consisted of a flat pump mirror which was antireflection coating for 0.7–1.0 µm (R<2%) and high-reflection coating for 1.8–2.1 µm (99.9%) and a flat output coupler (OC) having a transmission TOC of 1.5%, 3%, 5%, 10%, 20%, and 30% at 1.8–2.1 µm. The PM and the OC were placed close to the WG end faces with minimum air gaps with a cavity length around 7.9 mm and without any index matching liquid between the optical components to avoid burns in the coatings.

The laser output was collimated using an uncoated lens with $f = 15mm$. The nonabsorbed pump was blocked using a long-pass filter (FEL 1000, Thorlabs). The emission spectrum was measured using an optical spectrum analyzer (OSA) (AQ6375B, Yokogawa, Annex I). Imaging of the waveguide laser near-field output mode at 1850 nm wavelength was performed using a FIND-R-SCOPE near-IR camera (model 85726, ANNEX I). The output power was measured with an Ophir Nova P/N 1Z01500 power meter and numerically corrected taking account the losses in the low pass filter and the lens.

4.6. Slope efficiency.

The slope efficiency is the conversion efficiency of the light pumped in the crystal into laser radiation. It is understood as the slope of the line that relates the pump power absorbed by the crystal with the laser power generated by it [105].

In order to determine this value, it is essential to accurately calculate the power absorbed by the crystal. For this purpose, the losses in the crystal must be known. There are 4 sources of losses in a waveguide [106].

- Fresnel losses

On the faces of the crystal there is a change in the refractive index that gives rise to a partial reflection of the light, this is defined from the Fresnel formula of a beam perpendicular to the surface [107]:

$$R = \left|\frac{1-n}{1+n}\right|^2 \qquad (6)$$

Being R the reflectance and n the refractive index of the crystal.

- Pump coupling efficiency.

As explained in section 4.5, the laser beam is focused within a waveguide. This process is not perfect and entails a series of losses that are included in a coupling efficiency η_{coupl}.

- Pump absorption.

As the pump is transmitted through the crystal, it is absorbed to generate population inversion in the Tm^{3+}ions, giving rise to an absorption efficiency η_{abs}.

- Waveguide propagation losses

Within the waveguide there are several mechanisms that reduce the power of the pump as it propagates. The main one is the scattering that occurs within the guide. This is associated with an efficiency η_{prop} that will depend mainly on the geometry of the guide and its length.

Including all these processes the equation of the power transmitted to the waveguide is obtained, being:

$$P_{trans} = \left(1 - \eta_{prop}\right) (1 - \eta_{abs})\, \eta_{coupl}\, (1 - R)\, P_{in} \tag{7}$$

As explained in point 4.5, the incident power is regulated thanks to a $\lambda/2$ plate and a linear polarizer. This lets the vertical polarization pass through it and reflects the horizontal polarization to a powermeter. From the intensity that reaches it, it is possible to calculate the incident pump power with the formula:

$$P_{in} = c_1 P_0 - c_2 P_{PM} \tag{8}$$

Being $P_{in}$the incident pump power to the shample, taking account the losses in the focusing lens and pump mirror, P_0 the laser incident power (before the half wave plate) and P_{PM} the power recorded by the power meter. In addition, there are 2 empiric constants $c_1$and c_2 that are close to 1 and are determined numerically by measuring P_{in} vs P_{PM} before each experiment.

From the incident power being able to calculate the power absorbed by the crystal is necessary. To do this, the input power P_i vs the output power P_o is measured in the crystal without mirrors (without laser) at two different wavelengths, one in the absorption zone of the glass and the other outside it. For thulium, $\lambda \approx 800nm$ are usually used for the absorption zone and $\lambda \approx 850nm$ for the non-absorption zone [108]. The power in each case can be expressed as:

$$P_{o850} = P_{i850}\,(1 - R)\,\eta_{coupl}(1 - \eta_{prop}) \tag{9}$$

$$P_{o800} = P_{i800}\,(1 - R)\,\eta_{coupl}(1 - \eta_{prop})(1 - \eta_{abs(NL)}) \tag{10}$$

Being $P_{o850}, P_{i850}, P_{o800}, P_{i800}$ the input and output power at 850nm and 800nm respectively and $\eta_{abs(NL)}$ the absorption efficiency under non lasing conditions.

These equations can be simplified by encompassing the total transmission losses in a single L_{oss} value:

$$L_{oss} = 1 - (1 - R)\eta_{coupl}\left(1 - \eta_{prop}\right) \tag{11}$$

Being able to rewrite the equation (9) as:

$$P_{o850} = P_{i850}\,(1 - L_{oss}) \tag{12}$$

From this it is possible to obtain the total transmission losses by comparing the input and output power:

$$L_{oss} = 1 - \frac{P_{o850}}{P_{i850}} \tag{13}$$

This value must be constant regardless of the pumping power in the system. It is recommended to calculate the average value of a data series modifying the input power. It is also possible to rewrite the equations (10) and (9) including the total losses. Furthermore, it is accurate to assume that $L_{oss850} \cong L_{oss800}$ due to the small spectral deviation between both measurements [109].

$$P_{o800} = P_{i800}\,(1 - L_{oss})\,(1 - \eta_{abs(NL)}) \tag{14}$$

Being able to obtain the value of $\eta_{abs(NL)}$ from the previous formula as:

$$\eta_{abs(NL)}(P_{i800}) = 1 - \frac{P_{o800}}{P_{i800}\,(1 - L_{oss})} \tag{15}$$

It is relevant to explain that, under non lasing conditions the non-lasing absorption efficiency decreases with the incident pump power. This is due to the population inversion saturation [110].

Some lasers or amplifier devices exhibit a significant degree of excitation of the laser-active ions; this is particularly the case for those based on a quasi-three-level gain medium. The absorption is then saturated to some extent, simply because the density of atoms or ions in the ground state, from where they can absorb light, is depleted.

The degree of pump saturation will in general depend on the intensity of signal (laser) light. In a laser, for example, the lasing process may clamp the upper-state population to some relatively low level, so that the degree of pump saturation is also clamped (in steady-state operation) as soon as the laser threshold is reached: above threshold, there is no further dependence on pump power, except if the transverse profile of the excitation density is significantly power-dependent.

Due to this, the absorption efficiency under lasing conditions is considered equal to the absorption efficiency under non-lasing conditions when the incident power reaches the threshold $\eta_{abs} = \eta_{abs(NL)}(P_i = P_{TH})$ being able to calculate the absorbed pump power as:

$$P_{abs} = \frac{1 - Loss}{(1 - R)}\,\eta_{abs}\,P_i \tag{16}$$

With this calculous it is possible to measure P_{abs} vs P_o in order to estimate the slope efficiency.

4.7. Caird analysis to determine propagation losses.

The power inside the waveguide decreases during its propagation. This decrement is exponentially proportional to the length of the crystal and can be experimentally determined. There are some methods to obtain the propagation losses; like the Findlay-Clay method [111] suitable for the 4 level laser system and the Caird analysis [112] suitable for the quasi 3 level laser system. In this case the High-TOC Caird analysis is used [113]

This analysis relates the slope efficiency with the TOC by the formula.

$$\frac{1}{\eta} = \frac{1}{\eta_0} + \frac{2\gamma}{\eta_0} \frac{1}{\gamma_{oc}} \tag{17}$$

With $\gamma = -\ln(1 - L_{oss})$ and $\gamma_{oc} = -\ln(1 - T_{oc})$ being η_0 the intrinsic slope efficiency and L_{oss} the internal losses of the crystal.

By fitting this equation into a straight line with $Y = \frac{1}{\eta}$ and $X = \frac{1}{\gamma_{oc}}$ it is possible to retrieve the propagation losses L_{oss} being able to calculate the attenuation in the waveguide as:

$$\delta(dB/cm) = 4.34 \frac{L_{oss}}{l(cm)} \tag{18}$$

Being $l(cm)$ the length of the crystal.

4.8. Laser beam propagation.

It can be shown that the evolution of the width (defined according to the variance formula) of any spatial distribution (Gaussian, non-Gaussian, coherent, incoherent, singlemode, multimode...) follows a distribution in the focal zone as shown in **Figure 15.**

The area with the smallest beam width is called waist w_0, the area where $w_0 < w(z) < \sqrt{2}w_0$ is called the Rayleigh zone z_R which is considered the length where the beam is focused, and the divergence of the beam is Θ. This distribution can be expressed by the equation:

$$w^2(z) = w_0^2 + \left(\frac{M^2\,\lambda^2}{\pi w_0}\right)(z - z_0)^2 \tag{19}$$

Being $w(z)$ the with of the laser beam (FWHM), w_0 the waist or the minimum with of the pulse, λ the wavelength of the beam z_0 the minimum width position and M^2 the beam factor [114].

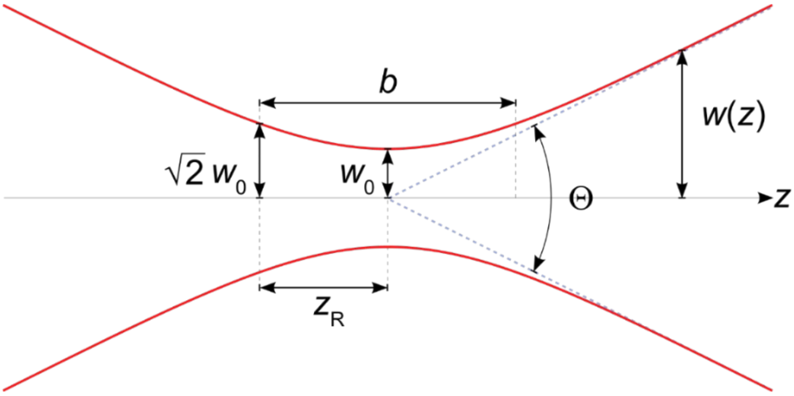

Figure 15. Scheme of the beam propagation in the waist area and surroundings.

M^2 provides an excellent metric for determining the higher-order mode content. Is a measurement that was originally designed to determine the quality of a real beam in comparison to a theoretically perfect fundamental mode Gaussian beam [115]. It is a value always bigger than 1 and close to this number, the closer to one the more gaussian the beam.

This factor has two components following the main axes of the laser M_x^2 and M_y^2 that must be measured separately and can take very different values.

It is possible to calculate the value of M^2 by measuring the divergence of the beam. For this, it is necessary to adjust the expression (19) to a hyperbola, being able to make a fitting in the form:

$$w^2 = a + b\,z + c\,z^2 \tag{20}$$

Substituting the values of a, b and c in equation (19), we get that the value of M^2 can be expressed as:

$$M^2 = \frac{\Pi}{8\lambda}\sqrt{4ac - b^2} \tag{21}$$

To carry out this measurement [116] it is necessary to be able to measure the waist and the Rayleigh zone. It is normally located inside the laser cavity, so it is not possible to measure it directly. However, another Rayleigh zone can be generated by placing a convergent lens in front of the beam and seeking the focus. For this a convergent long focal lens (Thorlabs, AC080-020-C), a knife placed on a 3D mobile base (Thorlabs, PT3) and a power meter (Thorlabs, S405C) is necessary.

To perform the measurement on the x axis (M_x^2), the base is placed with the blade vertically in the focal area and the power meter just behind. The base is moved to a certain position on the z axis and measurements are taken on the x axis when the blade allows the passage of 90% and 10% of the light, being able to relate the position in x with the width by means of the formula:

$$w = |x_{10} - x_{90}|/1{,}812388 \tag{22}$$

Sometimes it is difficult to measure at 90% -10%. In that case it can be done at 20% -80% being the real width:

$$w = |x_{20} - x_{80}|/1{,}19 \tag{23}$$

This measurement must be performed for different values of z. For an accurate regression, a minimum of 10 values must be performed, preferably 5 within the Rayleigh zone and 5 in its vicinity.

The same measurements will be made on the y axis (M_y^2) by placing the blade horizontally and moving the base in height.

4.9. Digital working environments.

In the development of this thesis, several optical devices capable of fulfilling relevant functions in industry 4.0 have been implemented. To program their functions, the use of programming languages and communication environments between devices such as Matlab or LabView has been essential. In this section the basic information of these programs are shown, as well as some of their utilities.

LabVIEW (acronym for Laboratory Virtual Instrument Engineering Workbench) is a software developed by National Instruments based on a visual interface (with block diagrams) designed to communicate a large number of devices making them work simultaneously, being able to automate processes with ease.

Its main feature is its ease of use, valid for both professional programmers and people with little programming knowledge who can make programs relatively complex, impossible for them to do with traditional languages. Among its objectives are to reduce the development time of applications of all kinds and to allow professionals from any other field to enter computing. LabVIEW can be combined with all types of software and hardware, both from the manufacturer itself - data acquisition cards, PAC, Vision, instruments and other Hardware - as well as from other manufacturers.

The programs developed with LabVIEW are called Virtual Instruments, or VIs, and their origin came from the control of instruments, although today it has been widely expanded not only to control all types of devices (Electronic Instrumentation) but also to its embedded programming, communications, mathematics, etc.

With LabVIEW you can create programs of thousands of VIs (equivalent to millions of pages of text code) for complex applications, automation programs of tens of thousands of input / output points, projects to combine new VIs with already created VIs, etc.

MATLAB (short for MATrix LABoratory) is a software widely used in universities and research centers that offers an integrated development environment (IDE) with its own programming language (M language). It is strongly oriented to numerical computation, providing libraries specially designed for the manipulation of matrices, the representation of data and functions, the lambda calculus [117] and the implementation of algorithms. In addition, it has advanced functions such as the creation of graphical user interfaces (GUI) and communication with programs in other languages and with other hardware devices. The MATLAB package has two additional tools that expand its capabilities:

Simulink (multidomain simulation platform) is Matlab's own tool that provides a visual interface based on block diagrams. In aesthetics and functionality it is similar to labview, presenting many of its functionalities.

App designer (Graphical user interface editor - GUI): Allows the development of graphical interfaces that allow the user to interact with the application using buttons, text boxes and other triggers instead of having to use commands to interact with the program.

Additionally, you can extend the capabilities of MATLAB with toolboxes; and those of Simulink with blocksets, allowing the development of software highly oriented to different fields of science in an easy and efficient way.

5

WAVEGUIDES INSCRIBED IN CRYSTALS

In this thesis, special attention has been paid to the development of waveguides using the femtosecond direct laser writing (FS-DLW) technique, as well as their applications. This technique allows to inscribe waveguides inside an optical crystal, obtaining a very good confinement of the light, taking advantage of all the optical properties of the crystal, such as its structure, its rigidity and its thermal dissipation capacity. This technique has been chosen thanks to its versatility, as well as the great knowledge of the subject that the FICMA group has; in which much of this work has been developed. Using this technology two branches of research have been discussed in this chapter. On the one hand, waveguide microchip laser systems and on the other, new types of waveguide-based sensors.

5.1. Waveguide lasers

Several solid-state lasers have been developed using various crystalline matrices $(KLuW, CALGO, SrF_2\ and\ MgWO_4)$ doped with Tm^{3+} ions to which a channel has been microfabricated inside using FS-DLW. As explained in point (3.2), thanks to this improvement it is possible to create a waveguide inside the crystal without damaging the crystalline structure of its central area, being able to confine much more density of photons per unit area of its interior without affecting the thermal dissipation of this, in addition, thanks to the confinement within the guide, it has been possible to considerably reduce the effects of the thermal lens and reduce the lasing threshold. Another very relevant factor when using waveguides is the ease of manufacturing with very different geometries, opening the door to generating various functionalities in the glass, as we will see below.

The results obtained in this research are presented in the following table:

Crystal	Type of channel	Slope (%)	Max power(mW)	Threshold(mW)
3.5% $Tm{:}CALGO$	Buried circular r=30um	71,2	810	200
3%$Tm{:}MgWO_4$	Surface circular r=30um	64,4	320	126
3% $Tm{:}SrF_2$	Buried circular r=30um	63,9	148	58,8
3%$Tm{:}KLUW$	Tappered circular r=25um	13,9	47,1	50

Table 1. Summary of the main data obtained from the most efficient waveguide depending on the glass used and the geometry of the guide.

To complement these results, this section will show all the scientific publications that have been made in this field achieving the following published research articles [P1-P3] and conferences papers [C1, C2]

Paper I

Ultrafast laser inscribed waveguide lasers in Tm:CALGO with depressed-index cladding

Opt. Express 28, 3528-3540 (2020)

VICTOR LLAMAS,[1,2] PAVEL LOIKO,[3] ESROM KIFLE,[1] CAROLINA ROMERO,[4] JAVIER R. VÁZQUEZ DE ALDANA,[4] ZHONGBEN PAN,[5,6] JOSEP MARIA SERRES,[1,2] HUALEI YUAN,[5] XIAOJUN DAI,[5] HUAQIANG CAI,[5] YICHENG WANG,[6] YONGGUANG ZHAO,[6,7] VIKTOR ZAKHAROV,[8] ANDREY VENIAMINOV,[8] ROMAIN THOUROUDE,[2] MATHIEU LAROCHE,[2] HERVÉ GILLES,[2] MAGDALENA AGUILÓ,[1] FRANCESC DÍAZ,[1] UWE GRIEBNER,[6] VALENTIN PETROV,[6] PATRICE CAMY,[3] AND XAVIER MATEOS[1]

[1] Física i Cristal·lografia de Materials i Nanomaterials (FiCMA-FiCNA)-EMaS, Dept. Química Física i Inòrganica, Universitat Rovira i Virgili (URV), Campus Sescelades, 43007 Tarragona, Spain

[2] Eurecat, Centre Tecnològic de Catalunya, Unitat Advanced Manufacturing Systems (AMS), Campus Sescelades, 43007 Tarragona, Spain

[3] Centre de recherche sur les Ions, les Matériaux et la Photonique (CIMAP), UMR 6252 CEA-CNRS-ENSICAEN, Université de Caen, 6 Boulevard du Maréchal Juin, 14050 Caen Cedex 4, France

[4] Aplicaciones del Láser y Fotónica, University of Salamanca, 37008 Salamanca, Spain

[5] Institute of Chemical Materials, China Academy of Engineering Physics, 621900 Mianyang, China

[6] Max Born Institute for Nonlinear Optics and Short Pulse Spectroscopy, Max-Born-Str. 2a, 12489 Berlin, Germany

[7] Jiangsu Key Laboratory of Advanced Laser Materials and Devices, Jiangsu Normal University, 221116 Xuzhou, China

[8] ITMO University, 49 Kronverkskiy Pr., 197101 St. Petersburg, Russia

Abstract: Depressed-index buried and surface channel waveguides (type III) are produced in a bulk 3.5 at.% Tm^{3+}:CALGO crystal by femtosecond direct-laser-writing at kHz repetition rate. The waveguides are characterized by confocal microscopy and μ-Raman spectroscopy. Under in-band-pumping at 1679 nm ($^3H_6 \rightarrow {}^3F_4$ transition) by a Raman fiber laser, the buried channel waveguide laser with a circular cladding (diameter: 60 μm) generated a continuous-wave output power of 0.81 W at 1866-1947 nm with a slope efficiency of 71.2% (versus the absorbed pump power) and showed a laser threshold of 200mW. The waveguide propagation losses were as low as 0.3 ± 0.2dB/cm. The laser performance under in-band

pumping was superior compared pumping at ~800nm ($^3H_6 \rightarrow {}^3H_4$ transition), i.e., the conventional pump wavelength. Vibronic laser emission from the WG laser above 2 µm is also achieved. The low-loss behavior, the broadband emission properties and good power scaling capabilities indicate the suitability of Tm^{3+}: CALGO waveguides for mode-locked laser operation at ~2 µm.

1.Introduction

Femtosecond (fs) Direct Laser Writing (DLW), also known as Ultrafast Laser Inscription (ULI) is a powerful method for the fabrication of passive and active photonic micro-structures such as optical waveguides (WGs) in transparent dielectric materials [1–3]. These materials absorb the energy of the fs pulses through nonlinear processes, leading to a permanent modification of the structure at the µm-scale and, consequently, a change of the refractive index Δ_n with respect to the unmodified (bulk) regions [1]. The advantages of fs-DLW include the fast fabrication time, short interaction time preventing serious damage of the material, high precision, a wide range of suitable materials (i.e., glasses, ceramics or crystals) and the ability to fabricate 3D structures as building blocks of photonic integrated circuits [4].

The classification of fs-DLW WGs is based on the refractive index change Δ_n which can be either positive or negative. In type I WGs (for $\Delta_n > 0$), the mode guiding is observed *within* the irradiated area (typically, in the form of a damage track). Such conditions are common for amorphous materials such as glasses [5,6] and certain crystals [7]. In type II WGs (for $\Delta_n < 0$), the guiding is achieved *between* a pair of damage tracks (the "dual-line" approach) or in the *vicinity* of a single track [8,9]. Within the irradiated areas, the refractive index decreases and between (near) the tracks, it is enhanced due to the photo-elastic effect. Compared to type I structures, type II WGs preserve their properties at increased temperature.

Recently, another geometry of depressed-index WGs was proposed [10] and classified as type III structures [1]. In type III WGs, the core is surrounded by a number of closely located damage tracks forming a quasi-continuous "wall" of reduced refractive index. The guided mode is then a bit separated from the WG cladding potentially reducing the propagation losses. Moreover, this approach allows one to control the transverse mode profile [11]. Typically, a circular geometry is more favorable as it fits the fiber technology.

WG lasers emitting in the eye-safe spectral range near ~2 µm are of interest for optical communications, spectroscopy, sensing of relevant bio- and atmospheric molecules, and for further wavelength conversion to the mid-IR. It is common to achieve the ~2 µm laser emission using thulium (Tm^{3+}) or holmium (Ho^{3+}) ions. Tm^{3+} ions typically feature large Stark splitting of the ground-state ($^3H_6$) leading to broadband luminescence and, thus, they are of interest for wavelength-tunable and ultrashort-pulse oscillators.

So far, efficient Tm WG lasers based on Liquid Phase Epitaxy (LPE) technology were demonstrated [12,13]. Van Dalfsen *et al.* reported on a Tm:$KY_xGd_yLu_z(WO_4)_2$ channel WG laser delivering up to 1.6 W at 1.84 µm with a slope efficiency of 75–81% employing a conventional pumping scheme (for the $^3H_6 \rightarrow {}^3H_4$ transition, at ~0.8 µm) [12]. For Tm WG lasers fabricated by fs-DLW, typically, lower output powers were extracted [14–19]. Lancaster *et al.* demonstrated a fs-DLW channel WG laser in bulk Tm:ZBLAN glass generating 205mW at 1.89 µm and reaching a slope efficiency of 67% (using a similar pump) [15]. Note that for conventional pumping, to reach high slope efficiency, one needs to rely on the cross-relaxation for adjacent Tm^{3+} ions [12] leading to the requirement of high Tm^{3+} doping which might deteriorate the WG quality.

Further advances in the field of fs-DLW Tm WG lasers require (i) the search for novel materials supporting power-scalable laser operation and (ii) the introduction of an alternative pumping scheme which may intrinsically bring the advantage of high laser efficiency at any Tm^{3+} doping levels. Towards the first goal, in this work, we propose to use Tm^{3+}-doped calcium gadolinium aluminate ($CaGdAlO_4$ or shortly CALGO) crystal. This host material was first considered for Yb^{3+} doping [20] leading to high-power [21] and ultrashort-pulse mode-locked [22,23] lasers, including thin-disk lasers [24]. The key advantages of rare-earth doped CALGO are (i) good thermal properties, namely high thermal conductivity showing a weak dependence on the doping level [25] with weak and positive thermal lensing [26], and (ii) a structural disorder leading to inhomogeneous broadening of the spectral bands [27]. Channel WG lasers were fabricated in bulk Yb^{3+}:CALGO by fs-DLW [28,29]. Hasse *et al.* reported on a WG laser based on the dual-line approach (type II) generating 2.4 W of output power at 1030–1042nm with a slope efficiency of 69% (WG propagation losses of ∼1.1dB/cm) [28].

Recently, the CALGO crystal and its yttrium isomorph (CALYO) were also implemented for Tm^{3+} doping. Hutchinson *et al.* first reported on spectroscopy of Tm:CALYO crystals [30]. Laser operation was first achieved by Moncorge *et al.* [31]. Recent studies focused on diode-pumped laser performance and wavelength tuning [32]. Wang *et al.* demonstrated a SESAM mode-locked Tm:CALGO bulk laser generating 650 fs pulses at 2021nm (emission bandwidth: ∼9nm) at a repetition rate of ∼100MHz [33].

The second goal is reached by implementing the so-called in-band or resonant pumping directly exciting the electrons to the upper laser level ($^3F_4$). This concept has been already demonstrated for bulk Tm lasers. W. Yao *et al*. developed an in-band-pumped Tm^{3+}:CALYO laser delivering 6.8 W at 1968 nm with a slope efficiency of ∼56% [34]. Recently, it was implemented for Tm WG lasers based on the LPE fabrication technology: Loiko *et al.* achieved 2.05 W at 1881nm with a very high slope efficiency of 78.3% [35]. The advantages of in-band pumping are high slope efficiencies approaching the Stokes limit even at low Tm^{3+} doping levels and reduced heat loading.

In the present work, we demonstrate the first Tm^{3+}:CALGO waveguide laser based on the fs-DLW fabrication method and implementing the in-band pumping scheme for reaching high slope efficiency and power scalability approaching the watt-level output.

2.Fabrication and characterization of waveguides

2.1. Femtosecond direct laser writing

As a gain material, we used bulk Tm:CALGO crystals grown by the conventional Czochralski method using Ar atmosphere in an Ir crucible and an [001]-oriented undoped seed [32]. Tm:CALGO is tetragonal (sp. gr. $I4/mmm$ - D^{17}_{4h}). The crystal composition was determined by Inductively Coupled Plasma Mass Spectrometry as $CaGd_{0.913}Lu_{0.052}Tm_{0.035}AlO_4$. Optically passive Lu^{3+} ions were added to induce additional spectral broadening. The actual concentration of Tm^{3+} ions N_{Tm} was 4.31×10^{20} cm^{-3} (3.5 at.% Tm).

The laser crystal (thickness t: 6.2mm, aperture: 3.2×3.1 mm^2) was cut for light propagation along the crystallographic c-axis (c-cut), i.e. for σ-polarization. Both its input and output faces were polished to a laser-grade quality and left uncoated.

Depressed-index WGs were fabricated in bulk Tm:CALGO by fs-DLW. Two types of structures were produced, namely buried channel WGs with a circular cladding (diameter: 60, 80 and 100 μm), and surface channel WGs with a half-ring cladding (diameter: 60 μm). The WG cladding was formed by a set of continuous damage tracks produced in the crystal by fs laser radiation. Light guiding is expected in the core located within the cladding showing a decreased refractive index ($\Delta n = n_{\mathrm{track}} - n_{\mathrm{bulk}} < 0$), Fig. 1. Depressed cladding WGs are the only technique based on fs-laser irradiation that has been demonstrated to allow the fabrication of WGs for interaction with surface.

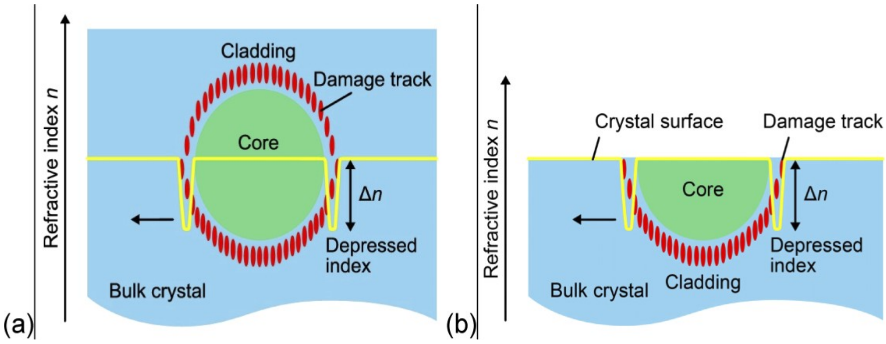

Fig. 1. Geometries of depressed-index (a) buried and (b) surface channel WGs (type III) fabricated in bulk Tm:CALGO crystal by fs-DLW.

For fs-DLW, we employed 120-fs, 795-nm pulses from a Ti:Sapphire regenerative amplifier operating at a repetition rate of 1 kHz [36]. The laser output was focused into the sample through the polished top surface using a 40× microscope objective (N.A.=0.65). Only a small fraction of the pulse energy was utilized and controlled with a λ/2 plate, a neutral density filter and a polarizer. The writing parameters were optimized in a set of test experiments as follows: incident pulse energy of 0.25 μJ (buried WGs) and 0.17 μJ (surface one), writing speed of 400 μm/s and track separation of 3 μm. To produce the damage tracks, the crystal was repetitively translated along its c-axis. The tracks were written along the entire length of the crystal. No post-writing repolishing of the crystal surfaces was applied as they were preserved undamaged.

2.2. Bulk crystal spectroscopy

Here, we briefly describe the spectroscopic properties relevant for laser operation. In the CALGO crystal, the Ca^{2+} and Gd^{3+}$_{|}$Lu^{3+} cations are statistically distributed over the same type of sites (C$_{4v}$ symmetry, IX-fold oxygen coordination). The Tm^{3+} ions replace the Gd^{3+} cations. The local disorder originates from the second coordination sphere of Tm^{3+} [27]. Consequently, smooth and broad spectral bands both in absorption and emission are observed.

CALGO is an optically uniaxial crystal (the optical axis is parallel to the $_{c}$-axis), so that there are two principal light polarizations, π and σ. At the wavelength of ~1.92 µm, its refractive indices are $_{no}$ =1.9021 and $_{ne}$ =1.9249 [37].

The absorption cross-section spectra, σ_{abs}, for the transition from the $^3H_6$ ground-state to the excited-states of Tm^{3+} in CALGO, $^3H_4$ (conventional pumping) and $^3F_4$ (in-band pumping), are shown in Fig. 2(a) for π and σ polarizations. For the $^3H_6 \rightarrow {}^3H_4$ transition, σ_{abs} is 0.67×10^{-20} cm^2 at 798 nm and the full width at half maximum (FWHM) of the absorption band is 18.6 nm. For the $^3H_6 \rightarrow {}^3F_4$ one, σ_{abs} =0.65×10^{-20} cm^2 at 1736 nm with a larger FWHM of ~120 nm (all values are specified for σ-polarization).

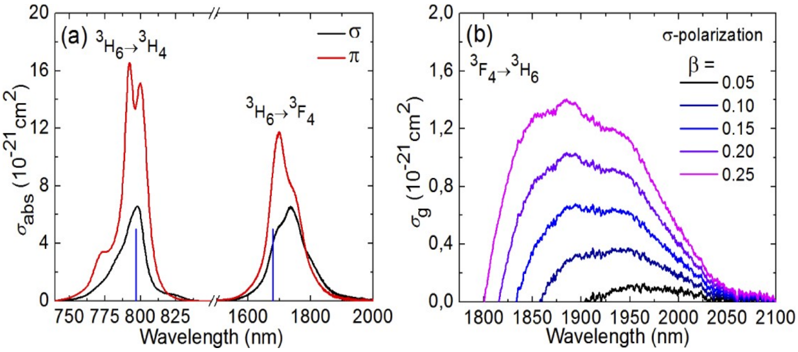

Fig. 2. Spectroscopy of Tm^{3+} ions in tetragonal CALGO crystals: (a) absorption crosssections, σabs, for the ^{3}H6 → ^{3}H4 and ^{3}H6 → ^{3}F4 transitions (π and σ light polarizations), *blue lines* indicate the pump wavelengths in this work; (b) gain cross-sections, σg =βσSE – (1 – β)σabs, for σ-polarization, β=*N*2(^{3}F4)/*N*Tm is the inversion ratio for the ^{3}F4 → ^{3}H6 transition.

For the $^3F_4 \rightarrow {}^3H_6$ laser transition, the maximum stimulated-emission (SE) cross-section σ_{SE} is 0.91×10^{-20} cm^2 at 1813nm for σ-polarization. Tm lasers operating on this transition represent a quasi-three-level laser scheme exhibiting reabsorption. To quantify this, the gain cross-sections for several inversion ratios are calculated in Fig. 2(b) for σ-polarization. The gain spectra of Tm:CALGO are smooth and broad. For an inversion ratio β of 0.20, the gain bandwidth is ~145nm. The upper laser level lifetime of Tm:CALGO is ~3.2ms.

2.3.Confocal microscopy

The geometry of the fabricated WGs was studied using a confocal laser microscope LSM 710 (Carl Zeiss). It was equipped with a rotatable polarizer (P), analyzer (A) and a blue GaN laser ($\lambda_=$405nm).

At first, we looked at one of the crystal end-facets in polarized light (P || *a*-axis). The confocal microscope image for the buried WG with a circular cladding is shown in Fig. 3(a).

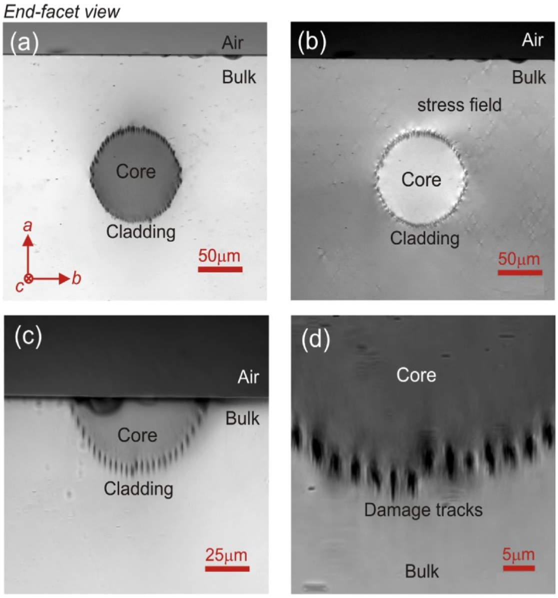

Fig. 3. WG end-face inspection: Confocal laser microscope images of depressed-index fs-DLW WGs in Tm:CALGO crystal: (a,b) buried WG with circular cladding (size: 100 μm); (c,d) surface WG with half-ring cladding (size: 60 μm). End-facet view, transmission mode, $\lambda_=$405 nm, light polarization (*E* || *a*) is vertical. Image (b) is obtained in crossed polarizers.

One can clearly see the WG cladding formed by individual damage tracks which appears darker than the surrounding bulk material, due to light scattering. The measured diameter of the cladding is 106 × 104 µm (horizontal × vertical) which is close to the targeted value (∼100 µm). The size of each individual damage track is 2 × 6 µm. This asymmetry is determined by the writing geometry (through the top surface). The separation between the tracks is ∼3 µm (horizontal) and 0–6 µm (vertical). The axis of the WG is located at ∼130 µm below the crystal surface. The area inside the cladding appears slightly darker (the greyscale colors are enhanced) possibly due to partial coupling of light into the WG and scattering at the cladding. There are no cracks originating from the fs-DLW.

By inspecting the same WG placed between two crossed polarizers (P || *a*, A || *b*), see Fig. 3(b), we observed a clear enhancement of the light intensity inside the WG cladding and around it. This is ascribed to the stress fields [38] caused by fs-DLW and inducing a local change of the optical indicatrix via the photo-elastic effect.

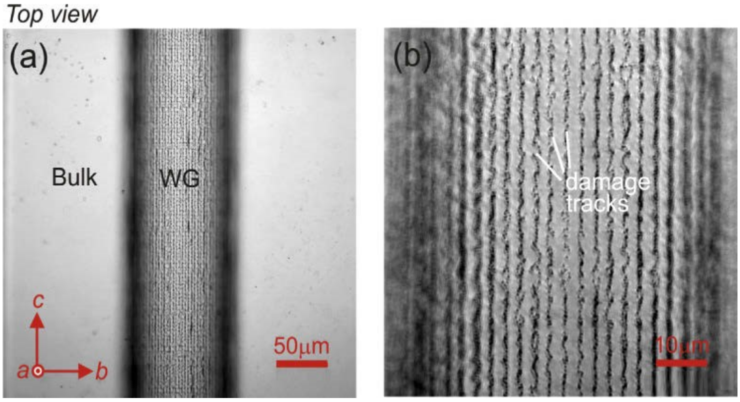

Fig. 4. WG top-surface inspection: Confocal laser microscope images of depressed-index fs-DLW WGs in Tm:CALGO crystal: (a,b) buried WG with a circular cladding (size: 100 µm). Top-view, transmission mode, λ=405 nm, light polarization (*E* || *c*) is vertical.

A similar study is performed for the surface WG, Fig. 3(c). The measured size of this WG is 72 × 40 µm (horizontal × vertical). The WG is located just beneath the crystal surface: the distance to the shallowest damage tracks is only 6 µm. The cracks in Fig. 3(c) originate from polishing of the WG end-facet before the fabrication of the WG. Figure 3(d) gives a close look on individual damage tracks.

Subsequently, we examined the top surface of the sample in polarized light (P || *c*). The canvas-like barrel-shape cladding of the buried WGs is clearly seen in Fig. 4(a). No cracks are observed in the surrounding bulk region. By observing the individual damage tracks, Fig. 4(b), we conclude that they are continuous along the writing direction. The width of the tracks is ~1 μm and the deviation from a straight line is less than 2 μm.

2.4. μ-Raman spectroscopy

Raman spectroscopy is sensitive to weak modifications of the structure of the host material. For μ-Raman studies, we used a Renishaw inVia Reflex confocal Raman microscope equipped with a 50× Leica objective and an Ar^+ ion laser (λ=514 nm). The Raman spectrum of the *c*-cut Tm:CALGO crystal is shown in Fig. 5. The maximum phonon energy is ~650cm^{-1}.

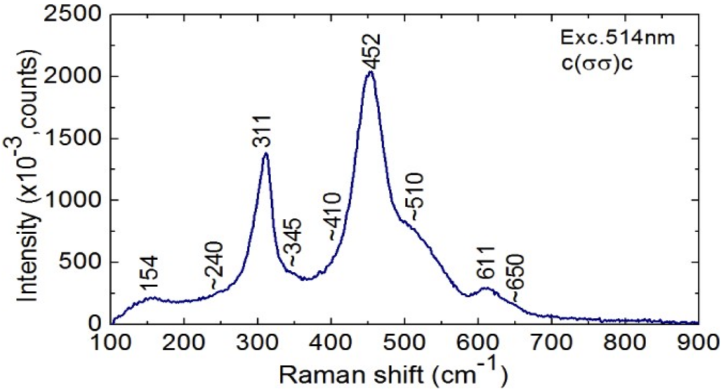

Fig. 5. Raman spectrum of the *c*-cut Tm:CALGO bulk crystal. The measurement geometry is ***c***(σσ)***c***, λexc =514 nm. The numbers indicate the Raman frequencies in cm^{-1}.

For μ-Raman mapping of the crystal end-facet, we selected the vibration at ~452 cm^{-1} and monitored this Raman peak intensity, width and position. The results for the buried WG with a circular cladding (diameter: 100 μm) are shown in Fig. 6. In the area containing the damage tracks, the Raman peak intensity decreases, the peak is broadened and a shift of its position is observed. These changes indicate modification of the material in the irradiated area, in particular, a reduction of its crystallinity [39]. In Figs. 6(b) and 6(c), one can also see a slight variation of the Raman response in the areas outside the cladding which are spatially matching the stress fields suggested by the confocal microscopy study, Fig. 3(b). In the WG core, the Raman response of the material is very close to that in the bulk crystal, confirming no alteration of the crystal structure in the core.

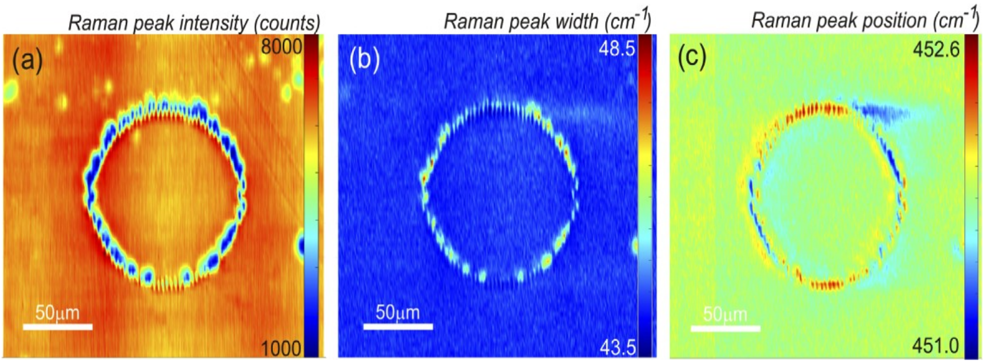

Fig. 6. μ-Raman mapping of a depressed-index buried channel WG with a circular cladding (size: 100 μm) fabricated in a Tm:CALGO crystal by fs-DLW: (a) peak intensity, (b) width (FWHM), (c) position; monitoring the ~452cm^{-1} mode in the $_c(\sigma\sigma)_c$ geometry, λexc =514 nm.

3.Laser operation

3.1. Laser set-up

The scheme of the in-band pumped WG laser is shown in Fig. 7(a). The crystal containing the WGs was mounted on a passively-cooled Cu-holder using a silver paste for better heat removal. The laser cavity was formed by a flat pump mirror (PM) coated for high transmission (HT, $T_=$93.0%) at 1.68 μm and for high reflection (HR) at 1.86-2.32 μm, and a set of flat output couplers (OCs) with transmissions $_{TOC}$ of 1.5%–50% at the laser wavelength. We also used a band-pass OC supporting laser oscillation above 2 μm. Both the PM and the OC were placed as close as possible to the crystal. No index-matching liquid was used to avoid damage to the optical elements.

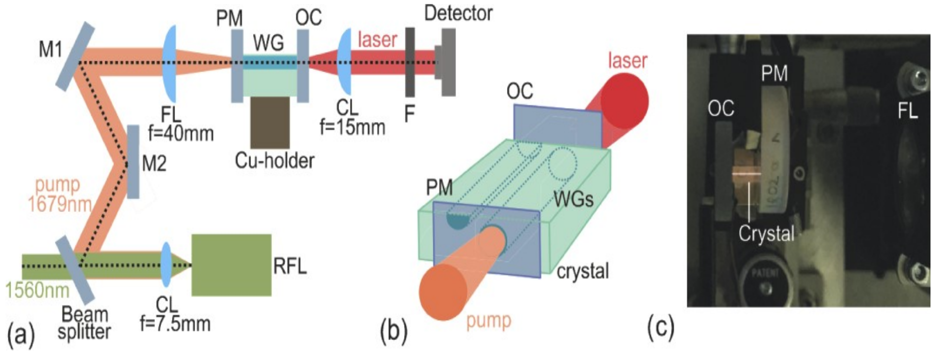

Fig. 7. Scheme of the in-band-pumped Tm:CALGO WG laser: (a) laser set-up, CL and FL – collimating and focusing lens, respectively, M1 and M2 – folding mirrors, PM – pump mirror, OC – output coupler, WG – waveguide, F – cut-on filter, RFL – Raman fiber laser; (b) geometry of the studied WG lasers (buried and surface); (c) photograph of the laser.

As a pump source for in-band pumping ($^3H_6 \rightarrow {}^3F_4$ transition), we used a home-made Raman fiber laser (RFL) delivering up to 2.9 W of linearly polarized output at 1679nm ($M^2 \approx 1$, emission bandwidth: < 1nm) [40]. The fundamental beam was provided by an erbium fiber master oscillator power amplifier (MOPA) configuration. The RFL was based on a single-mode polarization maintaining germanosilicate fiber (iXBlue Photonics; core diameter, 4.5 μm; length, 300 m) exhibiting a Raman-active mode with energy of ~440cm^{-1}. The output of the RFL was collimated with a lens (focal length: f=7.5mm), filtered from the residual pump at 1560nm using a beam-splitter and focused into the crystal through the PM with an uncoated spherical CaF_2 lens (f=40mm).

The measured pump spot diameter in the focus $2w_P$ was 30 ± 5 μm. The pump coupling efficiency η_{coupl} was estimated from the Fresnel losses at the uncoated input crystal facet to be 90.3% (n_o =1.9055 [37]). The single-pass pump absorption was calculated from the small-signal value, $\eta abs,0(1\text{−}pass) = 1 - \exp(-\sigma^P_{abs} N_{Tm} t) = 64.5\%$ ($\sigma^P_{abs} = 0.40 \times 10^{-20}$ cm^2 is the absorption cross-section at the pump wavelength λ_P for σ-polarization).

The geometry of the buried and channel WG lasers is shown in Fig. 7(b). A photograph of this laser is presented in Fig. 7(c).

The laser emission after the OC was collimated using a spherical CaF_2 lens (f=15 mm) and filtered from the residual pump using a dichroic mirror. The spectra of laser emission were measured using an optical spectrum analyzer (model AQ6375B, Yokogawa). The beam profile was captured using a FIND-R-SCOPE near-IR camera.

A similar set-up was used for pumping at ~800nm ($^3H_6 \rightarrow {}^3H_4$ transition), e.g., the conventional pump wavelength. For this, we employed a Ti:Sapphire laser (model Mira 900, Coherent) emitting up to 1.5 W at λ_P =798 nm ($M^2 \approx 1$). The pump light was collimated using a microscope objective (Mitutoyo M Plan NIR 10×, N.A.=0.28, f=20 mm, T=63.8% at 0.80 µm) resulting in $2w_P$ =20 ± 5 µm. The flat PM was coated for HT (T > 99%) at 0.80 µm and for HR at 1.8–2.1 µm and the set of flat OCs had a transmission T_{OC} of 1.5%–30% at the laser wavelength. The residual pump was filtered with a long-pass filter (FEL1000, Thorlabs).

The pump coupling efficiency was estimated from the pump-transmission measurements at ~850nm(outsidetheTm^{3+} absorption band), e.g., for the buried WG with a circular cladding(size: 60 µm), η_{coupl} =81 ± 2% (accounting for the Fresnel losses). The pump absorption at the threshold pump power was determined from similar measurements at 798nm, $\eta_{abs,L(1-pass)}$ =83 ± 2%, being close to the small-signal one.

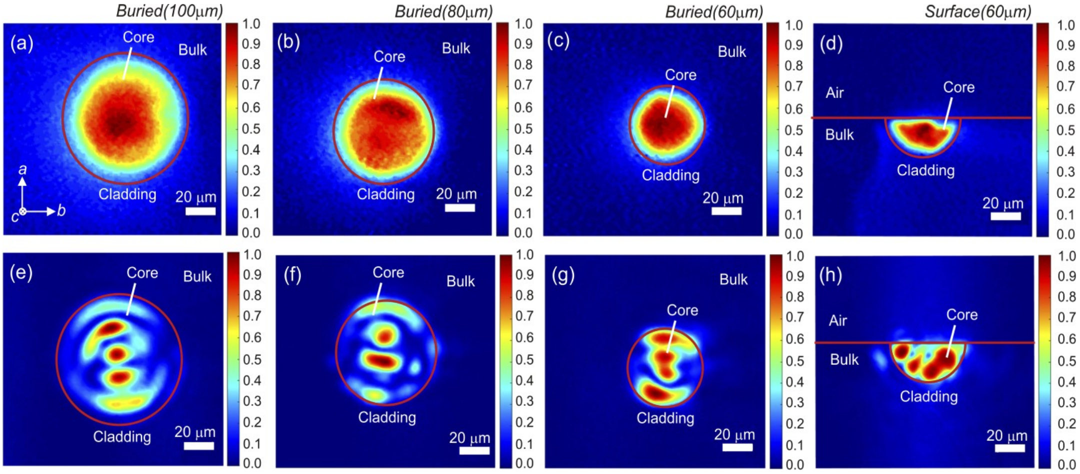

Fig. 8. Near-field pump modes for depressed-index fs-DLW channel WGs in Tm:CALGO: (a)-(c) λP =798nm, (e)-(f) λP =1679nm; buried WGs with a circular cladding and a diameter of (a,e) 100 µm, (b,f) 80 µm, (c,g) 60 µm and (d,h) surface WG with a half-ring cladding (size: 60 µm). The red circular lines indicate the cladding / crystal surface and are drawn as a guide for the reader.

The near-field profiles of the pump modes for the conventional (λ_P =798nm) and in-band (λ_P =1679nm) pumping are shown in Fig. 8. For λ_P =798nm, the pump radiation almost uniformly fills the volume of the WG core. At the wavelength of λ_P =1679nm, less modes are supported. Still, they are well confined within the WG cladding (shown by red circles).

3.2. WG laser pumped at 798 nm - conventional pumping

We started the laser experiments using the conventional pumping (λ_P =798nm). The input-output dependences for the buried channel WG (diameter: 60 µm) are presented in Fig. 9(a). The WG laser generated a maximum output power of 0.27 W at 1824-1832nm with a slope efficiency η of 50.3% (vs. the absorbed pump power P_{abs}) and a laser threshold of P_{th} =92mW. The optical-to-optical efficiency η_{opt} was 29.6% (vs. the incident power on the crystal). The highest output power corresponded to T_{OC} =30% (the maximum available output coupling in this experiment). We did not observe any thermal roll-over in the output dependences, damage of the WG end-facets or fracture of the WG itself. For lower output coupling, the slope efficiency gradually decreased.

The determined value of the slope efficiency exceeds the limit set by the Stokes efficiency, $\eta_{St} = \lambda_P/\lambda_L$ =43.6% (λ_L is the laser wavelength), which indicates the effect of cross-relaxation between adjacent Tm^{3+} ions.

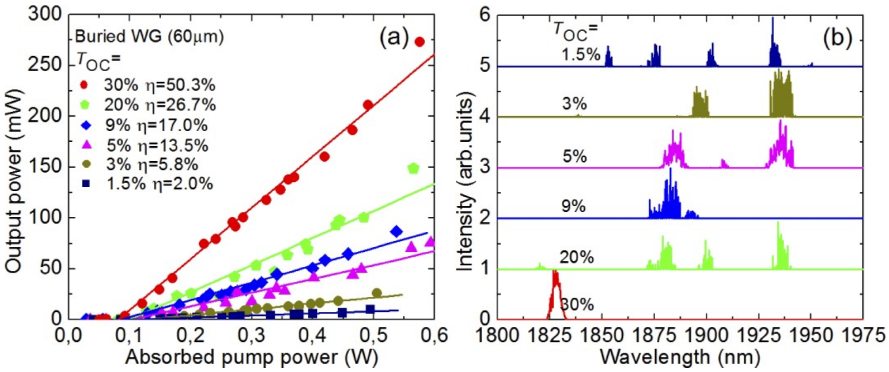

Fig. 9. Fs-DLW Tm:CALGO channel waveguide laser pumped at λP =798 nm (conventional pumping): (a) input-output dependences, η – slope efficiency; (b) laser emission spectra measured at Pabs =0.4 W. Buried WG with a circular cladding (diameter: 60 µm).

Typical laser emission spectra are shown in Fig. 9(b). For T_{OC} < 30%, the emission occurred in several spectral regions, at 1.85, 1.88, 1.90 and 1.93 µm. For example, for the lowest studied T_{OC} =1.5%, it was at 1851–1936nm. This spectral behavior is attributed to the broad gain spectra of Tm:CALGO, cf. Figure 2(b). For T_{OC} =30%, the emission wavelength was shorter, around 1.83 µm. The laser emission was unpolarized in all cases.

Typical modes of laser emission in the near-field for all four studied WGs are shown in Fig. 10. The laser modes are clearly different from the pump ones, Figs. 8(a)–8(d). This is because less transverse modes are supported for the same Δ_n at longer wavelengths and because of mode competition. In all cases, the laser mode was well confined within the WG cladding.

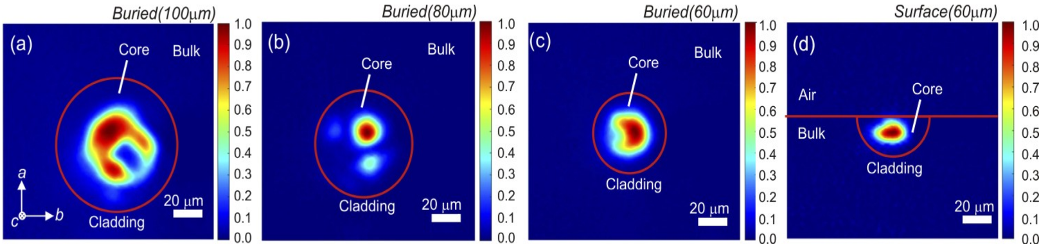

Fig. 10. Near-field spatial profiles of the laser mode for Tm:CALGO WG lasers using conventional pumping (λ_P =798nm): (a)-(c) buried WGs with a circular cladding (diameter: (a) 100 µm, (b) 80 µm, (c) 60 µm); (d) surface WG with a half-ring cladding (size: 60 µm). The red circular lines indicate the cladding / crystal surface and are drawn as a guide for the reader. T_{OC} =20%.

3.3. WG laser pumped at 1679 nm - in-band pumping

The performance of the buried channel WG laser (size: 60 µm) for different output coupling is shown in Fig. 11(a). The WG laser generated a maximum output power of 0.81 W at 1866-1947 nm with a slope efficiency η of 71.2% and showed a laser threshold P_{th} of 200 mW. The optical-to-optical laser efficiency η_{opt} amounted to 35.8%. These results were achieved for the optimum T_{OC} of 30%. For higher output coupling, the efficiency slightly deteriorated due to the upconversion losses related to high population inversion. The unpolarized laser emission was broadband, Fig. 11(b), similar as in the case of pumping at 798nm [Fig. 9(b)] due to the flat and broad gain spectra. The spectral behavior was also determined by the etalon (Fabry-Perot) effects at the crystal / mirror interfaces.

The performance of the in-band pumped WG laser is superior compared to the conventional pumping both in terms of the output power and slope efficiency.

The comparison of the laser performance of all four studied WGs is shown in Fig. 11(c) for the same T_{OC} =20%. For the buried WGs, the output power increased slightly with the WG diameter, reaching 0.88 W at 1907–1938nm with $\eta_{=}$69.7% and P_{th} =70mW for the WG with the largest cross-section (100 µm). The performance of the surface WG was inferior which is attributed to higher propagation losses: the surface WG laser generated 0.29 W at 1902–1913nm with lower η of 23.2% and increased P_{th} of 210mW. The laser emission spectra of different WG lasers are shown in Fig. 11(d) and they are similar.

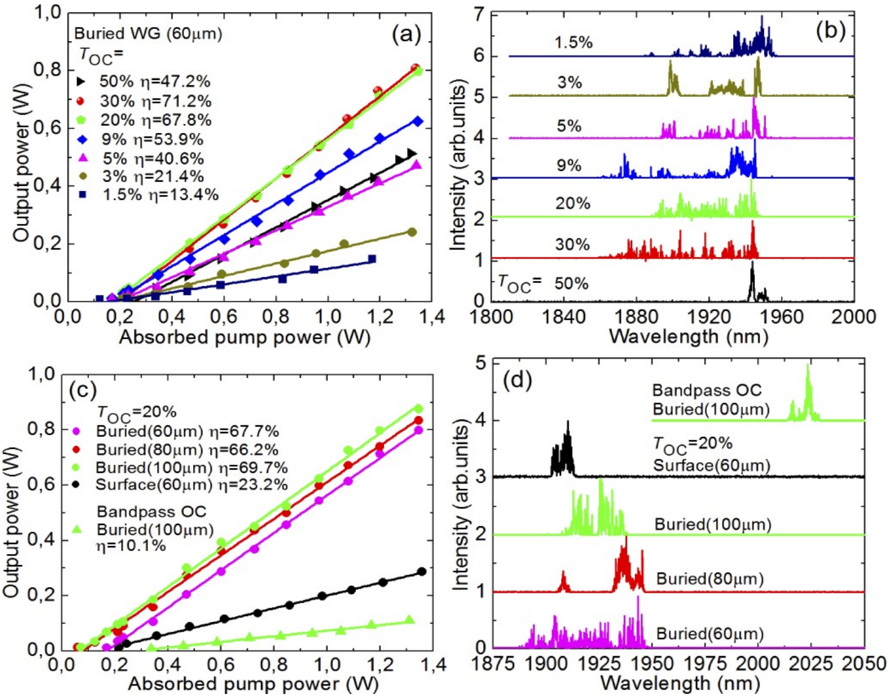

Fig. 11. Fs-DLW Tm:CALGO channel waveguide lasers in-band pumped at 1679 nm: (a,b) buried WG with a circular cladding (size: 60 µm), (c,d) comparison of buried (size: 60–100 µm) and surface (size: 60 µm) WGs, TOC =20%, (a,c) input-output dependences, η – slope efficiency; (b,d) typical laser emission spectra measured at P_{abs} =1.5 W.

The WG propagation losses estimated from the Caird analysis [41] were ~0.3 ± 0.2 dB/cm (for the buried channel WG with a diameter of 60 µm), Fig. 12. This value is comparable to that estimated for fs-DLW depressed-index WGs in bulk Tm^{3+}:ZBLAN glass (0.4 ± 0.2dB/cm) [15]. Compared to the previously reported type II WGs in Yb^{3+}:CALGO [28], we measured much lower propagation losses.

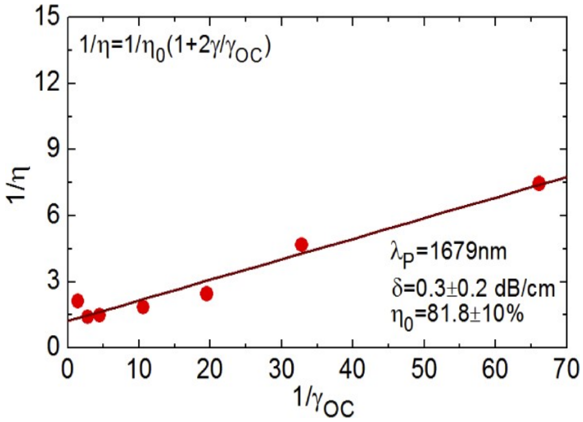

Fig. 12. Caird analysis of intracavity losses in the in-band pumped Tm:CALGO buried WG laser (circular cladding with a diameter of 60 µm): inverse of the slope efficiency, 1/η, vs. inverse of the output-coupling loss, 1/γ OC, circles - experimental data, line - their fit.

By implementing the band-pass OC, we achieved laser emission above 2 µm: the buried channel WG laser (diameter: 100 µm) generated up to 0.11 W at 2015–2028nm. However, lasing at such long wavelengths was at the expense of a reduced slope efficiency (η=10.1%) and an increased laser threshold (P_{th} =335mW). Let us analyze this operation regime. The Stark splitting for Tm^{3+} ions in CALGO is unknown. For the isostructural Tm:CALYO crystal [30], the longest wavelength of a purely electronic transition $^3F_4 \rightarrow {}^3H_6$ is 1959nm as it occurs between the sub-levels with energies of 5689 and 584cm^{-1}. The emission at longer wavelengths can be however observed due to the electron-phonon coupling (vibronic emission) [42]. In particular, the broad low-energy phonon mode at ~154cm^{-1}, cf. Figure 4, may participate in this process.

Typical laser emission modes for the in-band pumped WG lasers are shown in Fig. 13. The laser modes were well confined within the WG cladding. For all buried WGs, the emission was spatially multimode. For the surface WG, the mode was close to the fundamental transverse one maybe due to the smaller WG volume and stronger mode competition under higher losses.

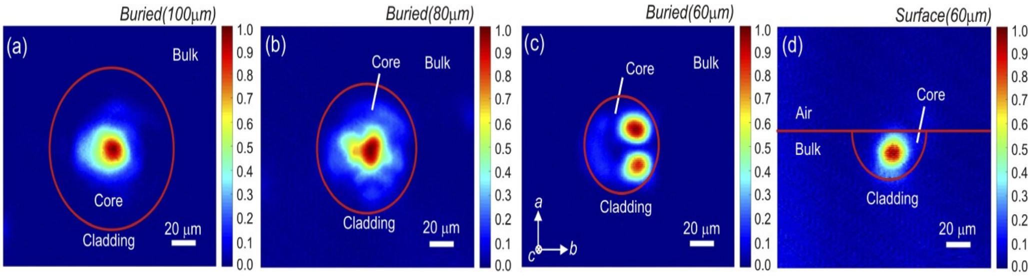

Fig. 13. Near-field profiles of the laser mode for in-band pumped Tm:CALGO WG lasers: (a)-(c) buried WGs with a circular cladding (diameter: (a) 100 µm, (b) 80 µm, (c) 60 µm); (d) surface WG with a half-ring cladding (size: 60 µm). The red circular line indicate the cladding / crystal surface and are drawn as a guide for the reader. TOC =20%.

For in-band pumping, the upper limit for the laser slope efficiency can be estimated from the Stokes one, $\eta_{St} \approx 87\%$. The achieved slope efficiency, Fig. 11(a), is close to this value. The main physical reasons for the reduced η are (i) non-perfect overlap of the pump and laser modes (a single transverse mode WG with a smaller diameter of the cladding is required to optimize the mode overlap) and (ii) possible upconversion losses in Tm^{3+}:CALGO associated with high inversion ratios β (populations of the upper laser level, $^3F_4$) which are expected to be suppressed with the optimization of the Tm^{3+} doping level.

4. Conclusion

The first ~2µm waveguide lasers based on the CALGO crystalline host have been demonstrated.

We have confirmed, Tm^{3+}:CALGO is a suitable crystalline material for efficient and powerscalable 2-µm waveguide lasers due to its high thermal conductivity, good thermo-mechanical properties, and broad and smooth Tm^{3+} emission bands originating from the structural disorder. Employing fs direct laser writing, we have fabricated low-loss depressed-index buried and surface channel waveguides with a circular and half-ring cladding (classified as type III). Confocal laser microscopy and µ-Raman spectroscopy confirmed the well-preserved single-crystalline nature of the material in the WG core region, its modification in the cladding and suggested the role of the stress fields in additional variation of the refractive index. The Tm:CALGO waveguide lasers feature high CW output power (approaching the watt-level), high laser slope efficiency of more than 70% and extremely broadband emission properties (free-running emission: 1866-1947nm, vibronic emission: 2015–2028nm). The excellent output performance was achieved employing the in-band pumping scheme.

The proposed scheme of in-band pumping using Raman fiber lasers paves the way towards multi-watt output from fs direct laser written Tm waveguide lasers. Indeed, in the present paper, we were mostly limited by the available power from the fiber laser which could be increased to >10 W. We expect that the optimization of the Tm^{3+} doping level and the WG length will allow for a simultaneous control of upconversion losses and pump absorption. Regarding the material, it is also promising to study ***a***-cut crystals giving access to π-polarization showing higher absorption cross-sections and linearly polarized laser output. In the present work, we selected ***c***-cut crystals because of the crystal growth direction.

Fs direct laser written Tm^{3+}:CALGO waveguides with a smaller cladding diameters (30–50 µm) are expected to support a single transverse mode which, together with low propagation losses and broadband emission, makes them promising for compact mode-locked oscillators operating at high (GHz-range) repetition rates.

References

1. F. Chen and J. R. Vázquez de Aldana, “Optical waveguides in crystalline dielectric materials produced by femtosecondlaser micromachining,” Laser Photonics Rev. **8**(2), 251–275 (2014).
2. R. R. Gattass and E. Mazur, “Femtosecond laser micromachining in transparent materials,” Nat. Photonics **2**(4), 219–225 (2008).
3. S. Nolte, M. Will, J. Burghoff, and A. Tuennermann, “Femtosecond waveguide writing: a new avenue to threedimensional integrated optics,” Appl. Phys. A **77**(1), 109–111 (2003).
4. G. D. Marshall, A. Politi, J. C. F. Matthews, P. Dekker, M. Ams, M. J. Withford, and J. L. O’Brien, “Laser written waveguide photonic quantum circuits,” Opt. Express **17**(15), 12546–12554 (2009).
5. K. M. Davis, K. Miura, N. Sugimoto, and K. Hirao, “Writing waveguides in glass with a femtosecond laser,” Opt. Lett. **21**(21), 1729–1731 (1996).
6. A. M. Streltsov and N. F. Borrelli, “Study of femtosecond-laser-written waveguides in glasses,” J. Opt. Soc. Am. B **19**(10), 2496–2504 (2002).

7. A. Rodenas and A. K. Kar, “High-contrast step-index waveguides in borate nonlinear laser crystals by 3D laser writing,” Opt. Express **19**(18), 17820–17833 (2011).
8. J. Siebenmorgen, T. Calmano, K. Petermann, and G. Huber, “Highly efficient Yb:YAG channel waveguide laser written with a femtosecond-laser,” Opt. Express **18**(15), 16035–16041 (2010).
9. G. A. Torchia, A. Rodenas, A. Benayas, E. Cantelar, L. Roso, and D. Jaque, “Highly efficient laser action in femtosecond-written Nd:yttrium aluminum garnet ceramic waveguides,” Appl. Phys. Lett. **92**(11), 111103 (2008).
10. A. G. Okhrimchuk, A. V. Shestakov, I. Khrushchev, and J. Mitchell, “Depressed cladding, buried waveguide laser formed in a YAG:Nd^{3+} crystal by femtosecond laser writing,” Opt. Lett. **30**(17), 2248–2250 (2005).
11. H. Liu, Y. Jia, J. R. V. de Aldana, D. Jaque, and F. Chen, “Femtosecond laser inscribed cladding waveguides in Nd:YAG ceramics: Fabrication, fluorescence imaging and laser performance,” Opt. Express **20**(17), 18620–18629 (2012).
12. K. van Dalfsen, S. Aravazhi, C. Grivas, S. M. García-Blanco, and M. Pollnau, “Thulium channel waveguide laser with 1.6 W of output power and ∼80% slope efficiency,” Opt. Lett. **39**(15), 4380–4383 (2014).
13. P. Loiko, R. Soulard, G. Brasse, J.-L. Doualan, B. Guichardaz, A. Braud, A. Tyazhev, A. Hideur, and P. Camy, “Watt-level Tm:LiYF$_4$ channel waveguide laser produced by diamond saw dicing,” Opt. Express **26**(19), 24653–24662 (2018).
14. D. G. Lancaster, S. Gross, H. Ebendorff-Heidepriem, K. Kuan, T. M. Monro, M. Ams, A. Fuerbach, and M. J. Withford, “Fifty percent internal slope efficiency femtosecond direct-written Tm^{3+}:ZBLAN waveguide laser,” Opt. Lett. **36**(9), 1587–1589 (2011).
15. D.G.Lancaster, S.Gross, A.Fuerbach, H.E.Heidepriem, T.M.Monro, andM.J.Withford, “Versatilelarge-mode-area femtosecond laser-written Tm:ZBLAN glass chip lasers,” Opt. Express **20**(25), 27503–27509 (2012).
16. Y. Ren, G. Brown, A. Ródenas, S. Beecher, F. Chen, and A. K. Kar, “Mid-infrared waveguide lasers in rare-earth-doped YAG,” Opt. Lett. **37**(16), 3339–3341 (2012).
17. J. Morris, N. K. Stevenson, H. T. Bookey, A. K. Kar, C. T. A. Brown, J.-M. Hopkins, M. D. Dawson, and A. A. Lagatsky, “1.9 µm waveguide laser fabricated by ultrafast laser inscription in Tm:Lu$_2$O$_3$ ceramic,” Opt. Express **25**(13), 14910–14917 (2017).
18. E. Kifle, P. Loiko, J. R. V. de Aldana, C. Romero, A. Ródenas, S. Y. Choi, J. E. Bae, F. Rotermund, V. Zakharov, A. Veniaminov, M. Aguiló, F. Díaz, U. Griebner, V. Petrov, and X. Mateos, “Passively Q-switched femtosecond-laserwritten thulium waveguide laser based on evanescent field interaction with carbon nanotubes,” Photonics Res. **6**(10), 971–980 (2018).
19. E. Kifle, P. Loiko, X. Mateos, J. R. V. de Aldana, A. Ródenas, U. Griebner, V. Petrov, M. Aguiló, and F. Díaz, “Femtosecond-laser-written hexagonal cladding waveguide in Tm:KLu(WO$_4$)$_2$: µ-Raman study and laser operation,” Opt. Mater. Express **7**(12), 4258–4268 (2017).

20. J. Petit, P. Goldner, and B. Viana, "Laser emission with low quantum defect in Yb:$CaGdAlO_4$," Opt. Lett. **30**(11), 1345–1347 (2005).
21. P. Loiko, J. M. Serres, X. Mateos, X. Xu, J. Xu, V. Jambunathan, P. Navratil, A. Lucianetti, T. Mocek, X. Zhang, U. Griebner, V. Petrov, M. Aguiló, F. Díaz, and A. Major, "Microchip Yb:$CaLnAlO_4$ lasers with up to 91% slope efficiency," Opt. Lett. **42**(13), 2431–2434 (2017).
22. Y. Zaouter, J. Didierjean, F. Balembois, G. Lucas Leclin, F. Druon, P. Georges, J. Petit, P. Goldner, and B. Viana, "47-fs diode-pumped Yb^{3+}:$CaGdAlO_4$ laser," Opt. Lett. **31**(1), 119–121 (2006).
23. P. Sévillano, P. Georges, F. Druon, D. Descamps, and E. Cormier, "32-fs Kerr-lens mode-locked Yb:$CaGdAlO_4$ oscillator optically pumped by a bright fiber laser," Opt. Lett. **39**(20), 6001–6004 (2014).
24. N. Modsching, C. Paradis, F. Labaye, M. Gaponenko, I. J. Graumann, A. Diebold, F. Emaury, V. J. Wittwer, and T. Südmeyer, "Kerr lens mode-locked Yb:CALGO thin-disk laser," Opt. Lett. **43**(4), 879–882 (2018).
25. P. Loiko, F. Druon, P. Georges, B. Viana, and K. Yumashev, "Thermo-optic characterization of Yb:$CaGdAlO_4$ laser crystal," Opt. Mater. Express **4**(11), 2241–2249 (2014).
26. F. Druon, M. Olivier, A. Jaffrès, P. Loiseau, N. Aubry, J. DidierJean, F. Balembois, B. Viana, and P. Georges, "Magic mode switching in Yb:$CaGdAlO_4$ laser under high pump power," Opt. Lett. **38**(20), 4138–4141 (2013).
27. P. O. Petit, J. Petit, P. Goldner, and B. Viana, "Inhomogeneous broadening of optical transitions in Yb:$CaYAlO_4$," Opt. Mater. **30**(7), 1093–1097 (2008).
28. K. Hasse, T. Calmano, B. Deppe, C. Liebald, and C. Kränkel, "Efficient Yb^{3+}:$CaGdAlO_4$ bulk and femtosecondlaser-written waveguide lasers," Opt. Lett. **40**(15), 3552–3555 (2015).
29. K. Hasse and C. Kränkel, "Yb:CALGO waveguide laser written with 1MHz-repetition rate fs-laser," in *Laser Congress 2019 (ASSL, LAC, LS&C)*, OSA Technical Digest (Optical Society of America, 2019), P. ATu1A.7.
30. J. A. Hutchinson, H. R. Verdun, B. H. Chai, B. Zandi, and L. D. Merkle, "Spectroscopic evaluation of $CaYAlO_4$ doped with trivalent Er, Tm, Yb and Ho for eyesafe laser applications," Opt. Mater. **3**(4), 287–306 (1994).
31. R. Moncorgé, N. Garnier, P. Kerbrat, C. Wyon, and C. Borel, "Spectroscopic investigation and two-micron laser performance of Tm^{3+}:$CaYAlO_4$ single crystals," Opt. Commun. **141**(1-2), 29–34 (1997).
32. Z. Pan, P. Loiko, J. M. Serres, E. Kifle, H. Yuan, X. Dai, H. Cai, Y. Wang, Y. Zhao, M. Aguiló, F. Díaz, U. Griebner, V. Petrov, and X. Mateos, ""Mixed" Tm:Ca(Gd,Lu)AlO_4 - a novel crystal for tunable and mode-locked 2µm lasers," Opt. Express **27**(7), 9987–9995 (2019).
33. Y. Wang, G. Xie, X. Xu, J. Di, Z. Qin, S. Suomalainen, M. Guina, A. Härkönen, A. Agnesi, U. Griebner, X. Mateos, P. Loiko, and V. Petrov, "SESAM mode-locked Tm:CALGO laser at 2µm," Opt. Mater. Express **6**(1), 131–136 (2016).
34. W. Yao, F. Wu, Y. Zhao, H. Chen, X. Xu, and D. Shen, "Highly efficient Tm:$CaYAlO_4$ laser in-band pumped by a Raman fiber laser at 1.7 µm," Appl. Opt. **55**(14), 3730–3733 (2016).

35. P. Loiko, R. Thouroude, R. Soulard, L. Guillemot, G. Brasse, B. Guichardaz, A. Braud, A. Hideur, M. Laroche, H. Gilles, and P. Camy, “In-band pumping of Tm:LiYF$_4$ channel waveguide: a power scaling strategy for ∼2 µm waveguide lasers,” Opt. Lett. **44**(12), 3010–3013 (2019).
36. E. Kifle, X. Mateos, J. R. V. de Aldana, A. Ródenas, P. Loiko, S. Y. Choi, F. Rotermund, U. Griebner, V. Petrov, M. Aguiló, and F. Díaz, “Femtosecond-laser-written Tm:KLu(WO$_4$)$_2$ waveguide lasers,” Opt. Lett. **42**(6), 1169–1172 (2017).
37. P. Loiko, P. Becker, L. Bohatý, C. Liebald, M. Peltz, S. Vernay, D. Rytz, J. M. Serres, X. Mateos, Y. Wang, X. Xu, J. Xu, A. Major, A. Baranov, U. Griebner, and V. Petrov, “Sellmeier equations, group velocity dispersion, and thermo-optic dispersion formulas for CaLnAlO$_4$ (Ln=Y, Gd) laser host crystals,” Opt. Lett. **42**(12), 2275–2278 (2017).
38. H.-D. Nguyen, A. Ródenas, J. R. Vázquez de Aldana, J. Martínez, F. Chen, M. Aguiló, M. C. Pujol, and F. Díaz,
“Heuristic modelling of laser written mid-infrared LiNbO$_3$ stressed-cladding waveguides,” Opt. Express **24**(7), 7777–7791 (2016).
39. E. Kifle, P. Loiko, C. Romero, J. R. V. de Aldana, A. Ródenas, V. Zakharov, A. Veniaminov, M. Aguiló, F. Díaz, U. Griebner, V. Petrov, and X. Mateos, “Femtosecond-laser-written Ho:KGd(WO$_4$)$_2$ waveguide laser at 2.1 µm,” Opt. Lett. **44**(7), 1738–1741 (2019).
40. R. Thouroude, H. Gilles, B. Cadier, T. Robin, A. Hideur, A. Tyazhev, R. Soulard, P. Camy, J. L. Doualan, and M. Laroche, “Linearly-polarized high-power Raman fiber lasers near 1670nm,” Laser Phys. Lett. **16**(2), 025102 (2019).
41. J. A. Caird, S. A. Payne, P. R. Staber, A. J. Ramponi, L. L. Chase, and W. F. Krupke, “Quantum electronic properties of the Na$_3$Ga$_2$Li$_3$F$_{12}$:Cr^{3+} laser,” IEEE J. Quantum Electron. **24**(6), 1077–1099 (1988).
42. P. Loiko, X. Mateos, S. Y. Choi, F. Rotermund, J. M. Serres, M. Aguiló, F. Díaz, K. Yumashev, U. Griebner, and V. Petrov, “Vibronic thulium laser at 2131nm Q-switched by single-walled carbon nanotubes,” J. Opt. Soc. Am. B **33**(11), D19–D27 (2016).

Paper II

Low-loss fs-laser-written surface waveguide lasers at >2 µm in monoclinic Tm^{3+}:MgWO$_4$

Optics Letters 45 (14), 4060-4063 (2020)

ESROM KIFLE,[1] PAVEL LOIKO,[2] JAVIER RODRÍGUEZ VÁZQUEZ DE ALDANA,[3] CAROLINA ROMERO,[3] VÍCTOR LLAMAS,[1,4] JOSEP MARIA SERRES,[1,4] MAGDALENA AGUILÓ,[1] FRANCESC DÍAZ,[1] LIZHEN ZHANG,[5] ZHOUBIN LIN,[5] HAIFENG LIN,[5] GE ZHANG,[5] VIKTOR ZAKHAROV,[6] ANDREY VENIAMINOV,[6] VALENTIN PETROV,[7] UWE GRIEBNER,[7] XAVIER MATEOS,[1,] LI WANG[7] AND WEIDONG CHEN[5,7]

[1]Universitat Rovira i Virgili (URV), Física i ristal·lografia de Materials i Nanomaterials (FiCMA-FiCNA)-EMaS, Marcel.li Domingo 1, 43007 Tarragona, Spain

[2]Centre de Recherche sur les Ions, les Matériaux et la Photonique (CIMAP), UMR 6252 CEA-CNRS-ENSICAEN, Université de Caen Normandie, 6 Boulevard du Maréchal Juin, 14050 Caen Cedex 4, France

[3]Aplicaciones del Láser y Fotónica, University of Salamanca, 37008 Salamanca, Spain

[4]Eurecat, Centre Tecnològic de Catalunya, Unitat Advanced Manufacturing Systems (AMS), Campus Sescelades, 43007 Tarragona, Spain

[5]Key Laboratory of Optoelectronic Materials Chemistry and Physics, Fujian Institute of Research on the Structure of Matter, Chinese Academy of Sciences, Fuzhou, 350002 Fujian, China

[6]ITMO University, 49 Kronverkskiy Pr., 197101 St. Petersburg, Russia

[7]Max-Born-Institute for Nonlinear Optics and Short Pulse Spectroscopy, 2A Max-Born-Str., 12489 Berlin, Germany

Surface channel waveguides (WGs) based on a half-ring (40–60-µm diameter) depressed-index cladding (type III) geometry are fabricated in monoclinic Tm^{3+}:MgWO$_4$ by femtosecond laser writing at a repetition rate of 1 kHz. The WGs are characterized by confocal laser microscopy and µ-Raman spectroscopy. A Tm^{3+}:MgWO$_4$ WG laser generates 320 mW at ~2.02 µm with a slope efficiency of 64.4%. The WG emits a tranverse single-mode and linear polarization ($E \,||\, N_m$). A remarkable low-loss of <0.1 dB/cm is measured for the WG. Vibronic laser emission at ~2.08 µm is also achieved.

Magnesium monotungstate ($MgWO_4$) has been recognized recently as an excellent host material for doping with trivalent thulium ions (Tm^{3+}) [1,2]. It belongs to the monoclinic crystal class (sp. gr. C^4_{2h} – $P2/c$, wolframite, [Fe,Mn]WO_4, type structure) [3] and shows a single crystallographic site for Tm^{3+} ions (the Mg^{2+} one, symmetry: C_2). Charge compensation for the heterovalent doping is provided by univalent alkali-metal cations (e.g., Na^+) in the flux [4]. $MgWO_4$ exhibits good thermo-mechanical properties, such as high thermal conductivity $<\kappa>$ = 8.7 $Wm^{-1}K^{-1}$ [5] and low anisotropy of the thermal expansion, α_a = 11.22, α_b = 8.09 and α_c = 8.77 [10^{-6} K^{-1}] [4], leading to promising power scaling capabilities.

For Tm^{3+} ions (electronic configuration: [Xe]$4f^{12}$), $MgWO_4$ shows attractive spectroscopic properties, i.e., intense and broad emission bands for the $^3F_4 \rightarrow {}^3H_6$ transition with polarized light, and large Stark splitting of the ground-state, $\Delta E(^3H_6)$ = 633 cm^{-1} [6]. Thus, the broad polarized emission bands of Tm^{3+}:$MgWO_4$ extend well above 2 µm avoiding the structured water vapor atmospheric absorption. The latter is a key issue for the generation of femtosecond pulses in mode-locked (ML) lasers in the 2 µm spectral range [7]. It was recently confirmed by a graphene ML Tm^{3+}:$MgWO_4$ laser which generated 86 fs pulses at a wavelength of 2017 nm (bandwidth: 53 nm) at a repetition rate of 87 MHz [2]. Furthermore, continuous wavelength tuning was achieved from 1897 to 2062 nm [2]. As $MgWO_4$ is an efficient Raman-active material, laser emission at even longer wavelengths (up to 2093 nm) was realized due to the electron-phonon coupling [6]. A continuous-wave (CW) Tm^{3+}:$MgWO_4$ laser generated 3.09 W at 2022-2034 nm with a slope efficiency as high as 50% [1].

Due to its attractive thermal and spectroscopic properties, Tm^{3+}:$MgWO_4$ is also promising for ML waveguide (WG) lasers above 2 µm. While Tm^{3+}-doped monoclinic double tungstate (MDT) bulk crystals have been widely explored to this aim [8], WG laser operation has never been demonstrated with monoclinic divalent-metal monotungstates. In the present work, we demonstrate the first Tm^{3+}:$MgWO_4$ WG laser featuring low passive losses and high laser efficiency, as a first step towards highrepetition-rate (GHz-range) ML WG lasers [9].

As a fabrication method, we selected femtosecond Direct Laser Writing (fs-DLW). This method is based on focusing a fs laser beam inside a small volume (few $µm^3$)

within a transparent material resulting in partial amorphization of the damaged area leading to a permanent refractive index variation ($\Delta n > 0$ or $\Delta n < 0$) [10]. The advantages of fs-DLW are: short interaction time and high precision, single step procedure, suitability for various materials *incl.* anisotropic crystals, variable WG geometries, moderate to low propagation losses. Efficient fs-DLW thulium WG lasers have been demonstrated [11,12]. Lancaster *et al.* reported on a buried channel WG laser inscribed in a Tm^{3+}:ZBLAN glass delivering 205 mW at ~1.89 µm with a slope efficiency η of 67% and low passive losses δ_{loss} of 0.4±0.2 dB/cm [11]. Kifle *et al.* demonstrated a surface WG laser in a $Tm^{3+}:KLu(WO_4)_2$ crystal generating 171 mW at ~1.85 µm with $\eta = 38\%$ and $\delta_{\mathrm{loss}} = 0.7\pm0.3$ dB/cm [12].

The $Tm^{3+}:MgWO_4$ crystal was grown by the Top-Seeded Solution Growth (TSSG) method using Na_2WO_4 as a solvent [13]. The Tm^{3+} doping level was 0.89 at.% ($N_{\mathrm{Tm}} = 1.41\times10^{20}\mathrm{cm}^{-3}$). A rectangular sample with dimensions $1.86(N_g)\times3.96(N_m)\times3.05(N_p)$ mm^3 was cut and polished along the optical indicatrix frame of this biaxial crystal [6]. The DLW was performed using 120-fs pulses with a central wavelength of 795 nm from a Ti:Sapphire regenerative amplifier at a repetition rate of 1 kHz. A small portion of the pulse energy (86 nJ, measured after the focusing optics) was employed with polarization $\boldsymbol{E} \parallel N_m$. The fs radiation was focused into the crystal along the N_g–axis through the top surface using a 40× microscope objective (N.A. = 0.65). The sample was translated at a speed of 400 µm/s along the N_p-axis producing damage tracks.
Surface channel WGs with a half-ring depressed-index cladding ($\Delta n > 0$, classified as type III microstructures [10]) were produced.

Their geometry was revealed using confocal laser microscopy, Fig. 1(a). The diameter of the cladding was 40, 50 or 60 µm. The axis of the WG was located at 20-30 µm beneath the top surface. Except of the damage tracks no cracks in the writing areas nor in the bulk volume were observed. The damage tracks passed continuously through the whole length of the 3.05 mm long sample (along the N_p-axis), Fig. 1(b). The study of the sample in crossed polarizers (P and A) revealed bright areas localized at the damage tracks indicating a local alteration of the size and orientation of the optical indicatrix, Fig. 1(c). The damage tracks reached the top surface of the WGs, Fig. 1(d) thus producing a shallow ablation groove at the external tracks.

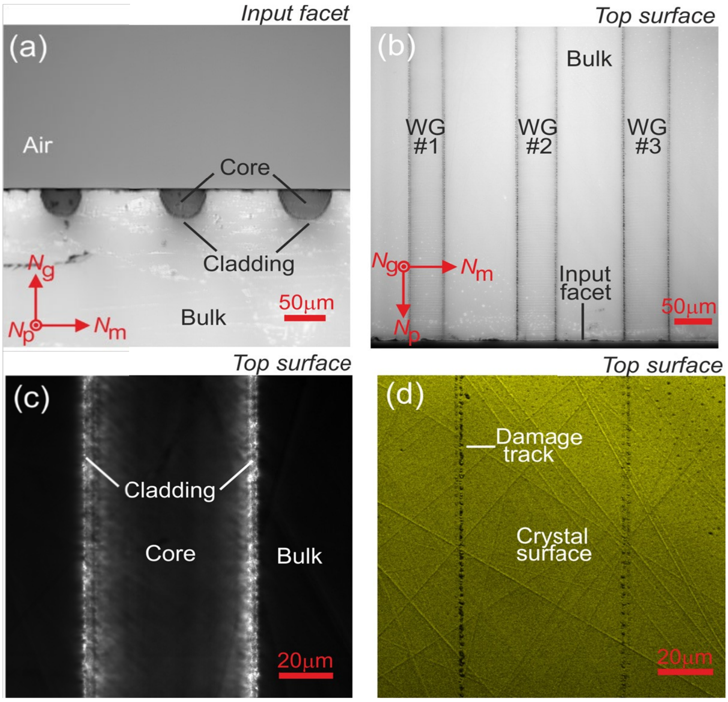

Fig. 1. Confocal microscopy study of fs-DLW surface channel WGs in Tm^{3+}:$MgWO_4$: (a) end-facet view, transmission mode, polarized light (P || N_g); (b,c) top surface view, transmission mode: (b) a general view in polarized light (P || N_p); (c) a close look on the 60 µm WG in crossed polarizers (P || N_p, A || N_m); (d) the same area as in (c) in reflection mode. λ = 405 nm. P – polarizer, A – analyzer.

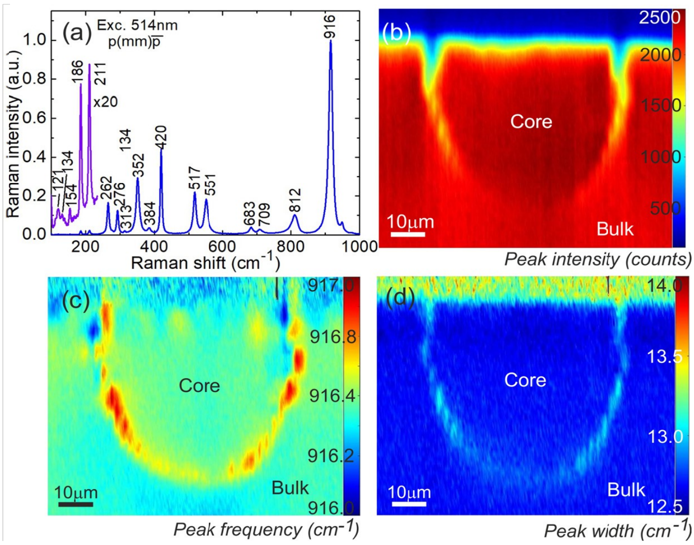

Fig. 2. Micro-Raman mapping of the fs-DLW surface channel WG (size: 50 µm) in $Tm^{3+}:MgWO_4$: (a) polarized Raman spectrum for the *p*(*mm*)p geometry, numbers denote the Raman frequencies in cm^{-1}, $\lambda_{exc} = 514$ nm; (b-d) maps of the crystal end-facet representing the variation of (b) peak Raman intensity, (c) peak frequency and (d) peak width (FWHM) for the ~916 cm^{-1} Raman band.

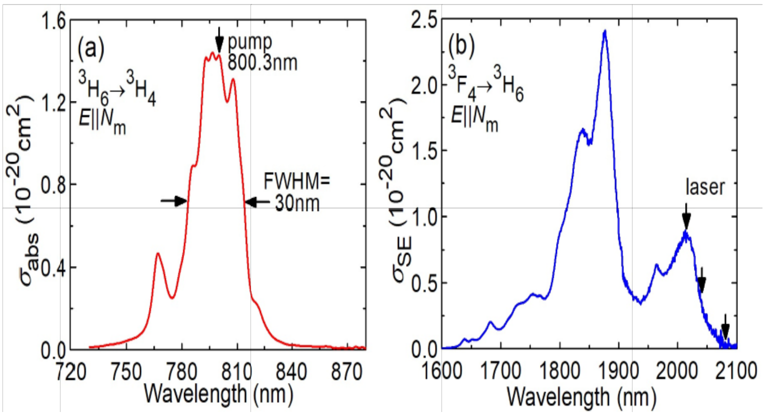

Fig. 3. Spectroscopy of Tm^{3+} ions in monoclinic $MgWO_4$: (a) absorption cross-section, σ_{abs}, for the $^3H_6 \rightarrow {}^3H_4$ transition, and (b) stimulatedemission (SE) cross-section, σ_{SE}, for the $^3F_4 \rightarrow {}^3H_6$ transition. The light polarization is ***E*** || N_m. The vertical *arrows* in (a),(b) indicate the pump and emission wavelengths for the waveguide laser, respectively.

Raman spectroscopy is a sensitive tool to study the structure alteration at the µ-scale [14]. The polarized Raman spectrum of the Tm^{3+}:$MgWO_4$ crystal for the $p(mm)$ geometry (Porto's notations) is shown in Fig. 2(a). The most intense Raman band denoted as $\nu_1(A_{1g})$ is observed at ~916 cm^{-1} and assigned to symmetric stretching W – O vibrations in the $[WO_6]$ octahedra [13]. The peak intensity, width (FWHM) and position were monitored over the sample end-facet resulting in µ-Raman maps, Fig. 2(c-d). In the damaged regions, a drop of intensity, broadening of the band and its shift to longer frequencies are observed indicating a reduction of crystallinity (a partial amorphization). The crystalline quality of the core is well preserved as manifested by the almost unchanged Raman response with respect to the bulk regions.

In Tm^{3+}:$MgWO_4$, the maximum absorption cross-section, σ_{abs}, for the $^3H_6 \rightarrow {}^3H_4$ pump transition is 1.43×10^{-20} cm^2 at 800.3 nm, Fig. 3(a). The peak stimulated-emission (SE) cross-section, σ_{SE}, at wavelengths >2 µm where the laser operation is expected, is 0.85×10^{-20} cm^2 at 2015 nm, Fig. 3(b). Both values are specified for $\boldsymbol{E} \,||\, N_m$. The upper laser level ($^3F_4$) lifetime is 1.93 ms [13].

The laser cavity comprised a flat pump mirror coated for high transmission, HT (T = 96%) at 0.80 µm and for high reflection, HR at 1.80-2.06 µm, and a set of flat output couplers (OCs) having a transmission T_{OC} = 1.5-30% at the laser wavelength. We also used a special bandpass OC coated for HT at <2 µm and providing T_{OC} = 1.6% at >2.05 µm. All the OCs provided HR at ~0.80 µm, so the WG was pumped in a double-pass. The crystal was mounted on a passively cooled BK7 glass block and placed between the cavity mirrors without index-matching among them. The mirrors were gently pressed towards the WG endfaces resulting in a geometrical cavity length of ~3.1 mm.

The pump power from a CW Ti:Sapphire laser was up to ~2 W at 800.3 nm ($M^2 \approx 1$). The pump, polarized with $\boldsymbol{E} \,||\, N_m$ (in the crystal), was focused using a 10× microscope objective (N.A. = 0.28, f = 20 mm, T = 75% at 0.80 µm) to a spot with a diameter of 25±5 µm. The pump coupling efficiency, η_{coupl}, was estimated to be 88.4±1% from pump-transmission measurements at 830 nm. The pump is confined in the slightly D-shaped cladding profile; no leakage into the bulk was detected, Fig. 4(a). The single-pass pump absorption under non-lasing conditions, $\eta_{abs,NL}$, determined at 800.3 nm by the end-fire method, gradually decreased with the incident pump power P_{inc} due to the ground-state bleaching. This effect was enhanced for smaller cladding diameters. The absorbed pump power P_{abs} was determined from $\eta_{\mathrm{abs,NL}}$ at the threshold power for each OC and accounting for double-pass pumping.

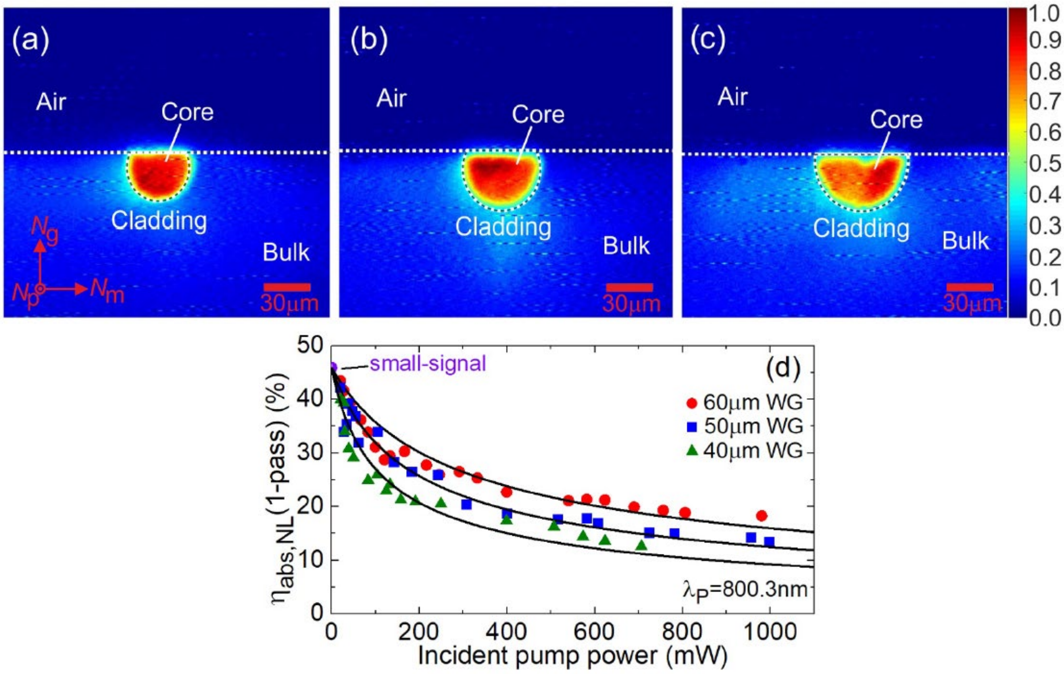

Fig. 4. (a-c) Pump modes at the output facet of the fs-DLW WGs in Tm^{3+}:$MgWO_4$: the WG cladding diameters are (a) 40 µm, (b) 50 µm and (c) 60 µm. *White dashed lines* indicate the WG cladding and the air/crystal interfaces; they are drawn as guides for the eye. The pump polarization (***E*** || N_m) is horizontal; (d) measured single-pass pump absorption in all the WGs under non-lasing conditions, $\eta_{\mathrm{abs,NL}}$: *symbols* – experimental data, *curve* – simulation with a rate-equation model using the spectroscopic data from [13]. The pump wavelength is 800.3 nm.

The input-output characteristics for the 60 µm WG are shown in Fig. 5(a). Exceptionally for the best-performing T_{OC} = 3%, we removed the optical elements placed to attenuate P_{inc} resulting in higher pump power. The laser generated 320 mW at ~2015 and 2036 nm with a slope efficiency η of 64.4% (vs. P_{abs}). The laser threshold was at P_{abs} = 126 mW and the optical-to-optical efficiency at the maximum pump level was 24.7% (vs. P_{inc}). The total pump absorption (in two passes) was 48.1%. The laser slope efficiency slightly increased with the output coupling, reaching η = 69.3% for T_{OC} = 20%. The laser threshold decreased for smaller T_{OC}, from 186 mW (30% OC) down to 117 mW (1.5% OC). No thermal roll-over in the output dependences was detected; the power scaling was limited by the available pump.

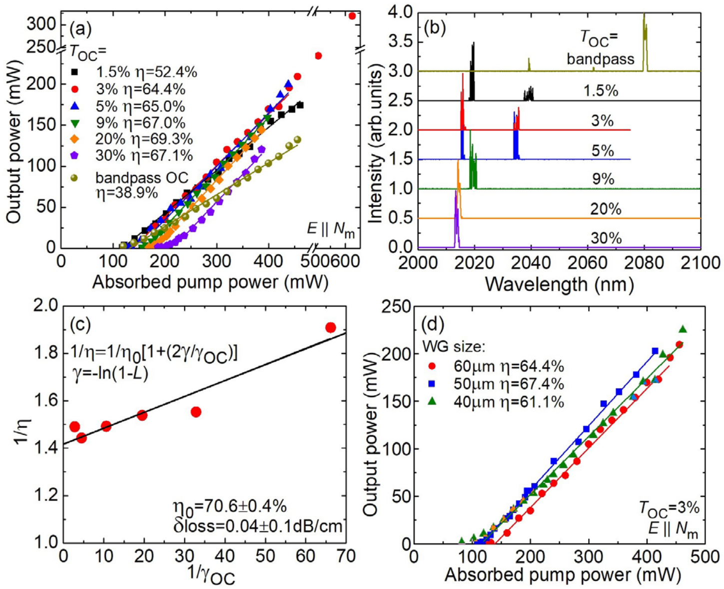

Fig. 5. (a-c) Fs-DLW $Tm^{3+}:MgWO_4$ surface channel WG (60 µm) laser: (a) input-output dependences, η – slope efficiency; (b) laser emission spectra measured at the maximum P_{abs}; (c) Caird analysis: the plot of inverse of the slope efficiency, $1/\eta$, vs. inverse of the output-coupling loss, $1/\gamma_{OC}$, $\gamma_{OC} = -\ln(1 - T_{OC})$; (d) Comparison of the output performance of WGs with cladding diameters of 40 – 60 µm: η – slope efficiency, T_{OC} = 3%. The laser polarization is ***E*** || N_m.

The polarization of the laser emission was linear (***E*** || *N*m), naturally selected by the strong anisotropy of the gain in Tm^{3+}:$MgWO_4$. The laser spectra are shown in Fig. 5(b). For small T_{OC} < 9%, the emission occurred at ~2.02 and 2.04 µm. For higher output coupling (9-30%), only the short-wavelength emission was supported due to the quasi-three-level nature of the $^3F_4 \rightarrow {}^3H_6$ Tm^{3+} laser scheme, i.e., influenced by reabsorption.

The passive losses in the 60 µm WG were estimated using the Caird analysis [15], Fig. 5(c). The resulting internal slope efficiency was η_0 = 70.6±0.4% and δ_{loss} = 0.04+0.1 dB/cm. This value is well below of those reported previously for fs-DLW WGs in Tm^{3+}:ZBLAN glass (0.4±0.2 dB/cm) [11]. Moreover, the passive loss is comparable with the best reports on surface channel (ridge) WGs in Tm^{3+}:MDT single-crystalline films fabricated by Liquid Phase Epitaxy (LPE) and Ar^+ ion beam milling (<0.11 dB/cm) [16].

We also studied the laser performance employing the bandpass OC, Fig. 5(a,b, dark green). The laser exhibited a low laser threshold of 120 mW and generated 132 mW at ~2080 nm with η = 38.9%. This wavelength is well beyond the limit for the purely electronic $^3F_4 \rightarrow {}^3H_6$ Tm^{3+} transition in $MgWO_4$ (2017 nm, between the Stark sub-levels with the energies 5591 cm^{-1} ($^3F_4$) and 633 cm^{-1} ($^3H_6$) [6]), i.e., the first demonstration of a vibronic WG laser. It is assigned to the electron-phonon coupling with the low-frequency Raman modes in $MgWO_4$ [17], Fig. 2(a), such as 121 (A_g), 134 or 154 (both B_g) cm^{-1}.

The performance of the surface WG lasers with different size of the cladding (40-60 µm) is compared in Fig. 5(d). The slope efficiency was similar for all the studied guides while the laser threshold clearly decreased for smaller cladding diameter: it amounted to 108 mW (50 µm WG) and 82 mW (40 µm WG), both for T_{OC} = 3%. The laser polarization for all the WGs was ***E*** || *N*m.

All the studied WG lasers operated in the fundamental transverse mode. The latter might benefit from additional mode "filtering" provided by the reabsorption (gain-guiding) [18]. An example of the mode for the 40 µm WG is shown in Fig. 6(a). It is well confined within the WG cladding. The 1D intensity profiles, Fig. 6(b), are well fitted to a Gaussian distribution (goodness of the fit: R^2 > 0.99) yielding mode diameters $2w_L$ ($|| N_g$) = 27.2 μm and $2w_L$ ($|| N_m$) = 24.5 μm. The mode ellipticity is weak (e = 1.11).

The numerical aperture (N.A.) of the guides was estimated by measuring the divergence of the laser beam ϑ (half-angle) as N.A. = $\sin\vartheta$. It was similar along the vertical and horizontal directions, N.A. = 0.082 and 0.087±0.005, respectively. Within the approximation of a set-index guide, $\mathrm{N.A.}^2 \approx 2n_{\mathrm{core}}\Delta n$, one obtains $\Delta n = n_{\mathrm{cladding}} - n_{\mathrm{core}}$ of about -1.7×10^{-3} (here, n_{core} ~2.03 for $\boldsymbol{E} || N_m$ [6]). A similar value was reported for Tm^{3+}:ZBLAN glass (Δn ~ -1.5×10^{-3}) [11].

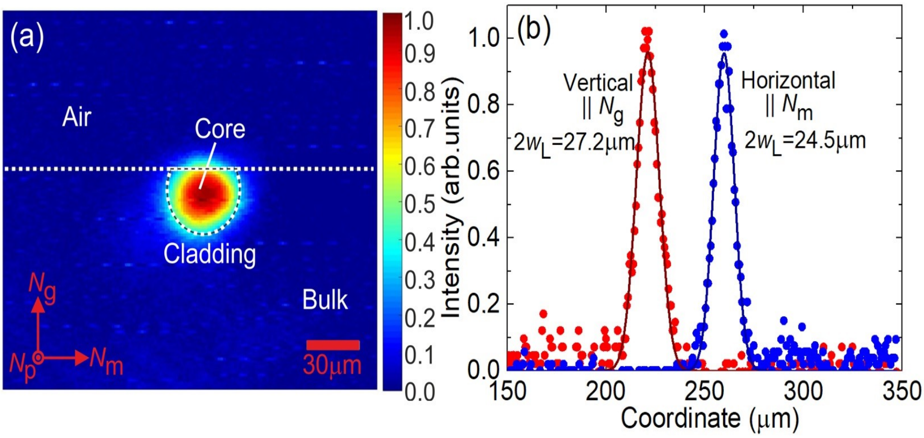

Fig. 6. (a) Spatial near-field laser mode profile of the 40 μm WG fabricated by fs-DLW in $Tm^{3+}:MgWO_4$. P_{abs} = 0.4 W, T_{OC} = 9%. The laser polarization is horizontal ($\boldsymbol{E} || N_m$). *White lines* indicate the WG cladding and the air / crystal interfaces; they are drawn as guides for the eye; (b) 1D intensity plots of the intensity profile: *symbols* – experimental points, *curves* – their Gaussian fits.

To conclude, the monoclinic crystal $Tm^{3+}:MgWO_4$ is promising for highly-efficient low-loss (<0.1 dB/cm) fs-DLW waveguide lasers at wavelength above 2 μm, due to its attractive spectroscopic, vibronic and thermal properties. In the present work, we achieved the highest slope efficiency (69.3%) and output power (320 mW) for any thulium waveguide laser fabricated by femtosecond direct laser writing. Furthermore, the first “vibronic” Tm waveguide laser with the longest emission wavelength of 2080 nm for Tm-doped WGs is also demonstrated. The designed photonic micro-structures with a size in the few millimeter range are highly attractive for the generation of ultrashort pulses in compact ML lasers operating at high repetition rates (GHz-range), as well as for surface activation, e.g., leading to pulsed operation via evanescent-field coupling.

References

1. P. Loiko, J. M. Serres, X. Mateos, M. Aguiló, F. Díaz, L. Zhang, Z. Lin, H. Lin, G. Zhang, K. Yumashev, V. Petrov, U. Griebner, Y. Wang, S. Y. Choi, F. Rotermund, and W. Chen, Opt. Lett. **42**, 1177 (2017).
2. Y. Wang, W. Chen, M. Mero, L. Zhang, H. Lin, Z. Lin, G. Zhang, F. Rotermund, Y. J. Cho, P. Loiko, X. Mateos, U. Griebner, and V. Petrov, Opt. Lett. **42**, 3076 (2017).
3. V. B. Kravchenko, J. Struct. Chem. **10**, 139 (1969).
4. L. Zhang, P. Loiko, J.M. Serres, E. Kifle, H. Lin, G. Zhang, E. Vilejshikova, E. Dunina, A. Kornienko, L. Fomicheva, U.Griebner, V. Petrov, Z. Lin, W. Chen, K. Subbotin, M. Aguiló, F. Díaz, and X. Mateos, J. Lumin. **213**, 316 (2019).
5. L. Zhang, Y. Huang, S. Sun, F. Yuan, Z. Lin, and G. Wang, J. Lumin. **169**, 161 (2016).
6. P. Loiko, L. Zhang, J.M. Serres, Y. Wang, M. Aguiló, F. Díaz, Z. Lin, H. Lin, G. Zhang, E. Vilejshikova, E. Dunina, A. Kornienko, L. Fomicheva, V. Petrov, U. Griebner, W. Chen, and X. Mateos, J. Alloys Compd. **763**, 581 (2018).
7. Y. Wang, G. Xie, X. Xu, J. Di, Z. Qin, S. Suomalainen, M. Guina, A. Härkönen, A. Agnesi, U. Griebner, X. Mateos, P. Loiko, and V. Petrov, Opt. Mater. Express **6**, 131 (2016).
8. K. van Dalfsen, S. Aravazhi, C. Grivas, S. M. García-Blanco, and M. Pollnau, Opt. Lett. **39**, 4380 (2014).
9. A. G. Okhrimchuk and P.A. Obraztsov, Sci. Rep. **5**, 11172 (2015).
10. F. Chen and J. R. Vázquez de Aldana, Laser Photonics Rev. **8**, 251 (2014).
11. D. G. Lancaster, S. Gross, A. Fuerbach, H. E. Heidepriem, T. M. Monro, and M. J. Withford, Opt. Express **20**, 27503 (2012).
12. E. Kifle, P. Loiko, J. R. V. de Aldana, C. Romero, A. Ródenas, S. Y. Choi, J. E. Bae, F. Rotermund, V. Zakharov, A. Veniaminov, M. Aguiló, F. Díaz, U. Griebner, V. Petrov, and X. Mateos, Photon. Res. **6**, 971 (2018).
13. L. Zhang, H. Lin, G. Zhang, X. Mateos, J. M. Serres, M. Aguiló, F. Díaz, U. Griebner, V. Petrov, Y. Wang, P. Loiko, E. Vilejshikova, K. Yumashev, Z. Lin, and W. Chen, Opt. Express **25**, 3682 (2017).
14. A. Ródenas, A. H. Nejadmalayeri, D. Jaque, and P. Herman, Opt. Express **16**, 13979 (2008).
15. J. A. Caird, S. A. Payne, P. R. Staber, A. J. Ramponi, L. L. Chase, and W. F. Krupke, IEEE J. Quantum Electron. **24**, 1077 (1988).
16. K. van Dalfsen, S. Aravazhi, D. Geskus, K. Wörhoff, and M. Pollnau, Opt. Express **19**, 5277 (2011).
17. P. Loiko, X. Mateos, S. Y. Choi, F. Rotermund, J. M. Serres, M. Aguiló, F. Díaz, K. Yumashev, U. Griebner, and V. Petrov, J. Opt. Soc. Am. B. **33**, D19 (2016).
18. J. I. Mackenzie, S. C. Mitchell, R. J. Beach, H. E. Meissner, and D. P. Shepherd, Electron. Lett. **37**, 898 (2001).

Paper III

Lasing properties of funnel and double funnel femtosecond-direct laser writing waveguides in 3%Tm:Kluw crystals

(In Progress to be submitted)

VICTOR LLAMAS,[1,2] PAVEL LOIKO,[3] ESROM KIFLE,[1] CAROLINA ROMERO,[4] JAVIER R. VÁZQUEZ DE ALDANA,[4] JOSEP MARIA SERRES,[1,2] MAGDALENA AGUILÓ,[1] FRANCESC DÍAZ,[1] UWE GRIEBNER,[5] VALENTIN PETROV,[5] PATRICE CAMY,[3] AND XAVIER MATEOS[1]

[1]*Física i Cristal·lografia de Materials i Nanomaterials (FiCMA-FiCNA)-EMaS, Dept. Química Física i Inòrganica, Universitat Rovira i Virgili (URV), Campus Sescelades, 43007 Tarragona, Spain*

[2]*Eurecat, Centre Tecnològic de Catalunya, Unitat Advanced Manufacturing Systems (AMS), Campus Sescelades, 43007 Tarragona, Spain*

[3]*Centre de recherche sur les Ions, les Matériaux et la Photonique (CIMAP), UMR 6252 CEA-CNRS-ENSICAEN, Université de Caen, 6 Boulevard du Maréchal Juin, 14050 Caen Cedex 4, France*

[4]*Aplicaciones del Láser y Fotónica, University of Salamanca, 37008 Salamanca, Spain*

[6]*Max Born Institute for Nonlinear Optics and Short Pulse Spectroscopy, Max-Born-Str. 2a, 12489 Berlin, Germany*

Abstract

Funnel (depressed cladding taper) and double funnel (depressed cladding straight) shaped buried channel waveguides are made in a bulk 3% Tm^{3+}:KLu(WO4)2 crystal by femtosecond direct-laser-writing at ~1kHz repetition rate with type III cracks. Confocal microscopy and µ-Raman spectroscopy have been studied showing a reduced crystallinity and stress-induced birefringence of the WG cladding with no damage in the surrounding crystalline structure. Under conventional pumping (795nm) by a Ti:Sa laser the double funnel shaped waveguide achieves a slope efficiency of $\eta = 13.9\%$ and 1841nm, with a maximum output power of $P_{out} = 47{,}1mW$. The propagation losses are $\delta = 3.9 \pm 0.3dB/cm$.

Thanks to femtosecond direct-laser-writing it has been possible to create waveguides with novel shapes that allow the pump to be coupled more efficiently within very reduced diameter waveguide channels, allowing to increase the density

of photons within the guide. This technology is expected to become an interesting tool in sensing applications.

1. Introduction

WG lasers emitting in the eye-safe spectral range near 2 µm are of interest for optical communications, spectroscopy, sensing of relevant bio- and atmospheric molecules, and for further wavelength conversion to the mid-IR[1-4]. It is common to achieve the 2 µm laser emission using thulium (Tm3+) or holmium (Ho3+) ions. Tm3+ ions typically feature large Stark splitting of the ground-state (3H6) leading to broadband luminescence and, thus, they are of interest for wavelength-tunable and ultrashort-pulse oscillators.

During the last years, femtosecond-laser direct-written (fs-DLW) waveguides in transparent amorphous and crystalline materials have emerged as an interesting technology to produce laser-active integrated photonic devices[5-7].

Among its many advantages is the ability to permanently generate a structure in the material with great precision and the desired shape, being able to generate structures never seen otherwise and keeping the crystalline structure of the material intact in the unwritten areas. In this case, funnel-shaped and double-funnel-shaped channels have been generated with the aim of better coupling the pumping at the inlet and outlet crystal faces, thus obtaining a greater power absorbed in the channel with the possibility of obtaining greater laser efficiency.

2. Waveguide fabrication

Depressed-index waveguides were fabricated in a bulk Tm:KLuW crystal doped with 3 at.% Tm^{3+} ($N_{Tm} = 2.15 \times 1020\ at/cm3$) by 3D fs-DLW. The crystal itself was grown by the Top-Seeded-Solution Growth (TSSG) Slow-Cooling method [8]. A rectangular 8.0 mm-thick sample was cut from this crystal oriented for light propagation along the *N*g optical indicatrix axis. Its aperture was 3.10 (*N*m) × 2.85 (*N*p) mm^2 and both *N*m × *N*p faces were polished to laser-grade quality.

For DLW, 795nm, 120fs pulses from a TI:Sa laser (Spitfire, Spectra Physics) were used. The device has a nano-precision motorized base, capable of moving in X, Y, Z and angularly, and a 40x microscope objective (N.A = 0.65) which focuses the laser generating cracks with a pulse energy of 61nJ at 1KHz repetition rate. The crystal was engraved at a constant speed of 500 µm/s along the N_g axis thus producing damage tracks with the $(E||N_m)$ polarization.

Two new types of waveguides have been created. On the one hand, double funnel guides have been generated, where the guide is wider at the entrance and exit, narrowing in its central area (**Figure 1.A**). On the other hand, funnel-shaped guides have been created, where the entrance face is substantially wider than the exit face (**Figure 1.B**).

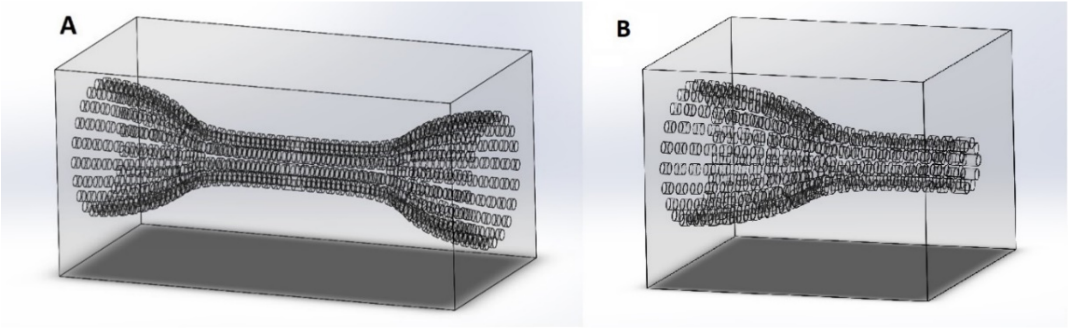

Figure 1. Scheme of the tapered channels. A) Depressed cladding Straight. B) Depressed cladding Tapper.

3. Waveguide characterization

3.1. Raman study

The crystal structure deformation in the WG core and cladding regions was further studied with µ-Raman mapping spectroscopy. A Renishaw inVia Reflex microscope with a 514 nm Ar ion laser and a 50× Leica microscope objective was used. The excitation laser was polarized with E||Nm in the crystal. The measurement geometry was g(mm)g. The most intense internal Raman mode at ~907 cm−1 was monitored. It was related to the W–O stretching vibrations in the distorted WO6 octahedra of KLuW [9]. The peak intensity, Peak width and position were studied in the inlet surface with spatial resolution of 0.4 µm. The results are shown in Fig.. The Raman peak intensity, the peak frequency (in cm−1) and the peak position are the same in the inside and the outside of the channel with the conclusion that the crystalline quality of the material in the core region is preserved. A reduction of the Raman peak intensity around 7000 counts, a change in the peak position of $0.5cm^{-1}$ a phonon energy shift of $\sim 0.8\ cm^{-1}$ to higher frequencies are observed in the cladding region. Those changes show an anisotropy in the material related with a crystalline deformation, all of them in consonance with the theoretical studies [10] also the presence of depressed index changes at tracks as well as collateral induced stress fields can be observed.

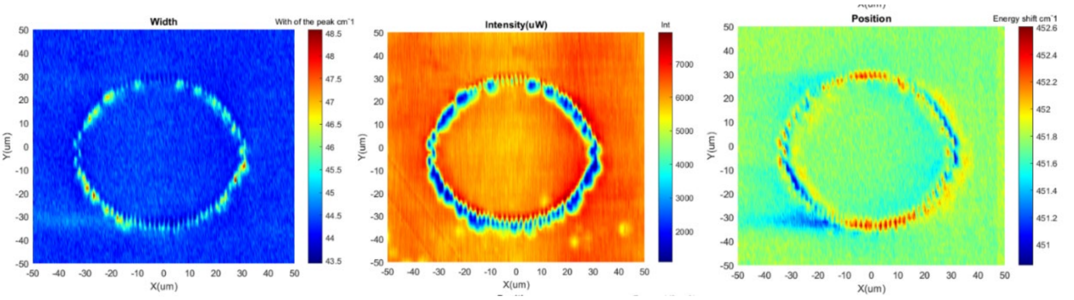

Figure 2. Ramman maping of a $\mathbf{R = 30\mu m}$ waveguide at its front face. Confocal microscopy

Using a LSM 710 (Carl Zeiss) laser confocal microscope, the top and front view of all the waveguides has been studied, **Figure 2**. In front view a clear dark ring of damage tracks having a length of 6 µm is observed. The surrounding bulk crystal does not contain any cracks and should maintain its crystalline structure. The inner part of the WG is darker because the light inside is coupled and does not scatter outside. In the top view you can see how the waveguides vary their width, being wider at the entrance and gradually reducing their diameter.

Figure 3. Top and frontal confocal microscopy of three funnel shaped waveguide channels with different radius ($\boldsymbol{30\mu m, 15\ \mu m\ and\ 30\ \mu m}$)

GUIDE	Measured energy	Energy on sample	Scan velocity	Track separation	Structure
Wg1	$10\mu J$	$0.061\mu J$	$500\mu m/s$	$1.5\mu m$	Depressed cladding, straight $R = 25\mu m$
Wg2	$10\mu J$	$0.061\mu J$	$500\mu m/s$	$1.5\mu m$	Depressed cladding, straight $R = 12\mu m$
Wg3	$10\mu J$	$0.061\mu J$	$500\mu m/s$	$3\mu m\ to\ 1.5\mu m$	Depressed cladding, Taper $R_{in} = 25\mu m, R_{out} = 12.5\mu m$
Wg4	$10\mu J$	$0.061\mu J$	$500\mu m/s$	$2\mu m$	Depressed cladding, straight $R = 25\mu m$
Wg5	$10\mu J$	$0.061\mu J$	$500\mu m/s$	$2\mu m$	Depressed cladding, straight $R = 12\mu m$
Wg6	$10\mu J$	$0.061\mu J$	$500\mu m/s$	$4\mu m\ to\ 2\mu m$	Depressed cladding, Taper $R_{in} = 25\mu m, R_{out} = 12.5\mu m$
Wg7	$11\mu J$	$0.067\mu J$	$500\mu m/s$	$2\mu m$	Depressed cladding, straight $R = 30\mu m$
Wg8	$11\mu J$	$0.067\mu J$	$500\mu m/s$	$2\mu m$	Depressed cladding, straight $R = 15\mu m$
Wg9	$11\mu J$	$0.067\mu J$	$500\mu m/s$	$4\mu m\ to\ 2\mu m$	Depressed cladding, Taper $R_{in} = 30\mu m, R_{out} = 15\mu m$
Wg10	$10\mu J$	$0.061\mu J$	$500\mu m/s$	$2\mu m$	Depressed cladding, straight $R = 30\mu m$
Wg11	$10\mu J$	$0.061\mu J$	$500\mu m/s$	$2\mu m$	Depressed cladding, straight $R = 15\mu m$
Wg12	$10\mu J$	$0.061\mu J$	$500\mu m/s$	$4\mu m\ to\ 2\mu m$	Depressed cladding, Taper $R_{in} = 30\mu m, R_{out} = 15\mu m$

Table 1. Data sheet of all the waveguides studied in this paper.

In **Table 2** data sheet of all waveguides can be observed, with the individual manufacturing values of each one. The so-called depressed Cladding straight have a double funnel shape and the depressed cladding taper have a single funnel shape (**Figure 1**). Some of them are not able to generate laser light, but they are useful for another applications.

4. Continuous-wave laser operation

4.1. Laser set up

The scheme of the laser setup is shown in **Figure 4**. The fs-DLW waveguide laser was pumped by a CW Ti:sapphire laser (MIRA 900, Coherent) tuned to ~795 nm. After it there are a half wave plate (WPV10L-780, Thorlabs) and a Glan-Laser calcite polarizer (GL10-B, Thorlabs) to control the incident power. This polarizer reflects the horizontal polarization to a power meter (S405C, Thorlabs) that is numerically adjusted with the vertical polarization power to easily obtain the input power without adding any other device.

The vertical polarization goes through another half wave plate (WPV10L-830, Thorlabs) that controls the polarization. It corresponded to E||Nm in the WG. It was coupled inside with a 10× microscope objective (N.A. = 0.28, focal length f =20 mm) resulting in a spot diameter of 40 µm at the focus located at the front end-face of the WG.

Under 795 nm pumping, the WGs exhibited blue (480 nm) upconversion luminescence (1G4 → 3H6 transition of Tm3+). The Tm:KLuW sample containing the fs-DLW WGs was placed on a passively cooled Al-Fe support. The laser cavity consisted of a flat pump mirror which was antireflection coated for 0.7–1.0 µm and high-reflection coated for 1.8–2.1 µm and a flat output coupler (OC) having a transmission T OC of 1.5%, 3%, 5%, 10%, 20%, and 30% at 1.8–2.1 µm. The PM and the OC were placed close to the WG end faces with minimum air gaps with a cavity length around 7.9 mm without any index matching liquid between the optical components to avoid burns in the coatings.

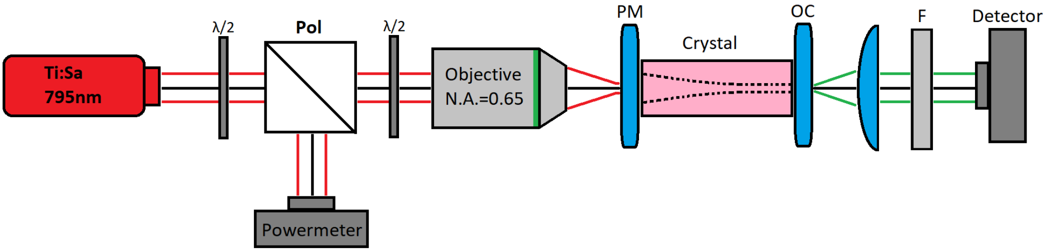

Figure 4. Operation scheme of the laser setup.

The laser output was collimated using an uncoated lens with $f = 15mm$. The nonabsorbed pump was blocked using a long-pass filter (FEL 1000, Thorlabs). The emission spectrum was measured using an optical spectrum analyzer (AQ6375B, Yokogawa). Imaging of the waveguide laser near-field output mode at 1850 nm wavelength was performed using a FIND-R-SCOPE near-IR camera (model 85726). The output power was measured with an Ophir Nova P/N 1Z01500 power meter and numerically corrected taking account the losses in the low pass filter and the lens.

4.2. Laser performance

4.2.1. Slope efficiency TOC 30% for all the waveguides

In this section the absorbed pump power versus the output power for each waveguide is going to be consider, achieving the slope efficiency for each waveguide. The absorbed pump power can be expressed as $P_{abs} = P_{in} * \eta_{abs} * \eta_{coup}$.

Being P_{in} the input power, η_{abs} the absorbed pump efficiency and η_{coup} the coupling efficiency. The coupling efficiency is determined by measuring the losses in the focusing lens, the pump mirror and the fresnell reflection, amounted to $64\% \pm 1\%$ in this experiment, The absorbed pump efficiency were determined from a combination of pump-transmission studies at 795 and at 850 nm (out of the Tm3+ absorption) and a rate-equation modelling accounting for the bleaching of the Tm3 ground-state (3H6) and CR for the Tm3 ions [11]. This value depends on the waveguide being around 50% to 70%.

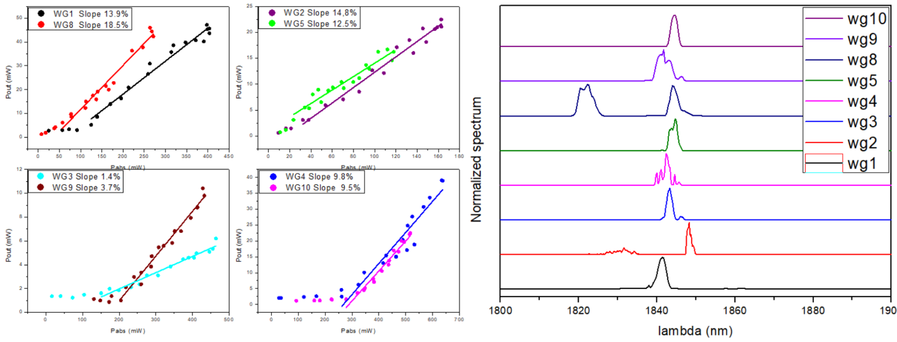

Figure 5. Laser results for each waveguide studied in this paper with a transmission output coupler $\boldsymbol{T_{oc}} = \mathbf{30}\%$. (Left) Laser output power vs absorbed pump power. (Right) Normalized spectrum.

In **Figure 5** the emission spectra of all the waveguides is shown. All of them are in the range of 1820 to 1860nm, a common emission in Tm: KLuW using waveguides [12]. In addition all the corresponding input–output dependences of the waveguides can be observed using a TOC 30% which theoretically is going to be the best TOC for achieving high power in waveguide microchip configuration [13]. The laser emission was linearly polarized, E||Nm (horizontal). The polarization was naturally selected by the anisotropy of the gain.

As can be seen in **Figure 5**. The waveguides with the best efficiency are WG1, WG2 and WG8. The waveguide 2 presents a maximum power of $P_{out} = 22.5mW$ and a slope of $\eta = 14.8\%$, interesting but not enough. The slope of the WG8 is the highest with a value of $\eta = 18.5\%$ and a maximum power of $P_{out} = 46.5mW$ with two peaks of 1824nm and 1846nm. Those two peaks can be explained as a two-mode competition laser, when two wavelengths have a similar emission-loss rate. This makes this waveguide the most efficient of all, but this mode competition makes its laser emission very irregular, so in this paper it was decided not to use it for further experiments. Finally, the waveguide one has a slope efficiency of $\eta = 13.9\%$ and 1841nm, with a maximum output power of $P_{out} = 47{,}1mW$, having twice the power than WG2 and a similar slope. In this waveguide there is no mode competition and its laser stability is good, so it was decided to analyze this one more deeply.

Laser emission modes and pumping can also be observed for the different waveguides with the infrared camera FIND-R-SCOPE near-IR in **Figure 6** the laser modes are clearly different from the pump ones, those are bigger and present a big halo around them. This is because fewer transverse modes are supported for the same refractive index at longer wavelengths and because of mode competition. In all cases, the laser mode was well confined within the WG cladding.

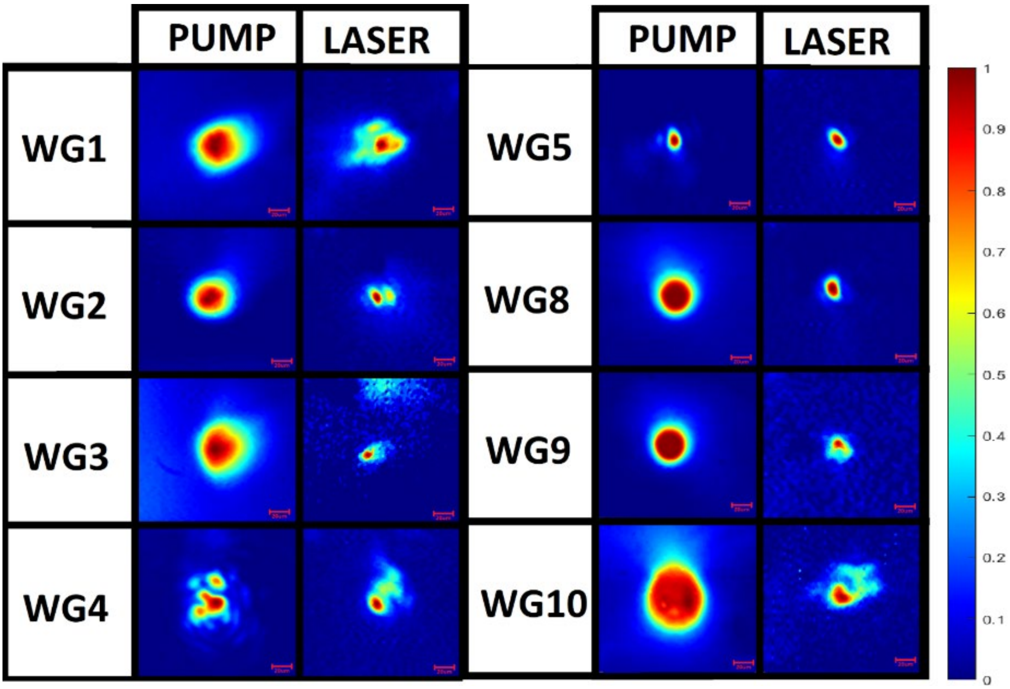

Figure 6. Laser and pump profiles for all the waveguides studied in this paper.

4.2.2. Waveguide 1 all TOC.

As explained in the previous section, it was decided that the WG1 was the most interesting to study with different T_{OC} thanks to its good efficiency, maximum power and stability. In **Figure 7** the behavior of the laser with respect to the transmission output power can be observed. It is clear that slope efficiency increases with increasing T_{OC} as it was expected from a Tm:KLuW waveguide laser [14]. Furthermore, with the increase of output coupling from 1.5% to 30%, the emission shifted to longer wavelengths. This behavior is due to the quasi-three-level nature of Tm3+ ions, and it is related to a decrease of reabsorption which produces an increase of β [15].

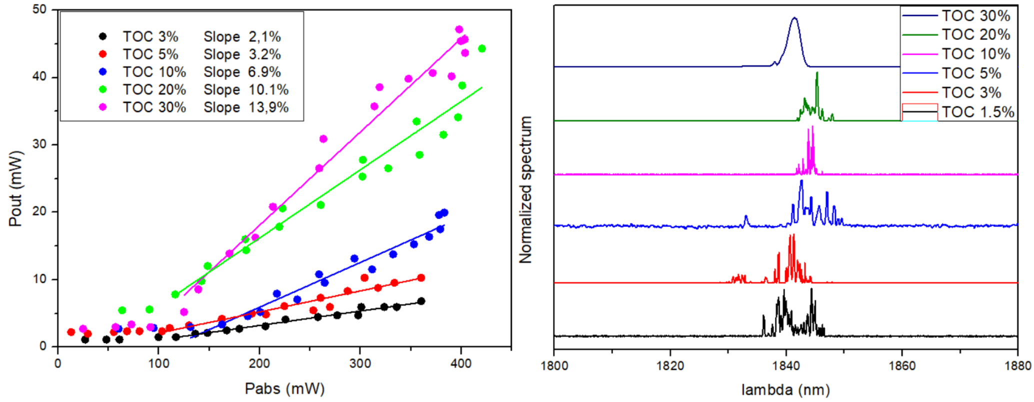

Figure 7. Laser results for a doble funnel shaped $\boldsymbol{R_{max} = 25\mu m}$(most efficient) waveguide with different $\boldsymbol{T_{oc}}$. (Left) Laser output power vs absorbed pump power. (Right) Normalized spectrum.

4.2.3. Waveguide propagation losses.

From the Caird analysis modified for high output coupling [16] it is possible to estimate the waveguide propagation losses. This analysis relates the slope efficiencies with the TOC by the equation $\frac{1}{\eta} = \frac{1}{\eta_0} + \frac{2\gamma}{\eta_0} * \frac{1}{\gamma_{oc}}$ with $\gamma = -\ln(1 - L_{oss})$ and $\gamma_{oc} = -\ln(1 - T_{oc})$ being η_0 the intrinsic slope efficiency and L_{oss} the internal losses of the crystal.

In **Figure 8** the inverse of the slope efficiency versus the inverse of γ_{OC} can be observed. All data are distributed in a straight line, adjusting them to a slope $Y = aX + b$ with $Y = \frac{1}{\eta}$, $X = \frac{1}{\gamma_{oc}}$. Thus we obtain $\eta_0 = \frac{1}{a} = 75.8 \pm 4\%$ and $\gamma = \eta_0 * \frac{b}{2} = 1.3 \pm 0.2$ achieving a propagation loss constant of $\delta = 4.34 * \frac{L_{oss}}{l} = 3.9 \pm 0.3 dB/cm$ with l the length of the crystal. Those propagation losses are between two and three times bigger than the usual for a straight channel waveguide [13], that is because of the construction of this new waveguide. The track separation and the shape are not perfectly optimized there are some modes that cannot be propagated properly. In future works it is expected to improve those parameters.

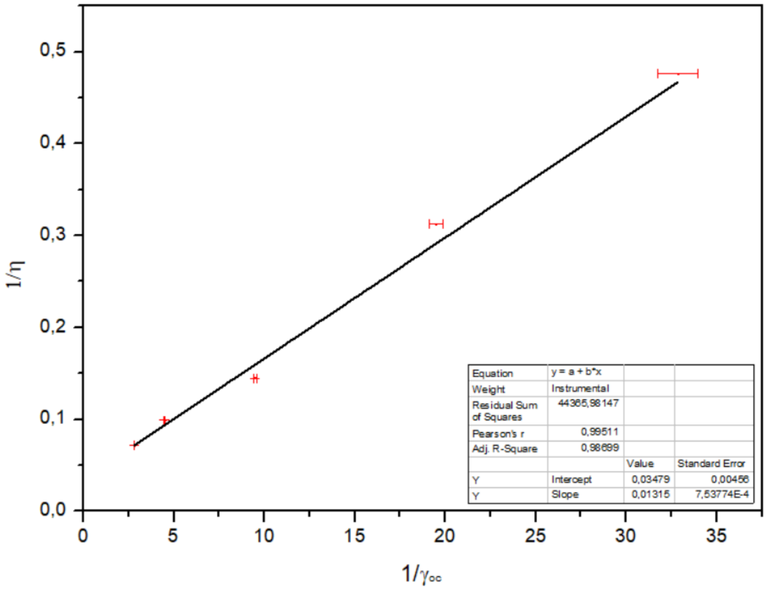

Equation	y = a + b*x		
Weight	Instrumental		
Residual Sum of Squares	44365,98147		
Pearson's r	0,99511		
Adj. R-Square	0,98699		
		Value	Standard Error
Y	Intercept	0,03479	0,00456
Y	Slope	0,01315	7,53774E-4

Figure 8. Caird analysis for the estimation of the waveguide 1 propagation losses.

5. Conclusion

In conclusion, two new types of waveguides (funnel and double funnel shaped) in 3% Tm^{3+}:KLu(WO4)2 have been created using femtosecond direct-laser-writing with type III cracks at ~1kHz repetition rate . Its main advantage is the possibility to couple a pump laser with a big spot size inside a much smaller waveguide more efficiently by reducing the coupling losses but maintaining the interesting properties of a reduced waveguide diameter. We have confirmed its lasing capabilities with a 795nm pump with an emission around 1850nm, slope efficiency of $\eta = 13.9\%$, with a maximum output power of $P_{out} = 47{,}1mW$. Confocal laser microscopy and µ-Raman spectroscopy confirmed the modification of crystalline structure of the material in the cladding without any modification in the crystalline structure of the core or the surrounding areas.

The propagation losses are $\delta = 3.9 \pm 0.3 dB/cm$, between twice and three times higher than a regular straight femtosecond laser written waveguides. It is expected that with an optimization of the geometry those losses can be improved drastically opening the door to the fabrication of very compact integrated lasers with a much better pump coupling efficiency.

6. **References**

[1] D. Geskus, K. van Dalfsen, K. Wörhoff, M. Pollnau, and S. Aravazhi, "Efficient KY1-x-yGdxLuy(WO4)2:Tm3+ channel waveguide lasers," Opt. Express, Vol. 19, Issue 6, pp. 5277-5282, vol. 19, no. 6, pp. 5277–5282, Mar. 2011, doi: 10.1364/OE.19.005277.

[2] A. Braud et al., "Tm,Ho:LiYF4 planar waveguide laser at 2.05 µm," Opt. Lett. Vol. 43, Issue 18, pp. 4341-4344, vol. 43, no. 18, pp. 4341–4344, Sep. 2018, doi: 10.1364/OL.43.004341.

[3] A. Fuerbach et al., "Fifty percent internal slope efficiency femtosecond direct-written Tm3+:ZBLAN waveguide laser," Opt. Lett. Vol. 36, Issue 9, pp. 1587-1589, vol. 36, no. 9, pp. 1587–1589, May 2011, doi: 10.1364/OL.36.001587.

[4] J. I. Mackenzie, S. C. Mitchell, R. J. Beach, H. E. Meissner, and D. P. Shepherd, "5 W diode-side-pumped Tm:YAG waveguide laser at 2 µ m," vol. 37, no. 14, 2001.

[5] F. Chen and J. R. V. de Aldana, "Optical waveguides in crystalline dielectric materials produced by femtosecond-laser micromachining," Laser Photon. Rev., vol. 8, no. 2, pp. 251–275, Mar. 2014, doi: 10.1002/LPOR.201300025.

[6] R. R. Gattass and E. Mazur, "Femtosecond laser micromachining in transparent materials," Nat. Photonics 2008 24, vol. 2, no. 4, pp. 219–225, Apr. 2008, doi: 10.1038/nphoton.2008.47.

[7] S. Nolte, M. Will, J. Burghoff, and A. Tuennermann, "Femtosecond waveguide writing: a new avenue to three-dimensional integrated optics," Appl. Phys. A 2003 771, vol. 77, no. 1, pp. 109–111, Jun. 2003, doi: 10.1007/S00339-003-2088-6.

[8] E. Kifle et al., "Growth, spectroscopy and laser operation of 'mixed' Tm:Ca(Gd,Lu)AlO4 – A novel crystal for mode-locked lasers," Laser Congr. 2018 (2018), Pap. ATu2A.21, vol. Part F121-ASSL 2018, p. ATu2A.21, Nov. 2018, doi: 10.1364/ASSL.2018.ATU2A.21.

[9] V. Petrov et al., "Growth and properties of KLu(WO4)2, and novel ytterbium and thulium lasers based on this monoclinic crystalline host," Laser Photon. Rev., vol. 1, no. 2, pp. 179–212, May 2007, doi: 10.1002/LPOR.200710010.

[10] F. Chen, S. Qu, X. Liu, and Y. Tan, "Preservation of fluorescence and Raman gain in the buried channel waveguides in neodymium-doped KGd(WO4)2(Nd:KGW) by femtosecond laser writing," Appl. Opt. Vol. 50, Issue 6, pp. 930-934, vol. 50, no. 6, pp. 930–934, Feb. 2011, doi: 10.1364/AO.50.000930.

[11] X. Mateos et al., "Efficient Micro-Lasers Based on Highly Doped Monoclinic Double Tungstates," IEEE J. Quantum Electron., vol. 53, no. 3, Jun. 2017, doi: 10.1109/JQE.2017.2681626.

[12] E. Kifle et al., "Fs-laser-written thulium waveguide lasers Q-switched by graphene and MoS2," Opt. Express, vol. 27, no. 6, pp. 8745–8755, Mar. 2019, doi: 10.1364/OE.27.008745.

[13] A. Ródenas et al., “Femtosecond-laser-written hexagonal cladding waveguide in Tm:KLu(WO4)2; Raman study and laser operation,” Opt. Mater. Express, Vol. 7, Issue 12, pp. 4258-4268, vol. 7, no. 12, pp. 4258–4268, Dec. 2017, doi: 10.1364/OME.7.004258.

[14] V. Llamas et al., “Ultrafast laser inscribed waveguide lasers in Tm:CALGO with depressed-index cladding,” Opt. Express, vol. 28, no. 3, pp. 3528–3540, Feb. 2020, doi: 10.1364/OE.384258.

[15] E. Kifle et al., “Low-loss fs-laser-written surface waveguide lasers at 2µm in monoclinic Tm3+:MgWO4,” Opt. Lett., vol. 45, no. 14, pp. 4060–4063, Jul. 2020, doi: 10.1364/OL.395811.

[16] J. A. Caird, S. A. Payne, P. R. Staver, A. J. Ramponi, L. L. Chase, and W. F. Krupke, “Quantum Electronic Properties of the Na3Ga2Li3F12:Cr3+ Laser,” IEEE J. Quantum Electron., vol. 24, no. 6, pp. 1077–1099, 1988, doi: 10.1109/3.231.

Conference I

Ultrafast Laser Inscribed Waveguide Lasers in Tm:CALGO (PUBLISHED)

Advanced Solid State Lasers, AM3A. 5 (2019)

Esrom Kifle[1], Pavel Loiko[2,*], Victor Llamas[1], Carolina Romero[3], Javier R. V. de Aldana[3], Zhongben Pan[4,5], Josep Maria Serres[1], Hualei Yuan[4], Xiaojun Dai[4], Huaqiang Cai[4], Yicheng Wang[5], Yongguang Zhao[5,6], Magdalena Aguiló[1], Francesc Díaz[1], Uwe Griebner[5],Valentin Petrov[5], Patrice Camy[2], and Xavier Mateos[1]

[1]Física i Cristal·lografia de Materials i Nanomaterials (FiCMA-FiCNA)-EMaS, Dept. Química Física i Inòrganica, Universitat Rovira i Virgili (URV), Campus Sescelades, E-43007 Tarragona, Spain
[2]Centre de recherche sur les Ions, les Matériaux et la Photonique (CIMAP), UMR 6252 CEA-CNRS-ENSICAEN, Université de Caen, 6 Boulevard du Maréchal Juin, 14050 Caen Cedex 4, France
[3]Aplicaciones del Láser y Fotónica, University of Salamanca, 37008 Salamanca, Spain
[4]Institute of Chemical Materials, China Academy of Engineering Physics, Mianyang, 621900, China
[5]Max Born Institute for Nonlinear Optics and Short Pulse Spectroscopy, Max-Born-Str. 2a, D-12489 Berlin, Germany
[6]Jiangsu Key Laboratory of Advanced Laser Materials and Devices, Jiangsu Normal University, 221116 Xuzhou, China

Abstract: Depressed-index channel waveguides are produced in Tm:CALGO by femtosecond direct-laser-writing. Under in-band-pumping at 1679 nm by a Raman fiber laser, the waveguide laser generates 0.81 W at 1866-1947 nm with a slope efficiency of 50.8%.

1. Introduction

Femtosecond (fs) Direct Laser Writing (DLW) is a powerful method of fabrication of passive and active photonic micro-structures such as optical waveguides (WGs) in transparent dielectric materials [1]. These materials absorb the energy of fs pulses through a nonlinear process in a short time, leading to a permanent modification of the structure in the µm-scale and a change of the refractive index that can be positive or negative. Fs-DLW features fast fabrication time, wide range of WG geometries and a variety of suitable materials (glasses, ceramics or even anisotropic crystals). It is promising for development of WG lasers emitting in the 2 µm spectral range [2] with potential applications in bio- and environmental sensing and on-chip spectroscopy.

In the present work, we report on the first WG laser based on tetragonal Tm:CALGO crystal employing fs-DLW as a fabrication method. It is known as a promising disordered crystal for CW and mode-locked (ML) oscillators at 2 µm [3].

2. Fabrication of waveguides

Depressed-index buried channel WGs with a circular cladding (diameter: 60-100 µm) and surface WGs with a half-ring cladding (diameter: 60 µm) were fabricated in bulk Tm:CALGO crystal (exact composition, as determined by the ICP-MS method: $CaGd_{0.913}Lu_{0.052}Tm_{0.035}AlO_4$; the Tm^{3+} ion density: 4.31×10^{20} at/cm^3). The fs-DLW was performed using 120 fs, 795 nm pulses from a Ti:Sapphire regenerative amplifier and a 40× microscope objective (N.A. = 0.65). The incident pulse energy was 0.2 µJ, the writing speed was 400 µm/s and the track separation was 3 µm. The Tm:CALGO sample was cut for light propagation along the [001] axis and it was 6,2mm-thick.

The fabricated WGs were studied by confocal laser microscopy, revealing damage-free WG core surrounded by a cylindrical cladding formed by the continuous damage tracks, as shown in Fig. 1(a,b) for the 100 µm-diameter WG. The WGs were also studied using the µ-Raman spectroscopy by monitoring intensity, width and peak position of a certain Raman band (~452 cm^{-1}), see Fig. 1(c,d). It reveals the modification of the material (reduced crystallinity) in the cladding and well-preserved crystalline quality of the WG core. The refractive index variation in the cladding was $<0.5\times10^{-3}$.

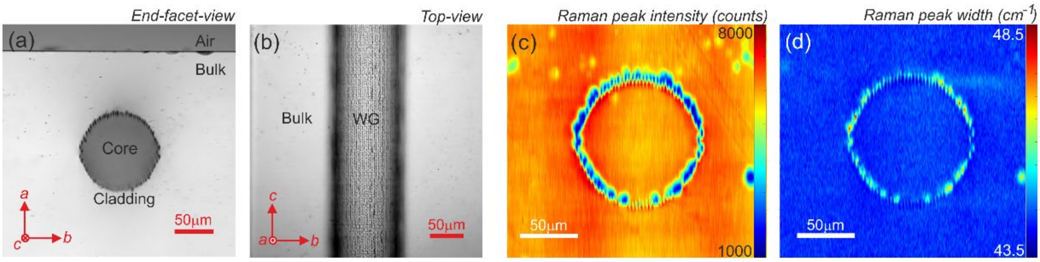

Fig. 1. Characterization of depressed-index buried channel WG with a circular cladding (diameter: 100 µm) produced in Tm:CALGO crystal by fs-DLW: (a,b) confocal laser microscopy: (a) end-facet view, (b) top view, λ = 405 nm, light polarization is vertical; (c,d) µ-Raman mapping: (c) peak intensity of the ~452 cm^{-1} Raman mode; (d) FWHM of this peak.

3. Results and Discussion

An overview of the spectroscopic properties of Tm:CALGO is given in Fig. 2. This crystal is tetragonal (sp. gr. I4/mmm) and optically uniaxial (the optical axis is parallel to the [001] axis). For the $^3H_6 \rightarrow {}^3F_4$ transition, the maximum absorption cross-section σ_{abs} is 0.34×10^{-20} cm^2 at 1735 nm and the absorption band is smooth and broad with a FWHM of ~120 nm (for σ-polarization available for the [001]-cut crystal), Fig. 2(a). The maximum stimulated-emission (SE) cross-section $\sigma_{SE} = 0.91\times10^{-20}$ cm^2 at 1813 nm for σ-polarization. The gain spectra, Fig. 2(b), are smooth and broad (the bandwidth is ~145 nm for small $\beta < 0.2$). The lifetime of the $^3F_4$ state is ~3.2 ms.

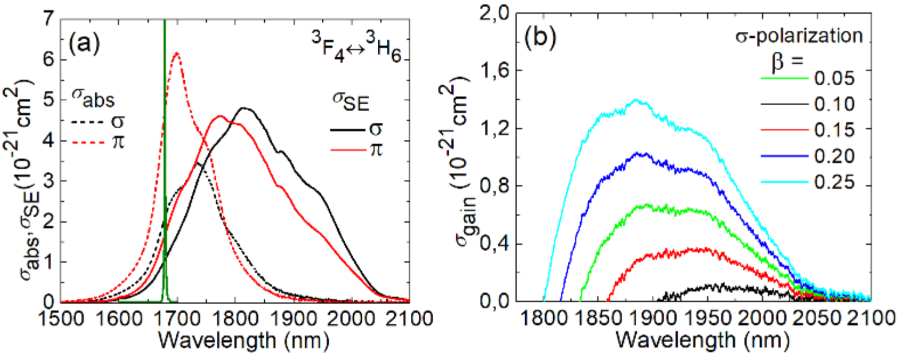

Fig. 2. Spectroscopy of the $^3F_4 \leftrightarrow {}^3H_6$ Tm^{3+} transition for tetragonal $Ca(Gd,Lu)AlO_4$ crystal: (a) absorption, σ_{abs}, and stimulated-emission, σ_{SE}, cross-section spectra for π and σ polarizations, green curve – spectrum of the 1679 nm Raman fiber laser; (b) gain cross-section, $\sigma_{gain} = \beta\sigma_{SE} - (1-\beta)\sigma_{abs}$, spectra for σ-polarization; $\beta = N_2(^3F_4)/N_{Tm}$ is the inversion ratio.

The laser operation was studied under in-band pumping (the $^3H_6 \rightarrow {}^3F_4$ transition) employing a Raman fiber laser delivering up to 3.5 W at 1679 nm [4]. The laser cavity was composed by a flat pump mirror coated for HT (T = 93%) at 1.68 µm and for HR at 1.86-2.32 µm, and a set of flat output couplers with a transmission at the laser wavelength T_{OC} = 1.5%...50%. The pump was focused into the WG to a spot with a dimeter of 30 µm using a spherical CaF_2 lens (f = 40 mm). The pump coupling efficiency was 90.2% and the pump absorption was 83% (for the 60 µm-diameter WG). The WG was mounted on a passively-cooled Cu-holder. The Tm:CALGO WG laser generated a maximum output power of 0.81 W at 1866-1947 nm with a slope efficiency of 50.8%

and a laser threshold of 280 mW (vs. the absorbed pump power, for the 60 µm-diameter WG and T_{OC} = 30%), Fig. 3(a). The laser emission was broadband, Fig. 3(b), due to the flat and broad gain spectra. The laser mode was slightly multimode and well-confined within the WG core, Fig. 3(c).

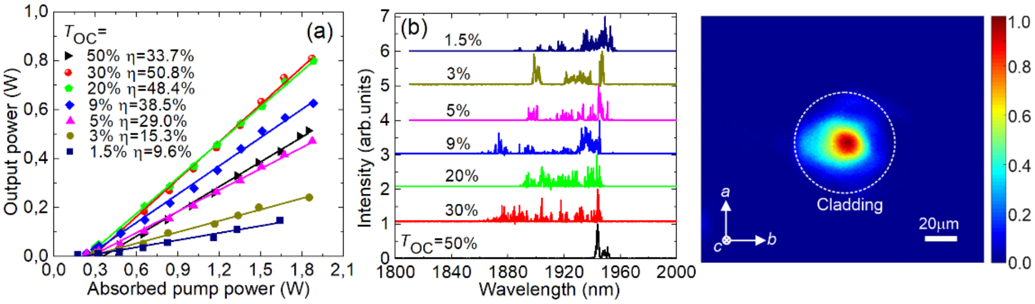

Fig. 3. In-band-pumped fs-DLW Tm:CALGO channel waveguide laser: (a) input-output dependences, η – slope efficiency; (b) typical laser emission spectra measure at P_{abs} = 1.5 W; (c) 2D laser mode profile at the output WG facet (T_{OC} = 20%).

4. Conclusion

To conclude, Tm:CALGO is a suitable material for efficient and power-scalable WG lasers at 2 µm due to a combination of its advantageous thermal (high thermal conductivity) and spectroscopic properties (broad and smooth emission bands originating from the structure disorder). We have demonstrated a watt-level Tm:CALGO channel WG laser with a slope efficiency of >50% and extremely broadband emission properties based on the fs-DLW method of fabrication and in-band pumping scheme leading to a weak heat loading. The developed WGs are promising for GHz-range ML oscillators.

[1] F. Chen and J. R. Vázquez de Aldana, "Optical waveguides in crystalline dielectric materials produced by femtosecond-laser micromachining," Laser Photonics Rev. 8(2), 251–275 (2014).
[2] D. G. Lancaster, S. Gross, H. Ebendorff-Heidepriem, K. Kuan, T. M. Monro, M. Ams, A. Fuerbach, and M. J. Withford, "Fifty percent internal slope efficiency femtosecond direct-written Tm^{3+}:ZBLAN waveguide laser," Opt. Lett. 36(9), 1587-1589 (2011).
[3] Y. Wang, G. Xie, X. Xu, J. Di, Z. Qin, S. Suomalainen, M. Guina, A. Härkönen, A. Agnesi, U. Griebner, X. Mateos, P. Loiko, and V. Petrov, "SESAM mode-locked Tm:CALGO laser at 2 µm," Opt. Mater. Express 6(1), 131-136 (2016).
[4] P. Loiko, R. Thouroude, R. Soulard, L. Guillemot, G. Brasse, B. Guichardaz, A. Braud, A. Hideur, M. Laroche, H. Gilles, and P. Camy, "In-band pumping of Tm:$LiYF_4$ channel waveguide: a power scaling strategy for ~2 µm waveguide lasers," Opt. Lett. 44(12), 3010-3013 (2019).

Conference II

Ultrafast Laser Inscribed Waveguide Lasers in Tm^{3+}:SrF_2

CLEO: Science and Innovations, SM3E. 7 (2020)

Victor Llamas[1,2], Pavel Loiko[1,3], Esrom Kifle[1], Carolina Romero[4], Javier R. Vázquez de Aldana[4], Josep Maria Serres[1,2], MauroTonelli[5], Eugenio Damiano[5], Viktor Zakharov[3], Andrey Veniaminov[3], Magdalena Aguiló[1], Francesc Díaz[1], Weidong Chen[6,7], Uwe Griebner[6], Valentin Petrov[6,*], and Xavier Mateos[1]

[1]Universitat Rovira i Virgili, Dept. Quimica Física i Inorgànica, (FiCMA-FiCNA)-EMaS, Campus Sescelades, 43007, Tarragona, Spain

[2]Eurecat, Centre Tecnològic de Catalunya, Unitat Advanced Manufacturing Systems (AMS), Campus Sescelades, 43007 Tarragona, Spain

[3]ITMO University, 49 Kronverkskiy Pr., 197101 St. Petersburg, Russia

[4]Aplicaciones del Láser y Fotónica, University of Salamanca, 37008 Salamanca, Spain

[5]Università di Pisa, Dipartimento di Fisica and MEGA Materials s.r.l. Largo B. Pontecorvo 3, 56127, Pisa, Italy

[6]Max Born Institute for Nonlinear Optics and Short Pulse Spectroscopy, Max-Born-Str. 2a, 12489 Berlin, Germany

[7]Key Laboratory of Optoelectronic Materials Chemistry and Physics, Fujian Institute of Research on the Structure of Matter, Chinese Academy of Sciences, Fuzhou, 350002 Fujian, China

Abstract: Depressed-index low-loss (0.38 dB/cm) buried channel waveguides with a circular cladding are fabricated in bulk Tm^{3+}:SrF_2 by ultrafast laser inscription. The waveguide laser generated 148 mW at 1.87 µm with a slope efficiency of 63.9%.

Cubic (sp. gr. $Fm\bar{3}m$) fluoride-type $M^{2+}F_2$ (M = Ca, Sr or Ba) crystals are attractive for doping with rare-earth ions such as thulium (Tm^{3+}) [1,2]. They combine good physical properties of the host (high thermal conductivity, low refractive index and wide transparency) and advantageous spectroscopic properties of the dopant ions, i.e., their strong clustering leading to smooth and broad spectral bands (a glassy-like behavior) [2]. For Tm^{3+}, this leads to a strong cross-relaxation (CR) enhancing the pump quantum efficiency. Efficient bulk Tm^{3+}:MF_2 lasers have been already demonstrated [1,2].

Thulium waveguide (WG) lasers emitting at ~2 µm according to the $^3F_4 \rightarrow {}^3H_6$ transition are of interest for bio- and environmental sensing applications and on-chip spectroscopy. While some WG studies devoted to the ~1 µm spectral range can be found in the literature, so far, the MF_2 crystals have been barely studied for such lasers at ~2 µm. In the present work, we report on the first $Tm:SrF_2$ WG laser using ultrafast laser inscription (ULI) as a fabrication method.

A bulk 5.2 mol% $Tm^{3+}:SrF_2$ crystal was grown using the Czochralski method [1]. At first, we characterized its spectroscopic properties. For the $^3H_6 \rightarrow {}^3H_4$ pump transition, the maximum absorption cross-section σ_{abs} is 4.2×10^{-21} cm^2 at 773 nm (FWHM of the absorption peak: 14.0 nm), Fig. 1(a). For the $^3F_4 \rightarrow {}^3H_6$ transition, the stimulated-emission (SE) cross-section at the laser wavelength (~1865 nm) is 3.9×10^{-21} cm^2, Fig. 1(b). The lifetime of the upper laser level ($^3F_4$) is 8.8 ms. The first-order Raman spectrum contains a single peak assigned to symmetric stretching vibrations of fluorine anions around the cations, centered at ~284 cm^{-1}, Fig. 1(c).

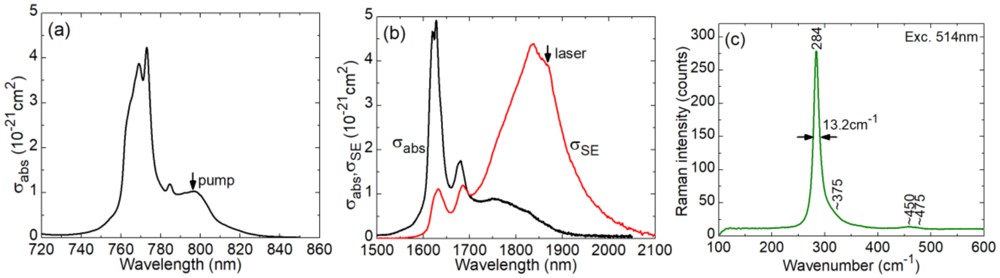

Fig. 1. Spectroscopy of the 5.2 mol% $Tm^{3+}:SrF_2$ crystal: (a) absorption cross-section, σ_{abs}, for the $^3H_6 \rightarrow {}^3H_4$ transition, (b) absorption, σ_{abs}, and stimulated-emission (SE), σ_{SE}, cross-sections for the $^3H_6 \leftrightarrow {}^3F_4$ transitions, (c) Raman spectrum, λ_{exc} = 514 nm. Numbers indicate the Raman frequencies in cm^{-1}. Arrows in (a,b) indicate the pump and laser wavelengths.

Depressed-index buried channel WGs were fabricated in the $Tm^{3+}:SrF_2$ bulk crystal by ULI. The sample had a rectangular shape (thickness: 8.8 mm). It was polished to laser quality and remained uncoated. For ULI, we used 120 fs, 795 nm pulses from a Ti:Sapphire regenerative amplifier. The laser beam was focused into the crystal using a 40× microscope objective. The incident pulse energy was 175 nJ, the crystal scanning speed was 400 µm/s and the track separation was 3 µm. The WGs had a circular cladding formed by individual tracks (diameter: 60, 80 or 100 µm). The WG geometry was studied with confocal microscopy, Fig. 2(a-c). A modification (a reduction of crystallinity) around the damage tracks and well-preserved crystallinity in the WG core were revealed by µ-Raman spectroscopy, Fig. 2(d-f).

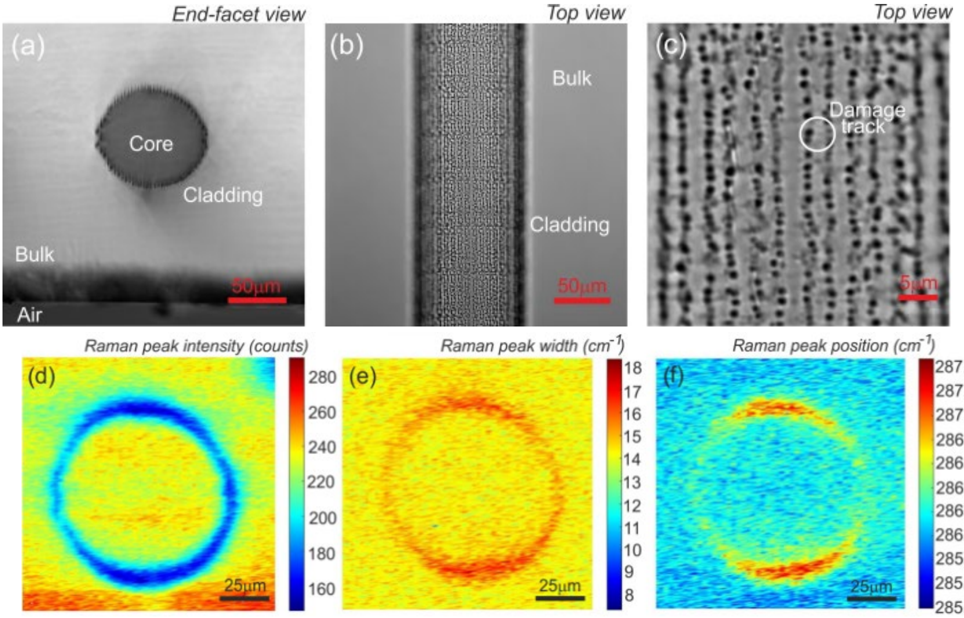

Fig. 2. Characterization of a buried channel WG in Tm^{3+}:SrF_2. (a-c) Confocal microscopy: (a) end-facet view, (b,c) top view, (c) a close look of the damage tracks. (d-e) Micro-Raman spectroscopy of the first-order peak at ~284 cm^{-1}: (d) peak intensity, (e) peak width and (f) peak position. The WG used had a circular cladding with a diameter of 80 µm.

Laser operation of Tm^{3+} in the SrF_2 WGs was achieved in a linear Fabry-Perot type cavity formed by a flat pump mirror coated for HT at ~0.8 µm and for HR at 1.8-2.1 µm and a set of flat output couplers (OCs) having a transmission T_{OC} of 1.5% - 30% at the laser wavelength. The pump source was a Ti:Sapphire laser tuned to ~797 nm. The pump coupling efficiency was 96.2%. The measured bleached pump absorption (single-pass pumping) was 39.0% - 42.8%, depending on the OC.

The highest output power was achieved for the WG with a cladding diameter of 80 µm: 148 mW at 1868-1878 nm with a slope efficiency η of 63.9% (vs. the absorbed pump power P_{abs}) and a laser threshold of 120 mW (for T_{OC} = 20%) of absorbed power, Fig. 3(a). The power scaling was limited by the available pump (the crystal was passively-cooled).

The laser emission was unpolarized and the wavelength experienced a slight blue-shift with increasing the output coupling, Fig. 3(b). The WG propagation losses estimated using the Caird method were 0.38 dB/cm. The near-field laser modes are shown in Fig. 3(c-e).

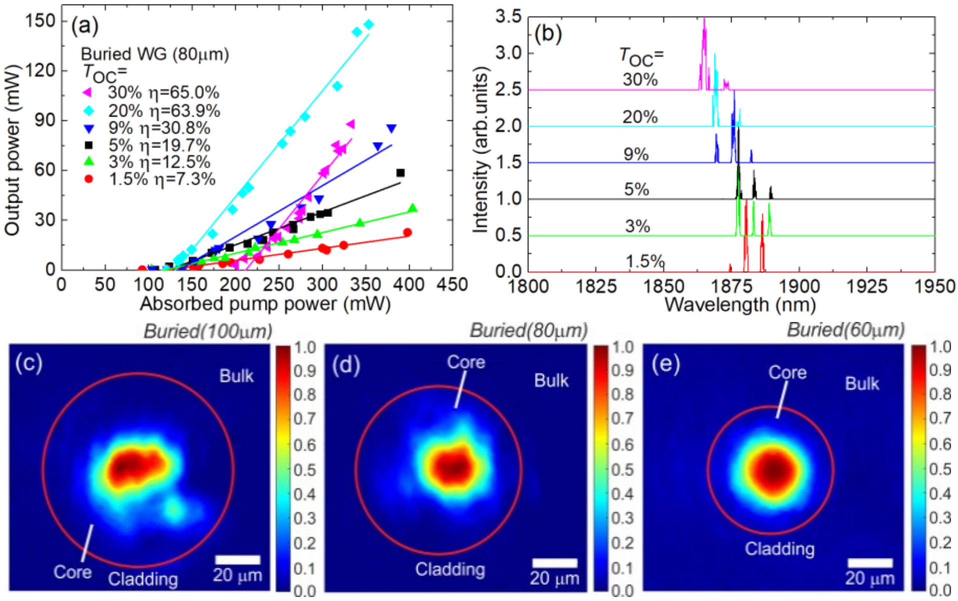

Fig. 3. Tm^{3+}:SrF$_2$ WG laser: (a,b) output performance of the WG with a cladding diameter of 80 µm: (a) input-output dependences, η – slope efficiency, (b) typical laser emission spectra measured at P$_{abs}$ ~300 mW; the laser emission is unpolarized; (c-e) laser modes in the far-field for the WGs with a cladding diameter of (c) 100 µm, (d) 80 µm and (e) 60 µm. Red circles – positions of the cladding.

To conclude, bulk Tm:MF$_2$ crystals are very suitable for fabrication of low-loss single-transverse-mode channel WGs by ULI. Strong ion clustering in these crystals leads to efficient CR enhancing the laser slope efficiency. The good energy storage capabilities of Tm:MF$_2$ crystals make them attractive for passively Q-switched WG lasers. Further power scaling can be achieved, e.g., by in-band pumping directly to the upper laser level using Raman fiber lasers at 1.7 µm.

[1] A. Sottile, E. Damiano, M. Rabe, R. Bertram, D. Klimm, and M. Tonelli, "Widely tunable, efficient 2 µm laser in monocrystalline Tm^{3+}:SrF$_2$," Opt. Express 26(5), 5368-5380 (2018).

[2] P. Camy, J. L. Doualan, S. Renard, A. Braud, V. Menard, and R. Moncorgé, "Tm^{3+}:CaF$_2$ for 1.9 µm laser operation," Opt. Commun. 236(4-6), 395-402 (2004).

5.2. Waveguide sensor

In order to develop sensors capable of detecting changes in the composition of water in real time, the waveguides inside crystals by the FS-DLW method has been studied.

As it has been seen in the previous section, we have worked with different crystalline matrices to study in detail the guiding of light within a crystal, as well as the losses generated within it. Once the results have been analyzed, we observe that the damage to the crystal produced by this manufacturing method does not affect the internal structure of the guided zone, maintaining all its optical and thermal properties. Thanks to this, it has been possible to carry out precise theoretical studies on the behavior of materials, being able to determine which ones would be the suitable for this purpose.

To study which material is the most convenient, we must decide what physical phenomenon to take advantage for this sensor. In our case, it has been determined that the two most interesting types of sensors are evanescence and Fabry-Perot interferometric sensors.

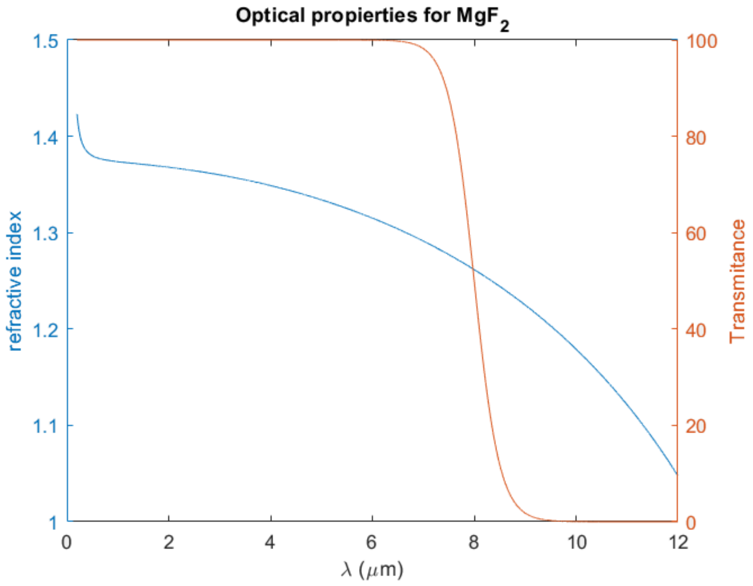

Figure 16. Transmittance and refractive index of MgF_2.

The evanescence sensor works by engraving a waveguide inside a crystal very close to its surface. With this it is possible to make the tails of the guided modes within the sensor interact with the liquid that is located right on the surface of the glass. If the refractive index of this liquid is greater than the index of the crystal, part of the light will be transmitted to it, gradually attenuating the signal, and measuring the spectrum at the outlet of the crystal it is possible to determine the composition of the liquid.

For this reason, a crystal that has a refractive index very similar to the liquid to be measured is necessary, in addition, most of the resonances that both water and any compound dissolved in it are found in the mid-infrared area, between $2\mu m$ to $10\mu m$. In order to measure these peaks, a material with a very large transmittance window in the IR has been sought. MgF_2 has been found to exhibit all of these characteristics as can be seen in **Figure 16**. Apart from its good optical properties, this glass has also been chosen for its good mechanical properties as can be seen in Table 2.

Transmission range	0,12 µm to 12 µm
Reflection loss	5.7% at 0.22 µm
Absorption coeficient	40 x 10-3 cm-1 at 2.7 µm
Density	3,18 g/cc
Melting point	1255ºC
Thermal conductivity	21(para) 33,6 (perp) W/(mk)
Thermal expansion	13.7 (para) 8.9 (perp) x 10-6 /K
Hardness	Knoop 415
Specific heat capacity	1003 J Kg m-1 K-1
Dielectric constant	4.87 (para) 5.45 (perp) at 1MHz
Solubility	0.0002g/100g water
Molecular wheight	62.32
Structure	Tetragonal P42/mnm

Table 2. Optical and mechanical properties of $\boldsymbol{MgF_2}$.

The Interferometric sensors work in a different manner. In them a coherent source (a laser) is focused inside the waveguide and interacts with itself. In particular, a Fabry-Perot interferometric system generates an interferential pattern in the spectrum of the light at the exit of the crystal that depends on the refractive index of the liquid in contact with it, as can be seen in the theoretical demonstration that is shown in the paper.

For our studies some crystals have been investigated to conclude that the most interesting crystal is the KLuW, since the interference figure obtained depends on the difference in refractive indices between the crystal and the liquid; the greater the difference, the better the interferences can be detected. As can be seen in **Figure 25** The refractive index of the KLuW is ideal for this, since it is greater than 2 in all the mid-IR spectrum [109] .

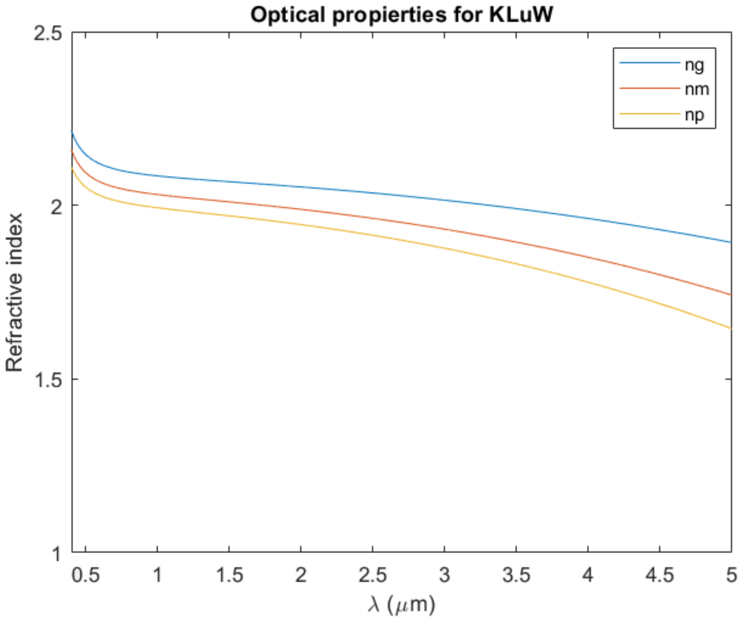

Figure 17. Refractive index of KLuw in each optic axis

Paper IV

Femtosecond-direct laser writing waveguide photonics-based sensing in MgF2 crystals

(In Progress to be submitted)

VICTOR LLAMAS,[1,2] CAROLINA ROMERO,[3] JAVIER R. VÁZQUEZ DE ALDANA,[3] JOSEP MARIA SERRES,[1,2] MAGDALENA AGUILÓ,[1] FRANCESC DÍAZ,[1] UWE GRIEBNER,[4] VALENTIN PETROV,[4] AND XAVIER MATEOS[1]

[1]Física i Cristal·lografia de Materials i Nanomaterials (FiCMA-FiCNA)-EMaS, Dept. Química Física i Inòrganica, Universitat Rovira i Virgili (URV), Campus Sescelades, 43007 Tarragona, Spain
[2]Eurecat, Centre Tecnològic de Catalunya, Unitat Advanced Manufacturing Systems (AMS), Campus Sescelades, 43007 Tarragona, Spain
[3]Aplicaciones del Láser y Fotónica, University of Salamanca, 37008 Salamanca, Spain
[4]Max Born Institute for Nonlinear Optics and Short Pulse Spectroscopy, Max-Born-Str. 2a, 12489 Berlin, Germany

Abstract

In this paper we have worked on the theoretical development and on the creation of two new types of sensors in the mid IR range formed by two crystals that have inside a waveguide made with the FS-DLW method.

The first device consists on a waveguide with a circular profile with R = 30μm. It has a cut on its surface $\mathrm{d} = 50\mu\mathrm{m}$ perpendicular to the waveguide by using the femtosecond-direct laser cutting technique. This device is designed to measure the refractive index of a liquid by working as a Fabri-Perot interferometer giving a spectral modulation that depend on the refractive index of the liquid that occupies this area.

The second crystal is a $\mathrm{MgF_2}$ with straight waveguide and circular profile $\mathrm{R} = 30\mu\mathrm{m}$ pretty close to the surface, with a gap of $\mathrm{G} = 10\mu\mathrm{m}$. In this guide a broad-spectrum light source is coupled that interacts with the water that is in its surface, generating an evanescent wave that depends on the composition of the liquid. This sensor takes full advantage of the optical properties of the MgF_2 and thanks to the

use of a crystal, a solid and monolithic sensor has been created, capable of being placed without problems in tap water sources.

Those systems solves many of the problems presented by fiber-guided devices [1-3]. Thanks to the use of a waveguide inscribed in a glass, its robustness is much higher, and it can be used in environments where water flows freely.

Introduction

Regulatory organisms that ensure safety and quality in the management of all types of water face new challenges every day, whether due to the use of new substances that can be harmful to humans or to the environment [4], or for security threats linked to terrorism. To face this challenge, the business sector linked to water management [5], works and asks for new tools linked to industry 4.0 [6], which allow it to monitor water parameters in real time, simulate new characteristics [7], and predict the evolution of the different variables [8]. To do this, they need new low-cost sensors to be able to distribute as many as possible, easy and inexpensive to maintain, but with higher capacities than the current ones, to be able to measure online or reach detection limits and species that until now were not measurable.

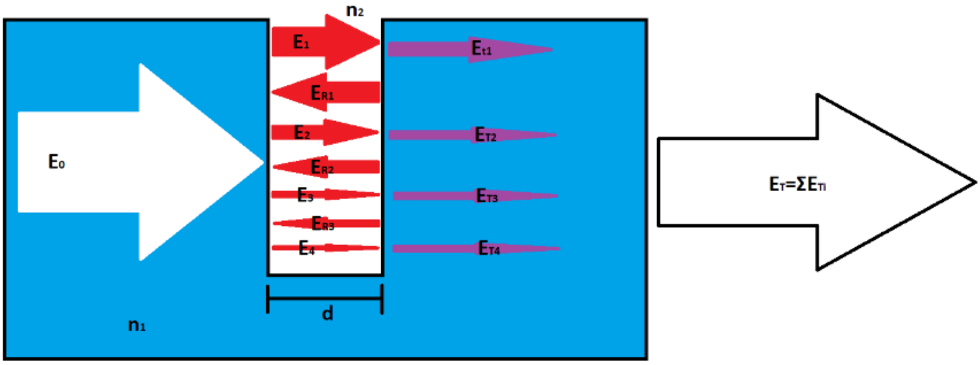

Figure 1. Scheme of the light reflections and transmission in a Fabry-Perot interferometer

This paper presents two new types of sensors capable of measuring the composition of water in real time, presenting a solid and robust device capable of being placed in any water source.

Principle: Fabry-Perot interferometer

Figure 1. represents a schematic drawing of the physical principle of our device. A plane wave passes through a material medium that has two flat-parallel plates called the etalon, this gives rise to multiple reflections in the central area and therefore several wave fronts are transmitted, the sum of all gives rise to an interferential figure.

To understand this phenomenon, it is necessary to understand the equations that govern it, we start from a plane wave that propagates through space in the form:

$$\mathrm{E} = \mathrm{E}_0\, \mathrm{e}^{\mathrm{i}\left(\frac{2\pi}{\lambda} \mathrm{n}\, \mathrm{x}\right)} \tag{1}$$

Where E is the electric field of the electromagnetic wave, E_0 is the initial electric field, λ is the wavelength, n is the refractive index of the material medium where the light propagates and x is the position. We consider that this wave propagates along the x axis, incident perpendicularly to the etalon; with which the reflection and transmission of light are guided by the Fresnel equations:

$$\mathrm{R} = \left|\frac{\mathrm{n}_1 - \mathrm{n}_2}{\mathrm{n}_1 + \mathrm{n}_2}\right|^2 \qquad \mathrm{T} = \left|\frac{4\, \mathrm{n}_1\, \mathrm{n}_2}{(\mathrm{n}_1 + \mathrm{n}_2)^2}\right| \tag{2}$$

Being R the reflectance, T the transmittance and n_1, n_2 the refractive index of each medium, n_1 for the crystal and n_2 for the liquid.

The first wave transmitted, E_1, will pass directly attenuating by transmission on both faces of the etalon. The second will be reflected twice, first on the second face of the etalon and then again on the first face, undergoing two reflections and traveling an extra distance $\mathrm{x}_2 = \mathrm{x} + 2\mathrm{d}$. The third will be reflected 4 times in the same way, being the equation for each one:

$$\begin{gathered} \mathrm{E}_{\mathrm{T1}} = \mathrm{T}^2\ \mathrm{E} \\ \mathrm{E}_{\mathrm{T2}} = \mathrm{T}^2\, \mathrm{R}^2 \mathrm{E}\, \mathrm{e}^{\mathrm{i}\left(\frac{2\pi}{\lambda} \mathrm{n}_2\, 2\mathrm{d}\right)} \end{gathered} \tag{3}$$

$$E_{T3} = T^2\ R^2 E\ e^{i\left(\frac{2\pi}{\lambda} n_2\ 4d\right)}$$

Thus, being the equation for the N wave:

$$E_{TN} = T^2\ R^{2(N-1)} E\ e^{i\left(\frac{2\pi}{\lambda} n_2\ 2(N-1)d\right)} \tag{4}$$

Being able to calculate the interference figure as the sum of all these waves:

$$E_T = \sum_{i=1}^{\infty} T^2\ R^{2(i-1)} E\ e^{i\left(\frac{2\pi}{\lambda} n_2\ 2(i-1)d\right)} \tag{5}$$

By operating it is obtained that the intensity of an FP interferometer is followed by the following equation.

$$I_T = I_0 \frac{1}{1 + \frac{4R}{(1-R)^2} \sin^2\left(\frac{2\pi}{\lambda}\ n_2\ 2d\right)} \tag{6}$$

From this it can be known that the intensity at the exit of the crystal depends on the refractive index of the two media and the width of the etalon. In order to estimate which parameters are the ideal ones for our experiment, a computer simulation has been carried out in Matlab MgF_2 Evanescent wave detector.

All materials have different refractive indices along their electromagnetic spectrum [9]. Its variation with wavelength in relation to the MgF_2 crystal has been studied in **Figure 2**. It is possible to observe how the refractive indices of each material are higher or lower than that of MgF_2 depending on its wavelength. Taking advantage of this characteristic it is possible to guide a wide spectrum laser beam inside the crystal, very close to the surface and, thanks to the properties of the evanescent wave, to measure which wavelengths have been attenuated, being able to directly relate them to the refractive index of each liquid.

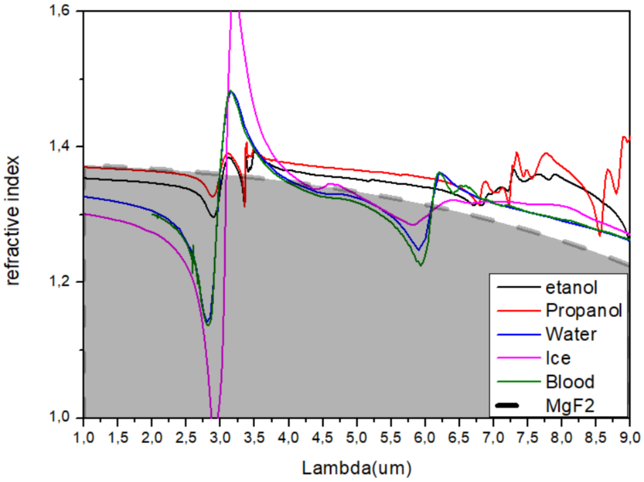

Figure 2. Refractive index vs wavelength for some liquids in comparison with $\mathbf{MgF_2}$.

As explained, the physical process that takes place is the evanescent wave depletion [10]. This process consists of the transmission of energy between a beam of light guided to another nearby medium. It occurs when the second medium has a higher refractive index than the medium that guides the light [11]. and is close enough for its evanescent wave, whose intensity decays exponentially, to interact with the medium in contact.

Simulations: Fabry-Perot interferometer

The equation (6) has been represented as a function of the wavelength for different parameters, to estimate which values are optimal for this experiment. The etalon distance, the crystal refractive index, and the light source have been studied, as well as acceptable noise values.

The width of the cut can be determined in **Figure 3.A.** The smaller the width, the greater the separation between peaks. This separation must be optimized for the working wavelength. If the separation is too wide, the maximum will be too close together and a slight change in the refractive index will move the position of the maximum ahead of the next one, making it impossible to detect. On the other hand, if the gap is too thin, the peaks will be very thick, making the index change not detectable. For this reason, it has been determined that an optimal measure of this gap is d≅50µm.

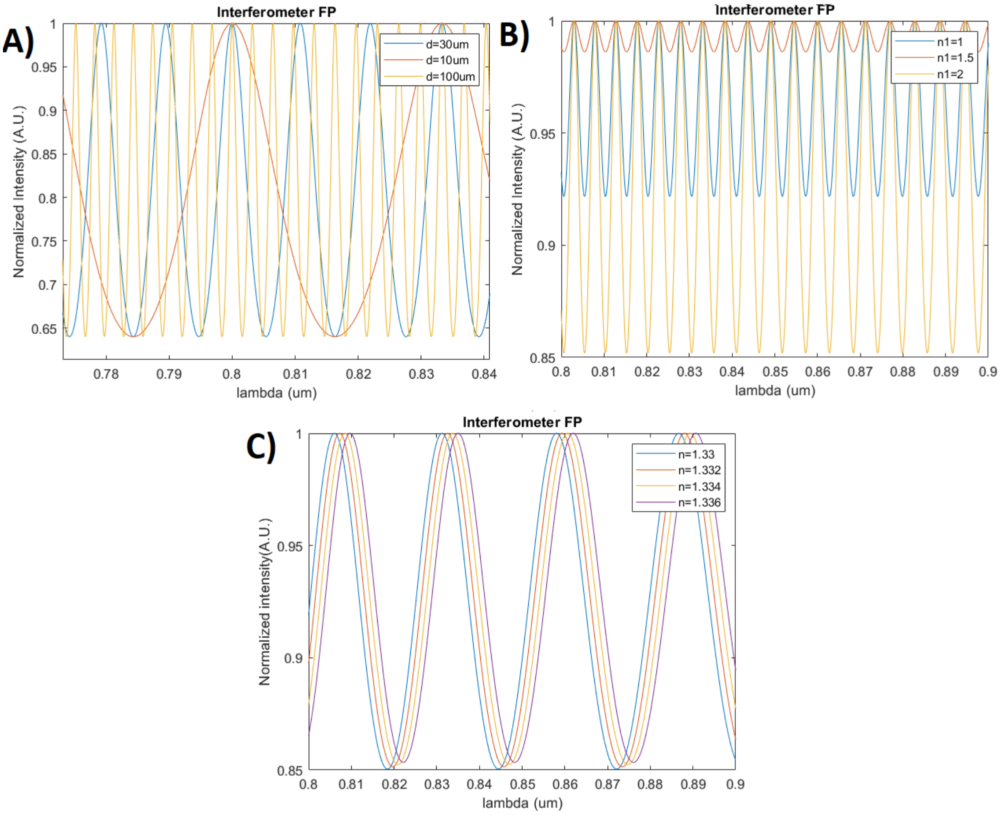

Figure 3. Studies of different parameters in a simulated FP interferometer. A) Study of the interference figure as a function of the width of the gap. B) Study of the interference figure as a function of the index of refraction of the crystal. C) Study of the interferential figure as a function of the variation of the refractive index in the liquid.

On the other hand, in **Figure 3.B.** the difference between the maximum and minimum of each peak depending on the refractive index of the crystal can be observed. The greater the difference between the index of refraction of the crystal and the medium, the greater the difference between maximum and minimum in the interference figure. As the refractive index of most liquids is around n≅1.3, it is mandatory to look for a crystal with a very high refractive index, around n ~ 2. There are crystals with higher refractive indices, for example diamond, but it is not feasible to use them for this experiment.

Finally, in **Figure 3.C**, a simulation of the interferential figure with respect to the refractive index of the liquid can be seen, in the graph small modifications in the refractive index give rise to modifications in the peaks of the figure. As can be observed, with the parameters defined above $\mathrm{n} = 2, \mathrm{d} = 50\mu\mathrm{m}$, the deviation of the peak's maximum is clearly differentiable.

Noise studies and treatments have also been done in order to improve the signal-noise ratio in our experiments. In **Figure 4.** can be seen the signal of a simulated interferential pattern with noise $\mathbf{n} = \mathbf{10\%\ I_{max}}$ randomly generated. Through signal filtering treatments [12] it has been possible to greatly reduce this noise to acceptable values for our experiment. Being possible to determine the refractive index after the filters with great accuracy.

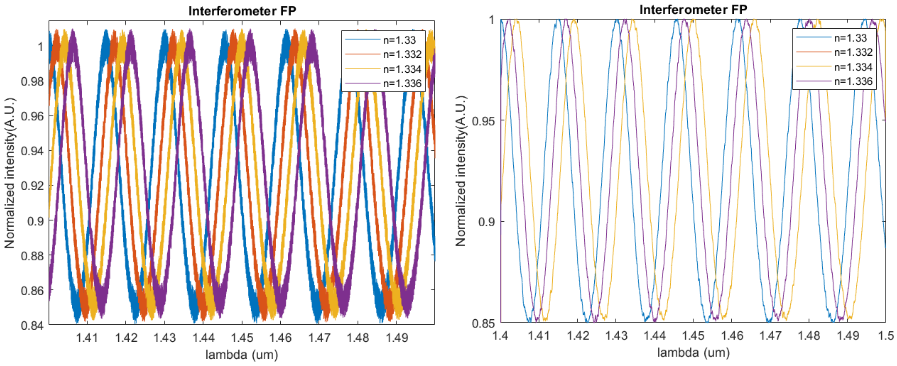

Figure 4. Noise management studies. (Right) Interferential figure obtained from a FP with a randomly generated noise of $\mathbf{n} = \mathbf{10\%\ I_{max}}$. (Left) Interferential figure treated for noise elimination.

Methods

By using a femtosecond laser (mira 900, coherent), several waveguides have been engraved inside a magnesium fluoride crystal ($\mathrm{MgF_2}$) by means of the femtosecond-direct laser writing (FS-DLW) method. These guides have different radius and depths in order to empirically find which is the most suitable for this experiment.

In addition, a cut has been made in its central area using the Femtosecond-direct laser cutting (FS-DLC) technique, creating a cutting area with a width of d≅50µm and a depth of h≅ 70µm. This crystal can be seen in **Figure 5.**

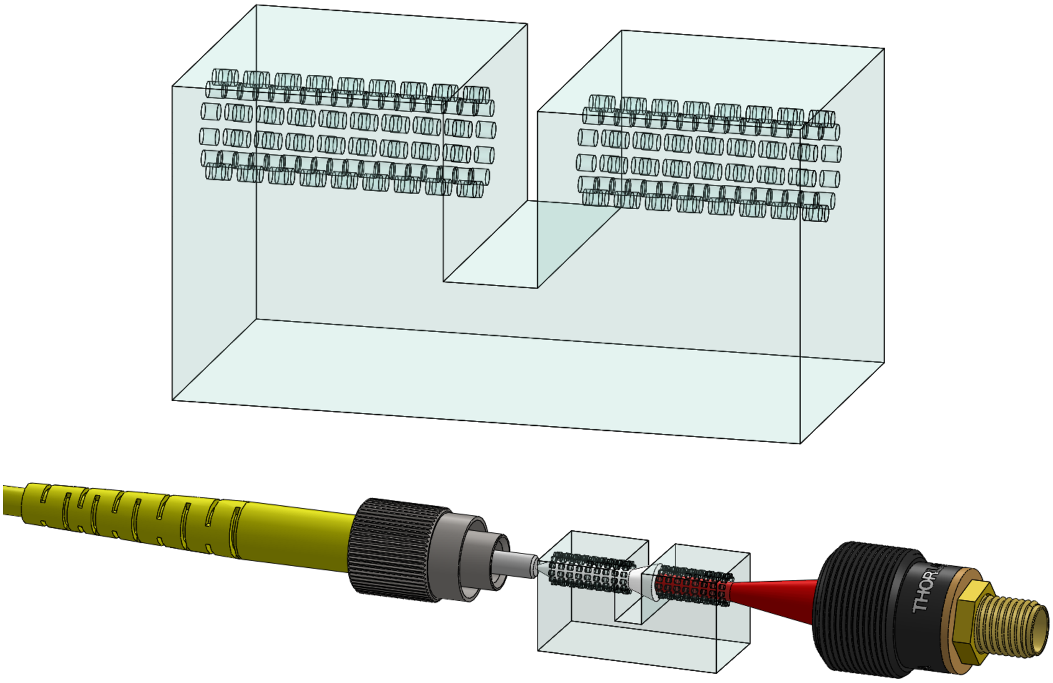

Figure 5. Experimental setup. In the upper image can be seen a 3D diagram of a crystal with a waveguide engraved inside with the FS-DLW technique and a cut in its central area made with the FS-DLC method. The lower image shows the assembly to measure compounds in water, it consists of a fiber that guides the light from a laser, the cut crystal of the upper image and a detector that measures the spectrum at its output.

This crystal has been used to guide light inside and detect the interference pattern that is obtained as it appears in **Figure 3**. A laser light source (REFERENCE) guided by a single-mode fiber (REFERENCE) has been used. This has been placed in contact with the guide inscribed in the crystal so that most of the light is guided inside. To ensure that the laser beam was in the correct position, an IR camera (FIND-R-SCOPE 85726 Near-IR Camera) was used, and the crystal was moved using a 4-Axis

Waveguide Manipulator with Differential Drives (MBT401D / M, Thorlabs) to the proper position. In **Figure 5** comparison of the guided and unguided light on the crystal can be observed.

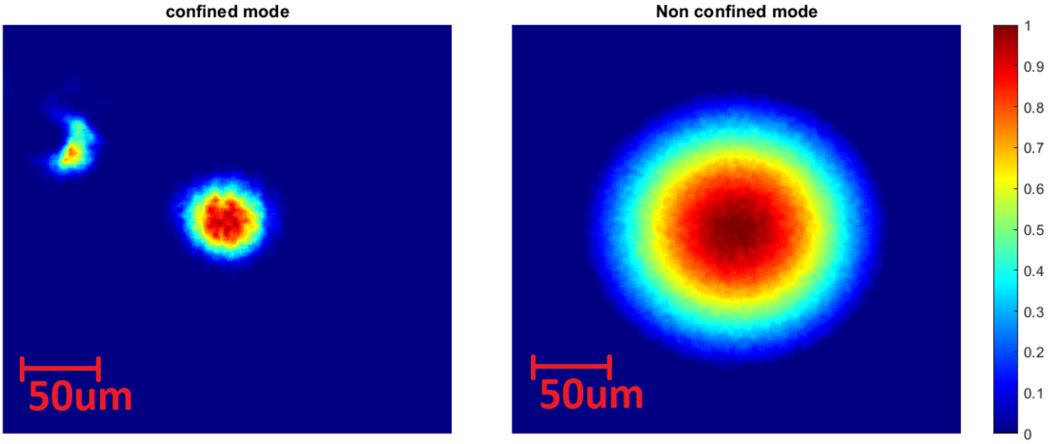

Figure 6. Images processed from the IR camera used to view the guiding of the light inside the crystal. On the right can be seen how the spot is reduced due to a correct guidance. On the right can be seen the laser spot when the light is not in any channel.

When a correct guidance has been obtained, **Figure 6**, the IR camera has been replaced by an optical spectrum analyzer (Optical spectrum analyzer AQ6375B, Yokogawa) in order to observe the spectrum at the output of the device by an optical fiber (M28L01, Thorlabs) placing the end as close as possible to the crystal, in order to receive only the signal from the guided area, avoiding laser radiation that has not been guided.

With this device aligned, several liquids have been placed on the surface of the crystal, making sure that they are strained inside the cut and the spectrum has been measured at the exit.

DETECTOR II: MgF_2 Evanescent wave detector.

Operation principle.

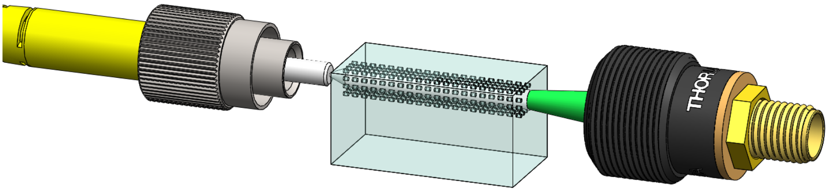

Figure 7. 3D model of the experimental setup. In the picture a single-mode fiber couples the light from a light source in a FS-DLW circular waveguide R = 30µm with a distance from the surface of G = 10µm. This light interacts with the liquid and its exit spectrum is detected by an optical spectrum analyzer.

To carry out this experiment, a white light source (OSL2 Halogen lamp, Thorlabs) guided by a single-mode fiber (REFERENCE) has been used. The outlet of this fiber has been placed just in contact with the crystal matching all the light inside the waveguide by using a 4-Axis Waveguide Manipulator with Differential Drives (MBT401D / M, Thorlabs) to the proper position. An IR camera (FIND-R-SCOPE 85726 Near-IR Camera) has been used to know the exact position of the mode. By moving the 4-Axis stage, it was possible to detect the coupling of the light beam in the camera, as can be seen in **Figure 8.**

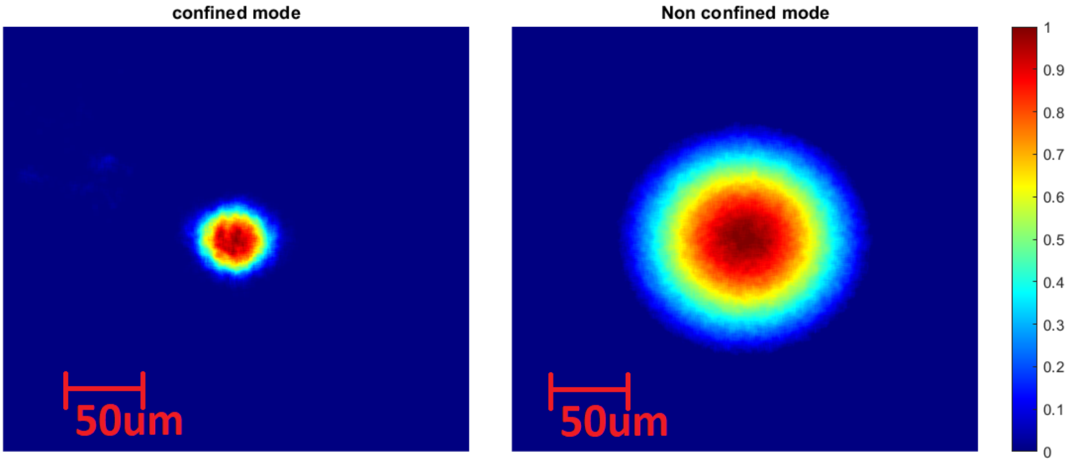

Figure 8. IR images of the light profile in the camera. In the left image can be seen the light guided inside a waveguide $\mathbf{r} = \mathbf{30\mu m}$ made by FS-DLW. The left images is the light without coupling in any mode.

Conclusions and future developments

In this article, two new types of femtosecond-direct laser writing waveguide sensors capable of detecting small changes in the refractive index of a liquid have been theoretically studied. The first device works by Fabri-Perot interferometry and the second by evanescence. In both cases, theoretical and computational studies have been carried out to obtain the ideal parameters for each working principle.

It is expected in the near future to carry out experiments with these crystals and working principles, thus obtaining fully functional devices able to be placed in any water supply to detect in real time water chemical composition.

References

[1] T. Wei, Y. Han, Y. Li, H.-L. Tsai, and H. Xiao, “Temperature-insensitive miniaturized fiber inline Fabry-Perot interferometer for highly sensitive refractive index measurement,” Opt. Express, vol. 16, no. 8, pp. 5764–5769, 2008, doi: 10.1364/OE.16.005764.

[2] C. R. Liao, T. Y. Hu, and D. N. Wang, “Optical fiber Fabry-Perot interferometer cavity fabricated by femtosecond laser micromachining and fusion splicing for refractive index sensing,” Opt. Express, vol. 20, no. 20, pp. 22813–22818, Sep. 2012, doi: 10.1364/OE.20.022813.

[3] Y. Wang, M. Yang, D. N. Wang, S. Liu, and P. Lu, “Fiber in-line Mach-Zehnder interferometer fabricated by femtosecond laser micromachining for refractive index measurement with high sensitivity,” J. Opt. Soc. Am. B, vol. 27, no. 3, pp. 370–374, Mar. 2010, doi: 10.1364/JOSAB.27.000370.

[4] R. K. Naik, M. M. Naik, P. M. D’Costa, and F. Shaikh, “Microplastics in ballast water as an emerging source and vector for harmful chemicals, antibiotics, metals, bacterial pathogens and HAB species: A potential risk to the marine environment and human health,” Mar. Pollut. Bull., vol. 149, p. 110525, 2019, doi: https://doi.org/10.1016/j.marpolbul.2019.110525.

[5] S. J. McGrane, “Impacts of urbanisation on hydrological and water quality dynamics, and urban water management: a review,” https://doi.org/10.1080/02626667.2015.1128084, vol. 61, no. 13, pp. 2295–2311, Oct. 2016, doi: 10.1080/02626667.2015.1128084.

[6] T. Kurfess, C. Saldana, K. Saleeby, and M. Parto-Dezfouli, “Industry 4.0 and Intelligent Manufacturing Processes: A Review of Modern Sensing Technologies,” J. Manuf. Sci. Eng., vol. 142, no. 11, Aug. 2020, doi: 10.1115/1.4048206.

[7] C. J. Tainter, P. A. Pieniazek, Y.-S. Lin, and J. L. Skinner, “Robust three-body water simulation model,” J. Chem. Phys., vol. 134, no. 18, p. 184501, May 2011, doi: 10.1063/1.3587053.

[8] J. M. Wagner, U. Shamir, and D. H. Marks, “Water Distribution Reliability: Simulation Methods,” J. Water Resour. Plan. Manag., vol. 114, no. 3, pp. 276–294, May 1988, doi: 10.1061/(ASCE)0733-9496(1988)114:3(276).

[9] P. S. R. Diniz, Adaptive Filtering: Algorithms and Practical Implementation, 5th ed. Springer, 2019.

[10] S. Singh, “Refractive Index Measurement and its Applications,” Phys. Scr., vol. 65, no. 2, p. 167, Jan. 2002, doi: 10.1238/PHYSICA.REGULAR.065A00167.

[11] A. Greenstein, A. Katzir, and A. Messica, “Theory of fiber-optic, evanescent-wave spectroscopy andsensors,” Appl. Opt. Vol. 35, Issue 13, pp. 2274-2284, vol. 35, no. 13, pp. 2274–2284, May 1996, doi: 10.1364/AO.35.002274.

[12] E. J. Smythe et al., “Evanescent-wave bonding between optical waveguides,” Opt. Lett. Vol. 30, Issue 22, pp. 3042-3044, vol. 30, no. 22, pp. 3042–3044, Nov. 2005, doi: 10.1364/OL.30.003042.

6

INDUSTRY 4.0 DETECTION DEVICES

In this thesis, several 4.0 devices have been developed, with a very clear objective: to provide companies with photonic devices capable of fulfill their needs at a competitive price. For this, research on photonic sensors, together with the development of a homemade software for each device, has been essential, as we are going to see in this chapter.

Taking these into account, we have been able to include the sensors developed in two big groups. On the one hand, multispectral detectors in the visible and infrared spectrum capable of obtaining spectral images with good resolution. On the other hand, artificial vision systems have been developed to detect different events in a production chain, such as errors, anomalies or rotations being able to convert this information into data easily understood by any computer.

6.1. Multispectral detectors

In order to develop sensor technologies for Industry 4.0, a window of opportunity was observed in the study of multispectral detectors in the infrared. Certain commercial devices exist in this niche, but in practice they are either extremely expensive or inaccurate. To take advantage of our capabilities in this field, three multispectral detection systems: an FTIR, a wiskbroom camera and a pushbroom camera, has been developed. These three technologies have the same objective: to obtain the spectrum of a certain area, but their technologies are very different, as well as their applications. On the one hand, the FTIR is used to determine the spectrum in the Mid infrared of a certain sample, while the pusbroom and the wiskbroom can obtain multispectral images of a target.

6.1.1. Hyperspectral cameras

In the past decades, different kinds of hyperspectral imaging methods and related technology have been proposed in acquiring the spectral data from an image. In this chapter two different methods have been stuidied and developed: the whiskbroom and pushbroom hyperspectral cameras [118].

The whiskbroom imaging mode, also known as the point-scanning method, was used originally by the Earth Resources Technology Satellites and then implemented by the Airborne Visible/Infrared Imaging Spectrometer [119]. In the whiskbroom sensor, a couple of X-Y position axis or rotating mirrors were used to scan the sample from side to side perpendicular to the direction of the sensor platform. This multispectral imaging method presents a superior spatial and spectral resolution in detriment of the imaging time.

As shown in **Figure 17.A**, a single point is scanned along two spatial dimensions (x and y) by moving either the sample or the detector, the light is collected into a spectrophotometer generating a 3D matrix $I(X, Y, \lambda)$.

The pushbroom approach, also known as line scanning, has been used by some earth observation satellite systems operating from space, such as the SPOT system and the Advanced Land Imager (ALI) [120].

In this method all the spectral information of a line is retrieved at once, as can be seen in **Figure 17.B**. In order to obtain the spectral image generating the 3D matrix

$I(X, Y, \lambda)$, either the object or the camera has to move synchronously and perpendicularly to the line. This method receives much more information for each row being able to generate an image in a quicker time, but the spectral information is not as accurate as in the wiskbroom method.

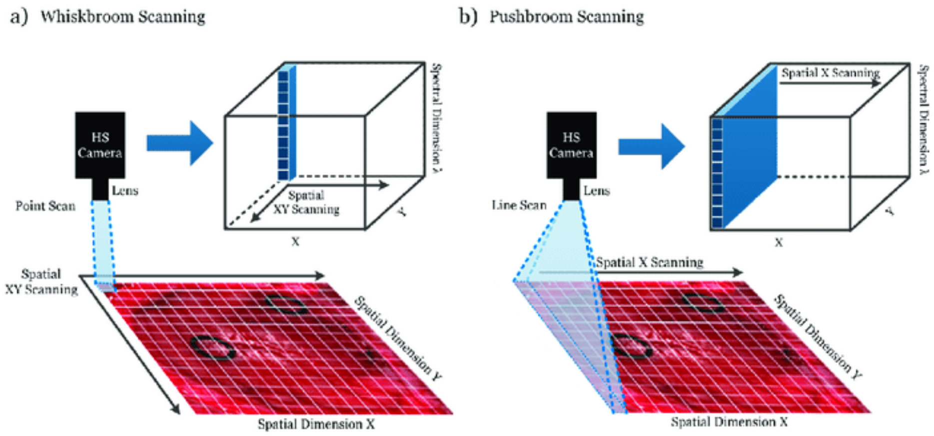

Figure 18. types of hyperespectral images A) Wiskbrooom scanning B) Pushbroom scanning [121]

6.1.2. Wiskbroom camera

Associated with a project to eliminate bacteria in water, the distribution of intensities and wavelengths of an array of UV LEDs was studied. These had to be placed in a widened part of a pipe, irradiating it in the best possible way, as seen in **Figure 19**. With the aim of optimizing its distribution to achieve the most homogeneous exposure possible with the least number of LEDs, exceeding the minimum power required to eliminate bacteria; a multispectral vision system known as a whiskbroom camera was developed. This system generates a multispectral image of an area with excellent precision.

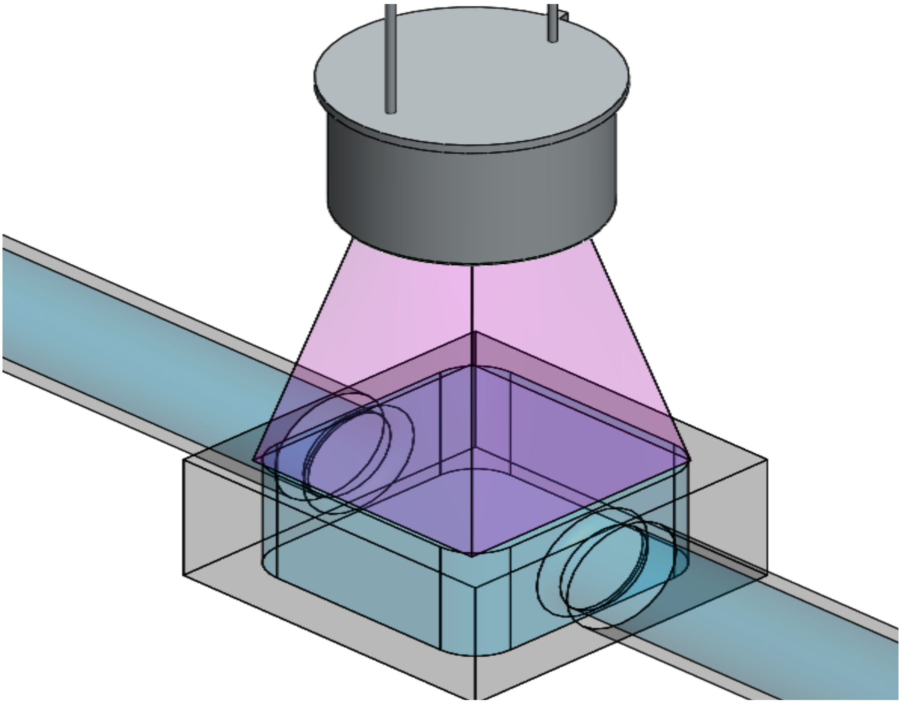

Figure 19. Diagram of the operation of the DEAD bacteria elimination system. An array of UV LEDs with different wavelengths irradiates a widened part of a pipe to eliminate pathogens.

The system is based on a pair of XY motors (Zaber X-XY-LSM100A), a powermeter (Thorlabs, S120VC) and a commercial spectrophotometer (OceanOptics, Flame) connected to an optical fiber as can be seen in **Figure 20**.

In it, the XY motors scan the work zone, moving themselves a small distance dx and dy, and performing an intensity and spectral measurement at each point. With the combination of the PM with the spectrophotometer it is possible to obtain $P(\lambda)$ in a much more precise way. For this, the spectrum in A.U is obtained, this spectrum is fitted with the PM efficiency curve $\epsilon(\lambda)$ to obtain an exact power value at each point and this is used to obtain the exact $P(x, y, \lambda)$.

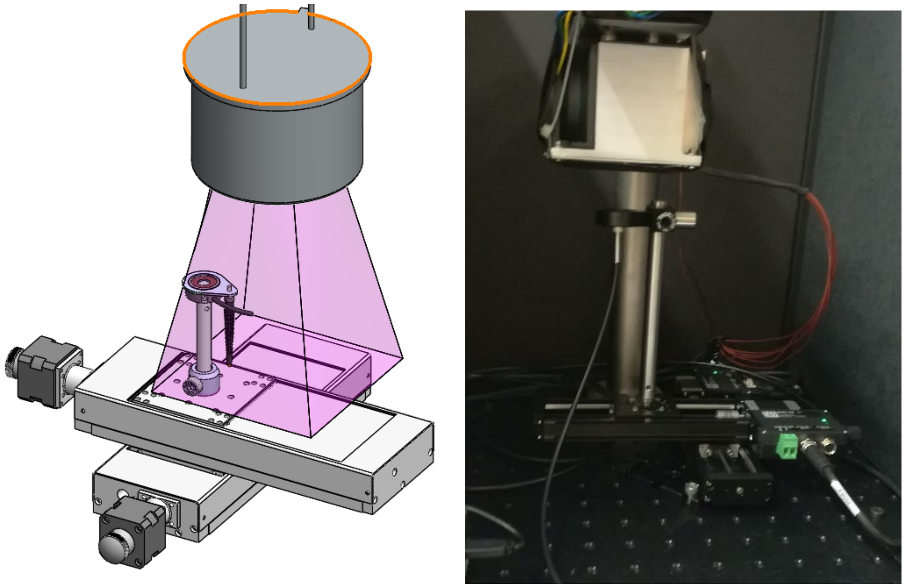

Figure 20. (Left) Operation diagram of the wiskboom camera created for the DEAD project. In the image you can see how some XY rails move the powermeter and the optical fiber. (Right) Experimental setup of our whiskbroom camera.

To manage the device, a graphical interface has been created in LabView where dx, dy and the exposure time of the spectrophotometer can be controlled. In addition, a data reading program has been created in Matlab that allows us to see the intensity of light at a certain wavelength, as well as the total intensity that reaches the PM and the spectrum at a point.

With this device it has been possible to make measurements of the aforementioned array of LEDs as can be seen in **Figure 21**. It has been possible to satisfactorily determine the intensity pattern of the led array with a resolution of $dx = 0.1mm$, $dy = 0.1mm$ and $d\lambda = 1nm$ in the range of $\lambda = 200 - 1100nm$, demonstrating a very good spatial and spectral resolution.

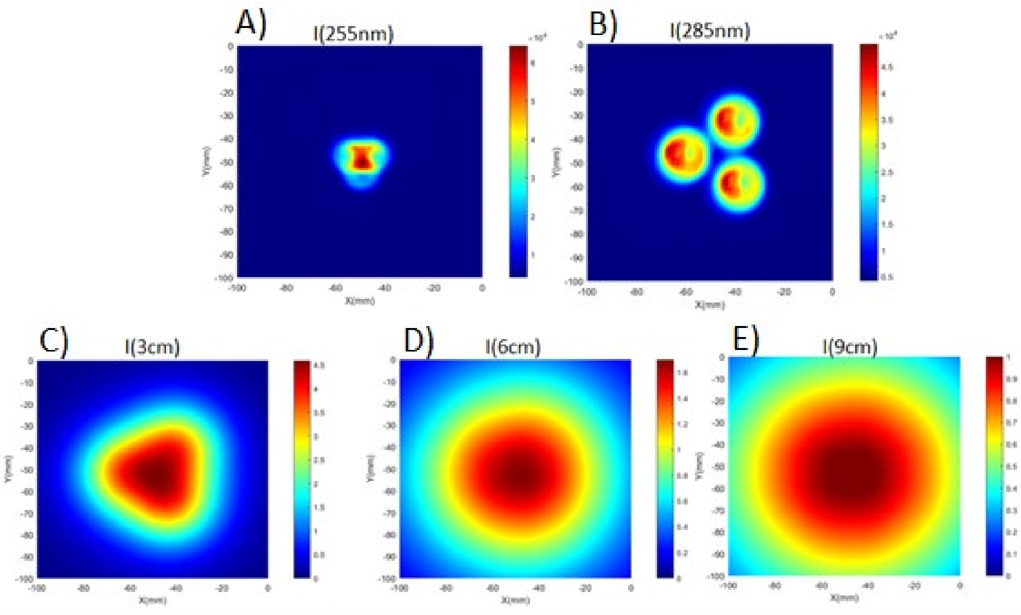

Figure 21. Fig. Images of an array of LEDs obtained with a whiskbroom camera. A) Intensity at 255nm at 3cm from the sample. B) Intensity at 285nm at 3cm from the sample. C) Total intensity 3cm from the sample. D) Total intensity 6cm from the sample. E) Total intensity at 9cm from the sample.

As can be seen in **Figure 21**. It has been possible to determine P (x, y, λ) of an array of LEDs with a whiskbroom camera in a satisfactory way, obtaining excellent precision at each point. However, the system took 2h for each image. With which it is concluded that this method is perfect for carrying out hyperspectral studies of static elements, where the data acquisition time is irrelevant, however, this type of cameras are not useful for quickly obtaining data, as well as for studying elements. whose spectral imprint changes with time.

6.1.3. Pushboom camera

In order to create a multispectral image in the Mid-IR range, the operation of pushbroom hyperspectral cameras has been studied and two models have been developed, one in the visible λ = 400nm-800nm and the other in the mid-IR λ = 2µm-6µm.

The manufactured device works as seen in Figure 22. The object to be measured is focused on the slit using a focusing lens. Through the slit passes only the information of one line, this is collimated using a converging lens and passes through a linear diffraction grating with its lines parallel to the slit. It separates the light angularly depending on its wavelength, and, by using another focusing lens, is focused on the CCD which detects $I(x, \lambda)$.

By moving the object or the device at a constant speed and perpendicular to the slit while the camera is recording, it is possible to retrieve a hyperspectral image of the target.

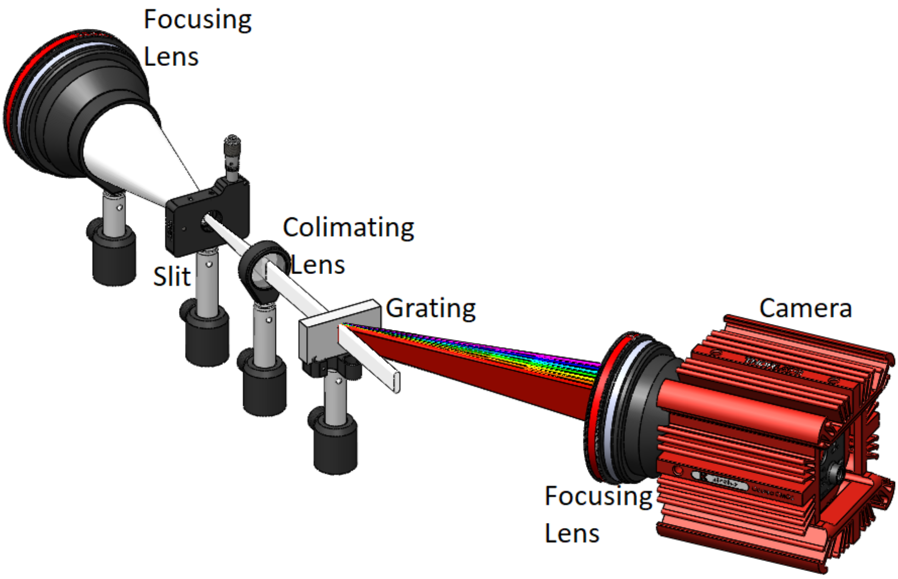

Figure 22. 3D diagram of the operation of a pushbroom hyperespectral camera.

To better understand how the image is captured, a series of parameters related to it must be understood:

Field Of View (FOV): This parameter is related to the angular aperture of the first focusing lens δ_{focus} and it delimits the amount of information that is collected in a line, the greater the angular aperture, the bigger the FOV.

Spectral resolution (SR): This parameter indicates the spectral range that can be captured on the camera. To understand it correctly, how the diffraction of light works in gratings must be understood. The light that passes through a linear grating is separated angularly depending on its wavelength following the equation:

$$\theta_m(\lambda) = \arcsin\left(\frac{m\,\lambda}{d}\right) \tag{24}$$

Where θ_m is the diffraction angle for each wavelength, m is the diffraction order, λ is the wavelength and d is the separation between two consecutive lines.

With these parameters it is possible to calculate which grating is ideal for the needs of the experiment. It must be taken into account that to avoid erroneous measurements the second order of diffraction of the lowest wavelengths should not overlap with the first order of the highest wavelengths.

In addition to the grating, it is also necessary to have a focusing lens that is capable of collecting all the light and focusing it correctly on the camera, with the sufficient angular aperture δ_{camera} for this.

Depth Of Field (DOF): This parameter gives us an idea of the area where the camera can be in focus. It is crucial that the object is within this range since otherwise we will not only have an erroneous measurement of where each pixel is located, but we will also be making an error when obtaining the spectrum. It can be expressed as:

$$D - \frac{L}{2} < Z < D + \frac{L}{2} \tag{25}$$

Being L the focal length and D the DOF.

Lateral Resolution (LR): Indicates the distance the device moves between one image and the next, the smaller this value, the more defined the image will be. It is expressed as:

$$\Delta Y = \frac{\vec{v}}{FPS} \tag{26}$$

Being $\vec{v}$ the relative speed of the system; and FPS are the frames per second of the camera. This formula works equally if the device or the sample moves.

A hyperspectral camera (**Figure 23**) in the range λ = 400-800nm has been developed in order to obtain the entire visible spectrum of an object. This device consists of two tetrafocal lenses, a slit (VA100, Thorlabs), a converging lens (LA1251, Thorlabs), a diffraction grating (GT13-06V, Thorlabs) and an ultra-fast camera (TIS-DMK-33UX264, The imaging source).

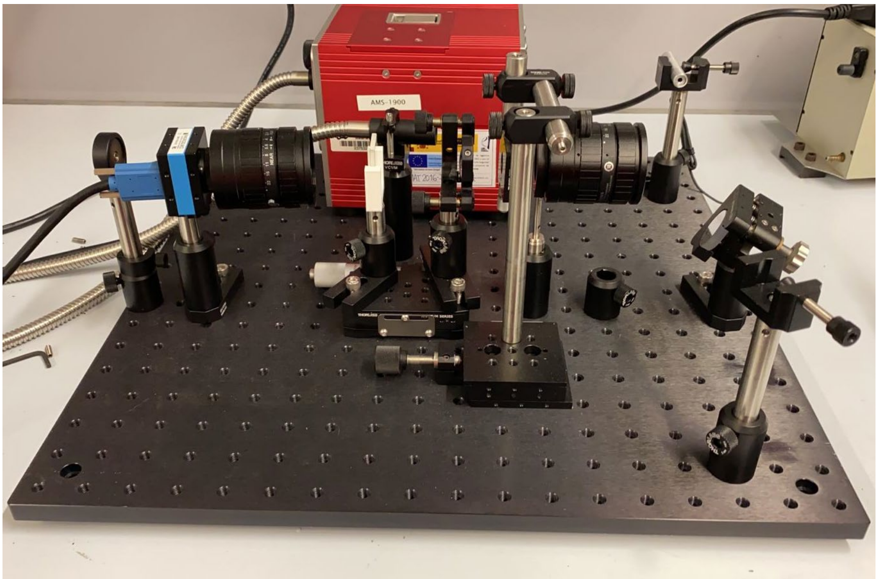

Figure 23. Experimental setup of a pushbroom camera in the range from 400nm to 800nm.

This device has been calibrated both in wavelength and in number of counts, from measurements of the spectrum and the power of various lasers so that its spectrum accurately reflects the relationship between wavelengths. Due to the fact that depending on the light source that affects the object, more or less exposure time will be needed on it, it has been decided not to try to calculate the power, since the calculation is too complicated and in general it is not a relevant measure.

In addition to the aforementioned device, other commercial pushbroom cameras (REFERENCE) have been used using the same algorithm adjusted to the device parameters and clear images of different targets have been obtained.

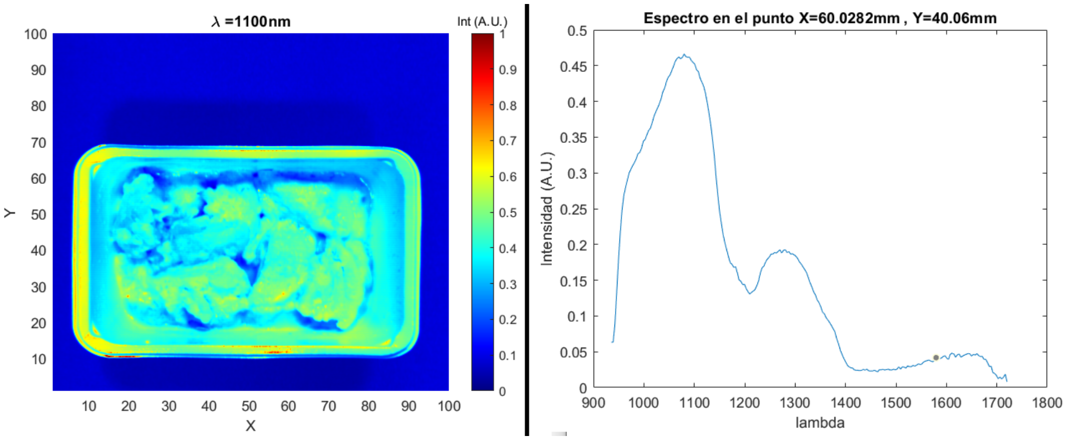

Figure 24. Hyperspectral images recorded with the hyperspectral camera (REFERENCIA). On the left intensity image at $\boldsymbol{\lambda = 1100nm}$. On the right the spectrum in the point $\boldsymbol{X = 60nm, Y = 40mm}$.

A device has been developed capable of quickly determining the emission spectrum of an object using the pushbroom system. For this, an experimental assembly of the device has been carried out, as well as all the numerical algorithms necessary for its correct operation. To demonstrate its correct operation, the algorithm created in a commercial device has been used. The main competitive advantage of this device in relation to the commercial ones is its price. The elements used for the development of this system are much cheaper than a conventional system, being able to open a gap in the market and facilitating its implementation.

6.1.4. Fourier Transform Infra-Red (FTIR)

With the aim of developing an IR sensor (from 2 to 6 μm) that can satisfy our precision and detection limits, a Fourier Transform Infra-Red (FTIR) spectrophotometer has been modeled and manufactured [122].

An FTIR is a photonic device capable of determining the IR spectrum of a light signal [123]. By using an optical fiber, the collected test light passes through a lens generating a collimated beam. This is split in two similar beams with different paths in the beam splitter (BS), one is reflected in a fixed mirror and the other in a motorized mirror. These two beams are reflected back to the BS where both superpose and focused on a photodetector [124]. Moving the motorized mirror in a controlled way, an interference pattern is obtained in the photodetector $I(x)$ that can be correlated with the infrared spectrum of the sample beam $I(\lambda)$ as seen in **Figure 25**.

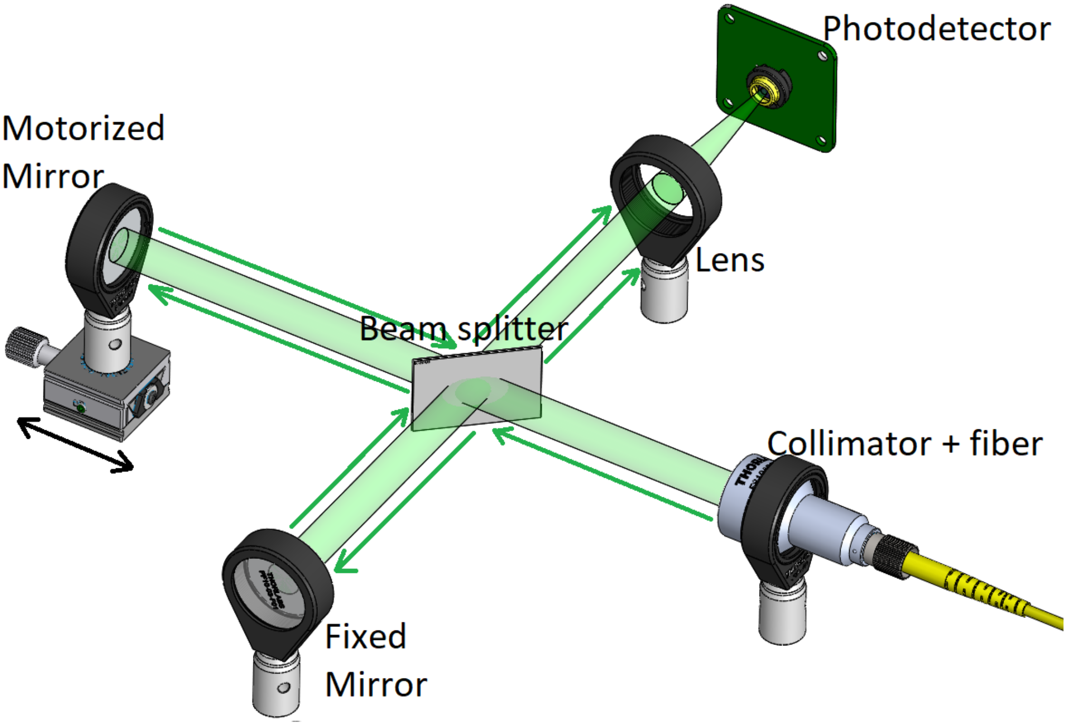

Figure 25. 3D model of the FTIR working scheme.

From the fiber a collimated beam is obtained that can be approximated to a plane wave:

$$E(\nu, x) = E_0(\nu)e^{i\left(\frac{\nu}{c}x\right)} \tag{27}$$

Being E_0 the initial electric field, $\nu(rad/s)$ the angular frequency and $x(m)$ the position (**Figure 26**.A.).

This beam is split in two in a BS and reaches two mirrors, one of them is fixed and the other is motorized to measure the intensity thar arrives to the detector vs the position of the motorized mirror. Both beams are reflected to the BS again and ends up in a detector as shown in **Figure 25**. In the detector, the electric field from each arm will be:

$$E_1(\nu, x_1) = E_0(\nu)e^{i\left(\frac{\nu}{c}x_1\right)} \qquad E_2(\nu, x_2) = E_0(\nu)e^{i\left(\frac{\nu}{c}x_2\right)} \tag{28}$$

Being E_1 the electric field which is reflected in the fixed mirror and E_2 the electric field reflected in the motorized mirror.

Those two plane waves are superimposed in the detector generating a total field E:

$$E = E_1 + E_2 = E_0(\nu)e^{i(\frac{\nu}{c}x_1)} + E_0(\nu)e^{i(\frac{\nu}{c}x_2)} \tag{29}$$

As the photodetector only can measure intensity, the total intensity is:

$$I = \frac{c\,n\,\epsilon_0}{2}\int_{-\infty}^{\infty} |E_1(\nu, x_1) + E_2(\nu, x_2)|^2\, d\nu \tag{30}$$

To simplify this equation, we are going to ignore the $\frac{c\,n\,\epsilon_0}{2}$ in the analysis. This term is only a constant not relevant in the theoretical development. In addition, it is possible to consider the superposition of these two waves in function of their trip difference, by considering the path of the fixed mirror as x_0 and the path difference as x.

$$x_1 = x_0 \qquad x_2 = x_0 + x \tag{31}$$

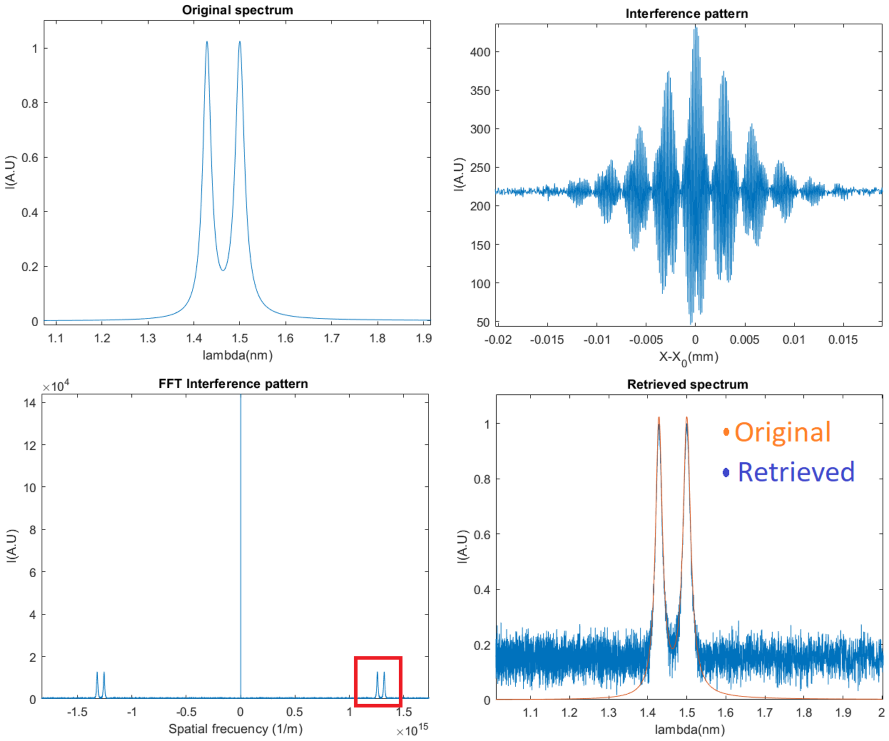

Figure 26. Simulation of an FTIR. A) Input spectrum. B) Interferential figure obtained in the detector. C) FFT of the interference figure. D) Spectrum obtained vs. original spectrum.

Operating in (29) the next integral is obtained:

$$I(x) = \int_{-\infty}^{\infty} |E_1(\nu, x_0)|^2 + |E_2(\nu, x_0 + x)|^2 + \\ +2\, E_1(\nu, x_0)E_2(\nu, x_0 + x)|d\nu \tag{32}$$

This presents three clearly differentiated terms. The first and second are independent constants that only generate an offset in the detector and the third one is the interferential term I_{int} that will cause beats in the detector as shown in **Figure 26.B**, being:

$$\begin{aligned} I_{int} &= \int_{-\infty}^{\infty} |E_0(\nu) e^{i\left(\frac{\nu}{c} x_0\right)} E_0(\nu) e^{i\left(\frac{\nu}{c}\,(x_0+x)\right)}|\, d\nu \rightarrow \\ \rightarrow I_{int} &= \int_{-\infty}^{\infty} |\, E_0(\nu)^2 e^{i\left(\frac{2\nu}{c} x_0\right)} e^{i\left(\frac{\nu}{c} x\right)}|\ d\nu \rightarrow \\ \rightarrow I_{int} &= \int_{-\infty}^{\infty} |E_0(\nu, x_0)^2| \cos\left(\frac{\nu}{c} x\right) d\nu \end{aligned} \tag{33}$$

By recurring to the identity $\cos(x) = \frac{e^{ix} + e^{-ix}}{2}$ and substituting I_{int} in (32) the total intensity is expressed as:

$$\begin{aligned} I(x) = &\int_{-\infty}^{\infty} (|E_1(\nu)|^2 + |E_2(\nu)|^2)\, d\nu + \\ &+ \int_{-\infty}^{\infty} |E_0(\nu, x_0)^2| e^{i\left(\frac{\nu}{c} x\right)} d\nu + \\ &+ \int_{-\infty}^{\infty} |E_0(\nu, x_0)^2| e^{-i\left(\frac{\nu}{c} x\right)} d\nu \end{aligned} \tag{34}$$

Now it is possible compare the equation (34) with the Fourier transform (FT) definition, expressed as:

$$g(\omega) = \frac{1}{\sqrt{2\pi}} \int_{-\infty}^{\infty} f(t) e^{i\omega t}\ dt \tag{35}$$

Then, if the FT is carried out in equation (34), three terms appear as can be seen in **Figure 26.C**. The first term, which is constant and independent of x, is transformed into a constant value multiplied by a Dirac delta centered at $\nu = 0$, the second and third terms are the intensity spectrum in the negative and positive angular frequencies:

$$I(+\nu) = \mathcal{F}\big(I_2(x)\big) \qquad I(-\nu) = \mathcal{F}(I_3(x)) \tag{36}$$

In such a way that if the Fourier transform of $I(x)$ is carried out and only the positive part of the spectrum is taken, without the low angular frequencies, it is possible to obtain the spectral intensity of the test light.

To carry out these calculations we have taken advantage of the Fast Fourier Transform [125], a computational algorithm that allows us to perform the Fourier transform much faster. However, it presents a series of limitations: the data must be equidistant on the x axis and the domain of the function obtained depends on the Nyquist–Shannon theorem [126].

In order to satisfy the Nyquist rules, it is essential to define the position axis. It has a total travel distance x_{max} and a point separation dx:

$$x = -\frac{x_{max}}{2} : dx : \frac{x_{max}}{2} \tag{37}$$

By employing the Nyquist transformations, the maximum angular frequency ν_{max} and angular point separation $d\nu$ are:

$$\nu_{max} = \frac{\pi\, c}{dx} \qquad d\nu = \frac{2\,\pi\, c}{x_{max}} \tag{38}$$

Obtaining an angular frequency axis:

$$\nu = \frac{-\nu_{max}}{2} : d\nu : \frac{\nu_{max}}{2} \tag{39}$$

Being possible to express it in wavelengths as:

$$\lambda = \frac{2\,\pi\, c}{\nu} \tag{40}$$

A computer program has been made in Matlab to estimate and simulate the behavior of an FTIR (annex 2). This program simulates an electromagnetic wave, propagates it, splits it in two waves that travels different distances and, superimposes them to generate $I(x)$ as shown in equation (29) and from $I(x)$ the FFT is performed to obtain $I(\lambda)$.

All these operations are represented in **Figure 26**, where can be seen the spectrum of the original wave **(Figure 26.A)** the intensity versus wave path difference (**Figure 26.B**), the FFT of $I(x)$ with its three clearly differentiated lobes (**Figure 26.C**), and the final spectrum obtained with this method in comparison it with the original one, (**Figure 26.D**)

The objective of this program is to estimate how the device will behave in a "realistic" environment, being able to simulate the absorption efficiency of the detector for each wavelength, the most appropriate x_{max} and dx for our interests in terms of spectral resolution and how the noise will affect the device.

A study has been carried out modifying x_{max} and dx to obtain the most suitable values to encompass the entire spectrum with the best spectral resolution as possible. For this, the Nyquist rules (37) have been followed, concluding that some realistic values would be:

$x_{max} = 1cm$

$dx = 1um$

It is important to note that the optimal optical path would have a zero path difference right at its midpoint, that is:

$$x_2 = x_1 - \frac{x_{max}}{2} : dx : x_1 + \frac{x_{max}}{2} \tag{41}$$

Since in this region the interferences are more intense, and therefore where there is more information about the spectrum.

The influence of the detector response with the wavelength has been numerically simulated since it is not trivial to include it in the theoretical development in equation (29). For this, a signal has been simulated that multiplies each value of the frequency by the responsiveness of the detector:

$$I = \frac{c\,n\,\epsilon_0}{2} \int_{-\infty}^{\infty} |E_1(\nu, x_1) + E_2(\nu, x_2)|^2\, G(\nu)\, d\nu \tag{42}$$

Different types of gates have been studied leading to the conclusion that the retrieved spectrum only changes in intensity, not affecting the distribution of peaks or the shape of the obtained function. Furthermore, it is possible to nullify this effect by dividing the retrieved spectrum by the gate function obtaining a correct reconstruction.

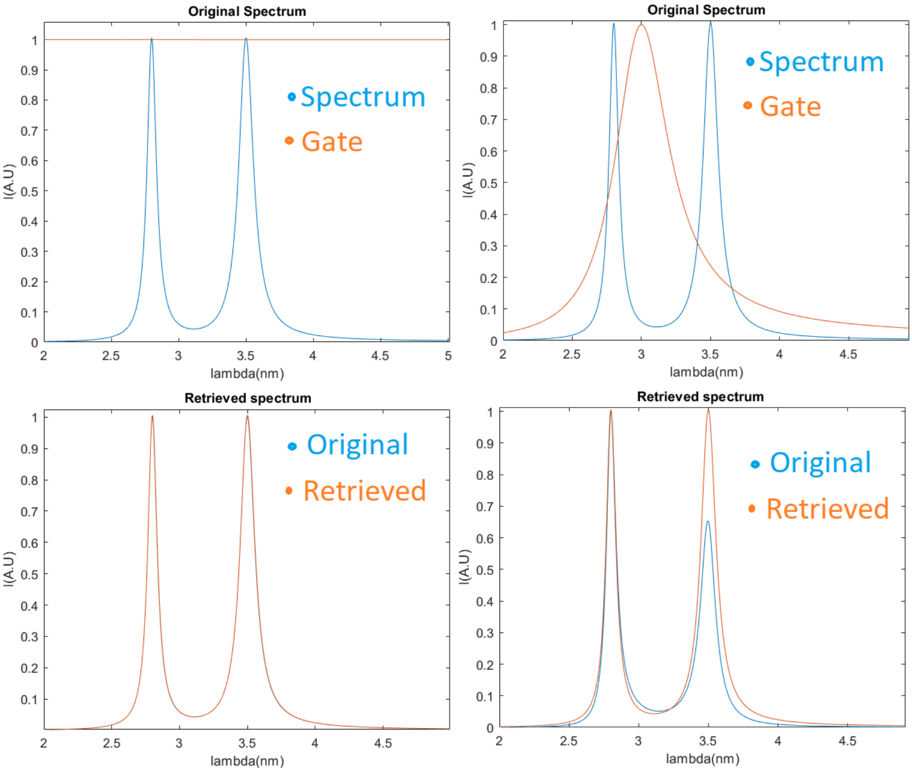

Figure 27. Representation of the gate influence in the retrieved signal. Without any gate (right) and with a gate (left)

How noise affects the signal reconstruction has been studied. For this, a random numerical noise has been simulated in the two key parameters of the device: the position of the motorized mirror and the intensity in the detector.

This study could have been carried out in a much more detailed and precise way [127], expressing divergence values with respect to the original signal, estimating the numerical signal to noise ratios, etc. But our objective is simply to estimate which precision values must be used to obtain an acceptable spectrum [128] since the final noise will be measured experimentally.

As can be seen in **Figure 28**.A if no noise function is introduced, the original and the retrieved signals are exactly the same, in fact, the retrieved cannot be seen as they overlap exactly.

In position some noise filters have been studied, from $n = 0.1\, rng\, dx$ to $n = 1\, rng\, dx$, observing that the maximum value would be close to 50% of dx. **Figure 27.B**

On the other hand, a noise filter relative to the maximum intensity has been created from $n = 0.01\, rng\, I_{max}$ to $n = 0.1\, rng\, I_{max}$, finding that the noise began to be worrisome for values greater than 5%.

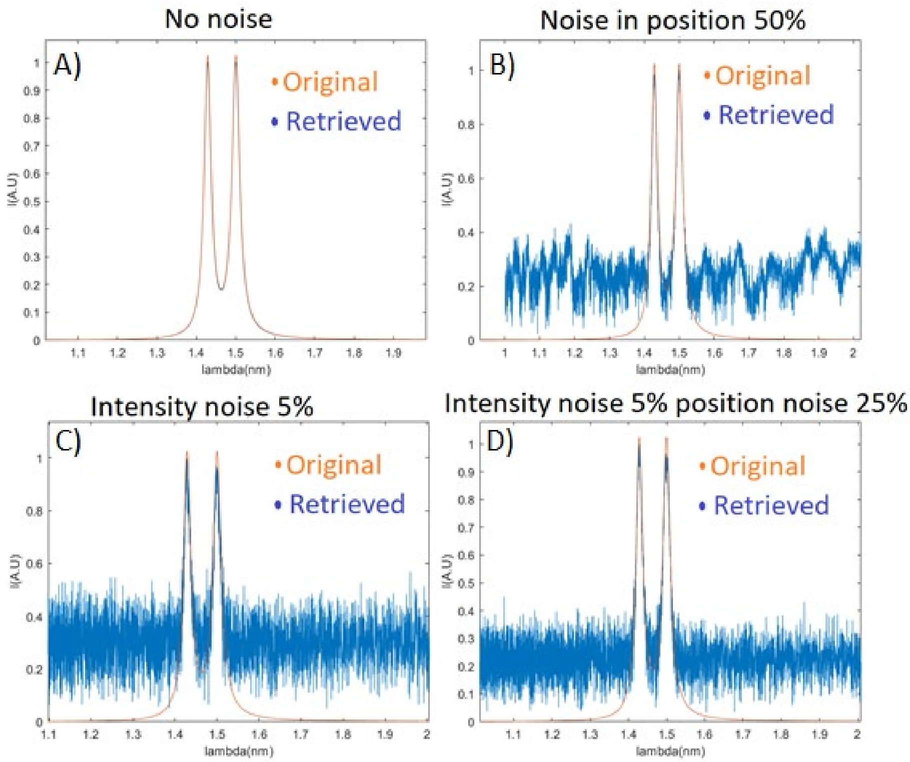

Figure 28. Different types of noise simulated in The FTIR algorithm. A) No noise. B) $\boldsymbol{noise = 0.5\, rng\, dx}$. C) $\boldsymbol{noise = 0.05\, rng\, I_{max}}$. D) $\boldsymbol{noise = 0.05\, rng\, I_{max} + 0.25\, rng\, dx}$

From the theoretical data obtained in the previous section (Figure **25**), an experimental setup has been carried out as shown in Figure **44**. A collimator (F028SMA-3450 Thorlabs), a couple of mirrors (PF10-03-G01 Thorlabs), a beam splitter (BSW511R Thorlabs), a neutral density filter (NDC-50S-1 Thorlabs), high precision linear guides (Zaber X-XY- LSM100A, ANNEX 1), a focusing lens (LA7542-E4 Thorlabs) and a set of detectors has been used. This setup is thought to let us easily change the wavelength range by simply replacing the detector fixed in a protoboard as can be seen in **Figure 29.**

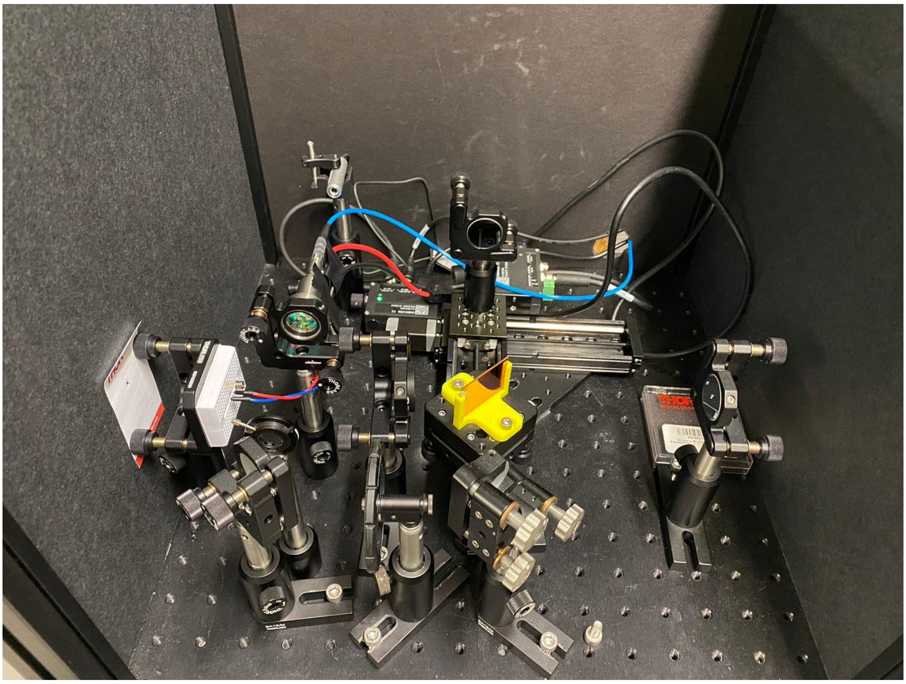

Figure 29. FTIR experimental setup.

For the communication between the linear guides with the mirror and the detector, LabView software has been used together with a DAQ (NI-USB-6212 National instruments, ANNEX I). By setting the speed of the guides, the start and stop position and the measurement frequency, it is possible to measure the interferential pattern needed for the retrieval. Labview also includes a numerical library able to perform a FFT and the Nyquist shanon theorem, directly obtaining the spectrum as can be seen in **Figure 30**.

Both the simulations and the experimental results carried out have resulted in the development of a functional equipment capable of detecting signals in the range from 1um to 6um.

The device has been tested with various light sources, including a quantum cascade laser at $\lambda = 3100nm$ and a diode laser $\lambda = 1500nm$ obtaining satisfactory results.

In the case of the diode, there are some peaks that should not appear at $\lambda = 4500nm$ and $\lambda = 3000nm$, those correspond to the second and third harmonic of the main frequency that appear due to noise and sampling limitations in our system [129]. It is expected that in future versions of this device it will be possible to reduce vibrations in the movement of the linear guides and thereby minimize the appearance of these "ghost peaks".

The main objective for the development of this device is to be able to create a competitive FTIR team. In this case, the equipment developed presents a good resolution using cheap sensors and detectors, which translates into the possibility of marketing this equipment at low cost, being able to take it to various points in the production chain.

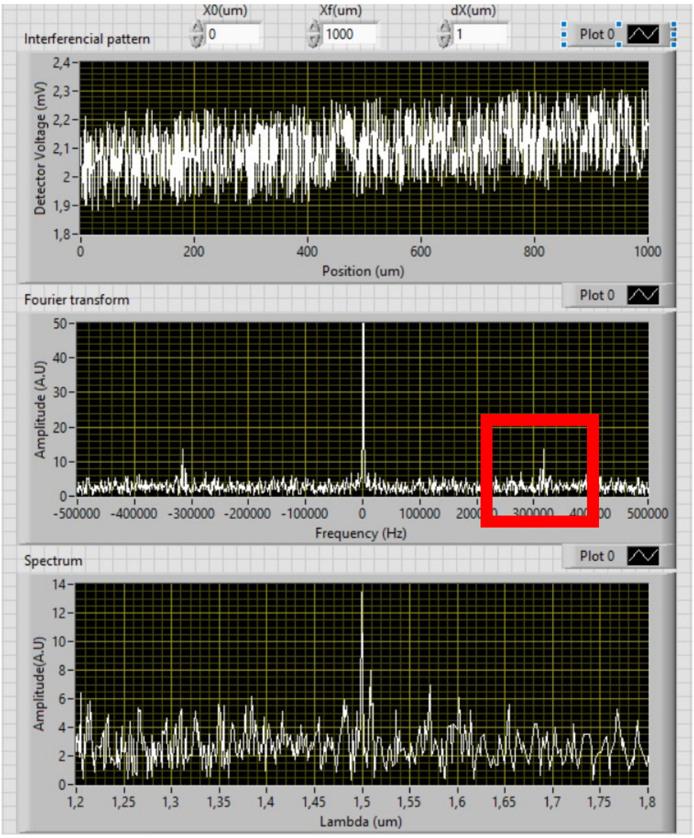
X0(um) 0
Xf(um) 1000
dX(um) 1

Figure 30. Labview front panel of the FTIR homemade software, in this it is possible to control the initial and final travel of the linear guides and the dx between measurements. Also, three plots are shown. The first one is the interferential pattern, the second the FFT of the signal and the third is the retrieved spectrum.

6.2. Industrial 4.0 devices.

This section will show the devices developed in this thesis to provide photonic solutions to industrial problems. The point of view followed has focused on developing innovative systems at low cost, using proprietary software and inexpensive equipment. The reason for this is that industry 4.0. it requires a large number of sensors capable of collecting data at different places in the production chain. Therefore so much emphasis has been placed on cost per sensor; if each one was too expensive, its implementation would be impossible.

For this, due to a confidential information, a brief summary of the device created, as well as the paper where its operation is explained in detail is going to be provided to the reader.

6.2.1 **Structured light profilometer system to measure imperfections in metallic surfaces.**

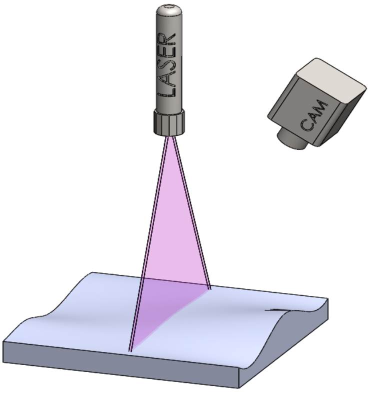

Figure 31. 3D model of the profilometry system developed for this experiment.

A 3D line laser scanner has been developed (**Figure 31**), capable of showing imperfections in metallic surfaces with a minimum with of 50µm and distinguishing what kind of defect presents (scratches, dents, breaks, etc.) as well as their magnitude, in real time at a target movement speed of 5cm/s as can be seen in **Figure 32**. This has been possible by using a structured light system, consisting of a high precision line laser with its wavelength in the near ultraviolet (405nm); and an ultra-fast high-resolution camera [130], **Figure 31**. Also, this device optimizes the performance of this technology in the assembly line, being able to optimize the depth of field and field of view for each situation and substantially reducing the price per unit in comparison with current commercial devices.

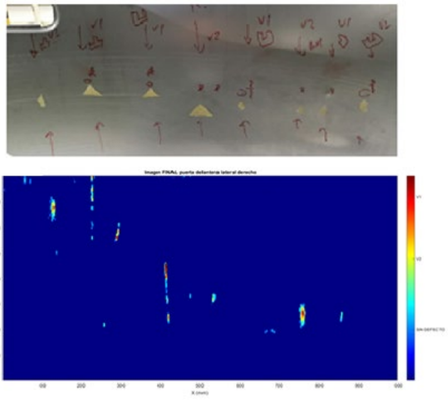

Figure 32. Final images of the profilometry defect detector. The upper image is the metallic surface to study and the bottom one is the retrieved image with a defect magnification algorithm.

6.2.2 **Nonflammable optical encoder.**

A photonic device capable of detecting small variations in the angle of rotation of a shaft (1.25º) by using optical fibers has been developed **Figure** 33.

The device couples a light source (OSL2, Thorlabs, ANNEX I) to an optical fiber using an SMA connection. This is divided into two independent fibers and each end is very close (almost touching) to the binary optical encoder in different sides. The light is reflected in the surface of the detector, which is coated with gold nanoparticles using spattering [131] in order to increase its reflectance [132]. When the light falls on the device depending on its angular position it will interact either with the metal surface or with a hole, reflecting or not the light coming from the fiber. These reflections are collected by the tips of the Y-shaped fibers, which work as an optical circulator [133], making light flow towards the detectors. Thanks to a computer program developed in LabView, the angular position of the encoder can be determined in live.

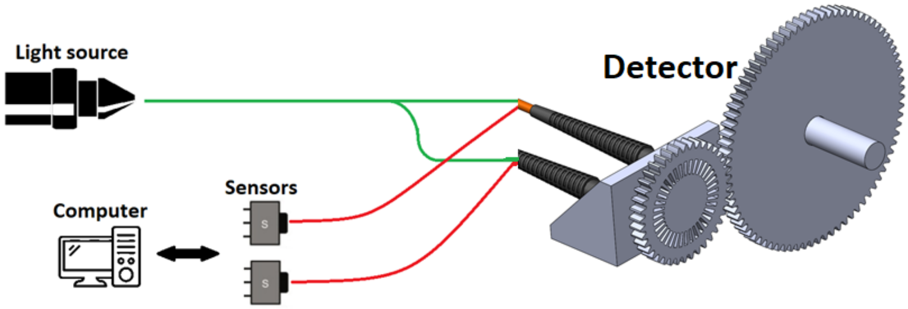

Figure 33. Operation scheme of the optical encoder.

This system does not have any electromechanical element in its work area, being suitable in flammable environments. In addition, thanks to the information transmission properties that optical fibers provide [134], it is possible to place these detectors several kilometers away from the final sensors [135], facilitating their implementation for Industry 4.0.

6.2.3 **Machine vision system for detection of needles and tabs issues in circular knitting machines.**

An artificial vision system has been created in order to bring 4.0 technology to circular knitting machines. The system is capable of detecting the relative position of the needles to each other, as well as the position between the needles and the tabs; being able to accurately determine the wear, breakage, or deformation of these elements. All this has been done thanks to an ultra-fast camera and the use of artificial vision algorithms [136].

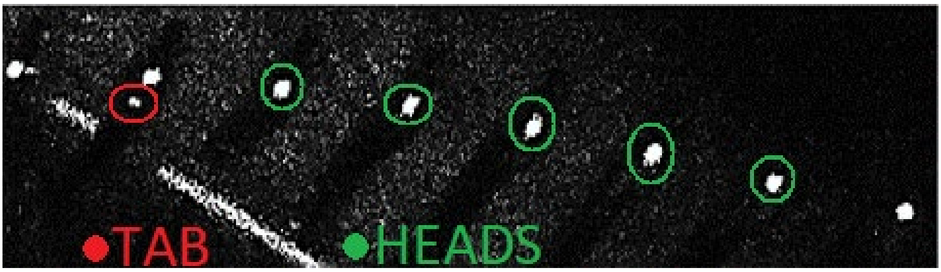

Figure 34. image captured by the ultra-fast camera. In green you can see white points that represent the heads of the pins and in red a smaller white point that are the tabs can be seen.

Seeing the good results obtained in the detection of failures in needles in a knitting machine with a single train of needles arranged vertically it is confirmed that the system can be applied to a double circular knitting machine technology with needle trains in vertical and horizontal arrangement.

6.2.4 Structured light profilometer system to measure wear in metallic molds

A 3D line laser scanner has been developed, capable of showing wearing in metallic molds in real time **Figure 35**. This has been possible by using a structured light system, consisting of a high precision line laser with its wavelength in the near ultraviolet (405nm), an ultra-fast, high-resolution camera and a band pass filer centered in 405nm to eliminate the surrounding light.

To do that, an artificial vision software has been developed, able to detect small imperfections in the shape and in the rugosity of the molds by measuring a series of parameters which are the slope of the grooves **s**, the height of these grooves **h**, the total width of the split part **w** and the surface gloss.

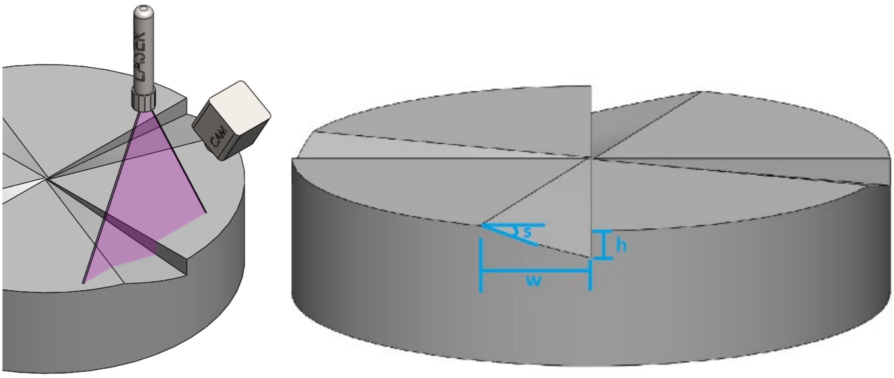

Figure 35. 3D image of the mold (right) and the operation of the device (left).

6.2.5 **Profilometry system applied to the development of a non-touch screen.**

Using a homemade profilometry system consisting of a camera [130] and a line laser with its wavelength in the near ultraviolet (405nm), a position detection system has been made as can be seen in **Figure 36**. Capable of transforming any surface into a non-touch interface. This System captures the position of the object in the camera and by means of a triangulation algorithm it is able to pinpoint with great accuracy where the object is on the desired surface. It is expected to be placed on any surface, thus allowing actioning buttons or communicating with screens without the need to maintain contact with the surface, being essential for the fight against the SARS Coronavirus-2 pandemic.

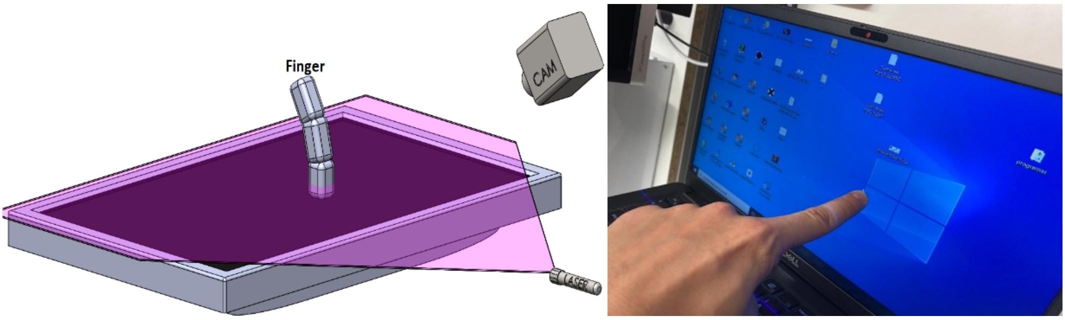

Figure 36. Images of our non-touch screen system. On the left a 3D diagram of its operation and on the right the system working in real time can be seen.

Paper V

Structured light profilometer system to measure imperfections in metallic surfaces.

(In progress to be submitted)

VICTOR LLAMAS,[1,2] JOSEP MARIA SERRES,[1,2] MAGDALENA AGUILÓ,[1] FRANCESC DÍAZ,[1] AND XAVIER MATEOS[1]

[1]Física i Cristal·lografia de Materials i Nanomaterials (FiCMA-FiCNA)-EMaS, Dept. Química Física i Inòrganica, Universitat Rovira i Virgili (URV), Campus Sescelades, 43007 Tarragona, Spain
[2]Eurecat, Centre Tecnològic de Catalunya, Unitat Advanced Manufacturing Systems (AMS), Campus Sescelades, 43007 Tarragona, Spain

Abstract

A 3D line laser scanner has been developed, capable of showing imperfections in metallic surfaces with a minimum with of 50μm and distinguishing what kind of defect presents (scratches, dents, breaks, etc.) as well as their magnitude, in real time at a target movement speed of 5cm/s, fat enough for its colocation in an assembly line. This has been possible by using a structured light system, consisting of a high precision line laser with its wavelength in the near ultraviolet (405nm); and an ultra-fast high-resolution camera[1].

Introduction

In the last 20 years due to rising raw power of computers [2] and the emergence of new sensorics technologies and manufacturing, a new industrial revolution, industry 4.0, is rising where machines and sensors that communicate with each other to allow the optimization of industrial processes[3].

One of the most interesting 4.0 technologies for the industry is computer vision[4]. This is based on using image systems [5] together with mathematical algorithms to synthesize the information captured by a camera and transform it into instructions easily understood by a control system. In this case, a device has been developed with the aim of detecting deformations in metal sheets in a production line, thus being able to discard defective units for repair.

Operation principle.

The system comprises a line laser and a camera, both separated from each other by a certain distance and angle. The laser emits a linear beam that is scattered on the testing surface and captured with the camera, that receives a curved line (**Figure 1**) With a mathematical software, this curve can be related with the depth of the test surface at each point and by sweeping the device or the object (Depending on the setup), a topographic map can be generated.

Since a laser scanner consists of optical sensors and mechanical moving parts, various constraints must be satisfied when measuring a certain point[6-7]. The goal of this section is to ideate an optimal scan plan that satisfies the following major constraints in our experiment. The operating diagram in the ZX and ZY planes can be seen in **Figure 1**.

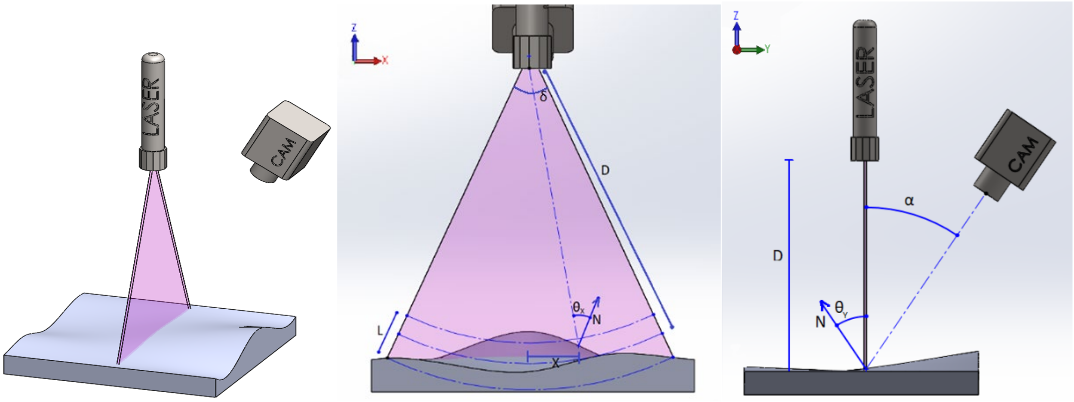

Figure 1. General (left), front (center) and lateral (right) view of a perfilometry system.

Field Of View (FOV): the measured point should be located within the length of the laser line. Otherwise, the system would be unable to measure the contour of the surfaces not exposed to the laser.

$$\delta_{laser} > \delta_{camera} \qquad (1)$$

Where δ_{laser} and δ_{camera} are the field angles for the camera and the laser, respectively.

Depth Of Field (DOF): the measured point should be within a specified range of distance from the laser source and the camera. If the laser or the camera are not correctly focused on the surface the measurement would not be correct and the error increases drastically.

For the laser, the surface should be inside the Rayleigh zone:

$$D - z_R < Z < D + z_r \tag{2}$$

Being z_R The Rayleigh distance and D the distance between the laser and the waist.

The restriction for the camera is related with its view zone and focusing depth, in this case it the main effect is the second. It can be expressed as:

$$D - \frac{L}{2} < Z < D + \frac{L}{2} \tag{3}$$

Being L the focal depth.

For commercial line lasers the Rayleigh zone is much longer than the camera focusing depth. So it is possible to consider the equation (2) negligible and only focus on the equation (3) for our estimations.

View Angle (VA) and occlusion: Another important parameter for a good measurement is the angle between the surface and the camera. If this surpass $\pm 90º$ there must be a part of the surface covered by another part of the object, so the restriction for this parameter is:

$$-90º < \theta_x - tg\left(\frac{X}{D}\right) < 90º \tag{4}$$

Being θ_x the angle between the surface and the vertical line and X the lateral position of the point it is measured.

$$-90º < \theta_y + \alpha < 90º \tag{5}$$

Being θ_y the angle between the vertical line and the normal vector to the surface and α the angle between the camera and the laser. In our case mostly all the defects are much smaller than this parameter.

Lateral Resolution (LR): The distance between one contour and the next should be expressed as:

$$\Delta Y = \frac{\vec{v}}{FPS} \tag{6}$$

Being $\vec{v}$ the relative speed of the system; and FPS are the frames per second of the camera. This formula works equally if the device or the sample moves. For our purposes the sample is moving at a constant velocity $\vec{v}$.

This parameter is extremely relevant for our experiments since a $50\mu m$ resolution between contours was necessary. This demanding precision could only be achieved either by strongly reducing the movement speed of the sample or by greatly increasing the FPS.

Experimental development

In a first approach to the project, some commercial devices that could be useful for this purpose has been studied [8][9], finding several ones based on this operation principle, however, their DOF is limited, with the impossibility of moving it away or bringing it closer according to our needs; so, it was difficult to locate them in a real test area. Due to this, it was decided to make our own device in the laboratory. Our device consists of:

- A laser (CPS405, Thorlabs) in the near ultraviolet wavelengths (405nm) with a cylindrical lens(LJ1695RM, Thorlabs) adapted to it, to generate a linear beam; in addition, a linear shutter is mounted to narrow the beam and make it as fine as possible.

- A high resolution (2K) monochrome camera (Sony XCG-CP51) with the Global Shutter CMOS image capture method. This operating mode allows us to collect all the information at the same time without having any lag shutter, which substantially reduces aberrations in our measurements (**Figure 2**)

These elements have been arranged at 20cm horizontally, 3 cm vertically and with a 35º relative angle between them; allowing us to detect profiles of 10cm wide at 50cm distance.

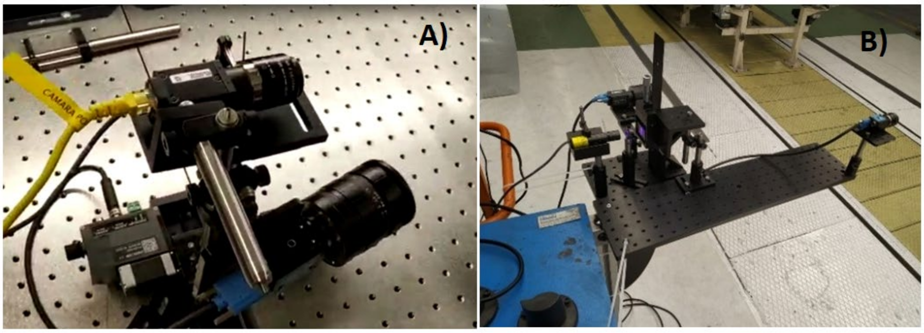

Figure 2. Laser line scan. A) lab prototype. B) Final device.

As explained above, a curved line is observed in the camera, where the height of each illuminated pixel can be correlated with the depth of the test surface at that point. For retrieving this, a numerical treatment; capable of obtaining a depth profile from each image, must be developed.

A graphical interface in LabView was created. In this, the height profile of the surface under study can be observed in real time. The software takes an image and retrieve its height profile before taking the next one, meanwhile two XY motors moves the camera and the laser. This means that all the numerical transformations must be performed between two consecutive images, so the frame rate dropped drastically, less than 30FPS. This software is useful for lab studies since it creates a 3D hyper dense mesh in real time. On the other hand, the low framerate of this method and our high precision limits for the LR $\Delta Y \leq 50\mu m$ correspond to a camera movement speed of $\vec{v} = 1mm/s$ which could not be fast enough for commercial uses.

This needing of increasing the framerate make us work in a hybrid software. In this, a video is first taken using the standard software from the ultra-fast camera IC capture, and then numerically processed in Matlab to obtain the beam profile. In addition, to minimize noise, it is necessary an algorithm that compares the spatial profile with a reference and an image correlation algorithm. With this, it is possible to increase the FPS up to 1000.

Results

A study was carried out with different pieces in the laboratory to obtain preliminary results, comparing the profile obtained in the camera with profiles from a confocal microscope, belonging to the FICMA group, verifying that there is a correlation between both.Figure 3.

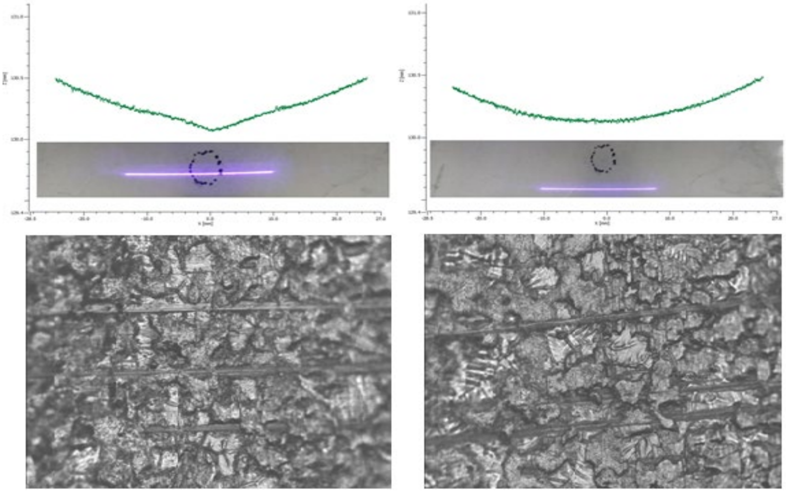

Figure 3. Spatial profile of a sheet metal retrieved with our system (top images) and with a confocal microscope (bottom).

Once the system was verified, different dents were made in both directions (from inside to outside and from outside to inside) and scratches were made on the surface of two small, easy-to-handle pieces **Figure 4.A**. Using the real-time system together with a high-precision stepper motor, it was possible to detect the imperfections correctly, as can be seen in **Figure 4.B**. The system also measures the curvature of the test surface, so a numerical filter was added to flatten the background and remark only the defects as can be seen in **Figure 4.C**. and **Figure 4.D.**

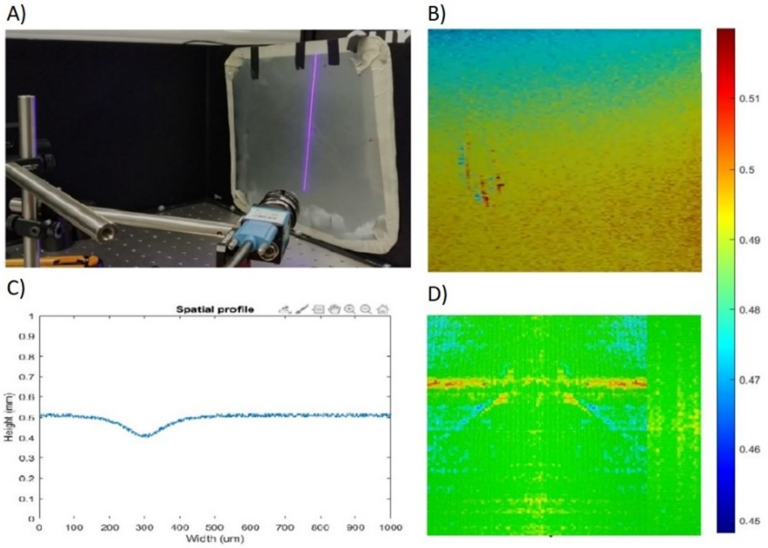

Figure 5. Lab studies with a damaged polished aluminum plate. A) Esperimental setup. B) Raw data acquired by the system. C) Height profile after filtering. D) Surface profile after filtering.

As explained in the previous section, the real time system needs a target movement speed of $\vec{v} = 1mm/s$, not commonly suitable for a real working situation. For this reason, the hybrid method was tested. For it a big, polished aluminum plate was damaged, generating scratches, dents, and cracks (**Figure 6.A.**) and is moved perpendicularly to the camera at a movement speed $\vec{v} = 5cm/s$, a commonly used speed in an assembly line.

The **Figure 5.B** corresponds to the data obtained from the surface in a continuous colormap. The scale was calibrated according to the standard typology (v1=big defect, v2=small defect). Dark blue corresponds to the background (without defects) and the bigger the defect the reddish. The scale is arbitrary, and this color was chosen to highlight the defects. In the figure nearly all the defects are visible, but in order to reduce the noise and make the map clear for an operator two more surface maps are made.

In **Figure 5.C** a customer inspired color mapping was made with only three colors, the blue one represents the background, the yellow represents the v2 (small defects) and v1 (big defects) are plotted in red. With this colormap the imperfections are clearer, but it is possible to ignore the smallest defects.

To improve the imperfection detection, **Figure 5.D** shows the image with a defect magnification algorithm in which each small defect is spatially enlarged. In this image, most of the defects present in **Figure 5.B** can be seen much more easily. All deformations, scratches and dents (from internal to external and vice versa) are detected with high precision.

Conclusions.

To carry out this project, a photonic device capable of detecting defects in metal surfaces using structured light has been implemented in a satisfactory way. This has been possible thanks to the employment of an ultra-fast camera and a UV line laser which can provide a spatial resolution inferior to $50\mu m$. This device optimizes the performance of this technology in the assembly line, being able to optimize the DOF and FOV for each situation; and substantially reduces the price per unit in comparison with current commercial devices.

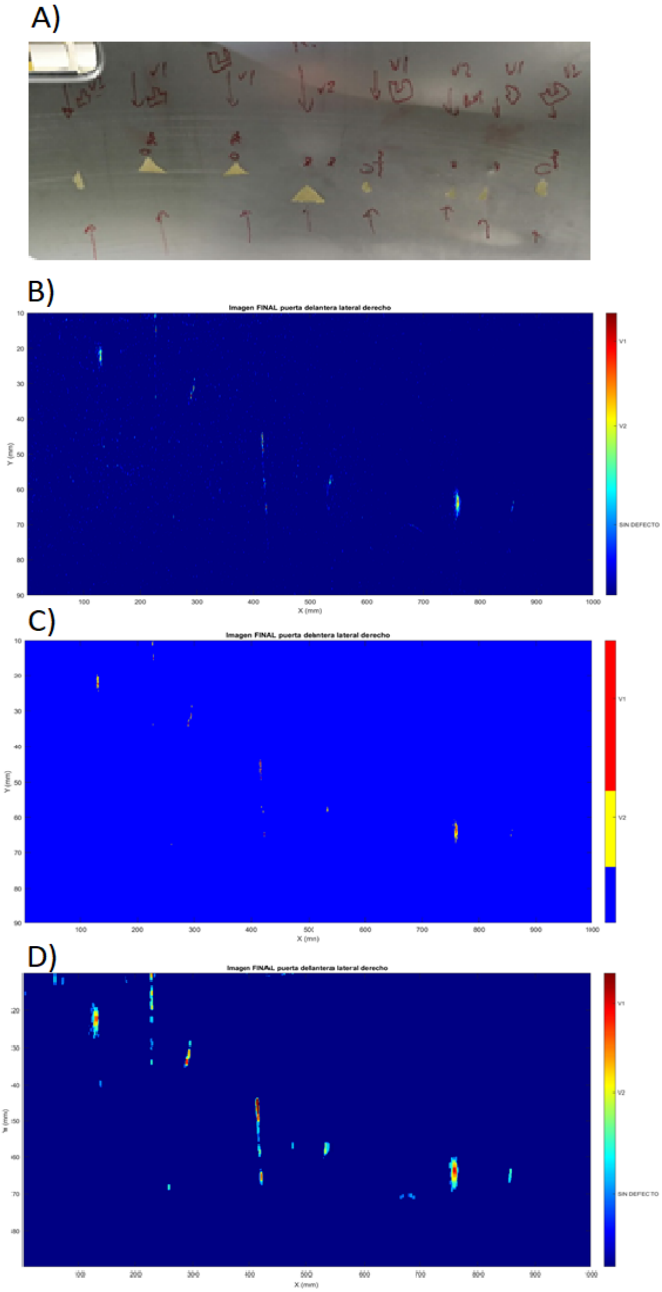

Figure 6. Final results of the metal sheet in the assembly line. A) Picture of the metal sheet. B) Raw map of the metal sheet. C) Imperfection mapping with three colors. D) Profile numerically modified to amplify defects.

References

[1] S. Son, H. Park, and K. H. Lee, “Automated laser scanning system for reverse engineering and inspection,” Int. J. Mach. Tools Manuf., vol. 42, no. 8, pp. 889–897, Jun. 2002, doi: 10.1016/S0890-6955(02)00030-5.

[2] C. Toumey, “Less is Moore,” Nat. Nanotechnol. 2016 111, vol. 11, no. 1, pp. 2–3, Jan. 2016, doi: 10.1038/nnano.2015.318.

[3] P. Ghelfi et al., “Microwave photonics technologies for 5G and industry 4.0,” IET Conf. Publ., vol. 2019, no. CP765, 2019, doi: 10.1049/CP.2019.0840.

[4] T. Brosnan and D. W. Sun, “Improving quality inspection of food products by computer vision––a review,” J. Food Eng., vol. 61, no. 1, pp. 3–16, Jan. 2004, doi: 10.1016/S0260-8774(03)00183-3.

[5] T. Skauli and J. Farrell, “A collection of hyperspectral images for imaging systems research,” https://doi.org/10.1117/12.2007097, vol. 8660, pp. 89–95, Feb. 2013, doi: 10.1117/12.2007097.

[6] E. Zussman, H. Schuler, and G. Seliger, “Analysis of the geometrical features detectability constraints for laser-scanner sensor planning,” Int. J. Adv. Manuf. Technol. 1994 91, vol. 9, no. 1, pp. 56–64, Jan. 1994, doi: 10.1007/BF01792868.

[7] F. Xi and C. Shu, “CAD-based path planning for 3-D line laser scanning,” Comput. Des., vol. 31, no. 7, pp. 473–479, Jun. 1999, doi: 10.1016/S0010-4485(99)00044-5.

[8] B. R. Barbero and E. S. Ureta, “Comparative study of different digitization techniques and their accuracy,” Comput. Des., vol. 43, no. 2, pp. 188–206, Feb. 2011, doi: 10.1016/J.CAD.2010.11.005.

[9] O. Semeniuta, S. Dransfeld, and P. Falkman, “Vision-based robotic system for picking and inspection of small automotive components,” IEEE Int. Conf. Autom. Sci. Eng., vol. 2016-November, pp. 549–554, Nov. 2016, doi: 10.1109/COASE.2016.7743452.

Annex: Code

```
clear all
%Open the ref video
vid=VideoReader('puertabien.avi');

%Define the number of frames
nframes=vid.NumberOfFrames;
frame1=read(vid,1);
a=frame1(:,:,1);

% Define matrix dimensions
nx=length(a(:,1));
ny=length(a(1,:));

% Algorithm to obtain the profile from each frame
mat=zeros(nframes,ny);
for k=1:nframes;
    frame=read(vid,k);
    vidframe=frame(:,:,1);
    for i=1:ny
        vector=vidframe(:,i);
        xm=find(vector==max(vector));
       vec2(i)=sum(xm)/length(xm);
    end
    mat(k,:)=vec2;
end

%Save matrix
mat=rot90(mat);
save('ref.mat','mat');

%Open test video
vid=VideoReader('puertarota.avi');

%Define the number of frames in the video test
nframes=vid.NumberOfFrames;
frame1=read(vid,1);
a=frame1(:,:,1);

% define matrix dimensions
nx=length(a(:,1));
ny=length(a(1,:));

%  Algorithm to obtain the profile from each frame
mat=zeros(nframes,ny);
for k=1:nframes;
    frame=read(vid,k);
    vidframe=frame(:,:,1);
    for i=1:ny
```

```
        vector=vidframe(:,i);
        xm=find(vector==max(vector));
        vec2(i)=sum(xm)/length(xm);
    end
    mat(k,:)=vec2;
end
med=rot90(mat);

% Open the ref file
open ref.mat;
ref=ans.mat;
clear ans

%filter 1
fx=exp(-(-5:1:5).^2/8);
a=sum(fx);
for i=1:length(ref(1,:))
    ref(:,i)=filter(fx,a,ref(:,i));
end
for i=1:length(ref(:,1))
    ref(i,:)=filter(fx,a,ref(i,:));
end
for i=1:length(med(1,:))
    med(:,i)=filter(fx,a,med(:,i));
end
for i=1:length(med(:,1))
    med(i,:)=filter(fx,a,med(i,:));
end

%Filter 2
    med=medfilt2(med,[5 5]);
    ref=medfilt2(ref,[5 5]);

%Filter 3
for  i=1:length(ref(1,:))
    ref(:,i)=sgolayfilt(ref(:,i),3,11);
end
for i=1:length(ref(:,1))
     ref(i,:)=sgolayfilt(ref(i,:),3,11);
end
for i=1:length(med(1,:))
     med(:,i)=sgolayfilt(med(:,i),3,11);
end
for i=1:length(med(:,1))
     med(i,:)=sgolayfilt(med(i,:),3,11);
end

%y1-yd1 test image, y2-yd2 ref image
y1=med(round(length(med(:,1))/2),:);
y2=ref(round(length(ref(:,1))/2),:);
yd1=zeros(1,length(med(1,:)));
```

```
yd2=zeros(1,length(ref(1,:)));
for i=2: length(med(1,:))-1
    yd1(i)=(y1(i-1)-y1(i+1)).^2;
end
for i=2: length(ref(1,:))-1
    yd2(i)=(y2(i-1)-y2(i+1)).^2;
end

 %x1 test image, x2 ref image
x1=1:1:length(med(1,:));
x2=1:1:length(ref(1,:));

% Find the maximum of the derivative to select second gate
% Number of frames backdoor approx 4600frames at 1000 fps camera.
% corresponds to 92 cm door with spaces of 200um.
% Number of frames backdoor approx 6900frames at 1500 fps camera.
% corresponds to 92 cm door with 133um spaces.
% 0.7 is a value to limit the matrix and not leave the door
% rear. TAKE MIDDLE FRONT DOOR MEASUREMENTS.

n1=find(yd2(1,1:round(length(ref(1,:))*0.5))==max(yd2(1,1:round(l
ength(ref(1,:))*0.5))));
n2=find(yd2(1,1:round(length(med(1,:))*0.5))==max(yd2(1,1:round(l
ength(med(1,:))*0.5))));

nframes=20000;
ref2=zeros(length(ref(:,1)),nframes);
med2=zeros(length(med(:,1)),nframes);

% We cut only rear door with 1500 images of delay
for i=1:nframes
    ref2(:,i)=ref(:,i+n2+1500);
    med2(:,i)=med(:,i+n1+1500);
end
med2=med2/max(max(med2));
ref2=ref2/max(max(ref2));
sigma = 100;
med2=imflatfield(med2,sigma);
ref2=imflatfield(ref2,sigma);

% Signal treatment
final=med2./ref2;

%Axis
xi=(1:nframes)/nframes*1000;
yi=(1:length(med2(:,1)))/length(med2(:,1))*100;
sigma = 100;
final = imflatfield(final,sigma);
final=abs(final-mean(final));
final=medfilt2(final,[5 5]);
```

```
% Blue map
map = [0 0 1; 0 0 1; 0 0 1; 1 1 0; 1 1 0; 1 1 0; 1 1 0; 1 0 0; 1
0 0; 1 0 0; 1 0 0; 1 0 0; 1 0 0; 1 0 0; 1 0 0];

%Green map
map = [0 1 0;0 1 0;0 1 0; 1 1 0; 1 1 0; 1 1 0; 1 1 0; 1 0 0; 1 0
0; 1 0 0; 1 0 0; 1 0 0; 1 0 0; 1 0 0; 1 0 0];

%Final image
figure(1)
imagesc(xi,yi,fliplr(final))
colorbar('Ticks',[0.0055, 0.015, 0.025], 'TickLabels', {'SIN
DEFECTO', 'V2', 'V1'})
colormap(map)
shading interp
axis([xi(1) xi(nframes) yi(round(length(final(:,1))*0.1))
yi(round(length(final(:,1))*0.9))    ])
caxis([0.006 0.03])
title('Imagen FINAL puerta delantera lateral derecho')
xlabel('X (mm)')
ylabel('Y (mm)')

% Treated final image
figure(2)
imagesc(xi,yi,fliplr(final))
colorbar('Ticks',[0.01, 0.017, 0.023], 'TickLabels', {'SIN
DEFECTO', 'V2', 'V1'})
colormap(jet(512))
shading interp
axis([xi(1) xi(nframes) yi(round(length(final(:,1))*0.1))
yi(round(length(final(:,1))*0.9))    ])
caxis([0.005 0.025])
title('Imagen FINAL puerta delantera lateral derecho')
xlabel('X (mm)')
ylabel('Y (mm)')

% Variable deffinition for the deeffect remark algorithm
n=10;
v2=0.009;
v1=0.03;
tol=50;
xx=round(length(final(1,:))/n-0.49);
yy=round(length(final(:,1)));
mat1=zeros(yy,xx);

% Noise filter
for i=1:xx
    mat1(:,i)=max(final(:,1+n*(i-1):n+n*(i-1))')';
end
```

```
% Eleimination of the background

mat2=zeros(yy,xx);
for i=1:xx
    for j=1:yy
        if mat1(j,i)>v2
            mat2(j,i)=mat1(j,i);
        end
    end
end

% Take the maximum value of a 3x3 area around each point,
magnifying defects
n2=3;
for i=n2+1:xx-n2
    for j=n2+1:yy-n2
        mat3(j,i)=max(max(mat2(j-n2:j+n2,i-n2:i+n2)));
    end
end

%  We make a filter to eliminate small noise peaks that may
remain
n3=10;
for i=n3+1:xx-n3-3
    for j=n3+1:yy-n3-3
        m1=mat3(j-n3:j+n3,i-n3:i+n3);
        if sum(sum(m1))<10*n3*v2
            mat3(j,i)=0;
        end
    end
end

% Axis
xi2=(1:length(mat3(1,:)))/length(mat3(1,:))*1000;
yi2=(1:length(mat3(:,1)))/length(mat3(:,1))*100;

% Plot with filter
figure(3)

imagesc(xi2,yi2,fliplr(mat3))
colorbar
colorbar('Ticks',[0.01, 0.017, 0.023], 'TickLabels', {'SIN
DEFECTO', 'V2', 'V1'})

colormap(jet)
shading interp

caxis([0.005 0.025])
axis([xi2(1) xi2(length(mat3(1,:)))
yi2(round(length(mat3(:,1))*0.1))
yi2(round(length(mat3(:,1))*0.9))    ])
```

```
title('Imagen FINAL puerta delantera lateral derecho')
xlabel('X (mm)')
ylabel('Y (mm)')
```

Paper VI

Profilometry system applied to the development of a non-touch screen.

(In progress to be submitted)

VICTOR LLAMAS,[1,2] JOSEP MARIA SERRES,[1,2] MAGDALENA AGUILÓ,[1] FRANCESC DÍAZ,[1] AND XAVIER MATEOS[1]

[1]*Física i Cristal·lografia de Materials i Nanomaterials (FiCMA-FiCNA)-EMaS, Dept. Química Física i Inòrganica, Universitat Rovira i Virgili (URV), Campus Sescelades, 43007 Tarragona, Spain*

[2]*Eurecat, Centre Tecnològic de Catalunya, Unitat Advanced Manufacturing Systems (AMS), Campus Sescelades, 43007 Tarragona, Spain*

Abstract

Using a homemade profilometry system consisting of a camera [1], a band pass filter centered at 405nm and a line laser with its wavelength in the near ultraviolet (405nm), a position detection system capable of track the XY position of an object in a surface has been implemented. This system is expected to be able to be place on any surface, thus allowing actioning buttons or communicating with screens without the need to maintain contact with the surface, being essential for the fight against the SARS Coronavirus-2 pandemic.

Introduction

Infectious diseases are constant challenges to public health around the world. Recent cases of pneumonia of unknown cause in Wuhan, China, have led to the discovery of a new type of Coronavirus (2019-nCoV), which are RNA enveloped viruses, commonly found in humans, other mammals, and birds, capable of cause respiratory, enteric, liver and neurological diseases [2]. To prevent its spread, new prevention measures are essential [3], such as the use of masks, hand washing, the use of hydroalcoholic gel and avoiding sources of contagion [4]. In this paper, a system has been developed to avoid maintaining contact with surfaces by using a homemade profilometry system, consisting of a camera, a band pass filter and a UV line laser.

Operation principle.

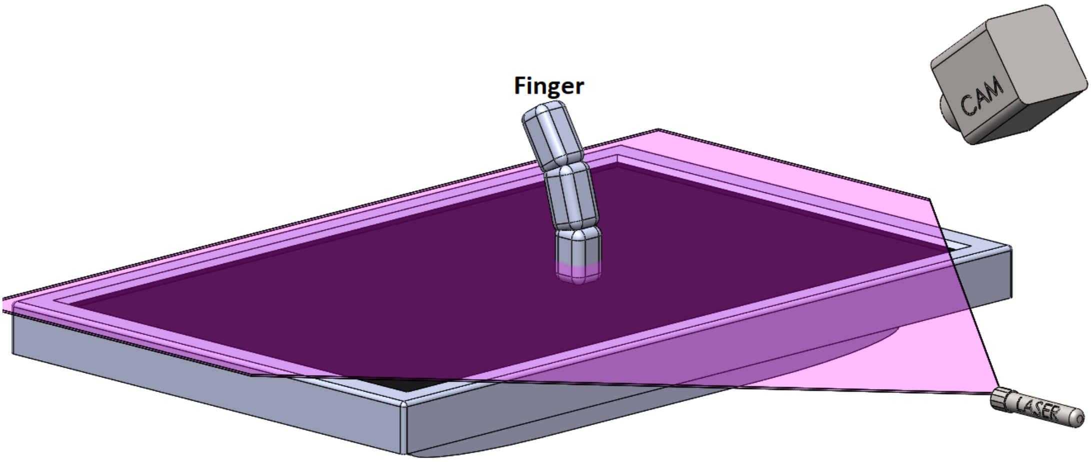

Figure 1. 3d model of the profilometry system. In the model can be seen how the camera records the contact zone between a finger and the laser.

The system comprises a line laser, a band pass filter and a camera, both separated from each other by a certain distance and angle. The laser emits a linear beam parallel to the surface at a certain height (around 3-4cm) and the camera is focused in the area we want to detect, with the band pass filter in front of it to suppress all the surrounding light. When some object is in the working area it intercepts the laser beam and the camera records a curved line as can be seen in **Figure 2**. After that, by the use of a computational algorithm the system determines its position in the surface.

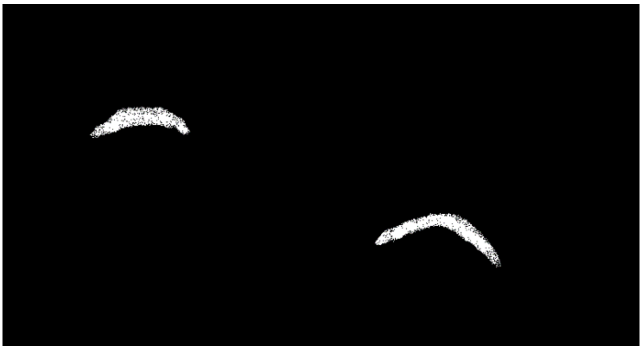

Figure 2. Camera binary image of two fingers interacting with the laser beam.

Optical parameters.

In order to obtain a correct measurement with a profilometer system some conditions must be satisfied [5-6]. The goal of this section is to ideate an optimal configuration that optimizes the space and the resources of the camera and the software. The operating diagram in the ZX and ZY planes can be seen in **Figure 3**.

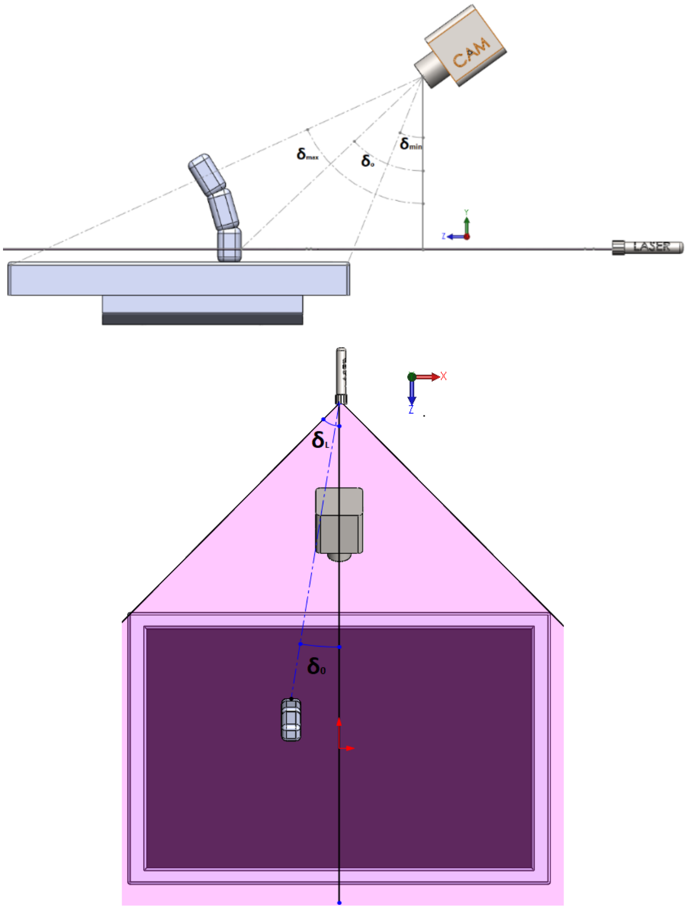

Figure 3. General (left), front (center) and lateral (right) view of a profilometry system.

Field Of View (FOV): the measured point must be within the aperture of the camera. Otherwise, the information would not be collected. In addition, the laser must have sufficient widespread angle to encompass the whole surface, otherwise there is not going to be an interruption of the laser from the object, thus the camera cannot capture the position of the object. For the YZ plane the object must meet the following relationship

$$\delta_{min} < \delta_0 < \delta_{max} \tag{1}$$

Where δ_{min} is the angle where the camera begins to collect data, δ_{max} is the angle where the camera finishes capturing data and δ_0 is the angle where the object is with respect to the camera and the vertical. For the XZ plane, a relationship must also be fulfilled, determined by:

$$\delta_0 < \delta_L \tag{2}$$

Where δ_0 is the angle of the object with respect to the laser and δ_L is the opening angle of the laser.

Depth Of Field (DOF): the measured point should be within a specified range of distance from the laser source and the camera. If the laser or the camera are not correctly focused on the surface the measurement would not be correct and the error increases drastically.

For the laser, the surface should be inside the Rayleigh zone:

$$D_L - z_R < Z < D_L + z_r \tag{3}$$

Being z_R The Rayleigh distance and D_L the distance between the laser and the waist.

The restriction for the camera is related with its view zone and focusing depth, in this case it the main effect is the second. It can be expressed as:

$$D_C - \frac{L}{2} < Z < D_C + \frac{L}{2} \tag{4}$$

Being L the focal depth and D_c the focus distance of the camera.

For commercial line lasers the Rayleigh zone is much longer than the camera focusing depth. So, it is possible to consider the equation (3) negligible and only focus on the equation (4) for our estimations.

Triangulation.

As explained in the previous section, from a complex numerical treatment, the position of the object is recorded in the camera as a curved line (**Figure 2**) and transformed in at a pair of points in the camera X_c, Y_c. These have to be correlated with the actual position of the object on the screen. This treatment is carried out assuming that each point on the screen X_S, Y_S corresponds to a point in the camera that can be expressed as:

$$\begin{aligned} X_s &= c_{X1} + c_{X2}X_c + c_{X3}Y_c \\ Y_s &= c_{Y1} + c_{Y2}X_c + c_3Y_c \end{aligned} \qquad (5)$$

Where X_S and Y_S are the positions of the object on the screen and c_{Xi} and c_{Yi} are the characteristic triangulation constants. A fitting of the type $X = c_1 + c_2 X_c + c_3 Y_c + c_4 X_c^2 + c_5 Y_c^2$ was also tested, reaching the conclusion that quadratic values were not necessary because the deviation was negligible and that including them increase computing time.

In order to obtain the best possible triangulation, we want the values of these constants to be the most suitable for all points. For this, 15 points have been obtained by correlating the values in the camera X_C and Y_C with the values on the screen X_S and Y_S as can be seen in **Figure 4**.

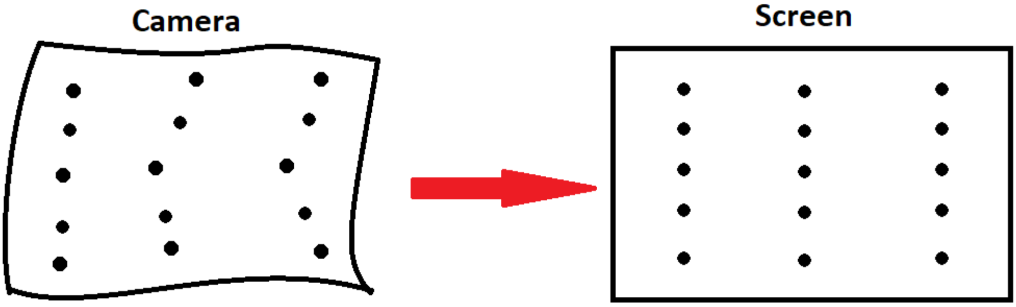

Figure 4. Schematic image of how the triangulation algorithm used modifies the space.

This algorithm is based on matrix equations for solving systems of equations of the $X * c = Y$, each variable being a matrix of the type:

$$X = \begin{pmatrix} 1 & X_{21} & X_{31} \\ 1 & X_{22} & X_{23} \\ 1 & X_{32} & X_{33} \\ \cdots & \cdots & \cdots \\ 1 & X_{n2} & X_{n3} \end{pmatrix} \qquad c = \begin{pmatrix} c_1 \\ c_2 \\ c_3 \end{pmatrix} \qquad Y = \begin{pmatrix} Y_1 \\ Y_2 \\ Y_3 \\ \cdots \\ Y_n \end{pmatrix} \tag{6}$$

If we want to obtain the values of c that meet the minimum deviation, we must start from the Sum of the Square Error (SSE) equation:

$$SSE = \sum_{i=1}^{n} (c_i - \bar{c})^2 = (Y - X * c)^T * (Y - X * c) \tag{7}$$

The minimum deviation will be obtained when the derivative of the $\frac{\partial SSE}{\partial c} = 0$. Operating on (7) we obtain that the triangulation constants with the minimum deviation from the formula:

$$c = (X^T * X)^{-1} * X^T * Y \tag{8}$$

Experimental setup

To carry out the detection system, a 405mn laser (CPS405, Thorlabs) was used together with a cylindrical lens (AYL108-A, Thorlabs) that transforms the collimated beam into a line which is parallel to the screen and 3-4cm above it. In addition, an ultra-fast camera (Sony XCG-CP51) with a band pass filter (FB405-10, Thorlabs) has been used for beam detection. Both are located at 50cm to the screen, separated from each other by 15 cm with a relative angle of $\theta \cong 15º$. With this configuration it is possible to place all the components together, being able to make a compact unit.

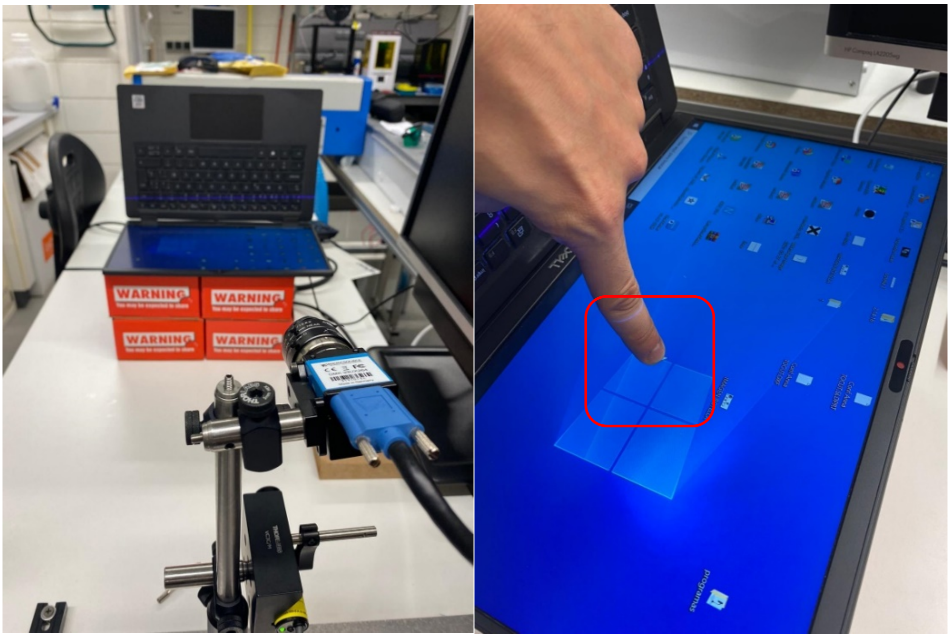

Figure 5. Experimental setup. The red rectangle in the right image indicates the point where the laser hits the finger. In the image the finger is situated ~1 cm above of the screen without touching it. The laser line in the right image is practillaly unperceptible by the bare eye, thanks to the lack of an UV filter in the camera used for this picture can be seen.

As can be seen in **Figure 5** the beam hits the object to be detected and by means of triangulation algorithms the exact position of this can be determined. In this experimental setup, the screen has been placed horizontally for reasons of comfort when handling the system, however there is no type of limitation when it comes to placing it vertically.

The equipment used in the experiment has a high cost, however, neither the laser nor the specifications of this camera are limiting factors when it comes to reducing costs, being able to use a generic line laser and a standard 720p monochromatic webcam, drastically reducing the cost of the device. The band pass filter is suited in the camera in order to eliminate all the background light and improve drastically the robustness of this device.

Results and conclusions

Using a video camera, a band pass filter and a line laser it has been possible to develop a system capable of detecting the position of an object in the laser plane, allowing a device (in this case a screen) to be controlled in real time without the need to maintain physical contact with this. Our device has an excellent response time, as well as great precision thanks to the calibration and triangulation algorithms used. Thanks to the low cost of the materials used, it is expected to market this device globally, being able to be placed in any public facility, helping to prevent the population from having direct contact with these surfaces and thereby reducing the spread of SARS coronavirus 2.

Similar devices have already been developed by other research groups [7]. In this case, our device uses a laser beam outside the visible range and a band-pass filter. This completely eliminates ambient light and preventing the light, from for example a screen, from being recognized by the camera, which generate measurement errors. On the other hand, when placing the laser 3-4cm above the surface, with the aim of not touching the surface, it is not trivial to perform an automatic triangulation, so it has been decided that the best solution is that the triangulation be manual at the beginning of use. In addition, using a monochrome camera lowers costs and reduces the computing time and resources required to run the computer program by using 1/3 of the pixels that an RGB camera uses.

References

[1] S. Son, H. Park, and K. H. Lee, “Automated laser scanning system for reverse engineering and inspection,” Int. J. Mach. Tools Manuf., vol. 42, no. 8, pp. 889–897, Jun. 2002, doi: 10.1016/S0890-6955(02)00030-5.

[2] T. Singhal, “A Review of Coronavirus Disease-2019 (COVID-19),” Indian J. Pediatr. 2020 874, vol. 87, no. 4, pp. 281–286, Mar. 2020, doi: 10.1007/S12098-020-03263-6.

[3] S. P. Adhikari et al., “Epidemiology, causes, clinical manifestation and diagnosis, prevention and control of coronavirus disease (COVID-19) during the early outbreak period: a scoping review,” Infect. Dis. Poverty 2020 91, vol. 9, no. 1, pp. 1–12, Mar. 2020, doi: 10.1186/S40249-020-00646-X.

[4] G. Bhardwaj, W. Bank, T. Esch, M. E. Soppelsa, and S. Wahba, Cities, crowding, and the coronavirus: Predicting contagion risk hotspots 1. .

[5] E. Zussman, H. Schuler, and G. Seliger, “Analysis of the geometrical features

detectability constraints for laser-scanner sensor planning," Int. J. Adv. Manuf. Technol. 1994 91, vol. 9, no. 1, pp. 56–64, Jan. 1994, doi: 10.1007/BF01792868.

[6] F. Xi and C. Shu, "CAD-based path planning for 3-D line laser scanning," Comput. Des., vol. 31, no. 7, pp. 473–479, Jun. 1999, doi: 10.1016/S0010-4485(99)00044-5.

[7] J. R. Liang, K. C. Lin, H. C. Chen, and W. J. Wang, "Turn any display into a touch screen using infrared optical technique," IEEE Access, vol. 6, pp. 13033–13040, Mar. 2018, doi: 10.1109/ACCESS.2018.2812756.

Main program

```
clear all
close all
%%
import java.awt.Robot
import java.awt.event.*
robot = java.awt.Robot(); % Open the Java robot to move the mouse
% Reed the video and set some parameters
vid = videoinput('winvideo', 2, 'Y800_2448x2048');
src = getselectedsource(vid);
vid.FramesPerTrigger = 1;
src.GainMode = 'manual';

src.Brightness = 240;
src.Exposure = -8;
src.Sharpness = 14;
vid.ROIPosition = [732 0 445 2041];

imagen=rot90(getsnapshot(vid));

%preview(vid);

%% constants from the interpolation program

ax=-0.89758;
ay=0.004027;
bx=0.375351578;
by=-3.8358;
cx=1683;
cy=1144;

%% Starts code

N=50;
nx=length(imagen(:,1));
ny=length(imagen(1,:));
```

```
vec2=zeros(1,ny);
matriz=zeros(2,N);
contador=0;
Xantes=0;
Yantes=0;
R=50;
for k=1: N
    imagen=rot90(getsnapshot(vid)); % Get a snapsot and rotate it

    for i=1: ny
        vector=imagen(:,i); % Take a line from the image
        if max(vector)>200 % If in this line there is some data
            ym=find(vector==max(vector));
            vec2(i)=sum(ym)/length(ym);
        else
            vec2(i)=0; %If there is no data gives a zero vector
        end
    end
    if sum(vec2)~=0   % If in the image there are some data
        Y=max(vec2);
        c1=find(vec2==max(vec2));
        X=sum(c1)/length(c1);
        %Here we use the triangulation algorythm to retrieve the
position
        %in the camera to the position in the screen.
        XP=round(ax*X+bx*Y+cx);
        YP=round(ay*X+by*Y+cy);
        robot.mouseMove( XP,YP); % Set mouse position
        robot.mouseMove( XP,YP); % set mouse position
        robot.mouseMove( XP,YP); % set mouse position
        % I put it 3 time because sometimes fails

        % Clicking algorithm
        if R>sqrt((XP-Xantes)^2+(YP-Yantes)^2) % if the finger
keeps some
            %time in the same position a click is made
            contador=contador+1;
            if contador >3
                robot.mousePress(InputEvent.BUTTON1_MASK);
                robot.mouseRelease(InputEvent.BUTTON1_MASK);
                contador=0;
            end
        end
        matriz(:,k)=[X; Y]; %Path saving for tests
        %figure(2)
        %plot(vec2)
        Xantes=XP;
        Yantes=YP;
    else
        contador=0;
    end
```

```
    %pause(0.1);
    matcont(k)=contador;
end
%stoppreview(vid);
close all
%%
figure (3)
plot(matriz(1,:),matriz(2,:))
```

Constants retrieval main program

```
clear all
close all

A=xlsread('calibracion.xlsx');
XP=A(:,1);
YP=A(:,2);
XC=A(:,3);
YC=A(:,4);
X=ones(17,3);
X(:,2)=XC;
X(:,3)=YC;
constantesX = calibracion(X,XP);
constantesY = calibracion(X,YP);
```

Constants retrieval subroutine

```
function [constantes] = calibracion(X,Y)

if length(X(:,1))<length(X(:,1))
    X=X';
end

if length(Y(:,1))<length(Y(:,1))
    Y=Y';
end
constantes=inv(X'*X)*X'*Y;

end
```

Paper VII

Machine vision system for detection of needles and tabs issues in circular knitting machines.

(In progress to be submitted)

VICTOR LLAMAS,[1,2] JOSEP MARIA SERRES,[1,2] MAGDALENA AGUILÓ,[1] FRANCESC DÍAZ,[1] AND XAVIER MATEOS[1]

[1]Física i Cristal·lografia de Materials i Nanomaterials (FiCMA-FiCNA)-EMaS, Dept. Química Física i Inòrganica, Universitat Rovira i Virgili (URV), Campus Sescelades, 43007 Tarragona, Spain
[2]Eurecat, Centre Tecnològic de Catalunya, Unitat Advanced Manufacturing Systems (AMS), Campus Sescelades, 43007 Tarragona, Spain

Abstract

An artificial vision system has been created in order to bring 4.0 technology to circular knitting machines. The system is capable of detecting the relative position of the needles to each other, as well as the position between the needles and the tabs; being able to accurately determine the wear, breakage, or deformation of these elements. All this has been done thanks to an ultra-fast camera and the use of artificial vision algorithms [1].

Introduction

Machine vision (MV) [2] is the technology and methods used to provide imaging-based automatic inspection and analysis for such applications as automatic inspection, process control, and robot guidance, usually in industry [3]. In this approach, we create a MV system capable of measuring the torsion or break of heads and tabs on a circular knitting machine [4] without requiring any specialist control.

After an exhaustive research [5], monochrome vision technology with image saturation due to high light intensity was concluded to be the most suitable technology for implementation [6], by employing an ultra-fast camera with a homemade machine vision system. In this case, the TIS-DMK-33UX264 camera from **The Imaging Source** has been used.

With these systems it is possible to carry out measurements while the machine is working, being able to find errors in the needles and thus avoiding manufacturing defective fabric, increasing production and reducing costs [7-8].

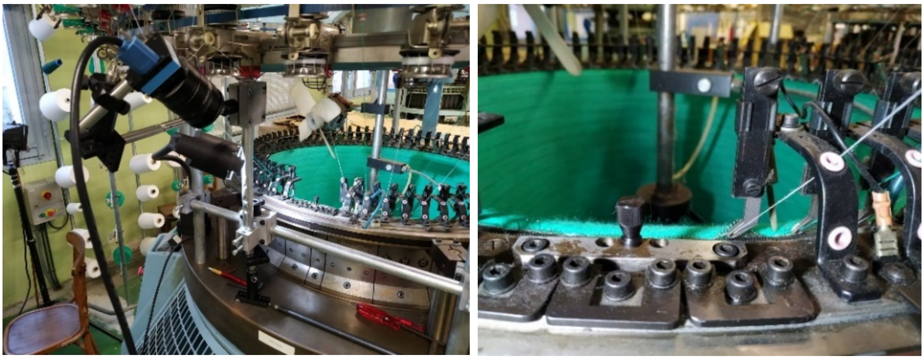

Figure 37. Experimental setup of an ultra-fast camera and a halogen lamp (left) focused on a part of a knitting machine (right) to detect the position of the needles.

Experimental setup.

The artificial vision system was installed as shown in Figure 1. The ultra-fast camera is focused in an area where all the needles are aligned, and the tab of the last needle contracted can be recorded (Figure 2). In addition, as can be seen in Figure 1, it was found that the ambient light was not always the same and is not always incident at the same angle, therefore, it was concluded that a halogen lamp located right next to the camera was necessary, in order to provide an always constant brightness in the same direction, allowing a homogeneity in the measurement throughout the detection process.

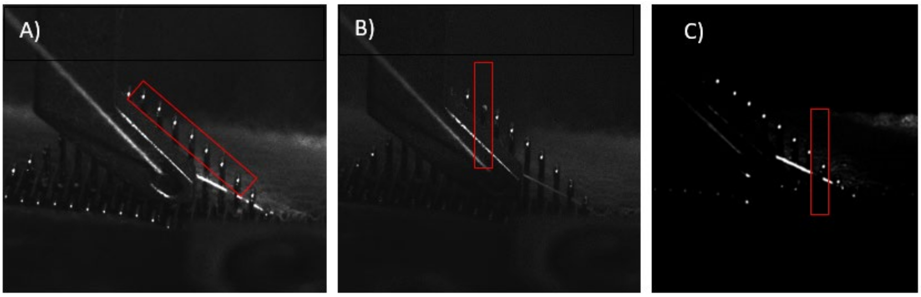

Figure 38. Image needle (A) needles train without defects, (B) head failure (C) tab failure.

In Figure 2.A. correct distribution of tabs without any error can be observed. The interest area is framed within the red rectangle. The largest points are the heads and the smallest point just below the lower right needle is the tab. In fig. B) an error can be seen in the head of the needle due to wear. In Figure 2.C. the absence of the tab just below the head can be observed.

The knitting machine rotates at 10 revolutions per minute, with an approximate number of 1800 needles a frame rate around 1500fps was necessary. To obtain this, settings need to be optimized. The camera was tilted 35º and the interest area was reduced to 400x80 (400 in X and 80 in Y).

With all these optimizations, the system could be accurately recorded. all the needles are seen when the knitting machine is at normal rotation speed. In Figure **3** the points with the largest radius are the heads of the needles and the small one below the second point from the left is the tab. In this case all the needles are correct, and the tab is in the correct position.

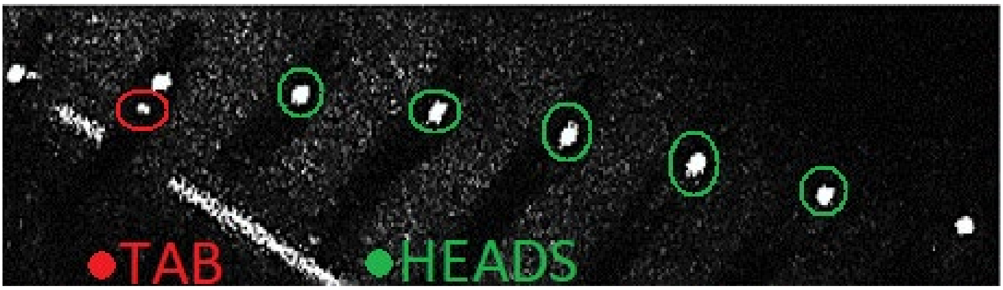

Figure 39. Interest zone with the needle heads and the tabs.

Code development

The Matlab code developed is based on a main program and several subroutines that must be explained in more detail. All the code can be found in annex.

From the **main** program several parameters can be modified in order to achieve a correct detection such as tolerances, distance between heads, detection heads, among others. In addition, there is the option of opening a saved video or recording the video through the **Camera** subroutine.

In the recognition stage, the program analyzes the video and keeps the frames in which the needles are in the ideal position to be measured, then these frames are sent to two subroutines: **tabs** and **heads**.

Both subroutines receive a frame and perform an object recognition algorithm. This is based on a subroutine that converts the image intensity scale ranging from 0 to 2^8 to a binary bitmap, then rotates the image, defines the position of each object, eliminates the elements with an area smaller than that indicated and, finally, by using a skeletonization algorithm, the central position of each object is defined. Based on these common transformations, each subroutine executes a series of commands: the subroutine **heads** obtain the lateral distance between each head of the needles and the subroutine **tabs** get the relative position between the head and the tab.

With these constants, another program called **errors** has been made, in this one by establishing tolerances we are able to determine if a head or tab is wrong, providing an error in the head or in the tab, marking the nail number and the frame in which can be observed.

Results

Using artificial vision, it has been possible to accurately measure the distance between the needles, being able to determine if any of them were bent laterally or broken. Furthermore, it has been possible to calculate the angle between the tabs and the needles, being able to also determine if they are bent or broken. The algorithm carried out allows the analysis of all these data from the capture of frames at high speed with their interpretation of the luminous points, Figure 3.

These data are presented in a table showing the needle number, the frame in which it was detected, the average distance from the next needle, the angle between the head and the tab and three control parameters. Those ones define whether there is an incorrect needle or reed, as well as a general error that does not distinguish the type of defect and has the function of indicating that the needle must be changed, regardless of the type of defect. Table 1 shows only the needles that present some type of defect. A total of 16 failures have been detected out of the total of the 112 needles analyzed. A visual check was made, and it was observed that there was indeed the defect that the program endorsed in each needle. Several correct needles were also checked to ensure that the tolerances were within the correct values. All the data obtained have a tolerance that can be adjusted by the user and can be more or less strict with the deformations of the needles.

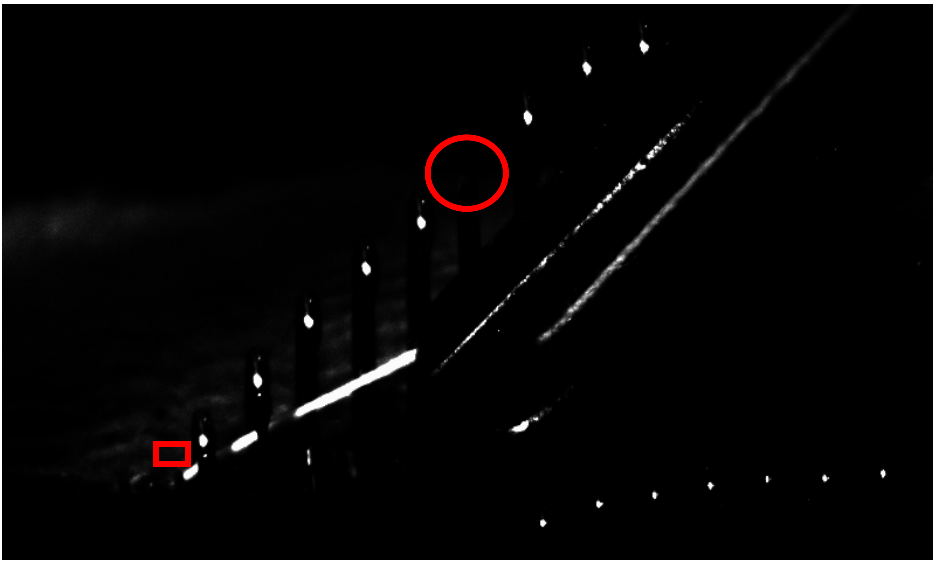

Figure 40. Image of the knitting machine with a broken needle. The computer program detects it perfectly. In red-square detection of the tab. In red-circle needle failure

Needle	N frame	Average distance	Tab angle	error head	error tab	error
5	128	47,75	21,80	1	0	1
21	561	43,50	23,96	1	0	1
61	1794	43,75	3,18	1	0	1
67	2234	45,75	66,80	0	1	1
69	2599	45,75	45,00	0	1	1
81	3209	42,25	26,57	1	0	1
84	3304	0,00	26,57	1	0	1
85	3509	0,00	29,05	1	0	1
86	3514	0,00	2,86	1	0	1

90	3636	45,50	85,24	0	1	1
93	3675	45,25	64,54	0	1	1
94	3680	45,75	65,56	0	1	1
95	3685	45,50	65,77	0	1	1
98	3700	45,50	65,56	0	1	1
102	3833	45,50	66,80	0	1	1
103	3865	47,00	75,53	0	1	1

Table 3. Summary of defects found in the analyzed needles.

4. Conclusions

An artificial vision system has been developed on circular knitting machines in order to determine defects in the needles during normal operation for continuous detection and monitoring. The device allows to equip the machine with a detection system aligned towards Industry 4.0 and thus allowing cost savings, greener system, and early detection of possible failures in the manufactured fabric. Some of those failures are caused by bent needles, broken heads, or misaligned or damaged tabs.

The effectiveness of this system has been demonstrated, being able to establish the position between the heads of a circular knitting machine, as well as the relative angle between heads and tabs in a continuous way and at normal machine rotation speed, being a scalable process for its machine implementation.

Seeing the good results obtained in the detection of failures in needles in a knitting machine with a single train of needles arranged vertically it is confirmed that the system can be applied to a double circular knitting machine technology with needle trains in vertical and horizontal arrangement.

To achieve its implementation, certain improvements must be made in the system, such as using two cameras (one for each rail) and optimize the imaging system to reduce the signal-to-noise ratio. In addition, the use of external triggering is proposed to uniquely determine the number of each needle and the use of Machine learning to reduce computation time.

References

[1] M. Baygin, M. Karakose, A. Sarimaden, and E. Akin, “Machine vision based defect detection approach using image processing,” IDAP 2017 - Int. Artif. Intell. Data Process. Symp., Oct. 2017, doi: 10.1109/IDAP.2017.8090292.

[2] D. Vernon, Machine vision : automated visual inspection and robot vision. Prentice Hall, 1991.

[3] P. S. Khude and S. S. Pawar, “Object detection, tracking and counting using enhanced BMA on static background videos,” 2013 IEEE Int. Conf. Comput. Intell. Comput. Res. IEEE ICCIC 2013, 2013, doi: 10.1109/ICCIC.2013.6724236.

[4] S. Nashat, A. Abdullah, and M. Z. Abdullah, “Machine vision for crack inspection of biscuits featuring pyramid detection scheme,” J. Food Eng., vol. 120, no. 1, pp. 233–247, Jan. 2014, doi: 10.1016/J.JFOODENG.2013.08.006.

[5] J. Molleda, R. Usamentiaga, D. F. García, F. G. Bulnes, and L. Ema, “Shape measurement of steel strips using a laser-based three-dimensional reconstruction technique,” IEEE Trans. Ind. Appl., vol. 47, no. 4, pp. 1536–1544, Jul. 2011, doi: 10.1109/TIA.2011.2155019.

[6] K. K. Patel, A. Kar, and M. A. Khan, “Monochrome computer vision for detecting common external defects of mango,” J. Food Sci. Technol. 2021, pp. 1–8, Jan. 2021, doi: 10.1007/S13197-020-04939-9.

[7] M. Baygin and M. Karakose, “A new image stitching approach for resolution enhancement in camera arrays,” ELECO 2015 - 9th Int. Conf. Electr. Electron. Eng., pp. 1186–1190, Jan. 2016, doi: 10.1109/ELECO.2015.7394569.

[8] P. Thammasorn, S. Boonchu, and A. Kawewong, “Real-time method for counting unseen stacked objects in mobile,” 2013 IEEE Int. Conf. Image Process. ICIP 2013 - Proc., pp. 4103–4107, 2013, doi: 10.1109/ICIP.2013.6738845.

Annex: Code

Main program (1/5)

```
clear all
close all
tic
%% Define the important camera parameters
P=[0 400 0 80]; % P[Xmin Xmax Ymin Ymax]
%674 279 163 510
nframes=10000; % number of frames
exposicion=-11; % Esposure time in seconds <1/fps
ganancia=34; % Gain
fps=110;
path='C:\Users\llama\Desktop\videotest2.avi';
 %% Video variables
 limit = 200;                  %if pixel value<limit -> black
pixel
error_relativo = 0.2;         %Relative error
distancia_fija = 45;          %Distance between needles
%% Needle head variable
Pc=[135 395 10 60];  %Pc[Xmin Xmax Ymin Ymax]
alfac =0;           %camera rotation angle
area_minc = 5;        %Minimum area to take account
%% tabs variables
Pl=[75 100 15 40];  %Pl[Xmin Xmax Ymin Ymax]
alfal = 0;             %camera rotation angle
area_minl = 2;         % Minimum area to take account
 %% Taking video

%[vid]=camara(P,nframes,exposicion,ganancia,fps,path);
 vid = VideoReader('finalmotor.avi');
%% Take each frame
%distcabezas=zeros(5, nframes);
%distlenguetas=zeros(1,nframes);
 Naguja=1;
  %Frame selection algorythm
Pbien=[40 80 15 30]; %xmin xmax ymin ymax
i = 1;
 V1=zeros(72,4);
V2=zeros(72,2);
control=zeros(72,1);
 while  (i < nframes)
frame = read(vid,i);                %Read frame
imag = frame(:,:,1);
    if
(sum(sum(imag(Pbien(1):Pbien(2),Pbien(3):Pbien(4))))>limit*40)
            [distcabezas]=cabezas(imag,limit,Pc,alfac,area_minc);

[distlenguetas]=lenguetas(imag,limit,Pl,alfal,area_minl);
            for j=1: length(distcabezas)
```

```
                V1(Naguja,j)=distcabezas(j);
                        end
            V2(Naguja,:)=distlenguetas;
        Naguja=Naguja+1;
        control(Naguja)=i;
        i=i+3; %When a frame is correct jump frames to avoid
repetition.
    else
        i=i+1;
    end
end
toc
save ('distcabezas.txt', 'V1', '-ascii')
save ('distlenguetas.txt', 'V2', '-ascii')
save ('control.txt', 'control', '-ascii')
```

Camera subroutine (2/5)

```
function
[videofinal]=camara(P,nframes,exposicion,ganancia,fps,path)
x0=P(1);
y0=P(3);
nx=P(2)-P(1);
ny=P(4)-P(3);
vid = videoinput('winvideo', 2, 'Y800_2048x1536'); %open vid
therminal
src = getselectedsource(vid);
vid.LoggingMode = 'disk'; % sabe in HDD.
diskLogger = VideoWriter(path, 'Uncompressed AVI');
vid.DiskLogger = diskLogger;
% TriggerRepeat is zero based and is always one
% less than the number of triggers.
vid.TriggerRepeat = 0;
vid.FramesPerTrigger = nframes;
src.Gain = ganancia;
src.Exposure = exposicion;
src.FrameRate = fps;
diskLogger.FrameRate = fps;
vid.ROIPosition = [x0 y0 nx ny];
start(vid);
videofinal=vid;
diskLogger =
VideoWriter('C:\Users\llama\Desktop\Arcadi\tests.avi',
'Uncompressed AVI');
open(diskLogger);
data = getdata(vid, vid.FramesAvailable);
numFrames = size(data, 4);
for ii = 1:numFrames
```

```
    writeVideo(diskLogger, data(:,:,:,ii));
end
close(diskLogger);
end
```

(3/5)

Head position subroutine

```
function[distances]=cabezas(imag,limit,P,alfa,area_min)
%imag: matrix NXxNY from 0 to 255
%limit: int from 0 to 255. Necessary for the filter
%P[Xmin Xmax Ymin Ymax] zoom zone in pixels
%alfa: camera rotation angle
%area_min: (int). Delete all the objects smaller than this size
%% chose the interest área and aply a black-white filter
% both of them are made at the same time to optimize time
imag_cab = imrotate(imag, alfa);
imag_cab_2 = zeros (P(4)-P(3), P(2)-P(1));
for a = 1:length(imag_cab_2(:,1))
    for b = 1:length(imag_cab_2(1,:))
        imag_cab_2(a,b) = imag_cab(a+P(3),b+P(1));
        if (imag_cab_2(a,b) < limit)
            imag_cab_2(a,b) = 0;
        else
            imag_cab_2(a,b) = 250;
        end
    end
end
%% Head tratement
 imag_cab_2 = imrotate(imag_cab_2, -1*alfa);
%Rotation
imag_cab_2 = bwareaopen(imag_cab_2, area_min);
imag_cab_2 = bwskel(imag_cab_2);
%skeletization
[imag_cab_3,n] = bwlabel(imag_cab_2);
%object ID
columna = 1;
distances = zeros(1,n-1);
puntos = zeros(1,n);
index = 1;
if (n > 1)      %If there is more than one element to compare
distances
    while (columna <= length(imag_cab_2(1,:)) &&
~(ismember(1,imag_cab_2(:,columna))))
        columna = columna + 1;
    end
    %check distancies
    while (columna <= length(imag_cab_2(1,:)) && (index < n))
```

```
        while (columna <= length(imag_cab_2(1,:)) &&
(ismember(1,imag_cab_2(:,columna))))
            columna = columna + 1;
        end
        puntos(1,index) = columna;
        while (columna <= length(imag_cab_2(1,:)) &&
~(ismember(1,imag_cab_2(:,columna))))
            columna = columna + 1;
            distances(1,index) = distances(1,index) + 1;
        end
        index = index + 1;
    end
end
end
```

(4/5)

Tabs detection subroutine

```
function[distances]=lenguetas(imag,limit,P,alfa,area_min)
%imag: matrix NXxNY from 0 to 255
%limit: int from 0 to 255. Necessary for the filter
%P[Xmin Xmax Ymin Ymax] zoom zone in pixels
%alfa: camera rotation angle
%area_min: (int). Delete all the objects smaller than this size
%% chose the interest área and aply a black-white filter
% both of them are made at the same time to optimize time
imag_cab = imrotate(imag, alfa);
imag_cab_2 = zeros (P(4)-P(3), P(2)-P(1));
for a = 1:length(imag_cab_2(:,1))
    for b = 1:length(imag_cab_2(1,:))
        imag_cab_2(a,b) = imag_cab(a+P(3),b+P(1));
        if (imag_cab_2(a,b) < limit)
            imag_cab_2(a,b) = 0;
        else
            imag_cab_2(a,b) = 250;
        end
    end
end
%% Tabs treatment
imag_cab_2 = imrotate(imag_cab_2, -1*alfa);
%Rotation
imag_cab_2 = bwareaopen(imag_cab_2, area_min);
%delete min area
imag_cab_2 = bwskel(imag_cab_2);                            %
skeletization
[imag_cab_3,n] = bwlabel(imag_cab_2);
%Object ID
%%--> Z
```

```
columna = 1;
distances_Z = zeros(1,n-1);
puntos_Z = zeros(1,n);
index = 1;
while (columna <= length(imag_cab_3(:,1)) && (
(~(ismember(1,imag_cab_3(columna,:)))) &&
(~(ismember(2,imag_cab_3(columna,:)))) ))
      columna = columna + 1;
end
if (columna <= length(imag_cab_3(:,1)) &&
ismember(1,imag_cab_3(columna,:)))     %if first N1
    distances_Z(1,1) = columna;
    columna = 1;
    while (columna <= length(imag_cab_3(:,1)) &&
((~(ismember(2,imag_cab_3(columna,:))))))
      columna = columna + 1;
    end
    distances_Z(2,1) = columna;
elseif (columna <= length(imag_cab_3(:,1)) &&
ismember(2,imag_cab_3(columna,:))) %If first N2
    distances_Z(2,1) = columna;
    columna = 1;
    while (columna <= length(imag_cab_3(:,1)) &&
((~(ismember(1,imag_cab_3(columna,:))))))
      columna = columna + 1;
    end
    distances_Z(1,1) = columna;
else
    distances_Z(2,1) = 0;
    distances_Z(1,1) = 0;
end
%%--> Y
fila = 1;
distances_Y = zeros(1,n-1);
puntos_Y = zeros(1,n);
index = 1;
imag_cab_3_90 = rot90(imag_cab_3);
while (fila <= length(imag_cab_3_90(:,1)) && (
(~(ismember(1,imag_cab_3_90(fila,:)))) &&
(~(ismember(2,imag_cab_3_90(fila,:)))) ))
      fila = fila + 1;
end
if (fila <= length(imag_cab_3_90(:,1)) &&
ismember(1,imag_cab_3_90(fila,:)))     %if first N1
    distances_Y(1,1) = fila;
    fila = 1;
    while (fila <= length(imag_cab_3_90(:,1)) &&
((~(ismember(2,imag_cab_3_90(fila,:))))))
      fila = fila + 1;
    end
    distances_Y(2,1) = fila;
```

```
elseif (fila <= length(imag_cab_3_90(:,1)) &&
ismember(2,imag_cab_3_90(fila,:)))     %If first N2
    distances_Y(2,1) = fila;
    fila = 1;
    while (fila <= length(imag_cab_3_90(:,1)) &&
((~(ismember(1,imag_cab_3_90(fila,:))))))
      fila = fila + 1;
    end
    distances_Y(1,1) = fila;
else
    distances_Y(1,1) = 0;
    distances_Y(2,1) = 0;
end
distances=[abs(distances_Y(2,1)- distances_Y(1,1))
abs(distances_Z(2,1)- distances_Z(1,1))];
end
```

Error detection program (5/5)

```
clear all
close all
V1=importdata('distcabezas.txt');
V2=importdata('distlenguetas.txt');
control=importdata('control.txt');
control(1) = [];
N=length(V2)-5;
j=1;
V3=zeros(1,N);
angulo=zeros(1,N);
final=zeros(N,7);
for i=1:N
    angulo(j)=atand(V2(i,1)./V2(i,2));
    if (V1(i,4)~=0) %If there is any head broken
        V3(j)=(V1(i,4)+V1(i+1,3)+V1(i+2,2)+V1(i+3,1))/4;
    else      % if there is a broken head
        if(V1(i+1,4)~=0)
           V3(j-1)=(V1(i-1,3)+V1(i,2)+V1(i+1,1))/3;
           V3(j)=(V1(i,3)+V1(i+1,2)+V1(i+3,1))/3;
           j=j+1; %          final(j,1)=j;
           V3(j)=(V1(i+1,3)+V1(i+2,2)+V1(i+3,1))/3;
        else
            V3(j)=0;
        end
    end
    final(j,1)=j;
    final(j,2)=control(i);
    j=j+1;
end
```

```
final(:,3)=V3;
final(:,4)=angulo;
%% Error vector
for i=1:N-1
    cabeza=0;
    lengueta=0;
    noterr=0;
    if (final(i,3)>47) && (final(i+1,3)<44)
        cabeza=1;
    end
    if (final(i+1,3)>47) && (final(i,3)<44)
        cabeza=1;
    end
    if(final(i,3)==0)
        cabeza=1;
    end
    final(i,5)=cabeza;
    if final(i,4)>40
        lengueta=1;
    end
    final(i,6)=lengueta;
    if (final(i,5)==0 && final(i,6)==0)
        noterr=1;
    end
    final(i,7)=1-noterr;
end
```

Paper VIII

Nonflammable optical encoder.

(In progress to be submitted)

VICTOR LLAMAS,[1,2] JOSEP MARIA SERRES,[1,2] MAGDALENA AGUILÓ,[1] FRANCESC DÍAZ,[1] AND XAVIER MATEOS[1]

[1]Física i Cristal·lografia de Materials i Nanomaterials (FiCMA-FiCNA)-EMaS, Dept. Química Física i Inòrganica, Universitat Rovira i Virgili (URV), Campus Sescelades, 43007 Tarragona, Spain
[2]Eurecat, Centre Tecnològic de Catalunya, Unitat Advanced Manufacturing Systems (AMS), Campus Sescelades, 43007 Tarragona, Spain

Abstract

A photonic device capable of detecting small variations in the angle of rotation of a shaft (1.25º) by using optical fibers has been developed. This system does not have any electromechanical element in its work area, being suitable in flammable environments. In addition, thanks to the information transmission properties that optical fibers provide [1], it is possible to place these detectors several kilometers away from the final sensors [2], facilitating their implementation for Industry 4.0.

Introduction.

In the last 20 years due to rising raw power of computers [3] and the appearance of new sensorics technologies and manufacturing [4], a new industrial revolution, industry 4.0, is rising where machines and sensors communicate with each other to allow the optimization of industrial processes [5].

One of the most popular fields in recent years is sensorics [6], here electronic devices are used to determine the correct operation of all systems in an industrial process. However, due to external factors it is not always possible to use conventional electronic devices. For this reason, an optical encoder has been developed, capable of being placed in flammable environments without the possibility of generating sparks or overheating.

Operation Principle.

In **Figure 1.** operation scheme of our sensor is observed. This consists of a light source that can be laser or white light (depending on the price and the distance that is needed), 3 Y-shaped fibers (BFY400HS02, Thorlabs), a rotation detector that has been modeled and manufactured in 3D and two light intensity sensors (SM1PD1B, Thorlabs) that are connected to a computer.

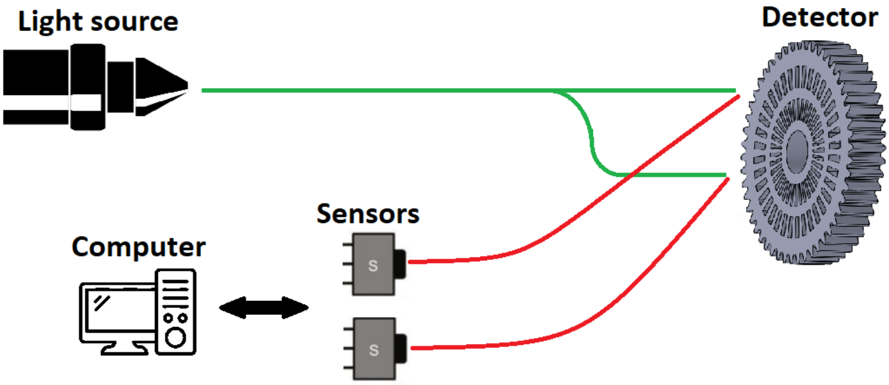

Figure 1. scheme of the optical encoder device.

The device couples a light source (OSL2, Thorlabs) to an optical fiber using an SMA connection. This is divided into two independent fibers and each end is very close (almost touching) to the binary optical encoder in different sides. The light is reflected in the surface of the detector, which is coated with gold nanoparticles using spattering in order to increase its reflectance [7-8]. When the light falls on the device depending on its angular position it will interact either with the metal surface or with a hole, reflecting or not the light coming from the fiber. These reflections are collected by the tips of the Y-shaped fibers, which work as an optical circulator [9], making light flow towards the detectors. Thanks to a computer program developed in LabView, the angular position of the encoder can be determined in live.

Optical encoder development.

Sensor development

After an exhaustive research [10], it has been determined that the most interesting system to build an optical encoder is by using a binary disk.

Two different binary disk designs were studied for this device. On the one hand, an absolute encoder was studied [11], **Figure 2** That is, a device capable of measuring the exact angular position of a shaft thanks to a perforated wheel. Its main advantages are that it is impossible to skip steps and its starting position is irrelevant when measuring angular displacements. Its disadvantages are its larger size, more complex manufacturing methods and the use of a lot of optical fibers. This device has a resolution of $\Delta\theta(º) = 360/n$, where n is the number of bits of information required, being necessary n detectors and $2\,n + 1$ fibers for each bit, making this device extremely expensive for acquiring a good resolution.

On the other hand, an incremental encoder has been studied [12], **Figure 2**. In this case, it starting position is determined as $\theta_0 = 0º$ and steps are added or subtracted as the device moves clockwise or counterclockwise. Its main advantages are its higher resolution (with just two fibers you can obtain very good response) and its much more adjusted cost, although it has an important disadvantage, there exists the possibility that the system skips steps if it rotates at high speed. Nevertheless, we decided on this system to create the prototype.

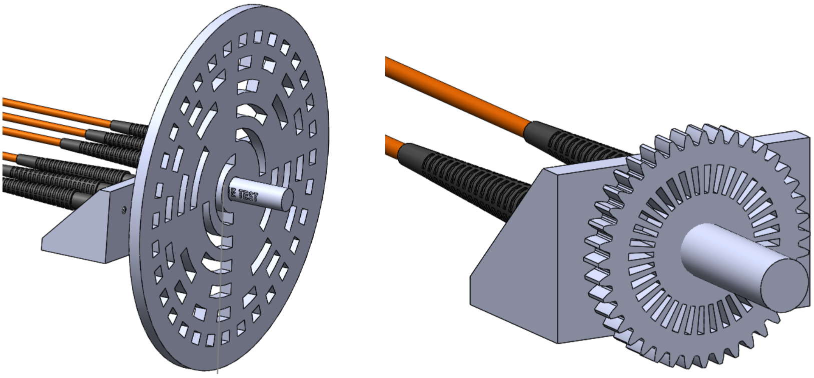

Figure 2. 3D model of the absolute (left) and relative (right) optical encoders.

The Anycubic photon resin 3D printer has been used to make all the pieces. This machine allows us to make the encoders with a precision of 0.05mm, obtaining excellent detail in each piece.

With this incremental design, resolutions of 2.5º per step are achieved. Promising enough for a first device. In this case the angular resolution is limited by the width of the holes, which are limited the 3D printer, so a great improvement could be done with another technologies like photolithography.

To improve our resolution, the encoder shaft has been coupled to another toothed wheel as can be seen in **Figure 3**. The large wheel, with radius 2r, would be the main shaft of the detector that is coupled to the device to be measured, while the small one of radius r, would be a passive axis connected to the fibers. With this we would be able to reduce the angular resolution in half, that is, each step would be 1.25º. It is possible to increase the gear ratio to reduce the angular resolution, but the size of the system increases drastically being less practical.

In addition, to increase the signal-noise ratio (SNR) in the detectors, a spattering [7] of the gear surface has been done, achieving a high reflective surface [8], which provides a much higher intensity in the detectors.

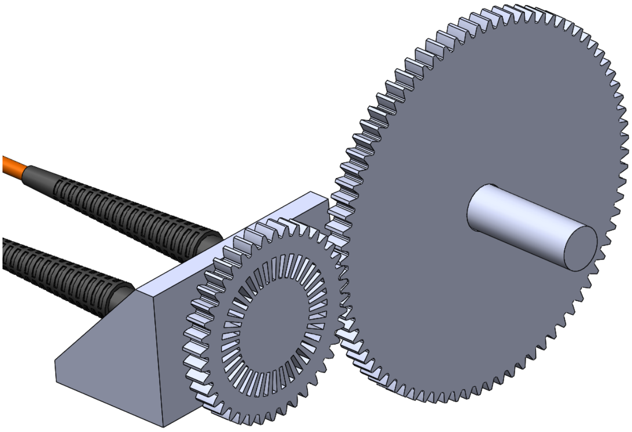

Figure 4 3D model of the relative optical encoder with a R-2R gear reductor.

Code development

LabView has been used as the digital working environment in this project. The main reason of develop the code in this software is because it allowed us a simple and effective communication with the detectors through the NI-USB-6212 DAQ while it was possible to clearly monitor the intensities in each one by measuring the voltage that reaches the analog inputs AI0 and AI1.

Codification principle

The code for this program is based on the 2-bit incremental codification principle used in any electrical encoder [13]. To determine the rotation direction of an encoder, a truth table such as the **Table 1.A**. is used:

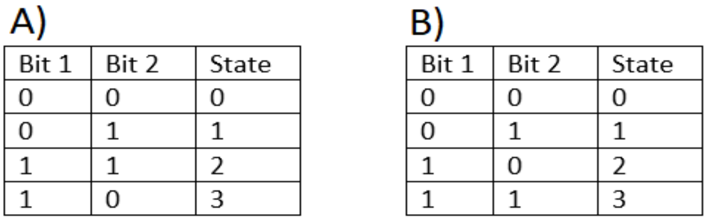

A)

Bit 1	Bit 2	State
0	0	0
0	1	1
1	1	2
1	0	3

B)

Bit 1	Bit 2	State
0	0	0
0	1	1
1	0	2
1	1	3

Table 1. Truth tables of a 2-bit binary encoder. A) Modified truth table. B) Standard truth table.

If the state increases by 1 it means that the encoder has rotated clockwise and if it decreases by 1 means that it has rotated counterclockwise. There is a border condition between states 0 and 3 that is easily programmable.

It should be noted that this truth table is not the common one [13], which is plotted in Table 1.B. This is because in the common table bit 2 has twice the angular frequency than bit 1 when the encoder rotates, entailing several problems: the first, two different perforation rings are needed for each bit with a different angular spacing between perforations, making its alignment substantially harder; the second, there are permutations such as $10 \rightarrow 01$ where both bits changes its values at the same time, making the program read for a short period of time an non-existent state, for example $10 \rightarrow 00 \rightarrow 01$, thus skipping a step, these are the so-called conflictive points in **Figure 5**.

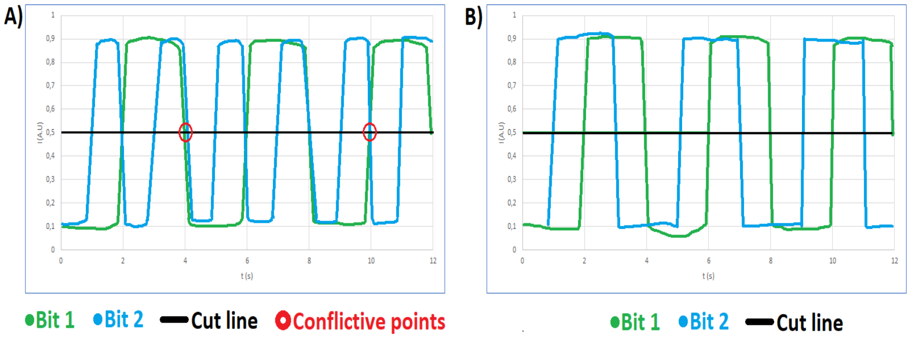

Figure 5. Intensity pattern when rotating the encoder. A) With a standard truth table. B) With the modified truth table.

With the modified truth table, it is only necessary create one perforation ring with both detectors offset 2.5º, which greatly simplifies the process, as can be seen in **Figure 3**.

Switching from an analog signal to a Boolean state.

In **Figure 5** an intensity vs real time graph for each detector can be observed. At the beginning the encoder is in its starting position and at 3 seconds it started to rotate in clockwise direction. With this graph it is possible to determine the maximum and minimum values of each detector, being able to stablish an average value for each one. In order to set Boolean values, we simply determine if the detector is above this average and stablish it with a logical <1>; and if it does not exceed it, a <0>.

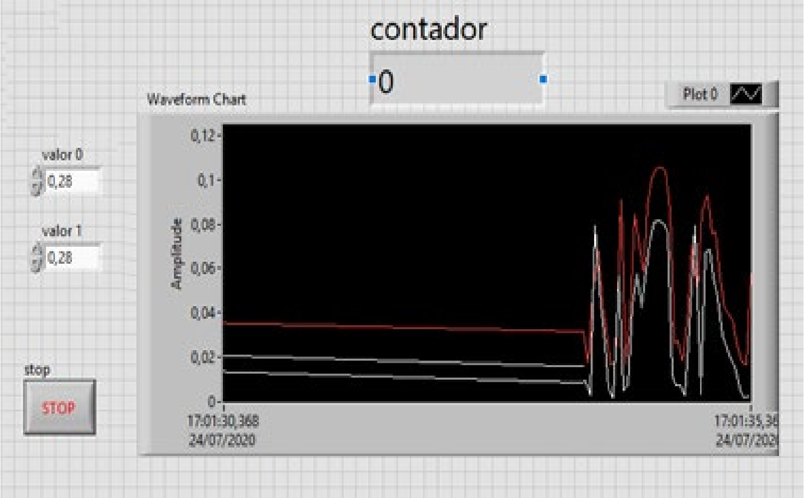

contador: 0

valor 0: 0,28

valor 1: 0,28

Figure 6. Labview main program.

Rotation direction code.

The rotation detection code consists of a set of nested chase structures where two pairs of bits are saved, two bits represent the current state and another two that represents the previous state. In addition, there is an integer number, the counter, which increases or decreases in a unity following the next conditions:

$$< 00 > \rightarrow \begin{array}{l} < 01 > \rightarrow +1 \\ < 10 > \rightarrow -1 \end{array}$$

$$< 01 > \rightarrow \begin{array}{l} < 11 > \rightarrow +1 \\ < 00 > \rightarrow -1 \end{array}$$

$$< 11 > \rightarrow \begin{array}{l} < 10 > \rightarrow +1 \\ < 10 > \rightarrow -1 \end{array}$$

$$< 10 > \rightarrow \begin{array}{l} < 00 > \rightarrow +1 \\ < 11 > \rightarrow -1 \end{array}$$

The states on the left are the previous states and those on the right are the current states. For more clarity, if, for example, in the previous instant the system was in state <00> and it goes to <01> the program will understand that the shaft is rotated one step clockwise, so the counter is increased by one. If after that we turn the shaft counterclockwise, from the state <01> to <00> the program understands this movement subtracting one step to the counter, coming back to the initial state. Any state that is not in the list above will be considered an exception and simply add 0 to the counter. This program has been developed in labview and is shown in **Figure 7**.

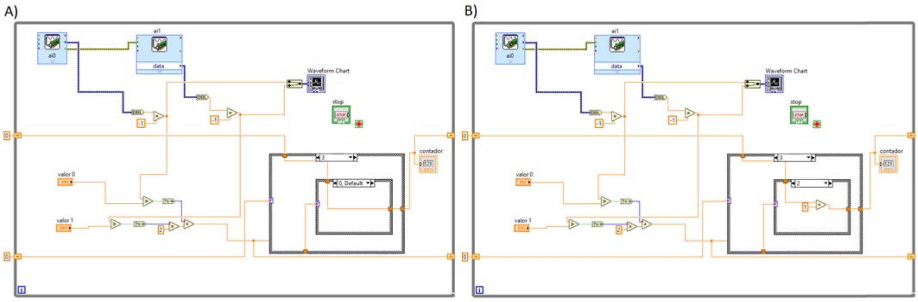

Figure 7. Optical encoder LabView block diagram. A) Default state. B) Rotation clockwise.

Results, conclusions and future improvements

An optical encoder with an angular resolution of 1.25º has been developed. Thanks of the absence of any electromechanical parts this device is suitable in flammable environments without presenting any danger, and the use of optical fibers makes it possible to place the sensor part far away to the detectors, being an optimal device for industry 4.0.

As explained in code section 3. Any state that is not represented in the contemplated changes would correspond to an exception and would not be counted. This makes it possible to skip steps, in laboratory tests if the angular speed is too high it is possible that this happens, although in general it works correctly. If similar code is executed in another program, such as C ++, which can manage much more data per second, this problem can be solved, being able to spin the shaft much faster without any miscount.

The size of the fiber core is relevant in terms of achieving better angular resolution. If smaller perforations are made without considering the fiber core size, the light area which emerges from the fiber could be too big and the holes could not be detected. This can be solved with smaller core fibers, but the amount of light that reaches the detector is also going to be reduced, so it will be necessary to find a balance between these parameters.

References.

[1] J. M. Senior, Optical Fiber Communications Principles and Practice Third Edition Optical Fiber Communications Optical Fiber Communications Principles and Practice Third Edition, 3rd ed. 2009.
[2] B. Lee, “Review of the present status of optical fiber sensors,” Opt. Fiber Technol., vol. 9, no. 2, pp. 57–79, Apr. 2003, doi: 10.1016/S1068-5200(02)00527-8.
[3] C. Toumey, “Less is Moore,” Nat. Nanotechnol. 2016 111, vol. 11, no. 1, pp. 2–3, Jan. 2016, doi: 10.1038/nnano.2015.318.
[4] E. Oztemel and S. Gursev, “Literature review of Industry 4.0 and related technologies,” J. Intell. Manuf. 2018 311, vol. 31, no. 1, pp. 127–182, Jul. 2018, doi: 10.1007/S10845-018-1433-8.
[5] P. Ghelfi et al., “Microwave photonics technologies for 5G and industry 4.0,” IET Conf. Publ., vol. 2019, no. CP765, 2019, doi: 10.1049/CP.2019.0840.
[6] A. Calabrese, N. L. Ghiron, and L. Tiburzi, “‘Evolutions’ and ‘revolutions’ in manufacturers’ implementation of industry 4.0: a literature review, a multiple case study, and a conceptual framework,” https://doi.org/10.1080/09537287.2020.1719715, vol. 32, no. 3, pp. 213–227, 2020, doi: 10.1080/09537287.2020.1719715.
[7] T. Schenkel, M. A. Briere, H. Schmidt-Böcking, K. Bethge, and D. H. Schneider, “Electronic Sputtering of Thin Conductors by Neutralization of Slow Highly Charged Ions,” Phys. Rev. Lett., vol. 78, no. 12, p. 2481, Mar. 1997, doi: 10.1103/PhysRevLett.78.2481.
[8] J. H. Weaver and S. Babar, “Optical constants of Cu, Ag, and Au revisited,” Appl. Opt. Vol. 54, Issue 3, pp. 477-481, vol. 54, no. 3, pp. 477–481, Jan. 2015, doi: 10.1364/AO.54.000477.
[9] H. J. R. Dutton, “Understanding optical communications,” p. 760, 1998.

[10] A. Ellin and G. Dolsak, “The design and application of rotary encoders,” Sens. Rev., vol. 28, no. 2, pp. 150–158, 2008, doi: 10.1108/02602280810856723.

[11] Y. Matsuzoe, N. Tsuji, T. Nakayama, K. Fujita, and T. Yoshizawa, “High-performance absolute rotary encoder using multitrack and M-code,” Opt. Eng., vol. 42, no. 1, pp. 124–131, Jan. 2003, doi: 10.1117/1.1523943.

[12] R. Dubey, P. Agarwal, and M. K. Vasantha, “Programmable logic devices for motion control - A review,” IEEE Trans. Ind. Electron., vol. 54, no. 1, pp. 559–566, Feb. 2007, doi: 10.1109/TIE.2006.885452.

[13] E. L. Post, “Introduction to a General Theory of Elementary Propositions,” Am. J. Math., vol. 43, no. 3, p. 163, Jul. 1921, doi: 10.2307/2370324.

Paper IX

Structured light profilometer system to measure wear in metallic molds

(In progress to be submitted)

VICTOR LLAMAS,[1,2] JOSEP MARIA SERRES,[1,2] MAGDALENA AGUILÓ,[1] FRANCESC DÍAZ,[1] AND XAVIER MATEOS[1]

[1]Física i Cristal·lografia de Materials i Nanomaterials (FiCMA-FiCNA)-EMaS, Dept. Química Física i Inòrganica, Universitat Rovira i Virgili (URV), Campus Sescelades, 43007 Tarragona, Spain
[2]Eurecat, Centre Tecnològic de Catalunya, Unitat Advanced Manufacturing Systems (AMS), Campus Sescelades, 43007 Tarragona, Spain

Abstract

A 3D line laser scanner has been developed, capable of showing wearing in metallic molds in real time. This has been possible by using a structured light system, consisting of a high precision line laser with its wavelength in the near ultraviolet (405nm), an ultra-fast, high-resolution camera [1] and a band pass filer centered in 405nm to eliminate the atmospheric light. To do that, an artificial vision software has been developed, able to detect small imperfections in the shape and in the rugosity of the molds by measuring a series of parameters which are the slope of the grooves, the height of these grooves, the total width of the split part and the surface gloss.

Introduction

The fourth industrial revolution and the underlying digital transformation, known as Industry 4.0 [2], is progressing exponentially in the last 20 years due to rising raw power of computers [3] and the emergence of new sensorics technologies. In this industrial revolution machines and sensors communicate with each other to allow the optimization of industrial processes [4].

One of the most interesting 4.0 technologies for the industry in the photonics field is computer vision [5]. This is based on using image systems [6] together with mathematical algorithms [7] to synthesize the information captured by a camera and transform it into instructions easily understandable by a control system. In this field, a device capable of measuring the wear of two metallic molds has been developed, thus being able to detect when the mold is worn out and must be discarded.

Operation principle.

This paper aims to study the wear of some steel molds used in the ceramic industry. These are designed as can be seen in **Figure 1**. They consist of a cylinder that has slits on its flat face to improve its grip with the material. With use, the metal surface wears and can become deformed, producing defective parts. To avoid this, a series of parameters have been defined to be studied in the mold, these are: the slope of the grooves $\boldsymbol{s}$, the height of these grooves $\boldsymbol{h}$, the total width of the split part $\boldsymbol{w}$ and the surface gloss.

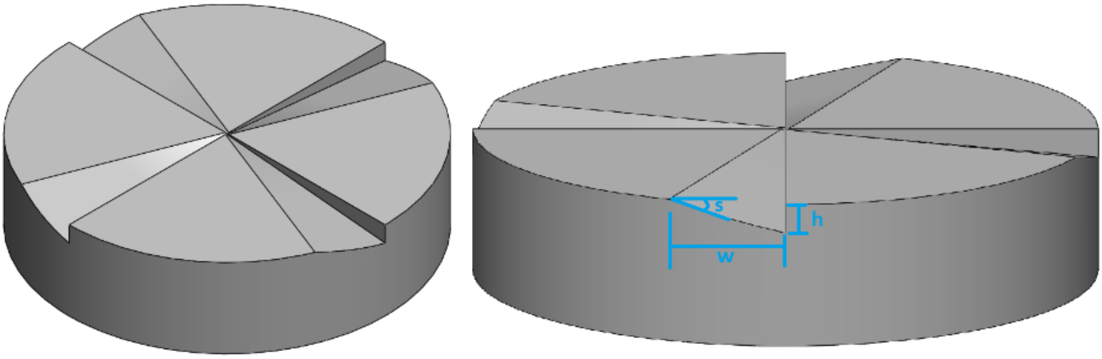

Figure 1. 3D image of the molds studied with the parameters of interest: $\boldsymbol{s}$ slope of the slits, $\boldsymbol{h}$ height of the slits, $\boldsymbol{w}$ total width of the split part.

Those parameters are studied with an artificial vision system using structured light with a profilometry system. This is formed by a line laser [8], a camera, and a band-pass filter. The laser, which focused on a cylindrical lens, emits a linear beam, it is scattered on the surface of the mold and captured with the camera, that receives a curved line (**Figure 4**).

In order to obtain a correct measurement with a profilometer system some conditions must be satisfied [9-10]. The goal of this section is to ideate an optimal configuration that optimizes the space and the resources of the camera and the software. The operating diagram in the ZX and ZY planes can be seen in **Figure 2**.

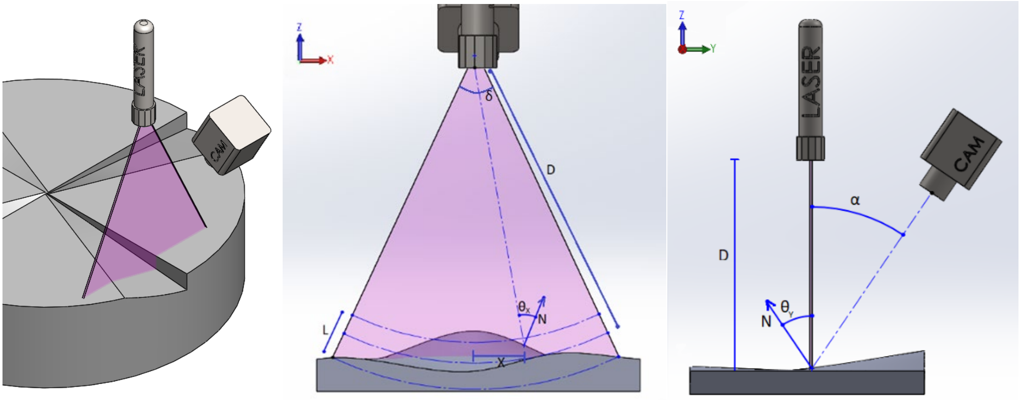

Figure 2. General (left), front (center) and lateral (right) view of a perfilometry system.

Depth Of Field (DOF): the measured point should be within a specified range of distance from the laser source and the camera. If the laser or the camera are not correctly focused on the surface the measurement would not be correct and the error increases drastically.

For the laser, the surface should be inside the Rayleigh zone:

$$D - z_R < Z < D + z_r \qquad (1)$$

Being z_R The Rayleigh distance and D the distance between the laser and the waist.

The restriction for the camera is related with its view zone and focusing depth, in this case it the main effect is the second. It can be expressed as:

$$D - \frac{L}{2} < Z < D + \frac{L}{2} \qquad (2)$$

Being L the focal depth.

For commercial line lasers the Rayleigh zone is much longer than the camera focusing depth. So, it is possible to consider the equation (1) negligible and only focus on the equation (2) for our estimations.

View Angle (VA) and occlusion: Another important parameter for a good measurement is the angle between the surface and the camera. If this surpass $\pm 90^{\circ}$ there must be a part of the surface covered by another part of the object, so the restriction for this parameter is:

$$-90º < \theta_x - tg\left(\frac{X}{D}\right) < 90º \tag{3}$$

Being θ_x the angle between the surface and the vertical line and X the lateral position of the point it is measured.

$$-90º < \theta_y + \alpha < 90º \tag{4}$$

Being θ_y the angle between the vertical line and the normal vector to the surface and α the angle between the camera and the laser. In our case mostly all the defects are much smaller than this parameter.

Field Of View (FOV): the measured point should be located within the length of the laser line. Otherwise, the system would be unable to measure the contour of the surfaces not exposed to the laser.

$$\delta_{laser} > \delta_{camera} \tag{5}$$

Where δ_{laser} and δ_{camera} are the field angles for the camera and the laser, respectively.

Experimental development.

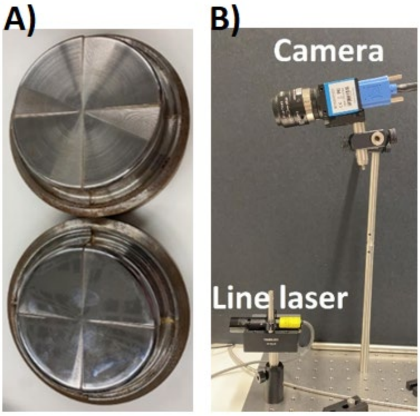

Figure 3. Laboratory images of the study. A) Images of the molds to be measured, correct (top) and worn (bottom). B) Image of the homemade profilometry system.

In the industry there are profilometry systems with very good precision [11-12], however, due to space limitations, VA and the FOV requirements, it has been decided to use a homemade one that allows us absolute control of all parameters. This device consists of three elements:

- A laser (CPS405, Thorlabs) in the near ultraviolet wavelengths (405nm) with a cylindrical lens (LJ1695RM, Thorlabs) adapted to it, to generate a linear beam; in addition, a linear shutter is mounted to narrow the beam and make it as fine as possible.

- A high resolution (2K) monochrome camera (Sony XCG-CP51) with the Global Shutter CMOS image capture method. This operating mode allows us to collect all the information at the same time without having any lag shutter, which substantially reduces aberrations in our measurements.

-A band pass filter centered in 405nm (FB405-10, Thorlabs) to eliminate the background noise and the Ambiental lights.

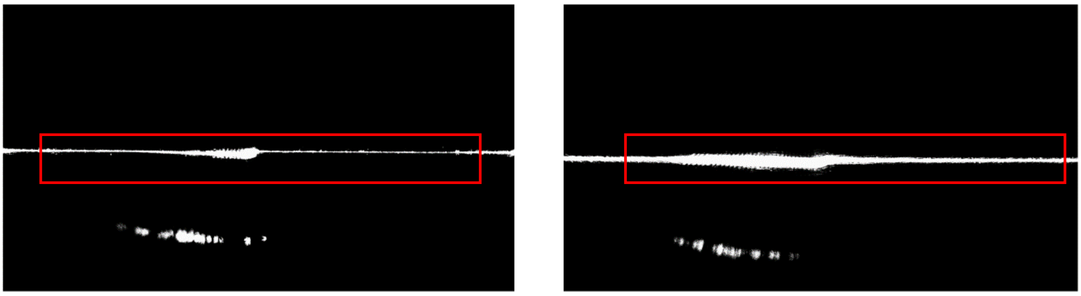

Figure 4. Images captured by the homemade profilometry system. The image on the right corresponds to a worn mold and the image on the left with a correct mold. The red rectangles represent the area of interest that has been numerically trimmed to perform the numerical calculations.

These elements have been arranged at 5cm horizontally, 15 cm vertically and with a 30º relative angle between them; allowing us to detect profiles of 5cm wide at 40cm distance.

With this system, the camera captures the image of a curved line as can be seen in **Figure 4**. By employing numerical calculations, this line can be transformed into a vector that relates each position with its height, thus obtaining the spatial profile of the piece. In a last step, the algorithm finds the slit part and performs a fitting to calculate all the parameters in the mold, as can be seen in **Figure 5**.

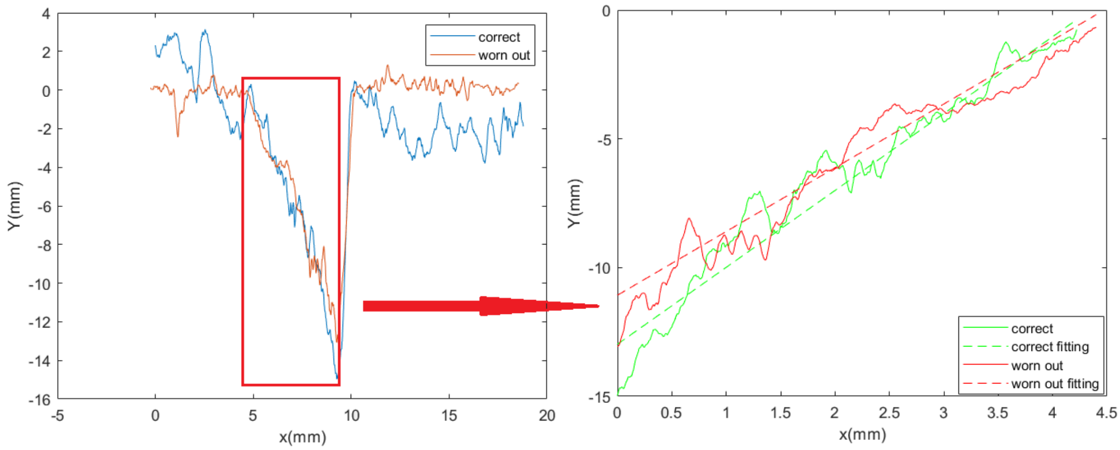

Figure 5. Numerically calculated spatial profiles of a correct and a worn-out mold. The left image is the total Profile captured by the camera and the right image is a zoom of the slope with its respective fitting.

Results.

From the numerical treatment carried out in the previous section, the characteristic parameters of the molds has been obtained obtained, these are: roughness, which is given by the brightness of the mold; the worn surface, which is given by the depth of the grooves and their width; and the deformation of the mold, which is given by the slope of the area with grooves. For these constants, the relative error between the average value of those constants in the pieces in good condition with respect to the pieces in poor condition has been studied with the formula:

$$\delta\% = \frac{|\bar{X}_{good} - \bar{X}_{bad}|}{\bar{X}_{good}} 100 \tag{6}$$

Obtaining the following results: $h = 14 \pm 5$ %, $w = 4 \pm 4\%$, $s = 8 \pm 6\%$ and $b = 62 \pm 3\%$ where h is the height of the notch, w is the width of the area where there are grooves, s the slope of the indented area and b the gloss of the mold.

Conclusions.

Using a structured light system based on a line laser and an ultra-fast camera, an artificial vision system has been made capable of unequivocally determining whether a ceramic mold works correctly or has worn out due to use. From the calculations carried out, it has been determined that the key parameters to measure to determine this wear have to be the gloss of the mold surface and the depth of the grooves.

References

[1] S. Son, H. Park, and K. H. Lee, "Automated laser scanning system for reverse engineering and inspection," Int. J. Mach. Tools Manuf., vol. 42, no. 8, pp. 889–897, Jun. 2002, doi: 10.1016/S0890-6955(02)00030-5.

[2] E. Oztemel and S. Gursev, "Literature review of Industry 4.0 and related technologies," J. Intell. Manuf. 2018 311, vol. 31, no. 1, pp. 127–182, Jul. 2018, doi: 10.1007/S10845-018-1433-8.

[3] C. Toumey, "Less is Moore," Nat. Nanotechnol. 2016 111, vol. 11, no. 1, pp. 2–3, Jan. 2016, doi: 10.1038/nnano.2015.318.

[4] P. Ghelfi et al., "Microwave photonics technologies for 5G and industry 4.0," IET Conf. Publ., vol. 2019, no. CP765, 2019, doi: 10.1049/CP.2019.0840.

[5] T. Brosnan and D. W. Sun, "Improving quality inspection of food products by computer vision––a review," J. Food Eng., vol. 61, no. 1, pp. 3–16, Jan. 2004, doi: 10.1016/S0260-8774(03)00183-3.

[6] T. Skauli and J. Farrell, "A collection of hyperspectral images for imaging systems research," https://doi.org/10.1117/12.2007097, vol. 8660, pp. 89–95, Feb. 2013, doi: 10.1117/12.2007097.

[7] R. Kudelić, "Monte-Carlo randomized algorithm for minimal feedback arc set problem," Appl. Soft Comput., vol. 41, pp. 235–246, Apr. 2016, doi: 10.1016/J.ASOC.2015.12.018.

[8] T. H. MAIMAN, "Stimulated Optical Radiation in Ruby," Nat. 1960 1874736, vol. 187, no. 4736, pp. 493–494, 1960, doi: 10.1038/187493a0.

[9] E. Zussman, H. Schuler, and G. Seliger, "Analysis of the geometrical features detectability constraints for laser-scanner sensor planning," Int. J. Adv. Manuf. Technol. 1994 91, vol. 9, no. 1, pp. 56–64, Jan. 1994, doi: 10.1007/BF01792868.

[10] F. Xi and C. Shu, "CAD-based path planning for 3-D line laser scanning," Comput. Des., vol. 31, no. 7, pp. 473–479, Jun. 1999, doi: 10.1016/S0010-4485(99)00044-5.

[11] B. R. Barbero and E. S. Ureta, "Comparative study of different digitization techniques and their accuracy," Comput. Des., vol. 43, no. 2, pp. 188–206, Feb. 2011, doi: 10.1016/J.CAD.2010.11.005.

[12] O. Semeniuta, S. Dransfeld, and P. Falkman, "Vision-based robotic system for picking and inspection of small automotive components," IEEE Int. Conf. Autom. Sci. Eng., vol. 2016-November, pp. 549–554, Nov. 2016, doi: 10.1109/COASE.2016.7743452.

7

CONCLUSIONS

Throughout this doctoral thesis, innovative photonic devices focused on the creation and implementation of new technologies in Industry 4.0 have been studied and developed. As has been observed, different systems have been made to solve the growing needs of the industry in the field of sensors, detectors and new light sources, adapting to the needs of each specific point in the production chain.

7.1. Microchip FS-DLW lasers.

4 studies of different materials have been carried out in order to develop new laser systems. For this, four different crystalline matrices doped with thulium ions have been used, these being $KLuW$, $CALGO$, SrF_2 and $MgWO_4$. Inside those crystals, waveguides have been microfabricated using the FS-DLW technique, allowing the development of highly efficient microchip lasers in the λ≅2μm range. This new typology allows the creation of very compact and efficient lasers ideal for medical and industrial applications.

7.2. Waveguide sensors.

Two types of sensors have been studied based on the microfabrication of a waveguide channel within a crystal. With this procedure it is possible to make light interact very efficiently with a liquid medium and thus be able to measure its composition.

On the one hand, it has been investigated on a Fabri perot interferometer inside a waveguide, capable of measuring with great precision the refractive index of water in real time, being able to determine changes in its composition.

On the other hand, an evanescent wave sensor has been studied, where by introducing a beam of light with a wide spectrum it is possible to detect the absorption peaks of the liquid in contact, being able to know the compounds dissolved in water.

7.3. Multiesperctal detectors.

Using inexpensive devices, three multispectral detection systems have been developed, their operation has been demonstrated, as well as some practical applications of these equipment.

The developed FTIR system is capable of measuring with good precision signals in the range of 2μm to 6μm, it has been used to measure the spectrum of various lasers in this range with good perspectives.

The pushbroom system developed allows to create hyperspectral images with very good precision throughout the vis to near-IR range, being used to measure the homogeneity of LED systems.

The whiskbroom hyperspectral camera that has been manufactured allows to generate hyperspectral images in the visible range to near IR in less time than the pushbroom camera, in exchange for a worse resolution. Own software has been created for this system that has proven its viability in production chain.

7.4 Profilometry on metallic surfaces.

Using a line laser and a monochromatic camera, a low-cost laser profilometry system has been developed with the ability to be positioned at the desired distance from the sample. Using this device together with algorithms for magnifying defects, an assisted vision system has been created that allows them to be easily appreciated, reducing the need to hire people focused only on this activity.

7.5. Profilometry in molds.

Using a line laser, a monochromatic camera together with a band-pass filter, a profilometry system has been created capable of detecting wear on mechanical parts. For the most efficient detection possible, a homemade aglorithm has been used capable of measuring different wear parameters at the same time, such as the width and length of the grooves or the surface gloss of the pieces in order to unequivocally determine when the piece is has worn out.

7.6. Artificial vision to measure wearing in knitting machines.

Using a monochrome camera and artificial vision algorithms, it has been possible to detect wear, deformation and breakage of the needles in a circular knitting machine, being able to create a real-time control system that informs an operator of the incidents of the machine. system thus being able to avoid the appearance of defects in the fabrics.

7.7 Optical encoder.

An optical encoder has been developed whose main characteristic is the absence of any electromechanical device, making it possible to use it in flammable environments without risk. Thanks to the properties of the optical fibers, it is possible to place this sensor several hundred meters from the detectors without any loss of signal, being especially useful in the chemical industry.

7.8. Non-touch screen

Using a line laser, a monochrome camera and a band pass filter, it has been possible to develop a system for tracking objects capable of following the movement of a finger letting people to interact with a device without contact. This system is thought to be inexpensive, and it is expected to be used in public devices for the fight against the SARS coronavirus 2 pandemic.

REFERENCES

[1] K. G. Deng, *Reconceptualizing the Industrial Revolution*, vol. 53, no. 6. Routledge , 2011.

[2] M. Huberman, C. M. Meissner, and K. Oosterlinck, “Technology and Geography in the Second Industrial Revolution: New Evidence from the Margins of Trade,” *J. Econ. Hist.*, vol. 77, no. 1, pp. 39–89, Mar. 2017, doi: 10.1017/S0022050717000018.

[3] D. C. Mowery, *Plus ca change: Industrial R&D in the “third industrial revolution,”* vol. 18, no. 1. Oxford Academic, 2009.

[4] L. Kleinrock, “An early history of the internet,” *IEEE Commun. Mag.*, vol. 48, no. 8, pp. 26–36, Aug. 2010, doi: 10.1109/MCOM.2010.5534584.

[5] *Kodak and the Digital Revolution (A)*. 2003.

[6] C. Toumey, “Less is Moore,” *Nat. Nanotechnol. 2016 111*, vol. 11, no. 1, pp. 2–3, Jan. 2016, doi: 10.1038/nnano.2015.318.

[7] P. Ghelfi *et al.*, “Microwave photonics technologies for 5G and industry 4.0,” *IET Conf. Publ.*, vol. 2019, no. CP765, 2019, doi: 10.1049/CP.2019.0840.

[8] T. Masood and J. Egger, “Augmented Reality: Focusing on Photonics in Industry 4.0,” *IEEE J. Sel. Top. Quantum Electron.*, 2021, doi: 10.1109/JSTQE.2021.3093721.

[9] T. Kurfess, C. Saldana, K. Saleeby, and M. Parto-Dezfouli, “Industry 4.0 and Intelligent Manufacturing Processes: A Review of Modern Sensing Technologies,” *J. Manuf. Sci. Eng.*, vol. 142, no. 11, Aug. 2020, doi: 10.1115/1.4048206.

[10] B. Stender, W. Mantei, A. Krupp, V. Ratz, F. Hilbert, and R. Houbertz, “High-precision 3D printing as a versatile tool for integrated photonics (Conference Presentation),” *https://doi.org/10.1117/12.2297404*, vol. 10586, p. 1058614, Mar. 2018, doi: 10.1117/12.2297404.

[11] V. M. Montaño-Serrano, J. M. Jacinto-Villegas, A. H. Vilchis-González, and O. Portillo-Rodríguez, “Artificial Vision Algorithms for Socially Assistive Robot Applications: A Review of the Literature,” *Sensors 2021, Vol. 21, Page 5728*, vol. 21, no. 17, p. 5728, Aug. 2021, doi: 10.3390/S21175728.

[12] A. A. Sawchuk and T. C. Strand, "Digital Optical Computing," *Proc. IEEE*, vol. 72, no. 7, pp. 758–779, 1984, doi: 10.1109/PROC.1984.12937.

[13] H. Mohajan, "The First Industrial Revolution: Creation of a New Global Human Era," May 2019.

[14] I. Ray, *Bengal industries and the British industrial revolution (1757-1857)*. Routledge, 2011.

[15] I. G. Ionescu, "The First Industrial Revolution and General Features of the World Economy Between the 16th Century and 1780," *SEA – Pract. Appl. Sci.*, vol. VI, no. 17, pp. 183–186, 2018.

[16] A. N. Saxena, *Invention of integrated circuits : untold important facts*. World Scientific, 2009.

[17] A. M. Turing, "Computing Machinery and Intelligence," *Parsing Turing Test Philos. Methodol. Issues Quest Think. Comput.*, pp. 23–65, 2009, doi: 10.1007/978-1-4020-6710-5_3.

[18] T. J. Berners-Lee, "The world-wide web," *Comput. Networks ISDN Syst.*, vol. 25, no. 4–5, pp. 454–459, Nov. 1992, doi: 10.1016/0169-7552(92)90039-S.

[19] T. Murphy, "40 Years After the First Cell Phone Call: Who Is Inventing Tomorrow?s Future?," *IEEE Consum. Electron. Mag.*, vol. 2, no. 4, pp. 44–46, Oct. 2013, doi: 10.1109/MCE.2013.2273653.

[20] S. Zanero, "Cyber-Physical Systems," *Computer (Long. Beach. Calif).*, vol. 50, no. 4, pp. 14–16, 2017, doi: 10.1109/MC.2017.105.

[21] J. Z. Gul *et al.*, "3D printing for soft robotics – a review," *http://www.tandfonline.com/action/journalInformation?show=aimsScope&journalCode=tsta20#.VmBmuzZFCUk*, vol. 19, no. 1, pp. 243–262, Dec. 2018, doi: 10.1080/14686996.2018.1431862.

[22] F. Wortmann and K. Flüchter, "Internet of Things," *Bus. Inf. Syst. Eng. 2015 573*, vol. 57, no. 3, pp. 221–224, Mar. 2015, doi: 10.1007/S12599-015-0383-3.

[23] S. P. Mirashe and N. V. Kalyankar, "Cloud Computing," *Smart Innov. Syst. Technol.*, vol. 132, pp. 167–185, Mar. 2010, Accessed: Aug. 17, 2021. [Online]. Available: https://arxiv.org/abs/1003.4074v1.

[24] J. Shi, J. Wan, H. Yan, and H. Suo, "A survey of Cyber-Physical Systems," *2011 Int. Conf. Wirel. Commun. Signal Process. WCSP 2011*, 2011, doi:

10.1109/WCSP.2011.6096958.

[25] Z. X. Khoo *et al.*, “3D printing of smart materials: A review on recent progresses in 4D printing,” *http://dx.doi.org/10.1080/17452759.2015.1097054*, vol. 10, no. 3, pp. 103–122, Jul. 2015, doi: 10.1080/17452759.2015.1097054.

[26] R. T. Azuma, “A Survey of Augmented Reality,” *Presence Teleoperators Virtual Environ.*, vol. 6, no. 4, pp. 355–385, Aug. 1997, doi: 10.1162/PRES.1997.6.4.355.

[27] N. Ali and H. T. S. Alrikabi, “Design and Implementation of Smart City Applications Based on the Internet of Things Article in International Journal of Interactive Mobile Technologies (iJIM) ·,” 2021, doi: 10.3991/ijim.v15i13.22331.

[28] D. M.Kalasar, *3D Printing in Medicine* . Woodhead Publishing, 2017.

[29] J. Zinkernagel, J. F. Maestre-Valero, S. Y. Seresti, and D. S. Intrigliolo, “New technologies and practical approaches to improve irrigation management of open field vegetable crops,” *Agric. Water Manag.*, vol. 242, p. 106404, Dec. 2020, doi: 10.1016/J.AGWAT.2020.106404.

[30] J. A. Sanahuja and S. Tezanos Vázquez, “Del milenio a la sostenibilidad: retos y perspectivas de la Agenda 2030 para el desarrollo sostenible,” *Política y Soc. 54(2) 2017 533-555*, vol. 54, no. 2, pp. 521–543, 2017, doi: 10.5209/POSP.51926.

[31] J. D. Sachs, “From Millennium Development Goals to Sustainable Development Goals,” *Lancet*, vol. 379, no. 9832, pp. 2206–2211, Jun. 2012, doi: 10.1016/S0140-6736(12)60685-0.

[32] “Comparativa de la Industria 4.0 entre España y el resto de países | Atria.” https://www.atriainnovation.com/comparativa-industria-4-0-espana-y-resto-paises/ (accessed Oct. 15, 2021).

[33] P. Maresova *et al.*, “Consequences of industry 4.0 in business and economics,” *Economies*, vol. 6, no. 3, Sep. 2018, doi: 10.3390/ECONOMIES6030046.

[34] L. Pérez, Í. Rodríguez, N. Rodríguez, R. Usamentiaga, and D. F. García, “Robot Guidance Using Machine Vision Techniques in Industrial Environments: A Comparative Review,” *Sensors 2016, Vol. 16, Page 335*, vol. 16, no. 3, p. 335, Mar. 2016, doi: 10.3390/S16030335.

[35] M. Bigas, E. Cabruja, J. Forest, and J. Salvi, “Review of CMOS image sensors,” *Microelectronics J.*, vol. 37, no. 5, pp. 433–451, May 2006, doi: 10.1016/J.MEJO.2005.07.002.

[36] M. G. Basset, F. Setzpfandt, F. Steinlechner, E. Beckert, T. Pertsch, and M. Gräfe, “Perspectives for Applications of Quantum Imaging,” *Laser Photon. Rev.*, vol. 13, no. 10, p. 1900097, Oct. 2019, doi: 10.1002/LPOR.201900097.

[37] X. W. Ye, C. Z. Dong, and T. Liu, “A Review of Machine Vision-Based Structural Health Monitoring: Methodologies and Applications,” *J. Sensors*, vol. 2016, 2016, doi: 10.1155/2016/7103039.

[38] V. Nandini, R. D. Vishal, C. A. Prakash, and S. Aishwarya, “A Review on Applications of Machine Vision Systems in Industries,” *Indian J. Sci. Technol.*, vol. 9, no. 48, Dec. 2016, doi: 10.17485/IJST/2016/V9I48/140308.

[39] J. Sachdeva, V. Kumar, I. Gupta, N. Khandelwal, and C. K. Ahuja, “A novel content-based active contour model for brain tumor segmentation,” *Magn. Reson. Imaging*, vol. 30, no. 5, pp. 694–715, Jun. 2012, doi: 10.1016/J.MRI.2012.01.006.

[40] A. V. Oppenheim and A. V., “Applications of digital signal processing,” *ph*, 1978, Accessed: Oct. 31, 2021. [Online]. Available: https://ui.adsabs.harvard.edu/abs/1978ph...bookR....O/abstract.

[41] R. N. Bracewell, “The Fourier Transform,” *Sci. Am.*, vol. 260, no. 6, pp. 86–95, 1989, [Online]. Available: http://www.jstor.org/stable/24987290.

[42] D. V. Widder, *Laplace Transform (PMS-6)*. Princeton University Press, 2015.

[43] H. F. Taylor, “An Electrooptic Analog-to-Digital Converter,” *Proc. IEEE*, vol. 63, no. 10, pp. 1524–1525, 1975, doi: 10.1109/PROC.1975.9987.

[44] G. Peyré, “The Numerical Tours of Signal Processing - Advanced Computational Signal and Image Processing,” *IEEE Comput. Sci. Eng.*, vol. 13, no. 4, pp. 94–97, 2011, Accessed: Oct. 31, 2021. [Online]. Available: https://hal.archives-ouvertes.fr/hal-00519521.

[45] W. T. Cochran *et al.*, “What is the fast Fourier transform?,” *Proc. IEEE*, vol. 55, no. 10, pp. 1664–1674, 1967, doi: 10.1109/PROC.1967.5957.

[46] A. J. Gross and T. R. W. Herrmann, “History of lasers,” *World J. Urol. 2007 253*, vol. 25, no. 3, pp. 217–220, Jun. 2007, doi: 10.1007/S00345-007-0173-8.

[47] "Laser Technology Market by Type, Revenue, Application | COVID-19 Impact Analysis | MarketsandMarkets^{TM}." https://www.marketsandmarkets.com/Market-Reports/laser-technology-market-795.html (accessed Jul. 13, 2021).

[48] A. J. Demaria, "Review of CW High-Power CO2 Lasers," *Proc. IEEE*, vol. 61, no. 6, pp. 731–748, 1973, doi: 10.1109/PROC.1973.9153.

[49] A. Lempicki and H. Samelson, "LIQUID LASERS," *Sci. Am.*, vol. 216, no. 6, pp. 80–92, 1967, [Online]. Available: http://www.jstor.org/stable/24926029.

[50] E. Tournié and A. N. Baranov, "Mid-Infrared Semiconductor Lasers: A Review," *Semicond. Semimetals*, vol. 86, pp. 183–226, Jan. 2012, doi: 10.1016/B978-0-12-391066-0.00005-8.

[51] A. Godard, "Infrared (2–12 μm) solid-state laser sources: a review," *Comptes Rendus Phys.*, vol. 8, no. 10, pp. 1100–1128, Dec. 2007, doi: 10.1016/J.CRHY.2007.09.010.

[52] C. Kränkel, G. Huber, and K. Petermann, "Solid-state lasers: status and future [Invited]," *JOSA B, Vol. 27, Issue 11, pp. B93-B105*, vol. 27, no. 11, pp. B93–B105, Nov. 2010, doi: 10.1364/JOSAB.27.000B93.

[53] U. Keller, "Ultrafast solid-state laser oscillators: a success story for the last 20 years with no end in sight," *Appl. Phys. B 2010 1001*, vol. 100, no. 1, pp. 15–28, May 2010, doi: 10.1007/S00340-010-4045-3.

[54] H. A. Haus, "Mode-locking of lasers," *IEEE J. Sel. Top. Quantum Electron.*, vol. 6, no. 6, pp. 1173–1185, Nov. 2000, doi: 10.1109/2944.902165.

[55] J. J. Zayhowski, "Microchip lasers," *Opt. Mater. (Amst).*, vol. 11, no. 2–3, pp. 255–267, Jan. 1999, doi: 10.1016/S0925-3467(98)00048-2.

[56] E. Snitzer, "Optical Maser Action of Nd3+ in a Barium Crown glass," *Phys. Rev. Lett.*, vol. 7, no. 12, p. 444, Dec. 1961, doi: 10.1103/PhysRevLett.7.444.

[57] M. Pollnau, "Dielectric waveguide lasers," *Int. Conf. Lasers, Appl. Technol. 2007 Adv. Lasers Syst.*, vol. 6731, p. 67310Y, Aug. 2007, doi: 10.1117/12.752833.

[58] F. Chen and Y. Jia, "Compact solid-state waveguide lasers operating in the pulsed regime: a review [Invited]," *Chinese Opt. Lett. Vol. 17, Issue 1, pp. 012302-*, vol. 17, no. 1, pp. 012302-, Jan. 2019, Accessed: Jul. 13, 2021. [Online]. Available: https://www.osapublishing.org/abstract.cfm?uri=col-17-1-012302.

[59] G. M. Hale and M. R. Querry, “Optical Constants of Water in the 200-nm to 200-µm Wavelength Region,” *Appl. Opt. Vol. 12, Issue 3, pp. 555-563*, vol. 12, no. 3, pp. 555–563, Mar. 1973, doi: 10.1364/AO.12.000555.

[60] K. Scholle, S. Lamrini, P. Koopmann, and P. Fuhrberg, “2 µm Laser Sources and Their Possible Applications,” *Front. Guid. Wave Opt. Optoelectron.*, Feb. 2010, doi: 10.5772/39538.

[61] H. Bennion and R. Battarbee, “The European Union Water Framework Directive: opportunities for palaeolimnology,” *J. Paleolimnol. 2007 382*, vol. 38, no. 2, pp. 285–295, Jun. 2007, doi: 10.1007/S10933-007-9108-Z.

[62] J. Von Freyberg, B. Studer, and J. W. Kirchner, “A lab in the field: High-frequency analysis of water quality and stable isotopes in stream water and precipitation,” *Hydrol. Earth Syst. Sci.*, vol. 21, no. 3, pp. 1721–1739, Mar. 2017, doi: 10.5194/HESS-21-1721-2017.

[63] E. Kifle *et al.*, “Femtosecond-laser-written hexagonal cladding waveguide in Tm:KLu(WO4)2: \&\#x00B5;-Raman study and laser operation,” *Opt. Mater. Express*, vol. 7, no. 12, pp. 4258–4268, 2017, doi: 10.1364/OME.7.004258.

[64] F. Chu, “Experimental study of plastic optical fiber TNT sensor based on evanescence absorption,” *https://doi.org/10.1117/1.OE.51.5.054403*, vol. 51, no. 5, p. 054403, May 2012, doi: 10.1117/1.OE.51.5.054403.

[65] R. D. Harris and J. S. Wilkinson, “Waveguide surface plasmon resonance sensors,” *Sensors Actuators B Chem.*, vol. 29, no. 1–3, pp. 261–267, Oct. 1995, doi: 10.1016/0925-4005(95)01692-9.

[66] T. Wei, Y. Han, Y. Li, H.-L. Tsai, and H. Xiao, “Temperature-insensitive miniaturized fiber inline Fabry-Perot interferometer for highly sensitive refractive index measurement,” *Opt. Express*, vol. 16, no. 8, pp. 5764–5769, 2008, doi: 10.1364/OE.16.005764.

[67] Y. Wang, M. Yang, D. N. Wang, S. Liu, and P. Lu, “Fiber in-line Mach-Zehnder interferometer fabricated by femtosecond laser micromachining for refractive index measurement with high sensitivity,” *J. Opt. Soc. Am. B*, vol. 27, no. 3, pp. 370–374, Mar. 2010, doi: 10.1364/JOSAB.27.000370.

[68] C. R. Liao, T. Y. Hu, and D. N. Wang, “Optical fiber Fabry-Perot interferometer cavity fabricated by femtosecond laser micromachining and fusion splicing for refractive index sensing,” *Opt. Express*, vol. 20, no. 20, pp. 22813–22818, Sep. 2012, doi: 10.1364/OE.20.022813.

[69] O. Silvestre, M. C. Pujol, M. Rico, F. Güell, M. Aguiló, and F. Díaz, “Thulium doped monoclinic KLu(WO 4) 2 single crystals: growth and spectroscopy,” *Appl. Phys. B 2007 874*, vol. 87, no. 4, pp. 707–716, May 2007, doi: 10.1007/S00340-007-2664-0.

[70] Institute of Electrical and Electronics Engineers, “2017 Conference on Lasers and Electro-Optics Europe & European Quantum Electronics Conference (CLEO/Europe-EQEC) : 25-29 June 2017.”

[71] K. Veselský, J. Šulc, H. Jelínková, M. E. Doroshenko, V. A. Konyushkin, and A. N. Nakladov, “Spectroscopic and laser properties of a broadly tunable diode-pumped Tm3+ :CaF2–SrF2 laser,” *Laser Phys. Lett.*, vol. 17, no. 2, p. 025802, Jan. 2020, doi: 10.1088/1612-202X/AB5F58.

[72] A. Veniaminov *et al.*, “Ultrafast laser inscribed waveguide lasers in Tm:CALGO with depressed-index cladding,” *Opt. Express, Vol. 28, Issue 3, pp. 3528-3540*, vol. 28, no. 3, pp. 3528–3540, Feb. 2020, doi: 10.1364/OE.384258.

[73] P. O. Petit, J. Petit, P. Goldner, and B. Viana, “Inhomogeneous broadening of optical transitions in Yb:CaYAlO4,” *Opt. Mater. (Amst).*, vol. 30, no. 7, pp. 1093–1097, Mar. 2008, doi: 10.1016/J.OPTMAT.2007.05.017.

[74] J. J. Carvajal, M. C. Pujol, and F. Díaz, “High-Temperature Solution Growth: Application to Laser and Nonlinear Optical Crystals,” *Springer Handb. Cryst. Growth*, pp. 725–757, 2010, doi: 10.1007/978-3-540-74761-1_21.

[75] V. Petrov *et al.*, “Growth and properties of KLu(WO4)2, and novel ytterbium and thulium lasers based on this monoclinic crystalline host,” *Laser Photon. Rev.*, vol. 1, no. 2, pp. 179–212, May 2007, doi: 10.1002/LPOR.200710010.

[76] M. Eichhorn, “Quasi-three-level solid-state lasers in the near and mid infrared based on trivalent rare earth ions,” *Appl. Phys. B 2008 932*, vol. 93, no. 2, pp. 269–316, Sep. 2008, doi: 10.1007/S00340-008-3214-0.

[77] J. O. White, “Parameters for quantitative comparison of two-, three-, and four-level laser media, operating wavelengths, and temperatures,” *IEEE J. Quantum Electron.*, vol. 45, no. 10, pp. 1213–1220, 2009, doi: 10.1109/JQE.2009.2020607.

[78] S. D. Jackson, “Cross relaxation and energy transfer upconversion processes relevant to the functioning of 2 µm Tm3+-doped silica fibre lasers,” *Opt. Commun.*, vol. 230, no. 1–3, pp. 197–203, Jan. 2004, doi: 10.1016/J.OPTCOM.2003.11.045.

[79] A. S. Yasukevich, A. V. Mandrik, N. V. Kuleshov, V. E. Kisel, and V. G. Shcherbitsky, “Modified reciprocity method in laser crystals spectroscopy,” *Adv. Solid-State Photonics (2004), Pap. WB8*, p. WB8, Feb. 2004, doi: 10.1364/ASSP.2004.WB8.

[80] X. Mateos *et al.*, “Efficient 2-µm continuous-wave laser oscillation of Tm3+: KLu(WO4)2,” *IEEE J. Quantum Electron.*, vol. 42, no. 10, pp. 1008–1015, Oct. 2006, doi: 10.1109/JQE.2006.881629.

[81] O. Silvestre *et al.*, “Ln3+:KLu(WO4)2/KLu(WO4)2 epitaxial layers: Crystal growth and physical characterisation,” *Mater. Sci. Eng. B*, vol. 146, no. 1–3, pp. 59–65, Jan. 2008, doi: 10.1016/J.MSEB.2007.07.045.

[82] E. Siegman, *Lasers*, 1st ed. Palo alto, California, 1986.

[83] E. Kifle *et al.*, “Growth, spectroscopy and laser operation of ‘mixed’ Tm:Ca(Gd,Lu)AlO4 – A novel crystal for mode-locked lasers,” *Laser Congr. 2018 (2018), Pap. ATu2A.21*, vol. Part F121-ASSL 2018, p. ATu2A.21, Nov. 2018, doi: 10.1364/ASSL.2018.ATU2A.21.

[84] A. DiChiara, S. Palaniyappan, A. Falkowski, E. Huskins, and B. C. Walker, “Cross-shell multielectron ionization of xenon by an ultrastrong laser field,” *Quantum Electron. Laser Sci. Conf.*, vol. 3, pp. 1974–1976, 2005, doi: 10.1109/QELS.2005.1549346.

[85] A. M. Rubenchik, B. C. Stuart, B. W. Shore, M. D. Feit, M. D. Perry, and S. Herman, “Optical ablation by high-power short-pulse lasers,” *JOSA B, Vol. 13, Issue 2, pp. 459-468*, vol. 13, no. 2, pp. 459–468, Feb. 1996, doi: 10.1364/JOSAB.13.000459.

[86] A. Rodenas and A. K. Kar, “High-contrast step-index waveguides in borate nonlinear laser crystals by 3D laser writing,” *Opt. Express*, vol. 19, no. 18, pp. 17820–17833, 2011, doi: 10.1364/OE.19.017820.

[87] A. K. Kar, H. T. Bookey, J. R. Macdonald, N. D. Psaila, R. R. Thomson, and S. J. Beecher, “Ultrafast laser inscription of near-infrared waveguides in polycrystalline ZnSe,” *Opt. Lett. Vol. 35, Issue 23, pp. 4036-4038*, vol. 35, no. 23, pp. 4036–4038, Dec. 2010, doi: 10.1364/OL.35.004036.

[88] M. Hashida, H. Mishima, S. Tokita, and S. Sakabe, “Non-thermal ablation of expanded polytetrafluoroethylene with an intense femtosecond-pulse laser,” *Opt. Express*, vol. 17, no. 15, pp. 13116–13121, Jul. 2009, doi: 10.1364/OE.17.013116.

[89] F. Chen and J. R. V. de Aldana, “Optical waveguides in crystalline dielectric materials produced by femtosecond-laser micromachining,” *Laser Photon. Rev.*, vol. 8, no. 2, pp. 251–275, Mar. 2014, doi: 10.1002/LPOR.201300025.

[90] G. Douglass, F. Dreisow, S. Gross, and M. J. Withford, “Femtosecond laser written arrayed waveguide gratings with integrated photonic lanterns,” *Opt. Express*, vol. 26, no. 2, pp. 1497–1505, 2018, doi: 10.1364/OE.26.001497.

[91] C. Miese, S. Gross, M. J. Withford, and A. Fuerbach, “Waveguide inscription in Bismuth Germanate crystals using high repetition rate femtosecond lasers pulses,” *Opt. Mater. Express*, vol. 5, no. 2, pp. 323–329, Feb. 2015, doi: 10.1364/OME.5.000323.

[92] T. Sabapathy, A. Ayiriveetil, A. K. Kar, S. Asokan, and S. J. Beecher, “Direct ultrafast laser written C-band waveguide amplifier in Er-doped chalcogenide glass,” *Opt. Mater. Express*, vol. 2, no. 11, pp. 1556–1561, Nov. 2012, doi: 10.1364/OME.2.001556.

[93] W. Yang, C. Corbari, P. G. Kazansky, K. Sakaguchi, and I. C. S. Carvalho, “Low loss photonic components in high index bismuth borate glass by femtosecond laser direct writing,” *Opt. Express*, vol. 16, no. 20, pp. 16215–16226, Sep. 2008, doi: 10.1364/OE.16.016215.

[94] L. Isaeva, G. Barbalinardo, D. Donadio, and S. Baroni, “Modeling heat transport in crystals and glasses from a unified lattice-dynamical approach,” *Nat. Commun. 2019 101*, vol. 10, no. 1, pp. 1–6, Aug. 2019, doi: 10.1038/s41467-019-11572-4.

[95] A. Ródenas *et al.*, “Refractive index change mechanisms in femtosecond laser written ceramic Nd:YAG waveguides: micro-spectroscopy experiments and beam propagation calculations,” *Appl. Phys. B 2009 951*, vol. 95, no. 1, pp. 85–96, Jan. 2009, doi: 10.1007/S00340-008-3353-3.

[96] F. Chen and J. R. V. de Aldana, “Three-dimensional femtosecond laser micromachining of dielectric crystals for photonic waveguiding applications,” *Pacific Rim Laser Damage 2015 Opt. Mater. High-Power Lasers*, vol. 9532, p. 95320M, Jul. 2015, doi: 10.1117/12.2182861.

[97] N. Pavel, G. Salamu, F. Jipa, and M. Zamfirescu, “Diode-laser pumping into the emitting level for efficient lasing of depressed cladding waveguides realized in Nd:YVO4 by the direct femtosecond-laser writing technique,” *Opt. Express*, vol. 22, no. 19, pp. 23057–23065, Sep. 2014, doi: 10.1364/OE.22.023057.

[98] P. Diamet, *Wave Transmission and Fiber Optics*. New York: Macmillan, 1990.

[99] A. G. Okhrimchuk, Y. P. Yatsenko, M. P. Smayev, V. V Koltashev, and V. V Dorofeev, “Nonlinear properties of the depressed cladding single mode TeO2-WO3-Bi2O3 channel waveguide fabricated by direct laser writing,” *Opt. Mater. Express*, vol. 8, no. 11, pp. 3424–3437, Nov. 2018, doi: 10.1364/OME.8.003424.

[100] B. Bendow and P. D. Gianino, “Optics of Thermal Lensing in Solids,” *Appl. Opt. Vol. 12, Issue 4, pp. 710-718*, vol. 12, no. 4, pp. 710–718, Apr. 1973, doi: 10.1364/AO.12.000710.

[101] H. Kogelnik and T. Li, “Laser Beams and Resonators,” *Appl. Opt.*, vol. 5, no. 10, pp. 1550–1567, Oct. 1966, doi: 10.1364/AO.5.001550.

[102] N. Davidson, U. Levy, and Y. Silberberg, “Mathematics of vectorial Gaussian beams,” *Adv. Opt. Photonics, Vol. 11, Issue 4, pp. 828-891*, vol. 11, no. 4, pp. 828–891, Dec. 2019, doi: 10.1364/AOP.11.000828.

[103] E. Zauderer, “Complex argument Hermite–Gaussian and Laguerre–Gaussian beams,” *JOSA A, Vol. 3, Issue 4, pp. 465-469*, vol. 3, no. 4, pp. 465–469, Apr. 1986, doi: 10.1364/JOSAA.3.000465.

[104] M. G. Littman and X. Wang, “Laser cavity for generation of variable-radius rings of light,” *Opt. Lett. Vol. 18, Issue 10, pp. 767-768*, vol. 18, no. 10, pp. 767–768, May 1993, doi: 10.1364/OL.18.000767.

[105] W. T. Silfvast, *Laser Fundamentals*, 2nd ed. 2008.

[106] V. Ter, “Fundamentals of Fiber Lasers and Fiber Amplifiers,” *Springer Ser. Opt. Sci.*, vol. 181, pp. 1–6, 2014, doi: 10.1007/978-3-319-02338-0_1.

[107] A. Fresnel, *Mémoire sur la double réfraction que les rayons lumineux éprouvent en traversant les aiguilles de cristal de roche suivant les directions parallèles à l’axe*. 1825.

[108] X. Mateos *et al.*, “Efficient Micro-Lasers Based on Highly Doped Monoclinic Double Tungstates,” *IEEE J. Quantum Electron.*, vol. 53, no. 3, Jun. 2017, doi: 10.1109/JQE.2017.2681626.

[109] M. C. Pujol *et al.*, “Structural redetermination, thermal expansion and refractive indices of KLu(WO4)2,” *J. Appl. Crystallogr.*, vol. 39, no. 2, pp. 230–236, Apr. 2006, doi: 10.1107/S0021889806004328.

[110] R. J. Beach, “CW Theory of quasi-three level end-pumped laser oscillators,”

Opt. Commun., vol. 123, no. 1–3, pp. 385–393, Jan. 1996, doi: 10.1016/0030-4018(95)00497-1.

[111] D. Findlay, R. A. Clay, D. Findlay, and R. A. Clay, "The measurement of internal losses in 4-level lasers," *PhL*, vol. 20, no. 3, pp. 277–278, Feb. 1966, doi: 10.1016/0031-9163(66)90363-5.

[112] J. A. Caird, S. A. Payne, P. R. Staver, A. J. Ramponi, L. L. Chase, and W. F. Krupke, "Quantum Electronic Properties of the Na3Ga2Li3F12:Cr3+ Laser," *IEEE J. Quantum Electron.*, vol. 24, no. 6, pp. 1077–1099, 1988, doi: 10.1109/3.231.

[113] J. Morris *et al.*, "1.9 \&\#x00B5;m waveguide laser fabricated by ultrafast laser inscription in Tm:Lu2O3 ceramic," *Opt. Express*, vol. 25, no. 13, pp. 14910–14917, Jun. 2017, doi: 10.1364/OE.25.014910.

[114] A. E. Siegman, "Defining, measuring, and optimizing laser beam quality," *Laser Reson. Coherent Opt. Model. Technol. Appl.*, vol. 1868, pp. 2–12, Aug. 1993, doi: 10.1117/12.150601.

[115] A. E. Siegman, "New developments in laser resonators," *Opt. Reson.*, vol. 1224, pp. 2–14, Jun. 1990, doi: 10.1117/12.18425.

[116] Y. Niu, Y. Wang, X. Liu, C. Zhang, and S. Zhu, "Laser beam quality factor M2 and its measurement," *Laser Process. Mater. Ind. Appl. II*, vol. 3550, pp. 378–382, Aug. 1998, doi: 10.1117/12.317915.

[117] A. A. Hilal, "The lambda calculus: Its syntax and semantics."

[118] Q. Li, X. He, Y. Wang, H. Liu, D. Xu, and F. Guo, "Review of spectral imaging technology in biomedical engineering: achievements and challenges," *J. Biomed. Opt.*, vol. 18, no. 10, p. 100901, Oct. 2013, doi: 10.1117/1.JBO.18.10.100901.

[119] S. A. Macenka and M. P. Chrisp, "Airborne Visible/Infrared Imaging Spectrometer (Aviris) Spectrometer Design And Performance," *Imaging Spectrosc. II*, vol. 0834, pp. 32–43, Jan. 1987, doi: 10.1117/12.942281.

[120] W. E. Bicknell, C. J. Digenis, S. E. Forman, and D. E. Lencioni, "EO-1 Advanced Land Imager," *Earth Obs. Syst. IV*, vol. 3750, pp. 80–88, Sep. 1999, doi: 10.1117/12.363501.

[121] M. Halicek, H. Fabelo, S. Ortega, G. M. Callico, and B. Fei, "In-vivo and ex-vivo tissue analysis through hyperspectral imaging techniques: Revealing the invisible features of cancer," *Cancers (Basel).*, vol. 11, no. 6, Jun. 2019, doi:

10.3390/CANCERS11060756.

[122] P. R. Griffiths and J. A. De Haseth, “Fourier Transform Infrared Spectrometry, 2nd Edition,” *Wiley-Interscience*, p. 278, 2007, Accessed: Jul. 20, 2021. [Online]. Available: https://books.google.com/books/about/Fourier_Transform_Infrared_Spectrometry.html?hl=es&id=C_c0GVe8MX0C.

[123] J. W. Brault, “New approach to high-precision Fourier transform spectrometer design,” *Appl. Opt. Vol. 35, Issue 16, pp. 2891-2896*, vol. 35, no. 16, pp. 2891–2896, Jun. 1996, doi: 10.1364/AO.35.002891.

[124] K. P. Zetie, S. F. Adams, and R. M. Tocknell, “How does a Mach-Zehnder interferometer work?,” Accessed: Jul. 20, 2021. [Online]. Available: www.qubit.org.

[125] M. T. Heideman, D. H. Johnson, and C. S. Burrus, “Gauss and the History of the Fast Fourier Transform,” *IEEE ASSP Mag.*, vol. 1, no. 4, pp. 14–21, 1984, doi: 10.1109/MASSP.1984.1162257.

[126] C. E. Shannon, “Communication in the Presence of Noise,” *Proc. IRE*, vol. 37, no. 1, pp. 10–21, 1949, doi: 10.1109/JRPROC.1949.232969.

[127] V. P. Tuzlukov, *Signal processing noise*. CLC press LLC, 2002.

[128] M. A. Mohamed, J. Jaafar, A. F. Ismail, M. H. D. Othman, and M. A. Rahman, “Fourier Transform Infrared (FTIR) Spectroscopy,” *Membr. Charact.*, pp. 3–29, Jan. 2017, doi: 10.1016/B978-0-444-63776-5.00001-2.

[129] M. P. Raele, L. V. G. Tarelho, C. L. da Silva Azeredo, I. B. Couceiro, and A. Z. Freitas, “Improving axial resolution in spectral domain low-coherence interferometry through fast Fourier transform harmonic artifacts,” *Opt. Eng.*, vol. 53, no. 7, p. 073106, Jul. 2014, doi: 10.1117/1.OE.53.7.073106.

[130] S. Son, H. Park, and K. H. Lee, “Automated laser scanning system for reverse engineering and inspection,” *Int. J. Mach. Tools Manuf.*, vol. 42, no. 8, pp. 889–897, Jun. 2002, doi: 10.1016/S0890-6955(02)00030-5.

[131] T. Schenkel, M. A. Briere, H. Schmidt-Böcking, K. Bethge, and D. H. Schneider, “Electronic Sputtering of Thin Conductors by Neutralization of Slow Highly Charged Ions,” *Phys. Rev. Lett.*, vol. 78, no. 12, p. 2481, Mar. 1997, doi: 10.1103/PhysRevLett.78.2481.

[132] J. H. Weaver and S. Babar, “Optical constants of Cu, Ag, and Au revisited,” *Appl. Opt. Vol. 54, Issue 3, pp. 477-481*, vol. 54, no. 3, pp. 477–481, Jan. 2015,

doi: 10.1364/AO.54.000477.

[133] H. J. R. Dutton, “Understanding optical communications,” p. 760, 1998.

[134] J. M. Senior, *Optical Fiber Communications Principles and Practice Third Edition Optical Fiber Communications Optical Fiber Communications Principles and Practice Third Edition*, 3rd ed. 2009.

[135] B. Lee, “Review of the present status of optical fiber sensors,” *Opt. Fiber Technol.*, vol. 9, no. 2, pp. 57–79, Apr. 2003, doi: 10.1016/S1068-5200(02)00527-8.

[136] M. Baygin, M. Karakose, A. Sarimaden, and E. Akin, “Machine vision based defect detection approach using image processing,” *IDAP 2017 - Int. Artif. Intell. Data Process. Symp.*, Oct. 2017, doi: 10.1109/IDAP.2017.8090292.

LIST OF PUBLICATIONS

The results of this thesis are based on the work of following publications and conferences.

[Paper 1] **Victor Llamas**, Pavel Loiko, Esrom Kifle, Carolina Romero, Javier R. Vázquez de Aldana, Zhongben Pan, Josep Maria Serres, Hualei Yuan, Xiaojun Dai, Huaqiang Cai, Yicheng Wang, Yongguang Zhao, Viktor Zakharov, Andrey Veniaminov, Romain Thouroude, Mathieu Laroche, Hervé Gilles, Magdalena Aguiló, Francesc Díaz, Uwe Griebner, Valentin Petrov, Patrice Camy, and Xavier Mateos, **"Ultrafast laser inscribed waveguide lasers in Tm:CALGO with depressed-index cladding**," Opt. Express 28, 3528-3540 (2020)

https://doi.org/10.1364/OE.384258

[Paper 2] Esrom Kifle, Pavel Loiko, Javier Rodríguez Vázquez de Aldana, Carolina Romero, **Víctor Llamas**, Josep Maria Serres, Magdalena Aguiló, Francesc Díaz, Lizhen Zhang, Zhoubin Lin, Haifeng Lin, Ge Zhang, Viktor Zakharov, Andrey Veniaminov, Valentin Petrov, Uwe Griebner, Xavier Mateos, Li Wang, and Weidong Chen, **"Low-loss fs-laser-written surface waveguide lasers at >2 µm in monoclinic Tm3+:MgWO4,"** Opt. Lett. 45, 4060-4063 (2020)

https://doi.org/10.1364/OL.395811

[Paper 3] **Victor Llamas**, Pavel Loiko, Esrom Kifle, Carolina Romero, Javier R. Vázquez de Aldana, Josep Maria Serres, Magdalena Aguiló, Francesc Díaz, Uwe Griebner, Valentin Petrov, Patrice Camy, and Xavier Mateos, **"Lasing**

properties of funnel and double funnel femtosecond-direct laser writing waveguides in 3%Tm:Kluw crystals," (In Progress to be submitted)

[Paper 4] **Victor Llamas**, Carolina Romero, Javier R. Vázquez de Aldana, Josep Maria Serres, Magdalena Aguiló, Francesc Díaz, Uwe Griebner, Valentin Petrov, and Xavier Mateos, **"Femtosecond-direct laser writing waveguide photonics-based sensing in MgF2 crystals,"** (In Progress to be submitted)

[Paper 5] **Victor Llamas,** Josep Maria Serres, Magdalena Aguiló, Francesc Díaz, and Xavier Mateos, **"Structured light profilometer system to measure imperfections in metallic surfaces,"** (In Progress to be submitted)

[Paper 6] **Victor Llamas,** Josep Maria Serres, Magdalena Aguiló, Francesc Díaz, and Xavier Mateos, **"Profilometry system applied to the development of a non-touch screen,"** (In Progress to be submitted)

[Paper 7] **Victor Llamas**, Josep Maria Serres, Magdalena Aguiló, Francesc Díaz, and Xavier Mateos, **"Machine vision system for detection of needles and tabs issues in circular knitting machines,"** (In Progress to be submitted)

[Paper 8] **Victor Llamas,** Josep Maria Serres, Magdalena Aguiló, Francesc Díaz, and Xavier Mateos, **"Nonflammable optical encoder,"** (In Progress to be submitted)

[Paper 9] **Victor Llamas**, Josep Maria Serres, Magdalena Aguiló, Francesc Díaz, and Xavier Mateos, **"Structured light profilometer system to measure wear in metallic molds,"** (In Progress to be submitted)

[Conf 1] E. Kifle, P. Loiko, **V. Llamas,** C. Romero, J. R. V. de Aldana, Z. Pan, J. M. Serres, H. Yuan, X. Dai, H. Cai, Y. Wang, Y. Zhao, M. Aguiló, F. Díaz, U. Griebner, V. Petrov, P. Camy, and X. Mateos, **"Ultrafast Laser Inscribed Waveguide Lasers in Tm:CALGO,"** in Laser Congress 2019 (ASSL, LAC, LS&C), OSA Technical Digest (Optical Society of America, 2019), paper AM3A.5.

https://doi.org/10.1364/ASSL.2019.AM3A.5

[Conf 2] **V. Llamas,** P. Loiko, E. Kifle, C. Romero, J. R. Vázquez de Aldana, J. M. Serres, MauroTonelli, E. Damiano, V. Zakharov, A. Veniaminov, M. Aguiló, F. Díaz, W. Chen, U. Griebner, V. Petrov, and X. Mateos, "**Ultrafast Laser Inscribed Waveguide Lasers in Tm3+:SrF2,**" in Conference on Lasers and Electro-Optics, OSA Technical Digest (Optical Society of America, 2020), paper SM3E.7.

https://doi.org/10.1364/CLEO_SI.2020.SM3E.7

During the thesis was achieved a register of patent, work not related to the study:

- European Patent Application no. 20382945.2, 3D printing device and 3D printing method
- International Application PCT / EP2021 / 080095, with priority of European Patent Application no. 20382945.2

ANNEX

Annex 1. Hardware

Sony XCG-CP51 Camera.

Polarimetric camera created by the SONY company. It has a sensor with polarizing filters at 0º, 45º, 90º and 135º capable of accurately determining the state of polarization of the incident light. This model, named Polarsens, is optimized for use within the artificial vision markets. The polarized camera features Power over Ethernet, PoE that enables power and information transfer with a single standard LAN infrastructure.

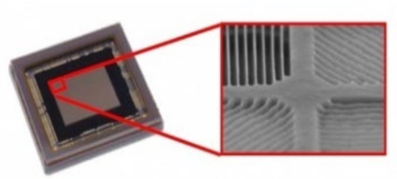

The main characteristics of the polarimetric camera are:

- 2k resolution, 2448 (H) x 2044 (V) with a speed of 23 fps with GigW Vision 1.2 / 2.0 with PoE cable
- The SNY-XPL-SDKW software is programmed from the factory with several modes that optimize the contrast between different polarization states, thus making it possible to magnify the defects on the surfaces.
- Uses polarized monochromatic filters to capture polarized light in four different planes: at 0º, 45º, 90º and 135º.
- Market technology Pregius Global Shutter High sensitivity CMOS capable of taking images at high speed without aberrations.

Ultrafast camera TIS-DMK-33UX264.

Commercial camera by The Imagining Source company. The model is the TIS-DMK-33UX264 with a Sony IMX264 sensor, USB 3.0 PC connection technology, 2448x2048 resolution and with a video capture of 35 images per second (FPS). To improve image capture, the sensor works with the Global Shutter CMOS image capture method. This operating method allows it to collect all the information at the same time without having any delay shutter.

OSL2 Halogen lamp.

Halogen lamp with three different outputs; High-Intensity Fiber bundle (fig.), FC / PC and SMA. This device works as an incoherent light source with a broad spectrum. Its main characteristics are:

- 50 W, 3200 K Halogen Bulbs
- OSL2 Comes with Pre-Installed OSL2B Bulb with Integrated Hot Mirror to Block Most IR Light
- Continuously Variable Output Power via Front Panel Knob
- SM1-Threaded Output Port with 91 cm (36") Long Fiber Bundle

These light sources have a built-in protection mechanism to prevent the unit from overheating and to turn off the lamp when the access door is opened. The LED indicator on the front panel is green during normal operation. If the unit overheats or if the access door is opened, power to the lamp is cut off and the LED turns red.

The OSL2 comes with a pre-installed OSL2B bulb that has an integrated hot mirror that blocks the majority of the IR light, having a typical wavelength range of 400 - 1600 nm, as can be seen in **Figure 36**.

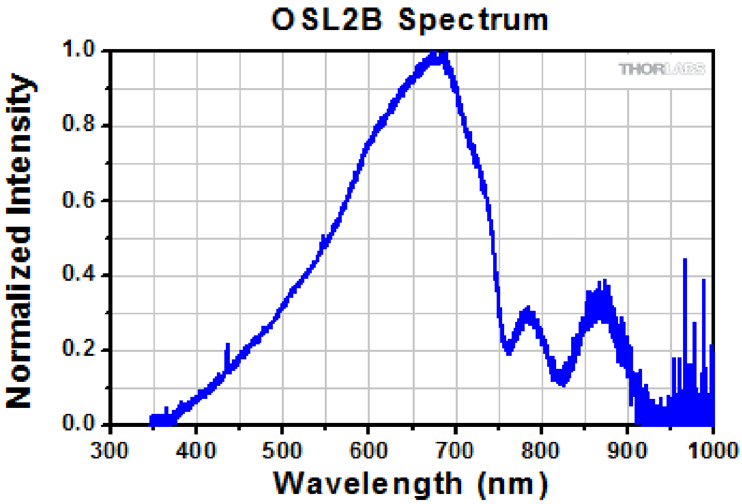

Figure 41. Emission spectrum of the OSL2 halogen lamp.

Bifurcated optical fiber BFY400HS02

Bifurcated Fiber Bundles, also known as fanout or Y-cables, are constructed from two high-grade optical fibers encased in stainless steel tubing for durability. ZrF_4 fiber bundles are particularly advantageous for spectroscopy, as they offer exceptionally broad transmission from the UV into the N-IR (400 nm – 2.2 µm).

All three ends of the cable are terminated with SMA905 connectors 400 µm core size. The stainless-steel sleeves of the connectors on the breakout legs of the cable are engraved to indicate the fiber type in each leg. The sleeve of the common connector is engraved with the fiber core size and numerical aperture (NA).

One leg of each bundle contains both fibers before passing through a junction where the cable splits into two legs, each containing a single fiber. Cables are 2 m long from the common end to the split ends. The two legs are threaded through a sliding clamp so that the breakout length of the cable can be adjusted. The clamp can be locked in place by tightening the 5/64" (2 mm) hex setscrew.

When using the common end as the input, these cables perform best when used with sources that provide even illumination across both fiber cores, such as LEDs with a large emitter angle or white light sources like OSL2 Halogen lamp. The general specifications of this bundle can be seen in **Figure 36.**

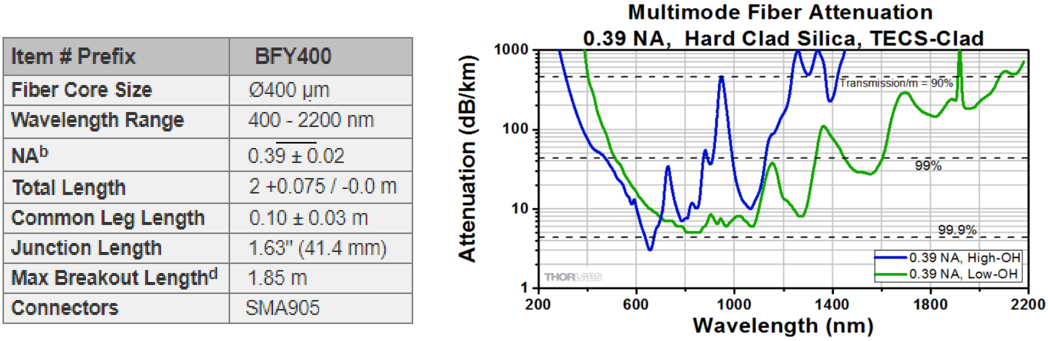

Item # Prefix	BFY400
Fiber Core Size	Ø400 µm
Wavelength Range	400 - 2200 nm
NA^b	0.39 ± 0.02
Total Length	2 +0.075 / -0.0 m
Common Leg Length	0.10 ± 0.03 m
Junction Length	1.63" (41.4 mm)
Max Breakout Length^d	1.85 m
Connectors	SMA905

Figure 42. BFY400HS02 Specifications (left) and attenuation curve (right)

SM1PD1B Detector

Photodiode of Si material mounted in convenient SM1 (1.035"-40) externally threaded tubes. The electrical output of the photodiode is provided through a standard SMA connector (SM05PD Series) for quick connection to the measuring circuit.

The photodiode come in a cathode grounded arrangement. This model is ideal for measuring pulsed and CW sources. The insulated external thread on the main body makes these photodiodes compatible with all Thorlabs SM1 Mounting Adapters. All the specifications are showed in **Figure 38.**

Please note that inhomogeneities at the edges of the active area of the detector can generate unwanted capacitance and resistance effects that distort the time-domain response of the photodiode output. Thorlabs therefore recommends that the incident light on the photodiode is well centered on the active area. This can be accomplished by placing a focusing lens or pinhole in front of the detector element.

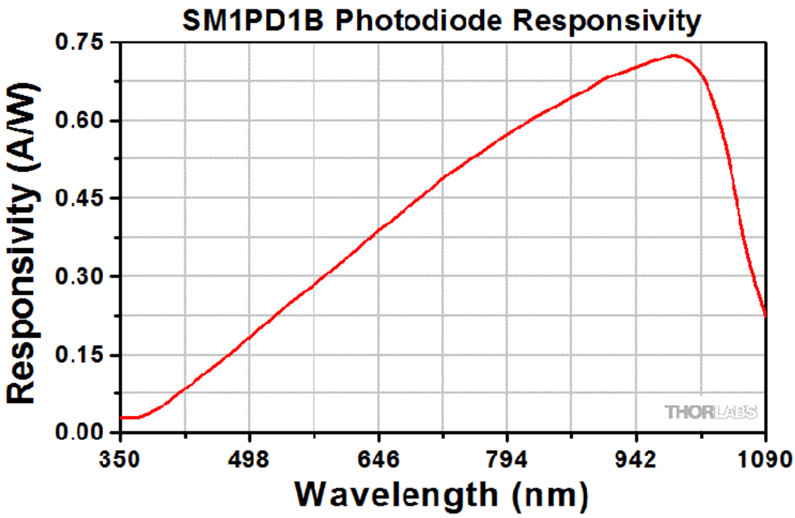

Rise/fall Time	65ns @632nm, 5V
Active area	10mmx10mm
NEP(W/Hz$^{1/2}$)	2.7·10^{13}
Dark Current	600nA @5V
Spectral range (nm)	350-1100
Material	Si
Junction capacitance	375pF @5V
Reverse Bias Voltaje	25V

Figure 43. SM1PD1B detector and Photodiode specs and responsivity.

DAQ model NI-USB-6212

USB Multifunction I / O Device, 16 AI (16 Bit, 400 kS / s), 2 AO (250 kS / s), Up to 32 DIO — The USB 6212 is a multifunction DAQ device. It offers analog input, digital input, digital output, and two 32-bit counters. The device provides a built-in amplifier designed for quick setups at high scan speeds. It also features NI Signal Streaming technology that enables high-speed, DMA-like, bi-directional data transfer over the USB bus. The device is ideal for design, control and test applications including portable data logging, field monitoring, embedded OEMs, vehicle data acquisition, and academic applications. The USB 6212 has a lightweight mechanical housing and is bus-powered for easy portability. The included NI DAQmx driver and configuration utility simplify configuration and measurements. They simplify configuration and measurements. All the technical data can be found in https://www.ni.com/pdf/manuals/375196d.pdf .

Femtosecond Laser Mira 900 coherent

Mira-900 is a Ti:Sa laser system pumped by a verdi Nd:YAG laser able to generate tunable laser radiation between 700nm-900nm in continuous-wave (fig..), and picosecond-femtosecond laser pulses, while passive Kerr lens modelocking provides greater ease-of-use and reliability.

The Optima control and diagnostics system enables easy adjustment of the output wavelength, pulse width and power. Optima features a fast photodiode, relative power monitor, ß-lock, CW detector, humidity sensor and an automatic starter. All the technical features can be seen in https://www.coherent.com/assets/pdf/Mira-Optima-900-D-Data-Sheet.pdf .

Features & Benefits

- Simple stable Kerr lens modelocking for ease-of-use and reliability.
- Femtosecond, picosecond, and continuous-wave operation.
- X-Wave single optics set allows wavelength tuning from 700 nm to 1000 nm.
- Verdi 532 nm pump sources between 5W and 12W deliver diode-pumped.
- Optima system provides advanced system monitoring and control.
- Sealed purgeable enclosure results in higher reliability and full wavelength coverage.
- Integrated pump steering optics make pump alignment easy.
- Auxiliary CW cavity for general setup and continuous- wave operation.

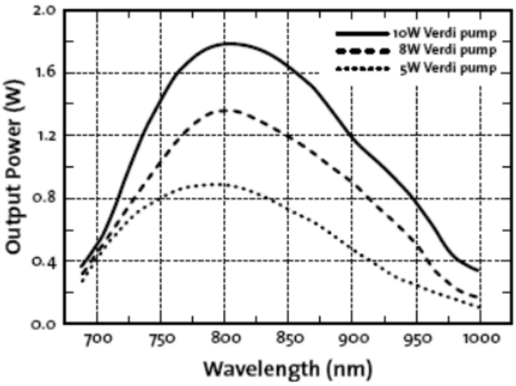

Figure 44. Typical tunning curve for Verdi pumped Mira Optima 900-F

Powermeter S405C

Thermal Power Sensor able to detect power ranges from 10 µW to 5 W and wavelength ranges from 190 nm to 20 µm (Fig..). This thermopile-based sensor is ideal choices for measuring broadband spectra from amplified spontaneous emission (ASE) sources, light emitting diodes (LEDs), filament lamps, swept-wavelength lasers, and other sources. In addition, thermal power sensors do not saturate, which makes them well suited to measuring pulsed sources with high pulse peak powers or long-duration pulses. These thermal power sensors also exhibit low dependency on the angle and position of the incident light beam. They are preferred for applications that cannot tolerate the strong wavelength dependencies and/or saturation thresholds of photodiode sensors. However, thermal power sensors generally have lower power resolutions and longer response times. All the specifications can be seen in Figure 39.

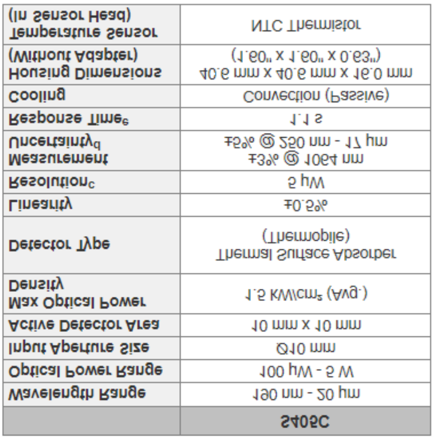

	S405C
Wavelength Range	190 nm - 20 µm
Optical Power Range	100 µW - 5 W
Input Aperture Size	Ø10 mm
Active Detector Area	10 mm x 10 mm
Max Optical Power Density	1.5 kW/cm² (Avg.)
Detector Type	Thermal Surface Absorber (Thermopile)
Linearity	±0.5%
Resolution[c]	5 µW
Measurement Uncertainty[d]	±3% @ 1064 nm ±5% @ 250 nm - 17 µm
Response Time[e]	1.1 s
Cooling	Convection (Passive)
Housing Dimensions (Without Adapter)	40.6 mm x 40.6 mm x 16.0 mm (1.60" x 1.60" x 0.63")
Temperature Sensor (In Sensor Head)	NTC Thermistor

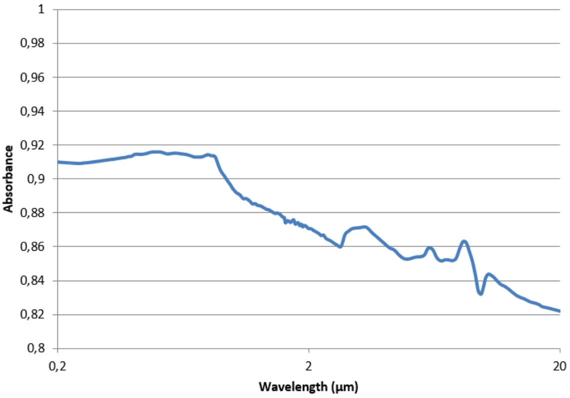

Figure 45. S405C Specifications (left) and absorbance curve (right).

IO-5-NIR-LP Optical Isolator

Optical isolators, also known as Faraday isolators, are magneto-optic devices that preferentially transmit light along a single direction, shielding upstream optics from back reflections. Back reflections can create a number of instabilities in light sources, including intensity noise, frequency shifts, mode hopping, and loss of mode lock. In addition, intense back-reflected light can permanently damage optics. This device has a peak isolation at 800nm, ideal for our needs. All the specifications can be seen in **Figure 41.**

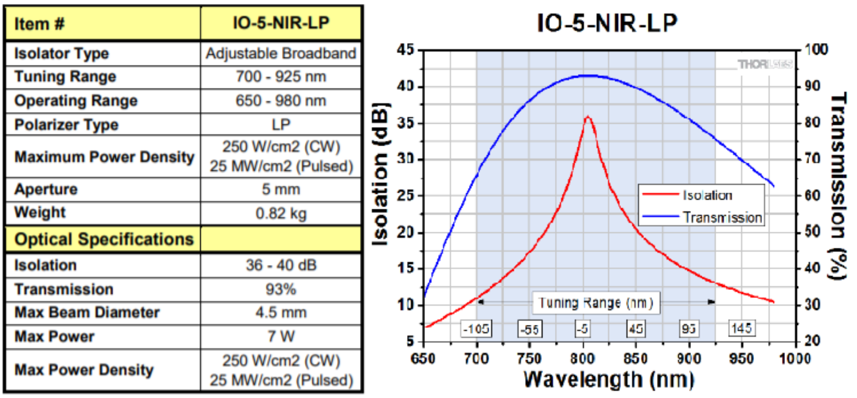

Item #	IO-5-NIR-LP
Isolator Type	Adjustable Broadband
Tuning Range	700 - 925 nm
Operating Range	650 - 980 nm
Polarizer Type	LP
Maximum Power Density	250 W/cm2 (CW) 25 MW/cm2 (Pulsed)
Aperture	5 mm
Weight	0.82 kg
Optical Specifications	
Isolation	36 - 40 dB
Transmission	93%
Max Beam Diameter	4.5 mm
Max Power	7 W
Max Power Density	250 W/cm2 (CW) 25 MW/cm2 (Pulsed)

Figure 46. Specifications (left) and optical isolation for the IO-5-NIR-LP optical isolator.

Optical spectrum analyzer AQ6375B, Yokogawa

The AQ6375B is a bench-top optical spectrum analyzer covering the long wavelengths, 1200 to 2400 nm, with the added benefits of gas purging input ports / output ports, a built-in cut filter for high order diffracted light, and a novel double speed mode which increases the sweep speed up to 2 times compared to the standard sweep mode.

Key feature summary:

- Long wavelength range: 1200 to 2400 nm.
- Gas purging ports to reduce water vapor effects.
- Built-In cut filter for high order diffracted light.
- Double Speed Mode to further enhance fast measurement speed.
- High sensitivity down to -70 dBm.
- High resolution to 0.050 nm.
- Wide close-in dynamic range (55dB).
- Fast auto-calibration.
- Free space optical input for maximum flexibility, low maintenance, and high reliability.
- Applicable to single-mode and multimode fibers.
- Excellent performance for environmental gas sensing Laser Spectroscopy.
- Indispensable tool for R&D and manufacturing of optical devices in the wavelength range from telecom band to 2.4µm.

FIND-R-SCOPE 85726 Near-IR Camera

The FIND-R-SCOPE®85726 is a Visible to Short-Wavelength Infrared camera operating in the 400-2200nm region of the electromagnetic spectrum. The camera includes an On-Board Electronic Viewfinder. These cameras utilize proven infrared viewing technology. The high-resolution infrared vidicon tube CCTV camera generates a clear view of objects, sources & images which cannot otherwise be seen with the naked eye. The specifications of this camera are shown in Figure 41.

This camera is coupled to a computer using a composite video to usb adapter operating thanks to a homemade matlab code.

Spectral Sensitivity	400-2200 nm (0.4 – 2.2 microns)
Output Signal	NTSC or PAL Video, 1Vp-p composite
Detector	25mm High Performance Infrared Vidicon
Output Connector	BNC
Standard Lens	“C” Mount 25 mm, ƒ/1.4 with manual iris
Gain	Selectable, Auto Gain and 4 fixed values
Standard Focal Range	101 mm, (4") to infinity
Regions Displayed	Visible, Near-IR, Short Wave-IR
Peak Sensitivity	600nm
Horizontal Resolution	Up to 700 TV Lines
Scanning (NTSC)	525 Lines/60 Fields/30 Frames
Scanning (PAL)	625 Lines/50 Fields/25 Frames
Power	100-240 Vac, 50/60Hz. 36 volts to camera
Signal to Noise Ratio	68db
Image Lag	45-60% after 3 TV fields (50ms)
External Connection	RS-170 Video Output via BNC Connector
Dimensions (w/o lens)	110.3 x 111.2 x 216.4 mm

Figure 47. Specs of the FIND-R-SCOPE 85726 Near-IR Camera.

Zaber X-XY-LSM100A

The X-XY-LSM100A is a two axis motorized stage manufactured by the Zaber company. It is made up of two high precision motorized linear guides easily programmable and compatible witch some standard softwares like labview and matlab with this following characteristics:

- 100mm per axis travel
- 50nm resolution per step
- 7um position precision
- 5kg maximum wheight

Annex 2. Code.

FTIR

```
%% Constants
l0=0.5e-6; %Lambda 0
lf=2e-6; %lambda final
N=4000;       %number of points in this axis
c=3e8;        %Speed of light

ruidox=0.05;  %Position noise
ruidoI=0.05;  %Intensity noise

nuf=2*pi*c/l0; %starting angular frequency
nu0=2*pi*c/lf; %ending angular frequency
dnu=2*pi*c/(lf-l0)/N; % diferential de frec angular

 nu=nu0:dnu:nuf;
 lambda0=2*pi./nu*c*10^6;

 %% An angular frequency function is created
 anchura=1e-13;
lc=.5e-6;
nuc=2*pi*c/lc;

% %Lorentzian
% funcion=1./((anchura*(nu-nuc)).^2+1);
 % %Gaussian
% funcion=exp(-1*(anchura*(nu-nuc)).^2);
 % Doble lorentzian
nuc2=2.5*pi*c/lc;
funcion=1./((anchura*(nu-nuc)).^2+1)+1./((anchura*(nu-
nuc2)).^2+1);

%% A gate function is created, which imitates the gain of the
detector
anchgate=2e-15;
lgate=1.5e-6; %lambda central
nugate=2*pi*c/lgate; %frec angular final
% lorentzian
gate=1./((anchgate*(nu-nugate)).^2+1);
% % no gate
% gate=ones(1,length(nu));
%% Here starts the experimet. By moving one mirror and creating an
interferential figure
xmax=1e-2;
dx=0.501e-6;
x=-xmax/2:dx:xmax/2;
x0=100;

 E1=funcion.*exp(1i/c.*nu*x0);
```

```
 %Nosie filters
 x2=100+x-dx/2+ruidox*dx*rand(1,length(x)); % Filtro de ruido
E2=funcion.*exp(1i/c.*nu.*x2');
 I=zeros(length(x),1);
 for i=1:length(x)
    I(i)=sum((abs(E1+E2(i,:)).^2).*gate);
end
I=I+max(I)*ruidoI*(rand(length(I),1)-0.5);

figure(1)
plot(lambda0,abs(E1),lambda0,gate)
title('Original Spectrum')
xlabel('lambda(nm)')
ylabel('I(A.U)')
 figure(2)
plot(x*100,I)
title('Interference pattern ')
xlabel('X-X_0(mm)')
ylabel('I(A.U)')

%% Applying the fast Fourier transform
 numax=pi/dx*c;
dnu2=2*pi*c/length(x)/dx;
nu2=-numax+dnu2:dnu2:numax;

Inueva=fftshift(fft(I));
figure(3)
plot(nu2,abs(Inueva))
title('FFT Interference pattern ')
xlabel('Spatial frecuency (1/m)')
ylabel('I(A.U)')

%% We focus only in the part we need

Irango=Inueva(round(length(Inueva)*0.65):round(length(Inueva)*1))
;
Irango=Irango/(max(Irango));
nurango=nu2(round(length(nu2)*0.65):round(length(nu2)*1));
 lambda1=2*pi./nurango*c*10^6;

figure(4)
plot(lambda1,sqrt(abs(Irango)),lambda0,abs(E1))
title('Retrieved spectrum ')
xlabel('lambda(nm)')
ylabel('I(A.U)')
```

UNIVERSITAT
ROVIRA i VIRGILI

eurecat
Centre Tecnològic de Catalunya